Universidade de Santiago de Compostela
Facultade de Fisica
Departamento de Fisica Aplicada

Self Assembled Photonic-Plasmonic Crystals for Light control at the Nanoscale

Cristais Fotónico Plasmónicos Autoensamblados para o control da luz na Nanoescala

Memoria presentada para obter o grao de Doutor en Fisica por
Memoria presentada para obtener el grado de doctor en Fisica por :

Martín López García

Tesis dirixida por / Tesis dirigida por:

Prof. Ceferino López Fernández
Dr. Juan Francisco Galisteo López

Titor / Tutor:

Prof. Vicente Moreno de las Cuevas

Consejo Superior de Investigaciones Cientificas (CSIC)
Instituto de Ciencia de Materiales de Madrid (ICMM)

Xuño 2011

Á Sara

Ós meus pais

Summary

This thesis is the result of more than five years of research on the study of several kind of photonic and plasmonic systems. Main body of this research has been performed in the Photonics Crystals Group at the Material Science Institute of Madrid, (center belonging to the national research council of Spain-CSIC) under the supervision of Prof. Ceferino López Fernandez and Dr. Juan F. Galisteo Lopez. As component of a experimentalist team, most of the experimental work presented in this thesis has been performed in the laboratories of the group. All the samples shown in this manuscript were grown and modify by different processes in the Photonic Crystal's Group chemical laboratories. The whole optical measurements (as well as the set-up for implementation Fourier imaging spectroscopy described in chapter 3) where performed at the optics group's laboratory as a main part of this thesis. The metallic films of gold and silver used as part of the samples were deposited by sputtering by Dr. Jorge Sanchez and Dr. Eva Cespedes from the Group of Electronic and Magnetic Materials and Heterostructures at the ICMM-CSIC. The AFM measurements shown in chapter 2 were performed with the help of Dr. Jorge Sanchez. The ellipsometry measurements to determine the refractive index of the materials forming the here studied structures were performed at the Institute of Microelectronics of Madrid by Prof. Gaspar Armelles. The FDTD calculations shown all along this thesis are the result of a collaboration with Dr. Antonio Garcia-Martin from the Institute of Microelectronics of Madrid.

Finally, i can't help to mention some other important work, not directly related with this thesis but which provided expertise directly related with the results here presented. In the first stage of this five years, research on the properties of opal based photonic crystals doped with metallic nanoparticles (gold) was performed in collaboration with the Colloidal Chemistry Group from the University of Vigo lead by Prof. Luis Marzán. Much of my background on plasmonics come from the investigation on metallic nanoparticles in opals performed within this collaboration. On the other hand, during the last three years, a permanent collaboration was established with the groups leaded by Prof. Anna Roig and Prof. Josep Fontcuberta in the Material Science Institute of Barcelona. In that research, the magnetoptical properties of colloidal photonic crystals infiltrated with magnetic nanoparticles was achieved. Although this issues are not included in this thesis, very useful knowledge on how to improve the optical spectroscopy set-up described in chapter 3 was retrieved from that collaboration and then applied to the subject of this thesis. Finally, i have to mention the collaboration with the group of Dr. Juiàn Rodríguez-Lòpez of the Faculty of Chemistry at the Universidad de Castilla la Mancha which reported me experience on fluorescence spectroscopy of organic molecules (in particular fluorescence dendrons) distributed within 3D colloidal photonic crystals. The work described in this

thesis has been reported in the following conferences and papers:

Publications in international journals:

- *"Intrinsic losses in self-assembled hybrid metallodielectric systems."* J. F. Galisteo-Lopez, M. Lopez-Garcia, A. Garcia-Martín and C. Lopez. Submitted (2011).
- *"Enhancement and Directionality of Spontaneous Emission in Hybrid Self-Assembled Photonic-Plasmonic Crystals."* M. Lopez-Garcia, J. F. Galisteo-Lopez, J. Sánchez-Marcos, C. Lopez and A. Garcia-Martín. Small 6(16): 1757-1761 (2010).
- *"High Degree of Optical Tunability of Self-Assembled Photonic-Plasmonic Crystals by Filling Fraction Modification."* M. López-García, J. F. Galisteo-López, C. Lopez and A. Garcia-Martín. Advanced Functional Materials 20(24): 4338-4343 (2010).
- *"Magnetophotonic Response of Three-Dimensional Opals."* J.M. Caicedo, O. Pascu, M. Lopez-Garcia, V. Canalejas, A. Blanco, C. Lopez, J. Fontcuberta, A. Roig and G. Herranz. ACS Nano 5(4): 2957-2963 (2010).
- *"New poly(phenylenevinylene)-methyl methacrylate-based photonic crystals."* S. Achelle, A. Blanco, M. Lopez-Garcia, R. Sapienza, M. Ibisate, C. Lopez and J. Rodriguez-Lopez. Journal of Polymer Science Part A: Polymer Chemistry 48(12): 2659-2665 (2010).
- *"Facile route to magnetophotonic crystals by infiltration of 3D inverse opals with magnetic nanoparticles."* J.M. Caicedo, E.Taboada, D.Hrabovsky, M. Lopez-Garcia, G. Herranz, A. Roig, A.Blanco, C. López and J. Fontcuberta. Journal of Magnetism and Magnetic Materials 322(9-12): 1494-1496 (2009).

Communications at international conferences presented by me:

- CLEO 2011. Munich (21-26 May) "Enhancement and tailoring of emisison by hybrid self-aasembled photonic-plasmonic crystals". M. López-García, J. F. Galisteo-López, C. Lopez and A. Garcia-Martín. **Oral**
- Imagenano 2011. Bilbao (11-14 April) "Tailoring the optical response of self-assembled photonic-plasmonic crystals". M. López-García, J. F. Galisteo-López, A. Blanco, A. Garcia-Martín and C. Lopez. **Poster**
- PECS 2010. Granada (September) "Tailoring the optical response of self-assembled photonic-plasmonic crystals". M. López-García, J. F. Galisteo-López, A. Blanco, A. Garcia-Martín and C. Lopez. **Poster**
- CEN 2010. Segovia (15-18 June) "Easy implementation tuning of self-assembled photonic-plasmonic crystals". M. López-García, J. F. Galisteo-López, A. Blanco, A. Garcia-Martín and C. Lopez. **Poster**
- SPIE Photonics Europe 2010. Brussels (12-16 May) "Enhanced emission in self-assembled photonic crystals by hybrid photonic-plasmonic modes". M. López-García, J.F. Galisteo-López,A. Blanco, C. López and A. García-Martín. **Oral**
- Nanospain 2010. Malaga (23-27 March) "Enhanced emission in self-assembled photonic crystals by hybrid photonic-plasmonic modes". M. López-García, J. F. Galisteo-López, A. Blanco, C. Lopez and A. Garcia-Martín. **Oral**

- CEN 2008. Tarragona (2-4 April) "Opal based photonic crystals heterostructuration by nanoparticle physical infiltration". M. López-García, P.D Garcia, A. Blanco and C. Lopez. **Poster**

Contents

Summary v

Table of contest ix

1 Introduction 1
- 1.1 Photonic crystals in 1D, 2D and 3D . . . 1
  - 1.1.1 2D PC Slabs . . . 5
- 1.2 Surface Plasmon resonances . . . 12
- 1.3 Hybrid Plasmonic-Photonic structures . . . 15
- 1.4 Spontaneous emission enhancement by photonic, plasmonic and hybrid structures . . . 16
- 1.5 Outline of this thesis . . . 19

I Experimental 21

2 Fabrication of monolayers of organic spheres 23
- 2.1 Introduction . . . 23
- 2.2 Fabrication method . . . 24
  - 2.2.1 Vertical deposition method . . . 24
  - 2.2.2 Wedge-shaped cell method . . . 28
- 2.3 Post-fabrication lattice modification . . . 31
  - 2.3.1 Oxigen plasma etching . . . 31
- 2.4 Conclusions . . . 35

3 Optical characterization by Fourier image spectroscopy 37
- 3.1 Introduction . . . 37
- 3.2 Optical Fourier transform for angular resolved measurements . . . 39
  - 3.2.1 Reflection Fourier imaging . . . 41
- 3.3 Set-up description . . . 42
  - 3.3.1 Microscope output . . . 44
- 3.4 Extracting data from the Fourier Image . . . 45
- 3.5 Application to photonic crystals: spectroscopy of photonic modes . . . 52
- 3.6 Conclusions . . . 54

II Study of hybrid monolayers as photonic-plasmonic colloidal structures **55**

4 Optical properties of a monolayer of close-packed spheres **57**
4.1 Introduction . . . 57
4.2 Monolayer on dielectric substrate . . . 58
4.2.1 Simplest case: free standing monolayer . . . 59
4.2.2 Energy leakage with substrate refractive index . . . 61
4.3 Metallic substrate . . . 65
4.3.1 SPP-like modes . . . 69
4.3.2 WG-like modes . . . 72
4.4 Conclusions . . . 73

5 Intrinsic and extrinsic losses of self-assembled metal-dielectric systems **75**
5.1 Introduction . . . 75
5.2 Extrinsic losses: effect of lattice defects . . . 76
5.3 Intrinsic Losses: effects of the optical constants of the metal substrate . . . 80
5.4 Conclusions . . . 83

6 Angle and polarization resolved spectroscopy of monolayers of organic spheres **85**
6.1 Introduction . . . 85
6.2 Dielectric substrate . . . 86
6.3 Metallic substrate . . . 89
6.3.1 Experimental dispersion relation . . . 92
6.3.2 Equifrequency surfaces . . . 95
6.3.3 High energy bands . . . 99
6.4 Conclusions . . . 101

III Emission and tuning of the optical properties: adding functionality to hybrid monolayers **103**

7 Strongly modified spontaneous emission in hybrid self-assembled photonic-plasmonic structures **105**
7.1 Introduction . . . 105
7.2 Dielectric substrate . . . 106
7.3 Metallic substrate . . . 109
7.4 Comparison beteween silver and gold substrates . . . 112
7.5 Study of equifrequency surfaces in emission . . . 114
7.6 Conclusions . . . 116

8 Tuning the optical properties of a monolayer of spheres **117**
8.1 Introduction . . . 117
8.2 Effect of filling fraction modification in the optical response of a monolayer of spheres on a metal substrate . . . 118
8.3 Tuning the spontaneous emission of dye dopped spheres . . . 121
8.4 Conclusions . . . 126

General Conclusions **127**

IV Appendixes **129**

A Finite difference time domain simulation **131**
A.1 Geometry and material properties definition 133
A.2 Sources definition 135
A.3 Retrieving information from simulations 135

B Fano line-shape: extracting Q factor of them modes from reflectance spectra **137**

Bibliography **139**

Agradecementos **153**

Chapter 1

Introduction

During the last three decades, photonic crystals (PCs) and plasmonic structures have become the two most efficient approaches to control light propagation at the nanoscale for frequencies in the visible (VIS)-near infrared (NIR) spectral range. Over the last years, the combination of both kinds of systems has shown exciting results which combine the best aspects of each type of structure.

PCs are periodically arranged dielectric structures while plasmonics systems are metallic materials able to support light propagating through surface resonances known as surface plasmon resonances (SPR). Although hybrid systems are found to present different meanings in several fields of physics, in of this thesis "hybrid photonic-plasmonic" refers for those metal-dielectric structures able to support, in the same spectral region, light confinement and propagation through either a dielectric material (photonic), a metal surface (plasmonic) or both of them at the same time.

The systems of interest in this thesis present, on the one hand, a periodic dielectric structure in the order of the working wavelength and on the other hand a metallic surface able to support SPRs. For this reason this Introduction has been divided into three well differentiated parts. In the first part we present a brief description of one two and three dimensional (1D, 2D and 3D) PCs specially focused on 2D PC slabs due to their similitude with the kind of systems that will be studied along this thesis. In the second part of this Introduction we present the basis of SPR propagation on a metallic film and how to couple/decouple to them by means of a corrugated surface. Finally we consider hybrid plasmonic-photonic systems and present the state of the art of this kind of structures. The last section presents a brief introduction to emission modification by the three kinds of systems previously defined.

1.1 Photonic crystals in 1D, 2D and 3D

Confining electromagnetic radiation to small volumes of the order of its wavelength represents a challenge for conventional materials. Within this context, PCs have emerged as one of the most promising approaches since they were first proposed by Othaka [1] and later by Yablonovitch [2] (as a means to control spontaneous emission and eventually lead to threshold-less lasers) and John (as a system to obtain 3D Anderson localization) [3]. A PC is in essence a dielectric material which presents a periodic modulation of its dielectric constant in 1D, 2D or 3D. The study of light propagation within PCs takes advantage of models in solid state physics for electrons moving in the periodic potential of atoms in a

lattice [4] with some additions like the presence of polarization. The starting point are the macroscopic Maxwell equations for light propagating in a material with no free charges or currents and with a periodic dielectric constant $\epsilon(\overrightarrow{r})$.

$$\begin{aligned} \nabla \times \mathbf{H}(\mathbf{r},t) - \frac{1}{c}\frac{\partial \mathbf{D}(\mathbf{r},t)}{\partial t} = 0 \qquad & \nabla \bullet \mathbf{B}(\mathbf{r},t) = 0 \\ \nabla \times \mathbf{E}(\mathbf{r},t) + \frac{1}{c}\frac{\partial \mathbf{B}(\mathbf{r},t)}{\partial t} = 0 \qquad & \nabla \bullet \mathbf{D}(\mathbf{r},t) = 0 \end{aligned} \tag{1.1}$$

These equations can be combined with the constitutive relations for a non magnetic dielectric material:

$$\begin{aligned} \mathbf{D}(\mathbf{r},t) &= \epsilon(\mathbf{r})\mathbf{E}(\mathbf{r},t) \\ \mathbf{B}(\mathbf{r},t) &= \mu_o \mathbf{H}(\mathbf{r},t) \end{aligned} \tag{1.2}$$

to obtain a wave equation for the magnetic $\mathbf{H}$ and electric $\mathbf{E}$. By separating $\mathbf{H}(\mathbf{r},t)$ into both temporal and spatial components we obtain the following wave equation:

$$\nabla \times [\frac{1}{\epsilon(\mathbf{r})}\nabla \times \mathbf{H}(\mathbf{r})] = (\frac{\omega}{c})^2 \mathbf{H}(\mathbf{r}) \tag{1.3}$$

It is the H field that is commonly solved given that in eq. 1.3 the operator acting over $\mathbf{H}(\mathbf{r})$ is Hermitian and the equation can be treated as an eigenvalue problem with orthogonal eigenvectors $\mathbf{H}(\mathbf{r})$ and real eigenvalues $(\omega/c)^2$ [1]. The most common approach to solve this equation is adapted from solid state physics and consists in using the plane wave expansion method [5].

PCs present by definition a discrete translational symmetry which means that $\epsilon(\mathbf{r}) = \epsilon(\mathbf{r}+\mathbf{a})$ where $\mathbf{a}$ is a lattice vector. Therefore, the Bloch's theorem can be applied and $\mathbf{H}(\mathbf{r})$ is found to have solutions in the form of a linear combination of Bloch modes described by:

$$\mathbf{H}_k(\mathbf{r}) = e^{i\mathbf{kr}} u_{nk}(\mathbf{r}) \tag{1.4}$$

where $u_{nk}(r)$ is a periodic function with the same periodicity as the PC and satisfy $u_{nk}(\mathbf{r}) = u_{nk}(\mathbf{r}+\mathbf{a})$. The eigenvalue problem can then be restricted to the First Brillouin Zone (FBZ). Therefore, it is found an infinite set of modes discreetly spaced in frequency for a given wavector $\mathbf{k}$. Each of these solutions is indexed by the integer n in eq. 1.4. Since $\mathbf{k}$ is a continuous value, it is expected that $\omega_n(\mathbf{k})$ varies continuously as $\mathbf{k}$ varies. This resulting set of values define the so called n-photonic band. An important property of photonic bands derived from Maxwell equation for non-dispersive media is the scalability of ω_n with the lattice parameter [6]. Several approximations and calculation methods are available to obtain the final photonic bands as a representation of $(\omega, |\mathbf{k}|)$ for the First Brillouin zone [7].

Fig. 1.1 shows two examples of photonic band structures calculated for 1D and 3D structures plotted in the same figure. The most noticeable feature in both band diagrams is the existence of frequencies ω where no modes are available in the direction of periodicity. Such regions are the so-called **photonic bandgaps** (PBG) and represent the main feature

[1] This properties does not apply for $\mathbf{E}$ which make its wavefunction solution more complicated

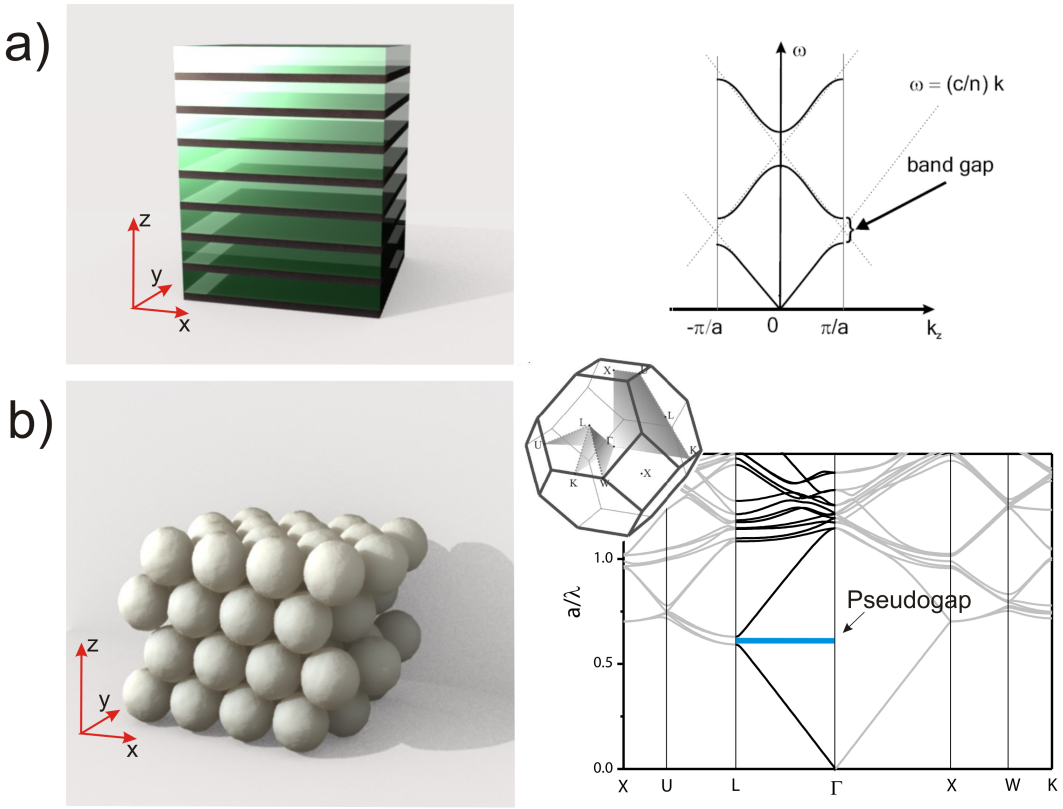


Figure 1.1: a) 1D PC and dispersion relation (courtesy of Dr. R. Sapienza) for light propagating along the z direction. b) 3D PC (artificial opal) and dispersion relation along the high symmetry directions shown in the FBZ of the diagram.

of PCs. For those frequencies contained within this spectral range light propagation within the sample is not allowed.

Depending on whether the gap takes place for every direction in reciprocal space or just for some of them one obtains a full PBG or a pseudogap respectively. Therefore full photonic gaps can happen just in some kind of 3D PCs [8] [9]. The modified dispersion relation implies that the density of states (DOS) for photons propagating within the crystal is redistributed both spatial and spectrally with respect to a homogenous medium.On the one hand, the DOS vanishes for those frequencies at a PBG. On the other hand, the DOS increases for those regions where the dispersion relation becomes almost flat. This happens at the bandgap edges, but also at those points where anticrossings between bands take place. Besides, the low dispersion of such photonic bands implies a low group velocity and therefore a higher light matter interaction [5] for those frequencies compared to a homogenous medium.

If we look at the particular case of the 1D periodicity (also known as Bragg stack) it represents the simplest PC and hence the one to be modeled in the most accurate manner. As observed in the example of the dispersion relation shown in Fig 1.1a light propagating along the direction of periodicity will encounter an energy gap whose spectral position and width depends on the refractive indices n_1 and n_2 and the periodicity of the modulation. Its relatively simple modeling and the existence of well developed fabrication process are the main reasons behind the use of this system to study fundamental concepts both

experimental and theoretically [10][11]. They have also been used in many applications as for example hollow optical fibers [12], sensors [13] or solar cells [14]. However, concerning the confinement of light, 1D PCs are not the most suitable structure given that they act as a homogenous medium for light propagation in the other two directions perpendicular to the periodicity.

Unlike the 1D case, 3D PCs can provide light confinement in all directions which can lead to new fundamental phenomena. The first to be proposed were the inhibition of spontaneous emission by means of a PBG [2] and 3D Anderson localization in the optical regime [3] although many other effects originating in the periodicity of the medium have been demonstrated as, for example, superprism effects [15]. Other important difference with respect to the 1D case is that a 3D periodicity allows changes in both symmetry an topology of the lattice. This introduces versatility in order to find a structure matching required photonic properties. Therefore, each different structure presents its own symmetry directions for the reciprocal lattice and hence a 3D FBZ which will depend on the chosen lattice. Also, plenty of structures with different building blocks forming the lattice have been studied and fabricated during the last two decades. Some of the most common fabrication techniques are photolithography [16], focus ion beam (FIB) [17], holographic lithography [18], direct laser writing, [19], direct ink writing [20] or self assembly [21].

Self assembly methods take advantage of the natural tendency of monodisperse colloidal particles to form ordered arrays under the appropriate conditions. Since they were first studied as 3D PC in the mid 90's [22], self assembled 3D PCs have become one of the most widespread PC fabrication methods. The resulting structures are known as artificial opals and consist of (mainly) face centered cubic (FCC) arrays of polymeric or inorganic spheres. Their porous nature makes them an appropriate structure to control its optical properties through infiltration with different materials within the lattice and subsequent removing of the original spheres leading to inverse structures.

Artificial opals are PCs whose building blocks are dielectric spheres with diameter (Φ) on the order of the operative wavelength and lattice parameter $a = \sqrt{(}2)\Phi$, immersed in a matrix of a different refractive index (typically air) (see Fig 1.1). This kind of structures have been experimentally shown a 3D PBG [9]. During the last years they have shown to be a good playground to understand light propagation in 3D PCs but also their utility for specific applications as, for example, biomedical applications [23], solar cells [24] or light emitting devices (LEDs)[25].

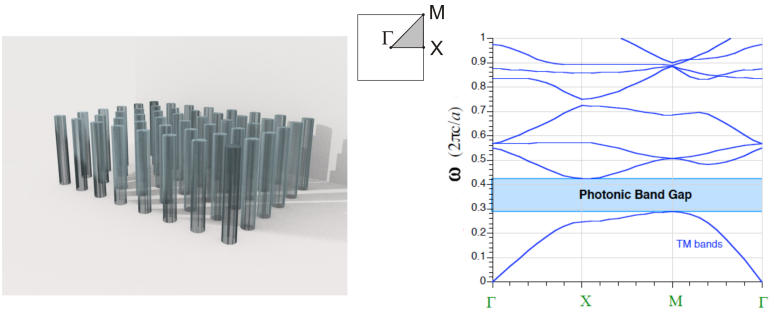


Figure 1.2: Artistic picture of a set of infinite high refractive index material in air forming a square lattice. Band structure for TM modes and FBZ. Dispersion relation taken from [26]

An intermediate point in terms of light confinement is that of 2D PC. We will pay special attention to this system as a first approximation to the structures studied in this

thesis. The structure most commonly used to describe 2D PCs is a set of cylinders of infinite height with a refractive index (RI) different from that of the matrix they are immersed in. Fig. 1.2 shows such structure with a square lattice. An example of photonic bands for wavectors propagating in the plane of periodicity is also shown. If the right RI, filling fraction, contrast and lattice parameter are chosen a PBG can open at a given spectral range. This system can be represented as a homogenous medium in the vertical direction and a periodic 2D lattice for light propagating in the plane.

It is worth defining here the two types of of modes present in these structures: transversal electric (TE) and transversal magnetic (TM), corresponding to those modes having **E** or **H** fields contained in the plane of periodicity. Therefore, for the case where the wavector is fully contained in the plane of periodicity ($\mathbf{k}(x, y)$), the structure presents well defined TE and TM modes. Although the band structure for TE and TM can be completely different, it is also possible to find a complete PBG, that is, PBG for TE and TM at the same frequencies [6]. However, if $k_z \neq 0$, the mirror symmetry is broken and there no longer exists a well defined difference between TE and TM modes. For the same reason, for out of plane propagation no gaps can exist.

As a result of the discussion above, these systems can not be used to confine light efficiently since there is no confinement mechanism in the vertical direction and hence light propagating with component κ_z will scape the system. Therefore, a mechanism for light confinement in the vertical direction needs to be incorporated to the 2D PC. The most efficient approach to solve this is the use of a design where the non periodic dimension is limited to a thickness of approximately the operating wavelength so that total internal reflection (TIR) can take place in the vertical direction similar to conventional waveguides. Such systems are called **PC slabs** or **planar PCs**.

1.1.1 2D PC Slabs

The simplest optical waveguide structure is the step-index planar slab waveguide which represents a starting point to model the kind of confinement obtained in 2D PC slab. It consists of a high refractive index dielectric layer (core) (ϵ_f) surrounded by lower-index materials known as substrate (ϵ_s) and cladding (ϵ_c). A diagram of such waveguide is shown in Fig. 1.3.

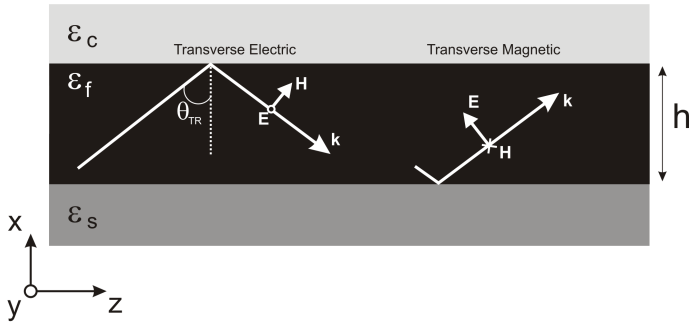


Figure 1.3: Diagram for vertical confinement by total internal reflection for an asymmetric planar waveguide. TE and TM modes are indicated.

If $\epsilon_f > \epsilon_s, \epsilon_c$ TIR takes place and light can be trapped inside the slab. Taking into

account the coordinate system defined in Fig. 1.3 light will zigzag (in a simple ray tracing model) down the z axis impinging on the interfaces at angles larger than the critical one given by:

$$\theta_{TIR} = arcsin(\sqrt{\frac{\epsilon_j}{\epsilon_f}}) \qquad j = s, c \tag{1.5}$$

Taking into account the previous definition for TE and TM modes, Fig. 1.3 shows that, for the coordinate system under consideration here, $\mathbf{E} = E_y\widehat{y}$ for TE while $E_y = 0$ for TM modes. In a source-free, linear and isotropic medium $\mathbf{E}$ and $\mathbf{H}$ satisfy the following equations:

$$\nabla^2\mathbf{E} - \mu\epsilon\frac{\partial^2\mathbf{E}}{\partial t^2} = 0 \tag{1.6}$$

$$\nabla^2\mathbf{H} - \mu\epsilon\frac{\partial^2\mathbf{H}}{\partial t^2} = 0 \tag{1.7}$$

We assume the waveguide to be excited by a source with frequency ω_0, wavector in vacuum $|\mathbf{k}_0| = \omega_0/c$ and polarization along the y axis (TE). The wave equation in 1.6 can be written in a scalar form for each material in the waveguide:

$$\nabla^2 E_y - k_0^2 n_i^2 E_y = 0 \tag{1.8}$$

where $n_i = n_f$, n_s or n_c depending on the region of the structure we consider. As the slab is infinite in the y direction, which means light is not confined in that direction, the trial solution we can write is of the form:

$$E_y(x, z) = E_y(x)e^{-j\beta_i z} \tag{1.9}$$

where β_i is the propagation coefficient along the z direction in each region of the slab, related with the total wavector modulus $|k_0 n_i|$ as shown in Fig. 1.4.

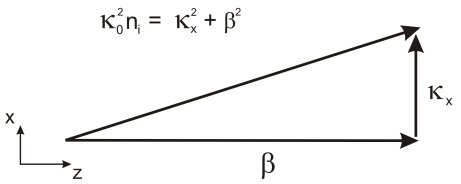


Figure 1.4: Wavector nomenclature used in the text. β and k_z are respectively the longitudinal and transversal components of the wavector k.

Using this solution in equation 1.8 we obtain the general wave equation for TE modes:

$$\frac{\partial^2 E_y}{\partial x^2} + (\kappa_0^2 n_i^2 - \beta^2)E_y = 0 \tag{1.10}$$

and introducing the boundary conditions given by the refractive index distribution along the x axis shown in Fig. 1.3 we obtain:

$$E_y(x) = E_0 e^{\pm\sqrt{\beta^2 - \kappa_0^2 n_i^2}x} \tag{1.11}$$

where E_0 is the electric field at $x = 0$. To be physically meaningful one has to consider the negative solution. Therefore, the transverse wave will have an oscillatory behavior if $\beta^2 < k_0^2 n_i^2$ ($n_i = n_c$, n_s and n_f). However, if $\beta > \kappa_0 n_i$ the solution is exponentially decaying in the corresponding medium. If we extrapolate this general result to the infinite slab waveguide case with $n_f > n_s > n_c$ three situations can be defined depending on the value of the z direction propagation wavector β .

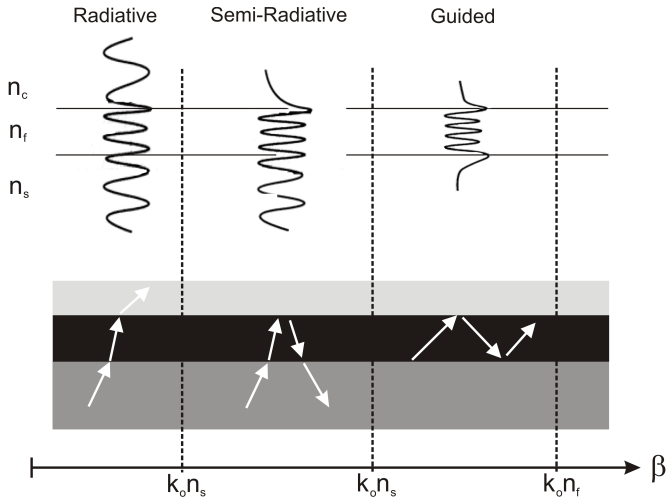


Figure 1.5: Diagram for the three kind of modes available in the planar waveguide depending on their effective propagation wavector β. Figure based on reference [27]

The possible situations are represented in Fig. 1.5. We have plotted a simplified ray picture for each case (bottom) while the top diagram shows the wave picture. For $\beta < \kappa_0 n_c$, solutions are oscillatory in all regions (radiative modes) since no TIR happens at any interface and no confinement can then take place. For $k_0 n_c < \beta < k_0 n_s$ the exponential decay (equivalent to TIR) take place just at the cladding-core interface. As plotted in the ray picture, light is total internally reflected at that interface while it refracts at the substrate-core interface. We call this type of mode semiradiative and can be thought of as leaking trough the substrate from the guiding structure. The third case is the one we are interested in and takes place when $k_0 n_s < \beta < k_0 n_f$. As shown in Fig. 1.5, for this situation the TIR condition is satisfied at both interfaces while it remains oscillatory inside the core. This solution represents the guided modes of the slab which have been depicted as a set of rays trapped between the two interfaces in Fig. 1.5. Furthermore, the general condition to obtain a guided wave in a dielectric slab is a universal condition regardless of its geometry which will be important for us in terms of light confinement in the kind of structures under study in this thesis.

Once the different regimes for light propagation have been described two questions remain: which are those values of β satisfying the TIR condition and how can a propagating wave in a surrounding medium be coupled to the guided modes of the slab and viceversa. The values that β can take for each frequency define the dispersion relation of the waveguide. If one imposes the boundary conditions and solves the coupled equation system one obtains an eigenvalue problem for both TE and TM modes:

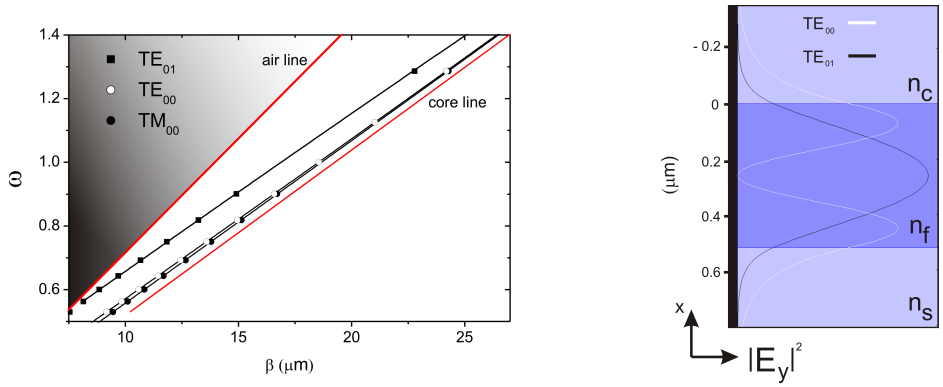
$$tan(hk_f) = \frac{\gamma_c + \gamma_s}{k_f[1 - \frac{\gamma_c \gamma_s}{k_f^2}]} \qquad TE \tag{1.12}$$

$$tan(hk_f) = \frac{k_f[\frac{n_f^2}{n_s^2}\gamma_s + \frac{n_f^2}{n_c^2}\gamma_c]}{k_f^2 - \frac{n_f^4}{n_c^2 n_s^2}\gamma_c\gamma_s} \qquad TM \tag{1.13}$$

with $\gamma_s = \sqrt{\beta^2 - k_0^2 n_s^2}$ and $\gamma_c = \sqrt{\beta^2 - k_0^2 n_c^2}$ being the exponential decay coefficients in cladding and substrate respectively. k_f is the transverse component (x direction) of the wave-vector within the guide. These two eigenvalue problems (known as characteristic equation) for a slab waveguide are transcendental and therefore have to be solved numerically or graphically.

Their solution provides the eigenvalues β_{TE} and β_{TM} that correspond to the allowed modes in the system. These equations finally give us the relation (β, ω) for each mode. However, in this thesis a normalized frequency $\omega = (4\pi)/(\sqrt{(3)}\lambda_0)$ will be used with λ_o being the wavelength in vacuum. Choosing this normalization has to do with the main symmetry directions of a hexagonal lattice and will be explained in depth in chapter 4.

We can now plot the solutions of equations 1.12 and 1.13 in order to find some fundamental properties of guided modes in the above structure. Fig. A.1 shows an example of calculation of three modes for a symmetric slab waveguide. Guided modes can only exist below the light line defined by the condition for TIR at the boundary between the core and the surrounding material with lower refractive index. Above this line there is a continuum of radiative modes known as the light cone (shown as a shaded area in Fig. 1.6a).



(a) (b)

Figure 1.6: a). Dispersion relation for TE_{00}, TE_{01} and TM_{00} modes of a symmetric waveguide with $n_s = n_c = 1$ and $n_f = 1.38$. The thickness of the core is $h = 0.52 \quad \mu m$. The shaded area represents the light cone. b) Intensity profile for TE_{00} and TE_{01} modes of the same structure in a) at $\omega = 0.75$ $(\lambda_0 = 0.6\mu m)$.

For guided modes, another relevant parameter is the modal confinement. That is, how the electric is field distributed inside the structure for each mode. Fig 1.6b shows a calculation [2] of the intensity profile for the TE_{00} and TE_{01} modes for normalized frequency $\omega = 0.75$ for the same structure used in Fig. 1.6a. It shows the field intensity distribution along the vertical direction of the waveguide with the expected oscillatory profile inside the

[2]The calculation was performed using the on-line software provided by Dr. Manfred Hammer on the web [28]

core and an exponential decay in the surrounding media. A useful parameter to quantify light confinement for a given mode is the normalized effective thickness, defined as:

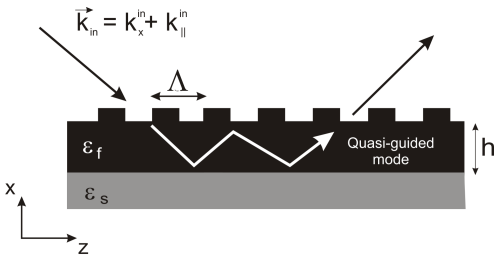
$$\Pi = k_0 h_{eff} \sqrt{n_f^2 - n_s^2} \tag{1.14}$$

with $h_{eff} = h + 1/\gamma_s + 1/\gamma_c$ and $\gamma_{s,c} = \sqrt{\beta_{s,c}^2 - k_0^2 n_{s,c}^2}$ (exponential decay parameters in substrate and cladding). Π is inversely proportional to the field confinement properties for a given mode. Hence, if one is looking for efficient light confinement one must seek low Π values which take place for low order modes and systems having large differences between modes in n_f and n_s.

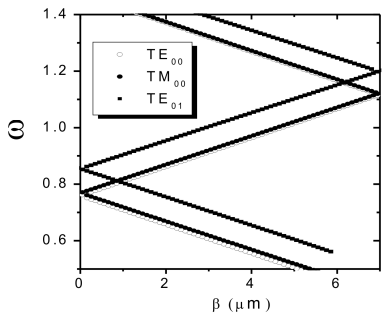
From guided to leaky modes in periodic slab waveguides

So far we have seen how slab waveguides can sustain truly guided modes. Here we will see how, by using a 2D PC structure, one can strongly modify such guided modes. This patterning introduces modifications in the dispersion relation of the guided modes bringing them above the light cone and allowing this way the coupling to radiative modes. We next present a simple picture of the effects of coupling a grating to the slab as shown in Fig. 1.7a.

As already mentioned, exciting guided modes from outside the guiding region can not be done directly. Among the many methods available for that purpose [29], the most widespread is the use of a periodic corrugation (usually a grating) over the dielectric slab.



(a)



(b)

Figure 1.7: a) Diagram of guided mode coupling/decoupling in a grating topped slab waveguide. b) Folding back into the FBZ of the dispersion relation of Fig. 1.6a. Chosen grating period is 400 nm.

Let's consider a grating of period d coupled to the slab (see Fig. 1.7a). Such corrugation adds the extra momentum needed for coupling between the light cone and guided modes by adding a reciprocal lattice vector to the incident wave-vector. Following the same nomenclature used so far we can now express the coupling condition of the parallel component of the wavevector:

$$\beta = k_{||}^{in} \pm m|\mathbf{G}| \tag{1.15}$$

where $k_{||}^{in}$ is the component of the incident wavevector parallel to the slab's mode propagation. $\mathbf{G}$ is the reciprocal lattice vector along the same direction as $k_{||}^{in}$ and takes a value $|\mathbf{G}| = 2\pi/\Lambda$ where d is the periodicity of the grating. Therefore, the original guided modes are no longer totally confined but loose some energy through radiation to the surrounding media as they propagate. Hence they are called leaky or quasi-guided modes.

In terms of light confinement, leaky modes present a finite lifetime for propagation inside the waveguide due to leakage which is determined by the efficiency of light coupling/decouppling by the periodic structure to the slab. It depends on several factors such as the refractive index contrast or the shape of the periodicity building blocks. The parameter that measures how long a mode propagates before leaking out of the structure is the Quality factor (Q). This parameter will be further discussed in chapter 4 when applied to the specific structure studied in this thesis. The field intensity inside the structure is also expected to be modified (according to the periodic vertical thickness) with respect to the guided mode of the unstructured guide.

Let's now study the effects of the periodical patterning on the in-plane propagation modes. From the above discussion, a complete description of the dispersion of the modes of the system can be extracted from the folding of each of those dispersions to the FBZ.

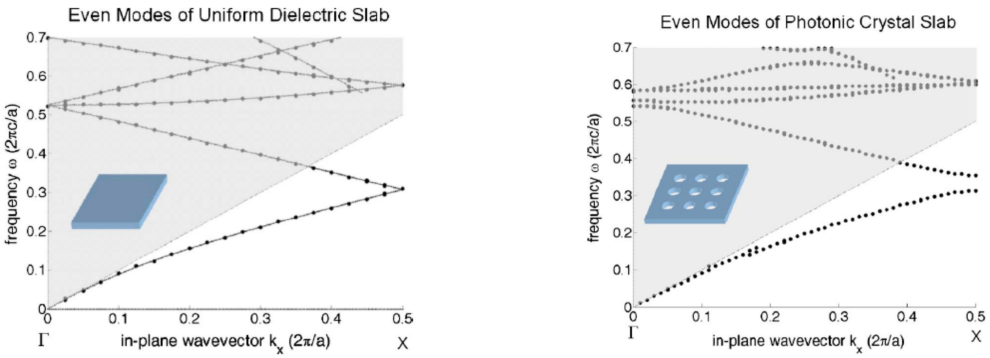
The simplest way to obtain the folded dispersion relation is the use of the so-called empty lattice approximation. In this approach, the folding is performed just by translation of the $\mathbf{k}$ vector to the FBZ by subtracting the corresponding lattice vector $\mathbf{G}$. Fig. 1.7b shows the result of applying that folding to the modes of a slab waveguide with a corrugation of period Λ in the direction of propagation.

However, the empty lattice approximation fails to fully explain the effect of the grating in the propagation of a leaky mode. In a more accurate picture, a leaky mode is multiply scattered during propagation which leads to the formation of Bloch modes for which stop bands can developed. Such photonic gaps will depend on the scattering-strength of the periodic lattice or its symmetry properties. Calculation of the exact shape of the photonic bands requires numerical simulations.

If instead of a grating, one considers a 2D periodic patterning along the whole waveguide thickness, strong light propagation control and confinement can be achieved. While coupling from outside the structure is also available due to modes lying above the light cone, the dispersion relation can be further engineered in every direction of propagation in the plane of periodicity as previously explained for infinite thickness 2D PCs. Therefore, these kind of structures provide TIR confinement in the vertical direction combined with 2D PCs properties (as PBGs). They are known as **PC slabs**.

In order to obtain the photonic bands of a 2D PC slab, Fan and co-workers demonstrated that the empty lattice approximation works appropriately [30] [31]. Fig. 1.8a presents an example of such an approximation. In this case plots have been extracted from reference [31]. The modes of a slab were calculated with the above expressions, and folded back into the FBZ along the ΓX direction in reciprocal space. As can be observed, the empty lattice model does not show interaction between different modes which, spe-

cially for large refractive index contrasts, produces the most important optical features in PCs. Therefore, for an accurate description, it is necessary to use numerical methods as for example the guided-mode expansion method [32] or Finite difference time domain (FDTD) as shown in Fig. 1.8b. In this case, important differences are evident with the empty lattice. The main features of PCs are now evident such as PBGs at the FBZ edge $\omega \sim 0.3$ or flat bands at the photonic gap edges. FDTD also shows that, in some cases, anticrossings take place for the real case evidencing the effects of multiple scattering at those points where bands cross for the empty lattice.



(a) (b)

Figure 1.8: a) Band structure for TE modes in a uniform dielectric slab ($n_f = 2.282$ and $n_c = n_s = 1$) folded back into the FBZ of a 2D square lattice of lattice constant **a**. b) Photonic bands (TE modes) for the PC slab made by the slab shown a) with a 2D lattice of cylinders (radius $0.2a$) drilled on it. Both plots taken from [31].

As a result, PC slabs have shown to be the most efficient 2D type of PC concerning light confinement [33]. Besides, the experimental implementation of this kind of structures has taken advantage of microelectronic fabrication methods to obtain high quality PCs. These two facts, have allowed PC slabs to achieve an optical performance which has rendered them ideal for applications in many fields of photonics such as slow light waveguides [34], optomechanical systems [35] , high efficiency solar cells [36] or ultra high Q cavities [37] to name a few.

PC slabs with complex building blocks

As shown above, PC slabs present a very efficient light confinement in the vertical direction by means of TIR. However, TIR conditions are strongly dependent on the refractive index profile in the vertical direction. Therefore, any complex shape introduced on the vertical profile of building blocks will introduce changes in the light confinement properties of the system. The most simple example of this effect are slot waveguides, where the electric field is mainly confined within a low refractive index sub-wavelength region introduced in the core of the waveguide [38].

But PC slabs can also be constructed from individual building blocks ordered in a 2D array rather than from holes drilled in a planar waveguide (WG) For the particular case of a 2D lattice formed by close packed spheres, the most accurate theoretical approach makes use of the Mie theory to calculate the scattering of each single sphere to next couple them in the periodic lattice configuration. This approach was widely studied by Othaka and Miyazaky [1][39] and has proven to correctly describe the optical properties of this kind

of systems. In this thesis we also deal with hybrid systems where monolayers of spheres are deposited on a metal, which can not be easily described by such an approximation. Although several methods [40] can be used to describe the monolayer metal interaction we have used mainly FDTD (see Appendix A) simulations in this thesis.

1.2 Surface Plasmon resonances

SPRs are light waves trapped at the surface of a metal due to the resonant oscillation of its free electrons [41]. The most attractive property of this kind of modes for light propagation is their ability to confine light at a metal-dielectric surface at subwavelenght scales [42]. Such a confinement provides extremely large light-matter interaction which makes systems supporting SPRs the most appropriate to be applied in many different fields of photonics. Some of the best known fields of application for SPR´s are sensors [43] or medicine [44].

If a metal-dielectric interface is considered one can solve Maxwell‘s equations at the interface between two media with ϵ_1 and ϵ_2 with the following boundary conditions:

- Propagation is fixed along the interface.
- Confinement in the normal direction to the interface. Hence, the field intensity must decay exponentially towards both media.

Using these two conditions, we can make use of the same equations shown for the slab case but with $h = 0$ (zero thickness). In that case, for $\Gamma_{1,2} > 0$ (exponential field decay in medium 1 and 2) it is found that just the TM zero order solution satisfies field continuity at the interface for a light wave propagating along it [41]. With the previous boundary conditions it is obtained that the wavector of the propagating modes must satisfy:

$$\kappa_{||}^2 = \frac{\epsilon_1\epsilon_2}{\epsilon_1+\epsilon_2}\kappa_0^2 = \frac{\epsilon_1\epsilon_2}{\epsilon_1+\epsilon_2}\frac{\omega^2}{c^2} \tag{1.16}$$

where $k_{||}$ is the component of the wavector parallel to the metal surface and k_0 is the wavector in vacuum at a given wavelength λ_0. For propagation along the normal direction:

$$\kappa_{j,z}^2 = \frac{\epsilon_j}{\epsilon_1+\epsilon_2}\kappa_0^2 \qquad j = 1,2 \tag{1.17}$$

where $\kappa_{j,z}$ is the wavector component along the normal to the surface within the ϵ_j medium. The same nomenclature can be applied to ϵ_2. Propagation along the surface requires a real $\kappa_{||}$ while the confinement in the normal direction is obtained for imaginary κ_z. From this condition it is found that one of the dielectric constants must be negative. As it is well known, noble metals, and specially gold and silver have large negative real parts of the dielectric constant along with a small imaginary part and therefore are good candidates to sustain long lived SPRs at their interface.

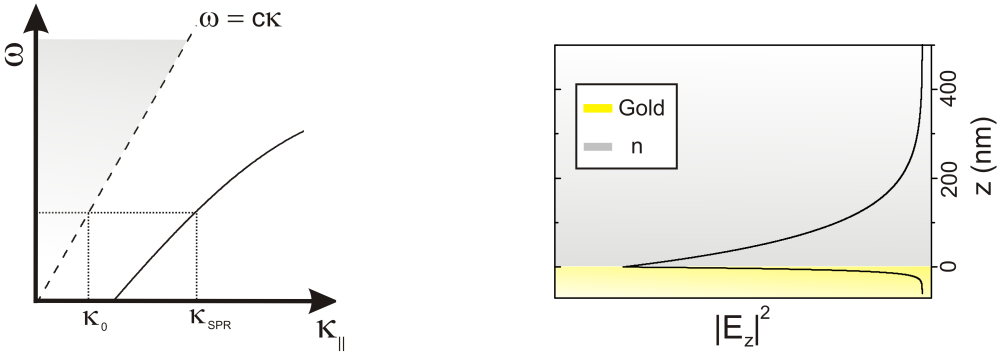
We can next assume a more realistic scenario, with ϵ_2 being a dielectric medium with negligible absorbtion. For ϵ_1 we include the imaginary part of a metal in order to take into account losses introduced by the resonances due to electron scattering (ohmic losses):

$$\epsilon_1 = \epsilon_1' + i\epsilon_1'' \tag{1.18}$$

leading to an imaginary wavenumber where the real part accounts for the phase and the imaginary part for the absorbtion during the plasmon propagation along the interface. If

we assume that $|\epsilon_1''| << |\epsilon_1'|$, after some further calculations we obtain the wavelength for the plasmon resonance:

$$\lambda_{SPR} = \frac{2\pi}{k_{||}'} \approx \sqrt{\frac{\epsilon_1' + \epsilon_2}{\epsilon_1' \epsilon_2}} \lambda_0 \tag{1.19}$$



(a) (b)

Figure 1.9: a) SPR dispersion relation and (b) field intensity decaying into each material of the metal-dielectric interface. In this case n=1.38.

Fig. 1.9a represents an example of the dispersion relation for a SPR for gold with a dielectric material with n=1.38 deposited on it. As for the guided modes of the PC slab presented in the previous section, the SPR dispersion relation lies below the light cone (grey shaded area) and then it is not possible to couple to it without adding an extra momentum to the incident beam.

Prior to introducing the different approaches to couple to SPRs other important points should be considered, such as its propagation distance. Again, similar to slab waveguides, the field confined for an SPR presents an exponential decay into both media forming the interface. Fig. 1.9b shows a calculation of the field distribution into each of the materials considered for the dispersion relation in Fig. 1.9a. For SPRs the exponential decay is always faster in the metallic part than in the dielectric due to the values of ϵ for each material. On the other hand, due to the ohmic losses introduced by ϵ_1'', as the SPR propagates along the interface the electric field will decay by a factor $1/e$ after a given propagating distance. Increasing that distance without affecting the other properties of SPRs is essential for many applications. As an example we can consider the dielectric constant for gold at $\lambda = 633$ nm ($\epsilon_1 = -11.6 + 1.2i$) and air ($\epsilon_2 = 1$). In this case we obtain a $1/e$ propagation distance of $\sim 10\mu m$ and a decaying of 1/e in the normal direction of 28 nm and 328 nm for gold and air respectively. This shows that the decay into the metal is much shorter than into the dielectric as expected from the previous discussion.

As mentioned at the beginning of this section, the extremely large field confinement makes SPR suitable for many applications. Besides the extremely short effective wavelengths of SPR allow for novel phenomena such as subwavelength focusing [45] or supertransmission [46] in reduced scales and makes SPR supporting systems ideal platforms to integrate photonic devices [47]. However, as mentioned above, two main issues have to be solved. On the one hand, in order to couple/deouple light to this kind of modes, the momentum mismatch with the radiative modes of the outside world has to be overcome. On the other hand, it is mandatory to reduce losses due to absorbtion of the metal to achieve large propagation lengths. For the latter, many approaches have been proposed

over the last years the most widespread being the use of a dielectric presenting optical gain to compensate for absorbtion. By appropriately tuning the gain spectrum with the plasmonic resonance a positive feedback can be obtained to maintain the plasmon propagation for distances as long as 1 cm at VIS-NIR frequencies [48].

Similar to the guided modes in a slab waveguide shown in the previous section (see Fig. 1.3), the plasmon dispersion lies below the light cone as expected for a confined mode. Therefore, several approaches have been developed to couple an incoming beam to a SPR as for example the so-called Kretschmann configuration [41] where coupling is provided by a dielectric having a refractive index larger than 1. However, the periodical patterning of the metallic surface is the most widespread approach to achieve SPR coupling [49]. It is essentially the same concept previously explained for excitation of guided modes in a slab waveguide. By adding a periodicity, typically a grating, an additional momentum is added to the incoming wave obtaining the necessary momentum to conserve the parallel component of the wavector and hence allow coupling to some of the SPR resonances. This way, the dispersion relation is folded back within the light cone allowing the continuum of modes available in the dielectric medium to couple to the SPR as can be seen in Fig. 1.10.

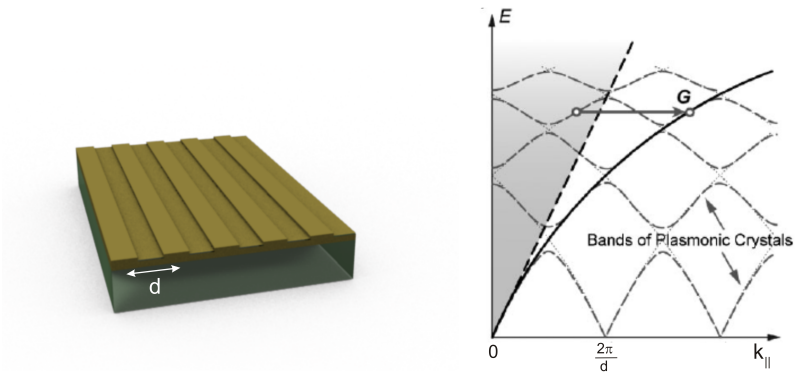


Figure 1.10: Diagram of a gold grating of period Λ on a dielectric substrate and dispersion relation of the SPR folded back within the FBZ, introducing part of the dispersion in the light cone (shaded area). G is the extra wavector added by the grating structure. Dispersion relation taken from reference [50].

Further, the proper engineering of the corrugation can lead to new phenomena for SPRs as it does for PC slabs. Besides using periodic corrugations for efficient coupling to SPRs, one can design the periodicity to extend the control of light propagation shown in PC to SPR. This kind of systems are known as **plasmonic crystals**. Specially relevant is the spectral region where no plasmon propagation can take place at any **k** as previously demonstrated for PCs known as plasmonic band gaps [51]. Therefore, the strong changes in the group velocity previously described in PCs can take place for plasmonic modes showing the same extraordinary effects (waveguiding [52], negative refraction [53], etc ...) but at the SPR's wavelength scale. Moreover, the control over the dispersion relation of the SPR provided by the 2D lattice makes it possible to obtain new regimes of propagation such as the transition from propagating to localized plasmons [54]. In this case, a strong similitude is found again between the dielectric PC slabs studied in the previous section and the SPRs modified by means of a periodic lattice. In both cases there is a confinement in the vertical direction by means of an exponential decay of the electromagnetic field while

the in-plane propagation properties are defined by the 2D periodicity.

1.3 Hybrid Plasmonic-Photonic structures

As already mentioned, light confinement in plasmonic systems and PC slabs are similar phenomena though presenting some differences. For the latter, light confinement is provided by the structure due to in-plane Bragg diffraction aided by TIR in the vertical direction. For the former, confinement is a intrinsic property of the material though some coupling mechanism is still needed to excite SPRs. These differences have arouseed a rising interest in combining both kind of systems during the last years. The aim of these hybrid structures is to increase the field confinement of PCs while overcoming SPR's short propagation distances. Therefore, we define a hybrid photonic-plasmonic system as that supporting both, photonic (field distributed within the dielectric) and plasmonic (field concentrated close to the metal) modes. In Fig. 1.11 some significant examples of hybrid systems that can be found in the literature are shown.

An interesting example of hybrid structures are those formed by dielectric or semiconductor microcavities (supporting resonant photonic modes) deposited on metallic films [55][56]. Fig. 1.11a shows an example where the field concentration provided by the SPR is combined with the photonic cavity mode of a semiconductor nanowire. It provides large propagations lengths of the hybrid modes formed within the metallic-semiconductor cavity as well as strongly enhanced light matter interaction which eventually leads to lasing emission at subwavelength scales [57].

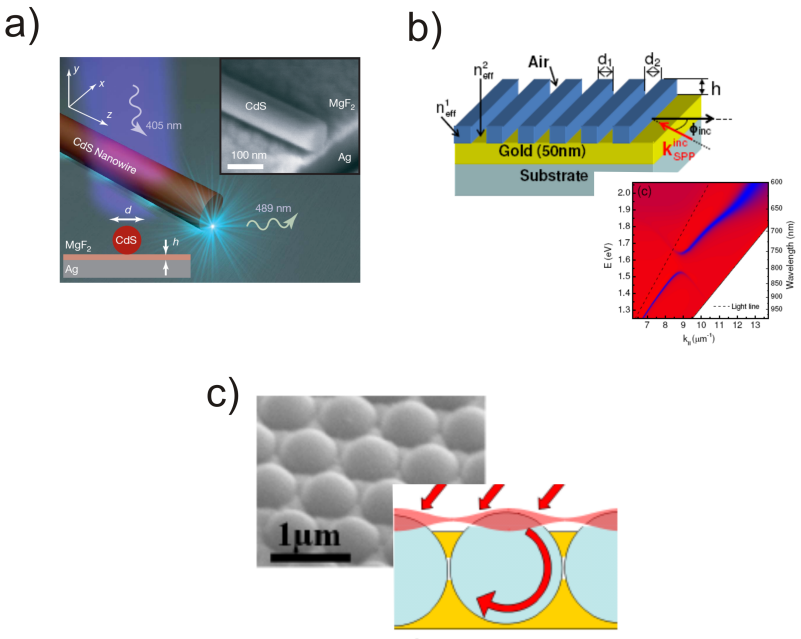


Figure 1.11: Images of different hybrid photonic-plasmonic structures. (a) CdS semiconductor nanowire on top of a silver substrate separated by a dielectric spacer of thickness h. (b) Dielectric grating on a gold film and SPR dispersion. (c) Microvoids of air surrounded by gold supporting localized and extended hybrid modes. (a), (b) and (c) taken from references [57], [58] and [59] respectively.

Maybe one of the simplest hybrid systems is that formed by a waveguide with a SPR supporting surface beneath [60]. In the case of a ridge waveguide, the SPR formed at

the metal-dielectric waveguide interface is guided by the dielectric ridge. Those systems are known as dielectric loaded waveguide for plasmons and have shown to provide large propagation lengths at the price of a slightly lower confinement than in a conventional metal-dielectric surface. Other similar approaches made use of different dielectric waveguides like cylindrical shaped ones. The later have shown [56] that hybrid modes can provide stronger field enhancement both into the dielectric (photonic) or close to the metallic surface (plasmonic).

Moreover, the loading dielectric material can be structured forming a 1D or 2D PC in such a way that propagating hybrid modes can show anticrossings or gaps as can be observed in the example of Fig. 1.11b where the SPR dispersion is modified by the dielectric grating on top of a metallic film. If the coupling is strong enough, a new kind of propagating mode can appear called waveguide-plasmon polariton [61].

Finally, and related with the structures dealt within in this thesis, self assembly 2D photonic-plasmonic crystals have also demonstrated [59] [62] to support hybrid modes both, localized [54] and extended [59][62] as shown in the example of Fig. 1.11c.

1.4 Spontaneous emission enhancement by photonic, plasmonic and hybrid structures

To understand how both photonic and plasmonic structures affect the emission of a light source placed close to or within it we shall begin by looking at the physics of how spontaneous emission takes place. Spontaneous emission results in the emitter decaying to a lower-energy level and a photon taking away the energy of excitation which determines the frequency of the emitted photon. The spontaneous emission rate ($\Gamma(\mathbf{r})$) is given by Fermi's Golden Rule [63] that we can simplify to be proportional to the density of states $\rho(\omega)$:

$$\Gamma(\mathbf{r}) \quad \alpha \quad \rho(\omega) \tag{1.20}$$

The density of states (DOS) for photons is defined as the total number of states available for photons with frequency ω per unit of volume. From Fermi Golden rule's, any modification in the DOS for a given frequency will modify the spontaneous emission rate. This control of the decay rate through the density of photonic modes was first proposed by Purcell in 1946 [64]. However, it was later demonstrated that, rigourously, the spontaneous emission depends on a local property, the local radiative density of states (LDOS) [65], which is the spatial dependent part of the total DOS. In particular, it departs from the total DOS for those systems where strong spatial field variations are present within the structure as, for example, in PCs [6].

Therefore, the LDOS is expected to change as a function of the position of the emitter within the structure producing different rates from those given by the total DOS. As a result, by controlling the LDOS on a system where an emitter has been placed allows to strongly modify its emission properties. Besides, such an emission rate can be tailored by choosing the appropriate position within the structure which is not possible if one considers just the total DOS.

Experimental implementations of this concept were first tested with optical cavities where the LDOS is modified by the modes of the structure inhibiting emission [66]. However, during the last two decades, PCs have demonstrated to be the most appropriate approach to strongly control LDOS. The strong variations in LDOS taking place in a PC

as a consequence of its microstructure allow an efficient control of the spontaneous emission of internal sources. Tuning the spontaneous emission to those frequencies matching a bandgap or its edges can therefore inhibit or enhance the emission rates. Experiments in that direction have demonstrated such effects in 2D and 3D PCs [67] [68]. Also, a combination of PCs with optical cavities included in the structure has probed the extreme modifications of the emission due to the LDOS distribution inside the cavity [69].

Additionally to an enhancement or inhibition of the emission, the effect of the PC lattice can lead to a modification on the emission angular pattern [70] [71]. This effect is derived from the folding of the confined modes to the light cone by the PC dispersion relation as shown in section 1.1. This property is specially important in PC slab technology and has been largely exploited in LED design where a compromise between emission enhancement and the amount of light coupling to the surrounding media with a given angular pattern is usually required [72].

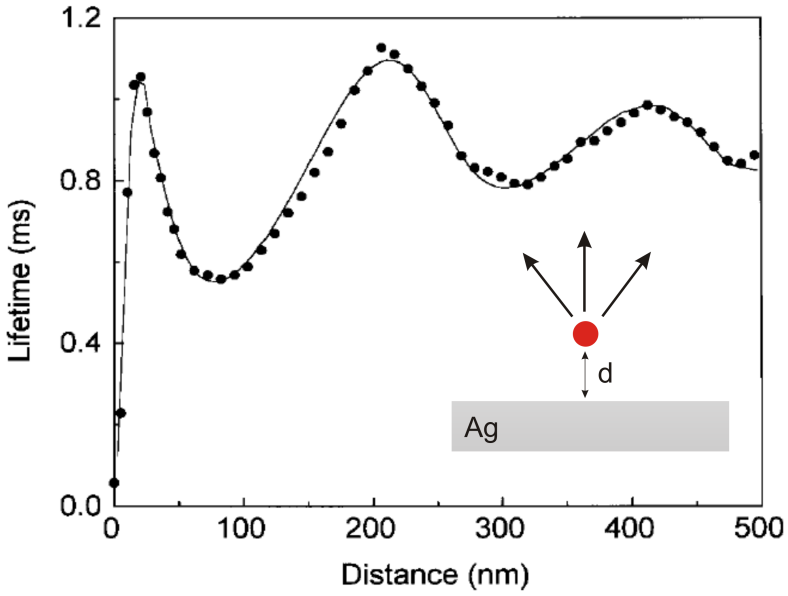


Figure 1.12: Decay time of an Eu^{3+} ion in front of a silver mirror as a function of separation between the ions and the mirror (Graph taken from [73]).

Another approach to modify the spontaneous emission of an emitter is by means of metallic surfaces [73] although the mechanism involved in the emission process near to a surface were first studied for a dielectric-dielectric interface [74]. An emitter surrounded by a dielectric medium and placed at a given distance from a metallic surface (Fig. 1.12) presents an spontaneous emission (shown as decay time in the figure) modified according Fermi Golden's Rule with the LDOS modify by the metallic surface. In that figure, two well define features can be observed. On the one hand, the oscillatory behavior of the decay time with separation is produced by the LDOS modification due to the surface as the phase of the reflected field changes with the distance producing interference between the emitted and reflected fields. On the other hand, it can be observed that for very short distances to the surface, the spontaneous emission is strongly quenched. This is due to coupling to non-radiative channels such as the excitation of SPR.

By patterning the metallic surface one can make the excited SPR to couple to radiative modes again so that radiation is emitted back to the surrounding media. If appropriately engineered, the combination of increased decaying rates of the emitter and reradiation

can lead to a large overall enhancement of emission at those frequencies where SPR is decoupled by the corrugation [75]. This kind of enhanced light-matter interaction is a common approach to improve surface enhanced raman spectroscopy (SERS) where by using a corrugated metallic substrate one can enhance by several orders of magnitude the SERS signals. Although in the last case surface patterning is not periodic but a random corrugation, periodic lattices have attracted attention during the last years. The most common structure consists of a 1D or 2D plasmonic crystal with an excited emitter on top [76] [77].

Several works about the fundamental physics of hybrid systems have appeared [78] along the last decade. However, it is the coupling of the plasmonic resonances to emissive photonic structures that has recently attracted large attention due to the possibility of generating laser emission at subwavelenght scales [57]. Oulton et al. showed [56] that for a cylindrical waveguided placed at a controlled distance from a metallic film a hybridization between the guided moded of the dielectric cylinder and the SPR of the dielectric-metal interface can happen. The hybrid modes obtained present field confined in a reduced volume in the cylinder-metal interface. In fact, despite this strong confinement, the hybrid mode's propagation length is larger than that of SPRs of the equivalent metal-semiconductor interface. For emitters placed at those positions where hybrid modes present large enhancements, lasing operation has been demonstrated [57].

Another method to obtain enhanced emission by plasmonic resonances is the one making use of localized plasmons. That is, structures where a well defined plasmonic resonance does not propagate such as metallic nanoparticles. By placing the emitter at the appropriate distance from a metallic nanoparticle it is possible to produce such a strong coupling between plasmon and emitter that a laser of only 20 nm cavity volume has been recently achieved [79]. Within this context, the concept of nanoantenna has been proposed [80], that is, a metallic nanoparticle (or an array of nanoparticles) with a specific shape that may induce directionality and polarization on a single emitter [81] which may find applications in many fields as for example nano-scale microscopy. Although localized plasmons are not the subject of this thesis they are worth mentioning, since the combination between localized and delocalized plasmonic resonances were studied from an emission enhancement point of view by Sugawara et al. [82] in a similar structure of close-packed spheres as the one studied in this thesis.

Hybrid structures for emission modification

We can now put together both systems, plasmonic and photonic, in order to take advantage of the control over emission that each of them provides on its own. Depending on which mode is available at a given frequency, the LDOS will be modified according to the mode's nature. Therefore, the position of the emitter within the hybrid structure will strongly determine which kind of mode will be responsible for a modification of its emission. Emitters close to the metal surface will be affected by modes having a plasmonic character [76].

For those emitters placed at a distance from the metal large enough to avoid coupling to SPR but still inside the dielectric part of the structure, the LDOS effect on the emitter is twofold depending on the nature of the dielectric part. On the one hand the metallic film introduces interference between the emitted and reflected beams as previously described (see Fig. 1.13a). On the other hand the confinement provided by a waveguide modifies the emission according to the field distribution for the guided mode (Fig. 1.13b). Finally, if the dielectric waveguide is patterned forming a PC, emission will also be modified according

to the light confinement in the plane of periodicity of the PC slab mode (Fig. 1.13b).

The latter structures, where lateral propagation is controlled by the periodicity and vertical confinement is aided by a metal, are similar to 2.5 PC slabs [83]. Only in such PC a dielectric mirror is used instead of a metal. It is worth to mention that the combination of a periodic dielectric structure with a reflector also presents an angular redistribution in its emission as a consequence of the former.

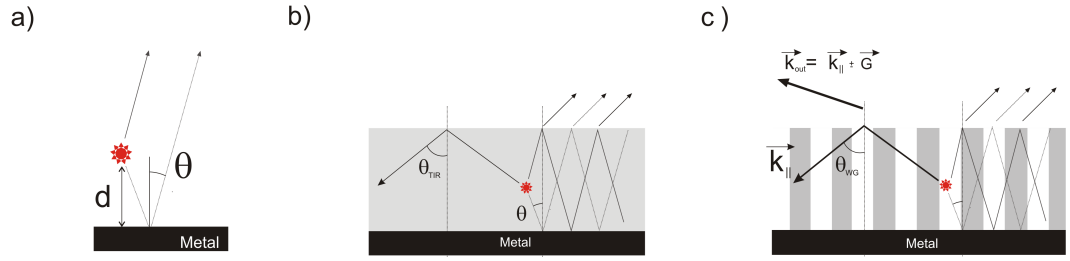


Figure 1.13: Diagrams of the three cases mentioned in the text: emitter close to a mirror surface (a), emitter enbebed in a slab over a mirror (b) and in a periodically structurated slab (c).

Finally, one should consider the case of a given distribution of emitters within the hybrid structure. In this case, for a specific frequency, the total emission is determined by the convolution between the LDOS distribution at the emitters frequency and the emitters spatial distribution inside the structure. This is an interesting case, specially for those systems where both plasmonic and photonic modes may happen at the same frequency which may allow "activation" of emitters placed both close to the metal (SPR) and within the dielectric (photonic) at the same time.

1.5 Outline of this thesis

The main subject of this thesis is the study of the optical properties of 2D self assembled PCs as passive and active systems with special attention on those grown on metallic substrates. In our approach we have treated the monolayer as a 2D PC slab and, in the particular case of metallic substrates, coupling between the guided modes and the SPR modes of the substrate are demonstrated to be possible obtaining a hybrid photonic-plasmonic crystal.

This thesis is divided into three parts. In the first one (Part I) the main experimental methods used for fabrication and characterization of the hybrid PCs are described. The second part (Part II) presents a study of the monolayer of spheres as a PC from both theoretical and experimental points of view. Spectroscopy is performed to investigate how light propagates through the structure but also on the mechanism for incident light to couple to the different supported modes. Finally, Part III considers monolayers of organic spheres as active structures and how emission can be strongly modified by tailoring the optical resonances of the system.

- Chapter 2 describes the two methods used to grow close-packed monolayers of organic spheres used in this thesis paying special attention to the case when metallic substrates are used. The samples are studied with Scanning electron microscopy (SEM) and optical microscopy to evaluate each fabrication technique in terms of size and crystalline quality. Finally, we present a simple post-processing method to tune the diameter of the spheres with oxygen plasma etching.

- In Chapter 3 we describe the optical experimental setup based on Fourier Imaging angle resolved spectroscopy used for the optical measurements in this thesis. First we introduce some notions on Fourier imaging. Next, the set-up is described and a complete calibration protocol is detailed. Finally we demonstrate its accuracy by performing angle-resolved measurements on opal based 3D PCs.

- In Chapter 4 we study from a theoretical point of view the optical properties of monolayers of dielectric spheres for free standing, dielectric and metallic substrate structures. By means of FDTD simulations we obtain the optical response (normal incidence reflectance) and the total field intensity distribution for the different modes of the structure which allow us to divide them between WG-like and SPR-like.

- In Chapter 5 we study the different channels of losses for a monolayer deposited on a metallic substrate. We divide them in intrinsic losses (unavoidable and related with the leaky character of the modes and with the metal absorbance) and extrinsic losses(related with induced disorder during the fabrication process).

- Chapter 6 presents angle and polarization resolved spectroscopy measurements performed on monolayers grown on dielectric and metallic substrates. Well resolved dispersion relations are obtained for both gold and silver substrates along the two high symmetry directions of the reciprocal lattice. Experimental results are interpreted with an empty lattice aproximation and the physical origin of the different modes is studied. Finally, we study experimental equifrequency surfaces (EFS) in a reflectance configuration.

- In Chapter 7, we study the emission properties of a close-packed monolayer of dye doped spheres. It is shown how spontaneous emission of internal sources is strongly modified, evidencing a spatial and spectral redistribution of the DOS. EFS are also collected in this case and compared with the reflectance configuration corresponding images.

- Finally in Chapter 8 we show how the post-processing technique presented in chapter 2 can be employed to tailor the optical response of the structures. We show that by reducing the diameter of the spheres while keeping the lattice parameter constant it is possible to accurately tune the spectral position of the resonances of the system. The evolution of the optical response both in reflection and emission is studied both numerically and experimentally as the sphere diameter is reduced.

Part I

Experimental

Chapter 2

Fabrication of monolayers of organic spheres

In this chapter we study the two different sample fabrication methods used in this thesis: vertical deposition and wedge cell method. They allow us to obtain high quality monolayers of spheres on top of metallic or dielectric substrates. A morphological study of the disorder of samples fabricated over gold substrate is presented. In the last section we show results on the modification of the filling fraction of the 2D lattice by means of oxigen plasma etching.

2.1 Introduction

As already mentioned in earlier chapters, one of the main advantages of self assembled photonic crystals (PCs) is their simple and fast fabrication procedures when compared to the usual microelectronics processes used for silicon (Si) based PCs. The well known high refractive index (RI) slab photonic crystals [84] are the best known example of such differences. Regarding this interest on self-assembly photonic crystals working in the ultraviolet (UV) - visible (VIS) and - infrared (IR) spectral regimes, many techniques have been developed during the last two decades to grow both two (2D) and three dimensional (3D) structures using nano and micro spheres as building blocks. Ever since Stober [85] obtained monodisperse inorganic spheres and Philipse et al [86] assembled them into a photonic structure, a large variety of new materials (organic and inorganic) and many assembly methods have been developed, for example: vertical deposition [87], electric field induced assembly [88], robotic manipulation [89], Langmuir-Blodgett deposition [90], spin coating assisted assembly [91] [92] or more recently wedge-cell assembly method [93]. It is important to notice that the natural tendency of a colloidal suspension is to order into hexagonal close-packed (HCP) lattices in 2D or face centered cubic (FCC) type structures in 3D. These two configurations are the most stable ones after dispersion evaporation and have therefore been the most widely studied. However, other periodicities can be forced offering more possibilities [94] [95] [96] if the growth process is directed with patterned substrates.

In this chapter we present the results obtained applying two of the aforementioned techniques to grow monolayers of spheres on different substrates, specially on metallic ones. In the first part, we describe the two methods used and the main parameters influencing sample growth. Results on the ordering of the samples are obtained by morfological

study. Special attention has been pay to on how to hydrofilize the substrates given that very different processes have to be applied depending on whether the substrate is dielectric or metallic.

On the last part we present an in depth study on the modification of the filling fraction of the ordered array by means of oxigen plasma etching whose effects on the optics of the sample will be studied in chapter 8.

2.2 Fabrication method

As just mentioned two methods have been used to fabricate the samples studied in this thesis: vertical deposition and wedge-cell. We have studied and compared them, and several differences in the quality of the samples have been found. Vertical deposition is a more versatile method (almost not limited by the substrate total area) while wedge-cell shows better results concerning quality of the sample but with a more limited substrate shape. Some of this conclusions have been previously reported by Sun et al. [93]. However, we have extended this study to metallic substrates. Next, samples are presented and morphologically studied.

2.2.1 Vertical deposition method

Vertical deposition has become the most widespread method to grow self-assembled photonic crystals, specially when a thick sample is to be grown (as for instance opaline structures). Nagayama et al. [97] first developed this method for monolayers and it has been extended to 3D opal based PCs, specially since 1999 [87].

The standard procedure to grow a monolayer consists in placing a flat substrate in a vial (typically a vial) containing the colloidal suspension of monodisperse spheres (see Fig. 2.1). A meniscus is formed at the interface between substrate, air and liquid. At the point where the meniscus is thinner than the diameter (Φ) of the spheres theses are pulled against the substrate and between them by capillary forces and the ordering process begins [98]. As evaporation takes places, the flow of solvent to the meniscus moves the spheres on the extra liquid to the growth region and incorporates them to the lattice. As the liquid of the colloidal suspension evaporates the lattice of spheres remain over the substrate forming the self-assembled structure. If the concentration of spheres is high enough, not a monolayer, but a 3D structure will be grown whose total amount of layers will be mainly dependent on the concentration of the dispersion [98].

.

As can be deduced from the mechanism explained above, the main parameters determining the appropriate growth are, on the one hand, the colloidal suspension concentration and on the other hand the temperature and humidity of the environment. These account for the growth velocity of the lattice and the first one determines the thickness of the main structure though all parameters have some effect on growth velocity and sample quality. By choosing the right conditions it is possible to select if one (2D) or several layers (3D) will be obtained for a given sphere diameter [87]. This general picture can be applied with to inorganic or organic colloidal particles. Although the first works on opal growth were performed with silica (SiO_2) spheres, polymers have shown better monodisperstity. Furthermore, due to the lower density of PS as compared with silica the former is more suitable to be used with large diameters (¿ 500 nm) given that sedimentation of the spheres before the growth process has finished is an issue with silica spheres opal growth.

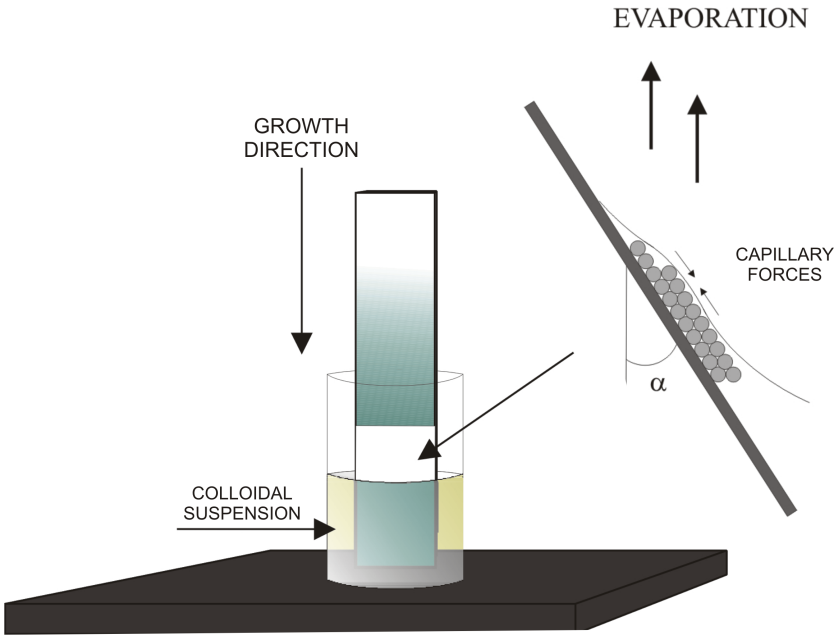


Figure 2.1: Diagram of the vertical deposition method.

As we will make use of 2D organic systems in this thesis, we will focus on the appropriate conditions for the polymeric structures.

The quality of the samples obtained by this method and, in general, for self-assembled PCs refers to how much the real structure differs from the ideal lattice formed by identical building blocks placed at exactly the same distance in the structure. From this definition, there can coexist many types of disorder in the real structures. Most common experimental sources of disorder are vibrations during the evaporation or temperature changes that can lead to different thickness in the sample and produce separations between different domains of the structure (craks). However, if steady environmental conditions are assumed, polidispersity of the spheres and substrate roughness become the two main parameters which affect the crystaline quality. Although controlling the substrate surface can force the colloid to organize following a pre-defined pattern [95] [94], it usually happens that unwanted defects on the substrate surface introduce distortions during the growth process that may end up in lattice disorder.

For a more general study we have employed four different materials as substrate: silicon , silica, gold (Au)and silver (Ag). Silicon and silica have been used before as substrates for many different kinds of self-assembled structures, from monolayers [99] to inverse 3D opals [9].

For the case of metallic substrates, we used gold and silver thin films grown by magnetron sputtering over silicon and glass substrates [1]. As we used silicon wafers as support for the metal, very high smoothness (around 1 nm) due to the conformal growth of the metallic layer on the silicon surface was obtained. Concerning the thickness of the metallic films, they were characterize by ellipsometry, Scanning Electron Microscopy (SEM) and Atomic Force Microscopy (AFM). Large homogeneity of $\sim 60nm$ thickness of the

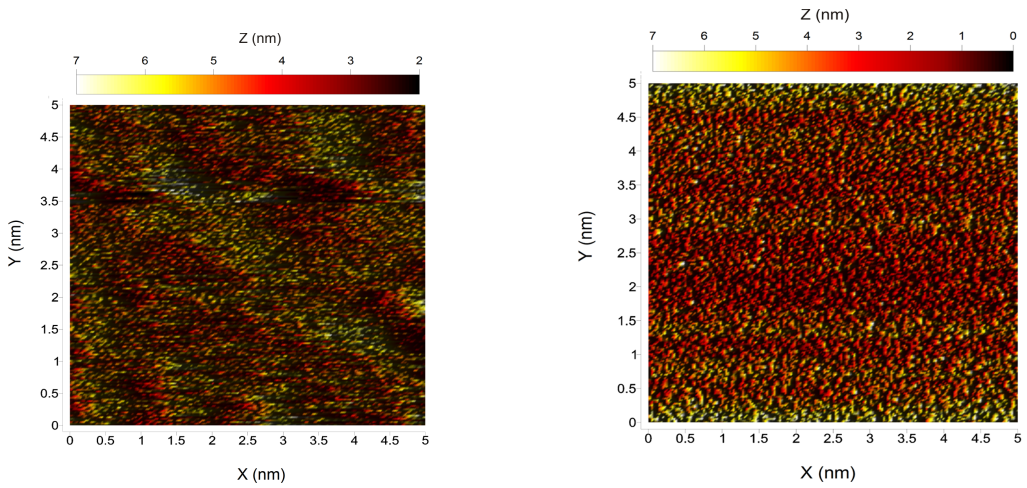
[1]Sputtering was performed by Dr. Jorge Sánchez-Marcos in the laboratories of the ICMM-CSIC

deposited layers were obtained over areas of 2 cm^2 .

Substrate hydrophillization

The commercial substrate surfaces we are using (silicon and silica) have very small roughness (less than 1 nm) as compared to the sphere diameter. Therefore, in order to obtain a high quality sample, the main source of disorder concerning the substrate comes from the growth process. From the growth process decribed before if follows that the meniscus where the lattice starts forming has to be positive and always thinner than the sphere diameter during evaporation. To ensure this behaviour the substrate must present a homogeneous hydrofilic surface. For the dielectric substrates the hydrofilization process is well stablished. In our case, silica substrates were clean glass microscope slides. They were hydrofilized by placing them in HCl 33% overnight and then rinsing them with de-ionized water. Finally they were dried in a nitrogen flow. Silicon wafers [2] were first introduced in a 1% HF solution for 10 minutes in order to remove the native silicon oxide formed on the surface due to air contact. After that, the wafers were introduced in a H_2SO_4/H_2O_2 solution (3:2 vol) for 30 minutes. Again rinsing with de-ionized water and drying with a nitrogen flow were the last steps.

For the metallic substrates more complex procedures were needed to achieve a homogenous hydrofilization. We used a temperature controlled oxigen plasma etching which is a cleaner technique than those based on wet chemical reactions. For the gold case we introduced the thin films on the oxygen plasma etching working at room temperature and 0.4 mbar pressure for 30 minutes. The gold surface quality showed no degradation after that process and a good hydrofilization was obtained [3] As can be assessed from AFM images in Fig. 2.2a very low roughness is observed after the whole fabrication process.



(a) (b)

Figure 2.2: a) AFM image of the surface for the silver films after oxygen plasma etching. b) AFM for gold substrate after the same process.

As an alternative to gold as metallic substrate we have also used silver. Owing to the

[2] Silicon wafers provided by ACM

[3] Bulk gold is oxidation-resistant in air even at elevated temperatures. However, Au_2O_3 can be prepared with radicals provided by an oxygen plasma [100] obtaining the hydrophilic surface character we are looking for.

low absorbance of silver in the visible it suits better our purposses for that spectral range while gold has better optical performance in the IR. However, silver, is not as oxidization resistant as gold. Its surface degrades after some days when exposed to air. In order to avoid oxidation after hydrofilization it is necessary to protect the metallic film from air contact. In our case, a thin (6 nm) Si_3N_4 film was deposited on top of the silver film previously deposited by sputtering on a silicon wafer. Several oxygen plasma etching conditions were tested to obtain the hydrofilization of the protective film while avoiding silver film oxidation. It was found that a 30 second treatment at room temperature in the same conditions of pressure and oxygen purity as for the gold films was enough to obtain a good hydrophilic surface. The resultant substrate did not show any sign of degradation one month after the plasma treatment. Larger oxygen plasma treatments leads to oxidation of silver surface and a fast degradation of the optical properties (as well as the surface quality) was observed.

Colloidal suspension

Opposite to, for example, silica ones, PS spheres present very high monodispersity with diameter deviation from the mean value below 2%. In our experiments, commercially available [101] [102] PS and polymethylmethacrylate (PMMA) spheres were used. Among the polystyrene spheres, two kind of suspensions were used, on the one hand pure polystyrene ones with very high quality, on the other hand colloidal suspensions of dye-doped polystyrene spheres in order to obtain active samples that will allow emission studies as will be shown on chapter 7. The latter spheres are homogenously dopped with a dye emitting at VIS wavelengths with a broad emission/absortion band [4]. Although no differences on the growing conditions were needed for this kind of spheres, a slightly larger polydispersity ($\sim 3\%$) has to be taken into account for the dopped ones. The liquid where the particles are dispersed is water in order to avoid agregation of the particles. Furthermore, the use of water provides an easy way to manipulate the meniscus properties as it was shown in the previous section.

In most of the samples fabricated during this study we have used polystyrene spheres of two diameters: 520 nm and 1 micronmicrometer. However, other diameters were tested too ranging from 250 nm to 2 microns. It is important to notice that due to the sphere fabrication process, the best monodispersity value for PS and PMMA is typically obtained for diameters between 400 and 900 nm. The effect of polydispersity on the crystalline quality of self-assembled systems has been studied in the past [103]. For the case of 2D systems it is well known to be responsible for the introduction of different types of defects which can degrade the optical properties such as dislocations, rotated domains or cracks.

By using a temperature/humidity controlled chamber we have applied the same environmental conditions for the growth of monolayers that previously showed good results for artificial opals. That is, humidity values where set to 30% and temperature was $45^{o}C$. The hydrofilic substrate was introduced overnight in a vial with 5 ml of colloidal suspension. In order not to get a thick opal but a monolayer we reduced the concentration (in weight) of the dispersion to 0.08 % while the growth of artificial opals usually requires concentrations above 0.1 %. The angle between the substrate and the surface of the dispersion which determines the meniscus size is a critical parameter too so we used the same configuration typically used for opals [104] where the substrate forms an angle of aproximately 20^{o} with the surface of the suspension.

[4] Optical properties of these spheres are presented on chapter 7

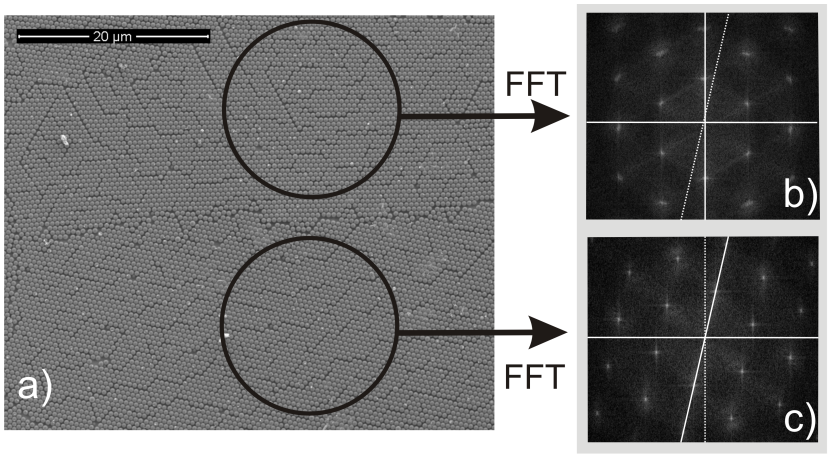


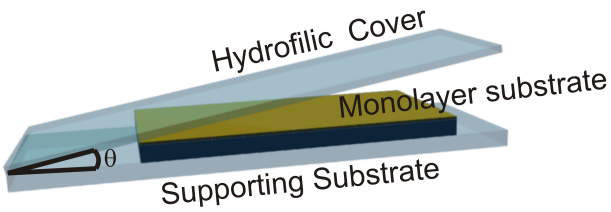
Figure 2.3: SEM image of a monolayer of $\Phi = 520nm$ PS spheres fabricated by the vertical deposition method over a silicon substrate (a) and spatial Fourier transform of two different regions the sample (b and c).

Fig. 2.3 shows a scanning electron microscopy (SEM) image (a) and the Fourier Transform (FT) of two different areas of the image (b and c) for a monolayer of spheres grown by vertical deposition. By observing these images we conclude that the samples obtained by this method present a good crystaline quality over short distances ($\sim 20\mu^2$). Inspection by SEM shows that random vacancies are present in all the samples but the lattice itself is closepacked. However, when large areas are inspected it is clear that several domains exist separated by abrupt rotation. It is clearly observed if one compares the two fast fourier transform (FFT) images in Fig. 2.3b) and c) where two lines have been plotted showing the orientation of the corresponding region (full line) and the comparison with the other area orientation axis (dashed line). The hexagonal pattern due to the lattice symmetry denotes the good crystaline quality at short distances as already commented. However, the rotation between the hexagonal pattern for each region tell us that the complete lattice is formed by slightly rotated clusters of spheres. This has direct implications on the optical response of the sample. So, if local measurements (just one cluster) are to be carried out, the quality provided by this method is good be enough. However, if measurements or applications where large areas of sample are necessary (for example gain length measurements) other fabrication methods should be used.

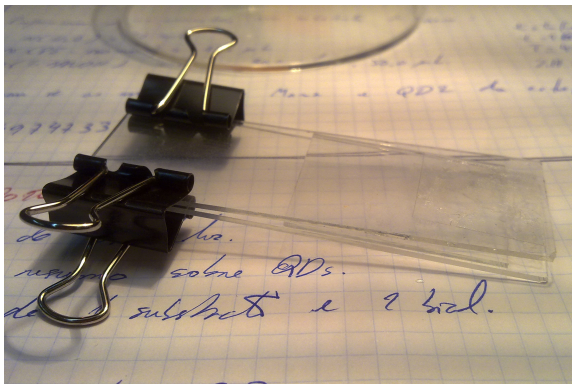
2.2.2 Wedge-shaped cell method

As shown before one of the main disadvantages of the vertical deposition method for monolayers is the rotation between relatively small domains. In order to improve this point a new method was recently published by Sun et al. [93] providing a simple way for obtaining large area monolayers with single domain lattices. Although they optimized it for 1 μm spheres and dielectric substrates, we have improved it to obtain large monolayers on the different substrates we are interested in and with the appropiate sphere diameter in each case.

In this method a wedge cell as the one shown in the diagram of Fig. 2.4 is used. The wedge shaped cell consists of two contact surfaces (a glass slide and the substrate itself) held at a given angle (θ) chosen according to a previous calibration for the substrate ma-



(a)



(b)

Figure 2.4: Diagram (a) and real structure (b) used to grow large area monolayers by the wedge cell method.

terial and the sphere diameter. We obtained that an angle of $\theta = 2^o$ works for most of the cases, including metallic substrates. As in the vertical deposition method, both surfaces have to be hydrofilic in order to obtain a good meniscus. Hydrofilization techniques already described before were also applied in this case.

The colloidal suspension is then introduced through one of the open sides of the cell using a micropipette. An important advantage of this method is that the area of the substrate can be as large as we want given that we are not limited by the container of the suspension as is in case of vertical deposition. In our case, monolayers as large as $\sim 6cm^2$ were obtained over a glass substrate. Another advantage of this method is that, due to the reduced space between the cover and the substrate, it is not necessary to use large dispersion volumes. Typically, less than 100 μl are enough to fill the cell. Dispersion concentrations of 0.5 % and 1% in volume were necessary for the case of $\Phi = 1\mu m$ and $\Phi = 520nm$ respectively.

Again, the evaporation rate and the dispersion concentration will determine the velocity and the quality of the fabrication process. The cell is kept in a horizontal position in the same temperature/humidity controlled chamber used for the vertical deposition method for 6 hours at room temperature and 90% humidity in order to avoid a rapid evaporation. These conditions are slightly different from those described by Sun et al. (20^oC and 30 % of humidity) but given that we are dealing with different substrates and sphere sizes the growth parameters had to be re-optimized for our purpose.

Once the solvent evaporates the cover is removed and a monolayer deposited over the substrate is obtained. As the cover has to be hydrofilic too, it can happen that a good quality monolayer is obtained in that surface. This may be useful if we are using for

example gold as a substrate and glass as cover given that we are obtaining two samples at the same time in two different substrates that could be easily compared later on.

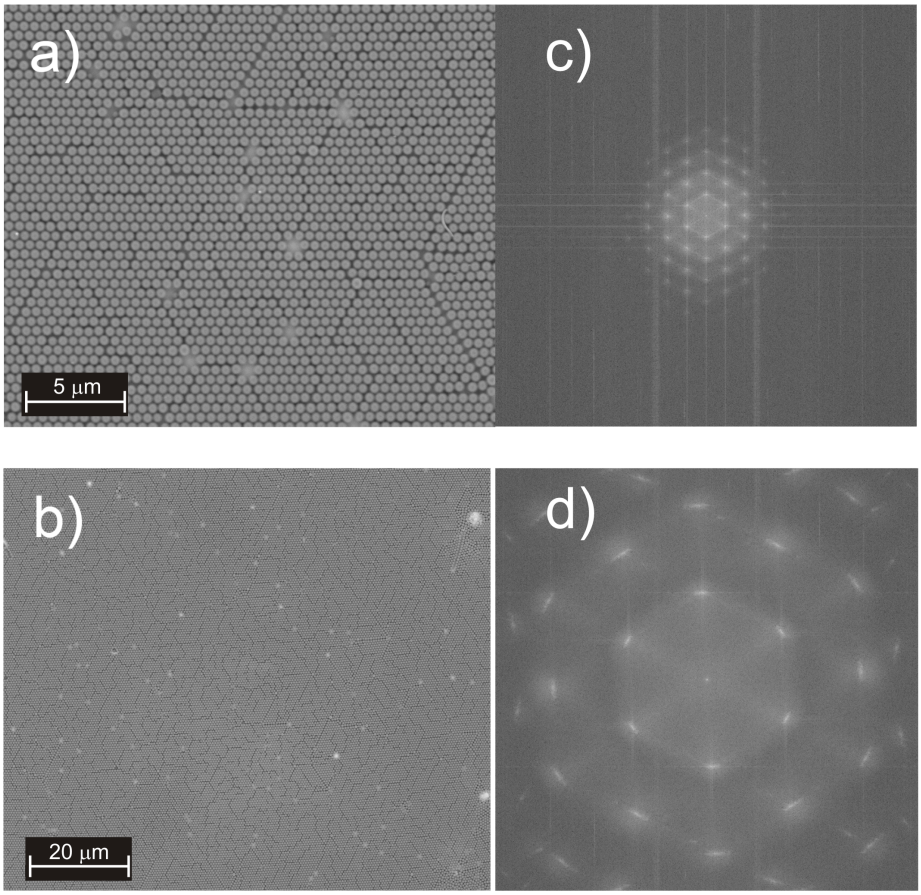


Figure 2.5: SEM images of the same lattice formed by $\Phi = 520nm$ PS spheres on silicon for an area of $25x25\mu m$ (a) and $100x100\mu m$ (b) respectively. c) and d) shows FFT calculated from images a) and b) respectively

.

Fig. 2.5 shows SEM images for $\Phi = 520nm$ PS spheres deposited on a silicon substrate by the wedge cell method. a) and b) show the same region of the sample at two different magnifications. It can be observed, specially at high magnification (a), that the spheres are monodisperse. Random vacancies are present and it is common to find a smaller particle at the void. In the same Fig., images c) and d) show FFT images for a) and b) respectively. It can be seen that a very well defined hexagonal pattern is obtained from image a). It is an expected result since we are considering a small region. However, when FFT from the c) image is calculated, the hexagonal pattern is still well defined. Despite the small rotation shown as a line instead of a point at each hexagonal vertex, the image shows that long range order is still high. From these results we can conclude that a single square domain of at least 100 μm side can be obtained when using the wedge cell method. This will determine the quality of the optical properties of the lattice so it has a crucial importance on the final structure. In the next chapters we will present an in depth study on how the different kinds of disorder lattice can affect the optical response of a monolayer

of organic spheres.

2.3 Post-fabrication lattice modification

In Chapter 1 it was mentioned that the use of polymeric structures in the context of photonic systems has many advantages. One of the main ones has to do with the ease of manipulation of organic materials. Polymers such as PS or PMMA are widely use in microelectronics photolithography techniques and very large control on their removal and modification has been demonstrated. For the case of colloidal photonic crystals based on polymers, reversible lattice modifications have been reported [21] and even commercialized [5]. However, in this case we will concentrate on how to perform permanent modifications in the lattice in order to obtain a structure adapted to our needs.

In the use of 2D colloidal lattices as a lithography mask for the deposition of other materials, the technique to selectively remove some of the polymer in the mask is crucial for the quality of the final structure. Different kinds of plasma have been applied in many fields for this selective etching. When working with colloidal lithography, chemical etching is a widespread technique [105] but is common for that kind of treatments to leave residual materials. Furthermore,when very accurate reductions (with the aim of partial removing but lattice modifications) are needed, chemical processes may be not controllable enough. In that case, the use of plasma etching (in our case oxigen) is the most extended technique. As our purpose is the filling fraction modification (by means of sphere reduction) of the lattice but not total removing of the polymer, oxigen plasma etching (OPE) was the chosen technique. The gas for the plasma chamber was chosen to be oxygen since the removing of organic material is very efficient while non organic parts of the structure are usually not affected.

In this section it is shown that using specific conditions of an OPE it is possible to modify the filling fraction of the lattice of polymeric spheres in a very precise way. Changes on the optical response (which are our goal) will be studied in depth on Chapter 8.

2.3.1 Oxigen plasma etching

This technique involves a high-speed stream of glow discharge (plasma) of an appropriate gas mixture being shot at a sample. The plasma source, known as etch species, can be either charged (ions) or neutral (atoms and radicals). During the process, the plasma will generate volatile etch products at room temperature from the chemical reactions between the elements of the material etched and the reactive species generated by the plasma. As a result, the reactive material is usually totally or partially removed from the sample. Concerning etching of polymeric materials, using oxygen as the reactive species is the best option due to the interaction reactions that take place between the oxygen and the polymeric chains [106]. An interesting side effect for our structure is that the metal-polymer adhesion can be enhance during the oxidization process.

Fig. 2.6 shows a diagram of the most common architecture for a plasma etching chamber as well as a simple diagram of how plasma will act over a 2D lattice of polymeric spheres. In our case we used a water cooled commercial plasma etching (Diener Pico model). As we will work mainly with PS and PMMA we have chosen oxigen as the reactive material.

[5] www.opalux.com

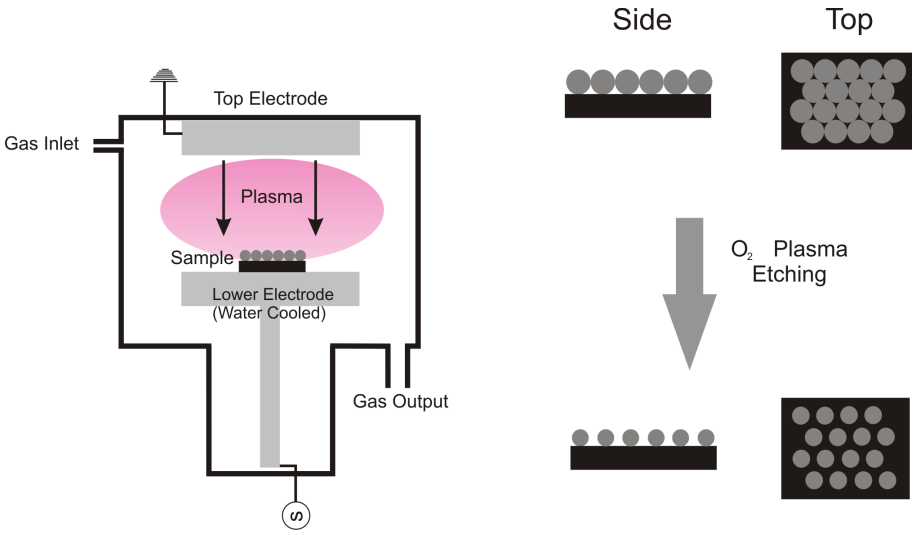


Figure 2.6: Diagram of a plasma etching chamber similar to the one used in our experiments. Right panel shows the a diagram of the evolution of a close packed monolayer of spheres with plasma etching exposure .

If a self-assembled 3D PC is introduced in an OPE chamber, the organic spheres will be reduced on diameter from top to bottom of the sample. OPE etching has been applied to bare opals in order to modify the spheres lattice. This technique allows the fabrication of very interesting structures such as opals with different sphere sizes within the same lattice [107]. On the other hand, reduction of spheres on a 2D hexagonal lattice is the best suited method to obtain a high quality hexagonal pattern on a surface that will be later functionalized with any other material as, for instance, a metal (plasmonics) or a semiconductor (microlectronics).

In our case, we have applied this plasma to monolayers of organic spheres fabricated by the methods explained before. Recently, Plet et al. [108] demonstrated that hexagonally ordered arrays of non close-packed spherical polystyrene (PS) particles can be obtained by means of OPE. We have taken advantage of the same method to obtain a non close-packed lattice whose optical properties will be shown in next chapters to strongly depend on how much the spheres are reduced.

In order to characterize the process we need to identify the main parameters defining the lattice under study. As already mentioned, in a triangular lattice of spheres the main quantity to be considered is the filling fraction that is defined as $ff = V_{sp}/V_t$ where V_t is the total volume of a unit cell of the original lattice (before reduction) and V_{sp} is the volume of that cell occupied by the spheres. A monolayer of closepacked spheres in a hexagonal lattice will have ff=0.6. For the sake of clarity we have defined a new parameter $\gamma = \Phi/\Phi_o$ where Φ and Φ_o are the final and original sphere diameter respectively. Then, we can write the ff as a function of γ as $ff = \gamma^3 \frac{\pi}{3\sqrt{(3)}}$.

Points on Fig. 2.7 show the reduction obtained for two different diameters of spheres ($1\mu m$ and 520 nm) after different steps of controlled exposure time. Working at room temperature avoids polymer melting and therefore, deformations of the sphere due to temperature are negligible. Each point on the graph was obtained by inspection of SEM images taken after each plasma treatment. A red line has been traced as a guide to the eye.

The first thing to be noticed is the non-linear reduction rate of the spheres. Reduction

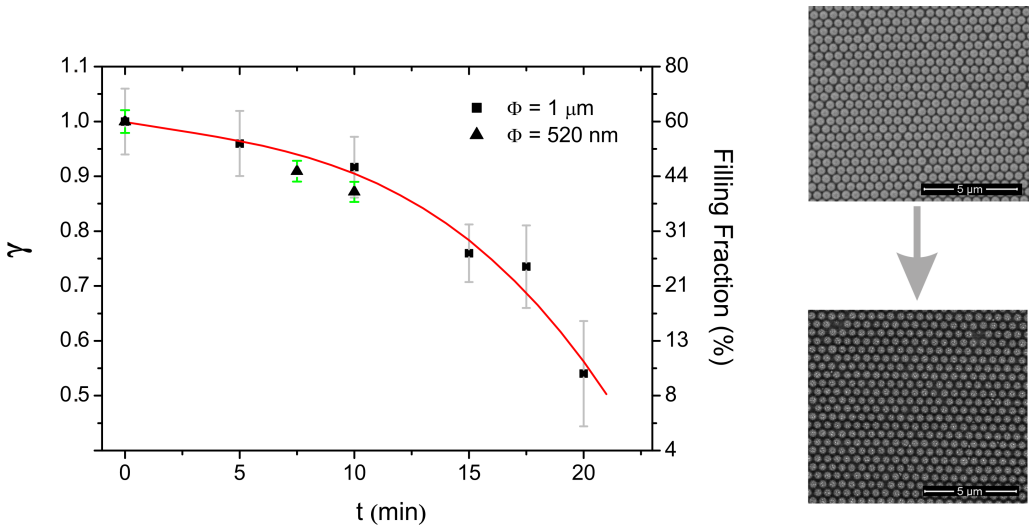


Figure 2.7: Calibration plot for the reduction of PS spheres as a function of time of oxigen plasma etching exposition. SEM images correspond to $\Phi = 520$ nm PS spheres before (top) and after (bottom) 7.5 minutes of oxigen plasma exposure.

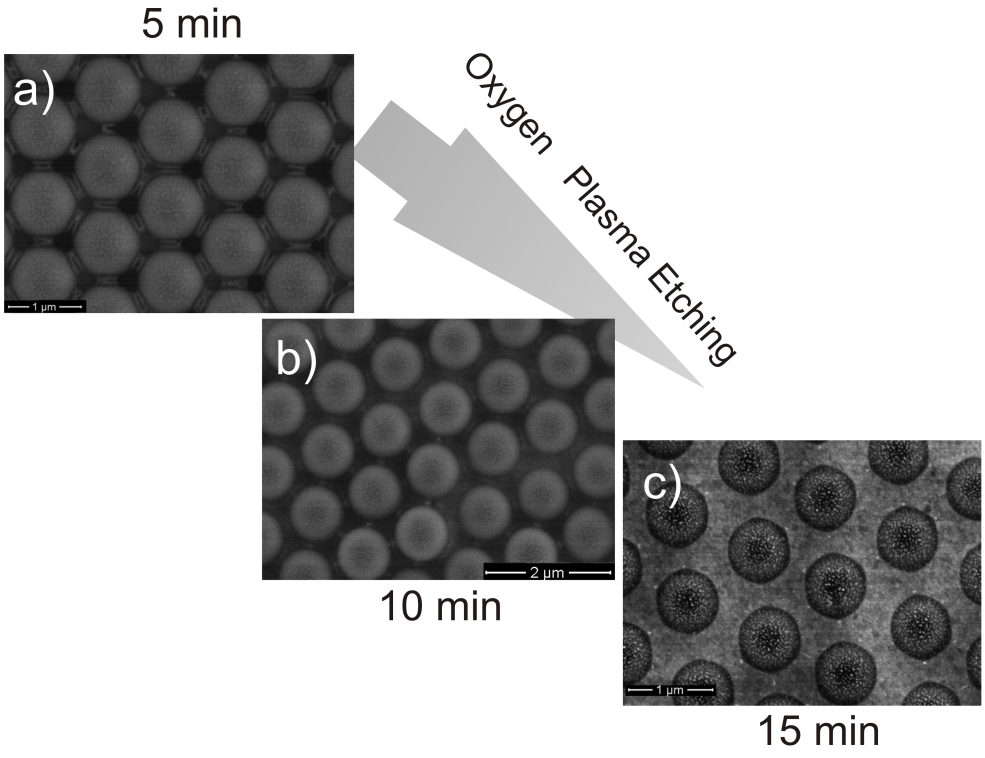


Figure 2.8: Close SEM images for three different stages on sphere reduction by oxigen plasma etching applied on $\Phi = 1\mu m$ sphere monolayer over gold substrate

rate is clearly seen to become larger as etching times increase. A similar behavior has been observed when an etching plasma is applied on organic spheres [109]. It is worth mentioning that, although smaller diameter spheres ($\Phi = 520nm$) seem to present faster reduction rates it fits for a similar non linear reduction curve.

A second consideration concerns the effect of the plasma on the material that forms

the spheres. It is well known that the surface rugosity of the spheres is increased with OPE treatment [110]. The usual method to recover the sphere smooth surface is a time-controlled annealing at low temperature ($\sim 70^{o}$). This effect can be observed in e 2.8, which shows the evolution of the $\Phi = 1\mu m$ PS spheres considered here at different plasma times. It can be observed that the surface of the spheres is modified as we increase the etching time. In particular, it is observed that a grainy surface is obtained after 15 minutes exposure ($\gamma_{final} = 0.75$). A similar effect has been reported on etched polymeric particles [108]. Several approaches can be adopt to increase the smoothness of the reduced spheres surface as for example the use of anisotropic etchings or performing a low temperature annealing after spheres reduction. However, given that we are interested in optical features taking place at wavelengths similar to the diameter of the spheres, important effects aren't expected from this nanometer scale roughness. Furthermore, the annealing process is likely to deform the spheres and, as the sphericity of the building blocks is a key parameter in the optical response of this kind of system, we have taken the conservative approach of non-anealing.

Another important feature to be noticed on figure 2.8 is that some material remains deposited between the spheres after short times of plasma (see figure 2.8a) , mainly in the contact points between spheres. This effect has to do with the way the plasma is applied to the the sample (top to bottom). The more packed (larger γ) the lattice is, the lower the uniformity of the plasma action over the sample. For larger γs more material is removed from the upper part of the spheres and then, shapes as the one shown for 5 minutes of exposure in Fig. 2.8a are obtained. This issue, as for the case of the grainy surface, is not expected to be optically relevant. If longer exposure times are considered, the spheres get completly separated as can be observed in the same image for 15 minutes. We have obtained similar results for $\Phi = 520nm$ diameter spheres, regardless of the fact that they are dye-doped or not.

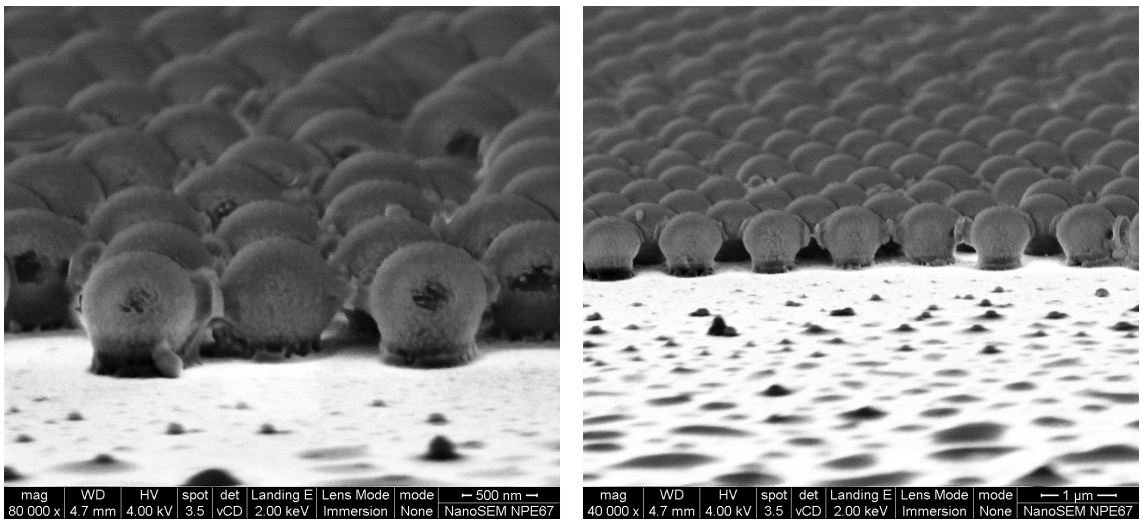


Figure 2.9: SEM images at different magnifications of $\Phi = 1\mu m$ PS spheres monolayer after 10 minutes plasma etching.

The final parameter that should be considered is how much the spheres keep their original shape as the plasma acts on the sample. Plett et al. [108] demonstrated that etching at low temperatures it is possible to avoid non spherical final shapes if very large reductions are needed. We have checked the shape of our samples after room-temperature

OPE as shown in figure 2.9. As can be observed, a non-spherical final shape is obtained after a relatively long plasma etching time. As we will not perform such large reductions, the sphericity of our samples will be enough in order not to modify the optical response. In any case, if required, better sphericity could be obtained calibrating sphere reduction with new plasma parameters such as the temperature of the chamber.

2.4 Conclusions

We have shown that it is possible to grow high quality monolayers of polymeric spheres with different sphere diameter over dielectric as well as metallic substrates. Two different methods have been demonstrated to work properly depending on the substrate requerirments. It has also been mentioned how large area monodomain 2D lattices can be grown by the wedge-cell method over previously hydrofilic metallic substrates. Finally, we have shown that oxigen plasma etching is a very simple but effective technique to tailor the filling fraction of the polymeric lattice by means of sphere reduction which can serve as a means to tune/tailor the optical response of the whole system.

Chapter 3

Optical characterization by Fourier image spectroscopy

In this chapter an in-depth description of the main experimental technique used to characterize the photonic crystals under study in this thesis is presented. Such technique is based on direct inspection of the spacial optical Fourier Transform of the response of the sample. Both monochromatic and white light spectroscopy configurations are presented. Examples of measurements performed on systems where the angular response is known are used as a means of calibration of the system.

3.1 Introduction

Optical spectroscopy is one of the most obvious techniques to characterize one (1D), two (2D) or three (3D) dimensional photonic crystals (PCs). Reflectance and transmittance measurements can reveal how light propagates through/within the system under study. Within the set of techniques available for optical spectroscopy, normal and oblique (angle resolved) reflectance/transmittance is the most commonly used one in PCs characterization given that they allow demonstration of the main features of 2D and 3D PCs. Normal incidence configuration can reveal, for instance, information about confined modes for 2D PCs [111] or pseudogaps [112], full photonic gaps [9] or localized states at defects [113] for 3D self-assembled PCs. On the other hand, if one want to measure the dispersion relation for a given structure, angle and polarization resolved optical spectroscopy is the most straightforward technique. It has been used in the past to map dispersion relations along high symmetry directions of 2D [111] and 3D [114] PCs. Finally, it is worth to mention that for those systems where an emitter is affected by the dispersion relation of a PC, angle and polarization resolved measurements are a must to in-depth characterize the system. This kind of set-ups have been applied for 2D [115] and 3D [116] PCs in the past.

For the measurements presented in this thesis a set-up has been designed and realized in order to be able to obtain a full angle/polarization resolved optical characterization of the samples described in the previous chapter in an automated way. The usual and most simplest technique for angle resolved spectroscopy consists in two branches mounted on a goniometer which are able to rotate in a controlled way around a sample. An interesting example of this kind of systems is shown in reference [117] and is plotted in Fig. 3.1.

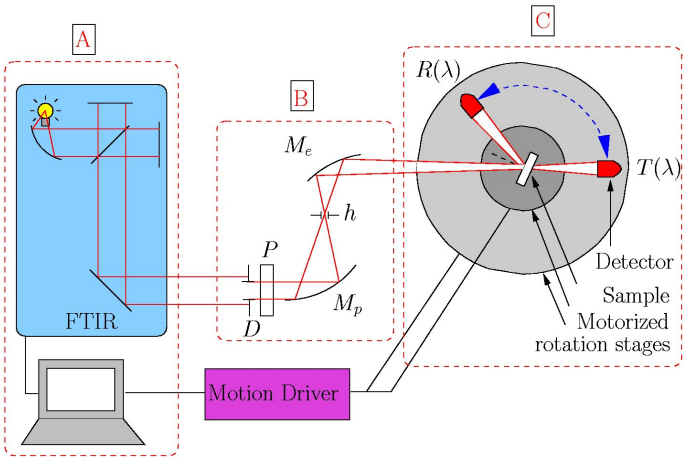


Figure 3.1: Simplified diagram of a conventional angle-resolved spectroscopy set-up. In this case, signal collected in the rotation stage is taken to an FTIR spectrometer. Image from reference [117]

In that diagram, each of the branches holds the illumination and the detection elements respectively. There are many approaches to this technique as for example using fiber coupled ilumination/detection or keeping the mechanical branches fixed while the sample is rotated. However, one main drawback of these systems is the lack of control to choose the point in the sample to be measured. Given that large magnification lenses are required to allow choosing a small region of the sample, it is necessary to work at short working distances. This makes it difficult to rotate the sample for an angle resolved characterization. Another disadvantage is that, as the angle of incidence increases the projection of the incident beam over the sample becomes an ellipse so that the probed area is increased as the angle in increased and therefore the optical response measured at different angles might not be comparable. In order to avoid those problems our approach consisted in the use of a high numerical aperture (HNA) microscope objective coupled to an external optical set-up where the angular response is obtained from the optical Fourier Image formed by the HNA objective.

Imaging the back focal plane (BFP) of a HNA objective is a widespread technique in many fields where not just the spectral, but the spatial properties of the probe beam is relevant. As it is well known in optics, an optical system produces in its BFP an image which is the spatial Fourier transform of the object at its focus [118]. Therefore, studying the image of the Fourier plane has been employed to obtained in-sample propagating wavevectors [1]. It has been used for example in plasmonic systems [60] where measurements of the effective refractive index of the propagating plasmon can be obtained. Furthermore, the angular response can be easily related with the Fourier Image at the BFP which has made this technique applicable to angle resolved photoluminescence spectroscopy in polaritons [119] or photonic crystals [115]. Recently Cottrell *et al.*. [120] presented a set-up to measure angle resolved scattering of single polymeric spheres with applications in medicine. The set-up presented in this thesis is similar to that one.

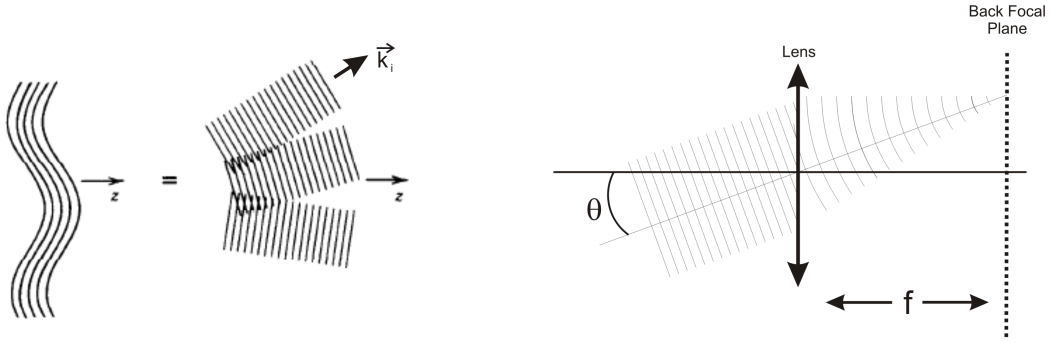
In this chapter we will present the improvements we have performed on this kind of set-up and how we have adapted it for the optical study of PCs of different dimensionality. In the first part the set-up is presented and its main characteristics are described. After that we describe how to extract and process data from the direct measurements. Finally,

[1] Note that reciprocal space is calculated as the Fourier transform of the real one.

some examples on its applications to the optical study of photonic structures (mainly self-assembled ones) will be shown.

3.2 Optical Fourier transform for angular resolved measurements

The propagation of a light beam in free space can be conveniently described by Fourier analysis. In particular, the complex amplitude of a monochromatic wave can be described as a combination of a set of plane waves of wavector $\overrightarrow{k_i}$ and amplitude u_i whose interference will produce the final propagating wavefront (see diagram in Fig. 3.2a). On the other hand, a plane wave impinging on a lens of focal f forming an angle θ with the optical axis of the system will be focused at a point placed a distance f (BFP) of the lens and a distance d from the optical axis [121] as can be observed in the diagram of Fig. 3.2b.



(a) (b)

Figure 3.2: (a) Any wavefront for a propagating beam in free space can be decomposed in a superposition of plane waves (image taken from [118]). (b) Diagram for focusing by a lens of a plane wave into a point of the BFP.

Therefore, if we consider a complex wavefront in a (x,y) plane at a distance d from the lens, it is expected the lens to form an intensity pattern in the BFP. In this pattern each point can be related with a given incident plane wave on the lens with the corresponding amplitude. After some mathematics [118], for a complex amplitude wavefront $f(x, y)$ at a given distance d from the lens the expression for the intensity at the BFP results on a proportional relation to the Fourier Transform of $f(x, y)$ as seen in Fig. 3.3.

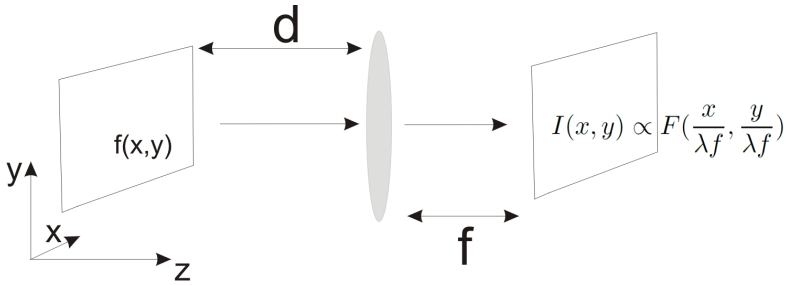


Figure 3.3: Intensity pattern $I(x, y)$ produced in the BFP by a lens for a wavefront $f(x, y)$ placed at a distance d of the lens.

where F is the Fourier transform of $f(x, y)$ with $(\frac{x}{\lambda f})$ and $(\frac{y}{\lambda f})$ being the spatial frequencies in the plane at which $f(x, y)$ is evaluated by the Fourier transform. For the particular case of a a wavefront placed at a distance d = f (front focal plane) of the lens, the complex amplitudes at the front and back focal planes of the lens are related by Fourier transform in both magnitude and phase. This case is known as 2-f system and present particular properties concerning the phase of $f(x, y)$. Although we are interested in intensity measurements, we have chosen this configuration to make it compatible with our microscope set-up were the sample is always placed at the focal plane of the objective.

If one considers a microscope objective as the lens in the previous study the small size of its BFP has to be considered. Therefore, it is usually necessary to magnify that plane if one wants to inspect the information contained in the Fourier transform of optical signal at the focal of the objective.

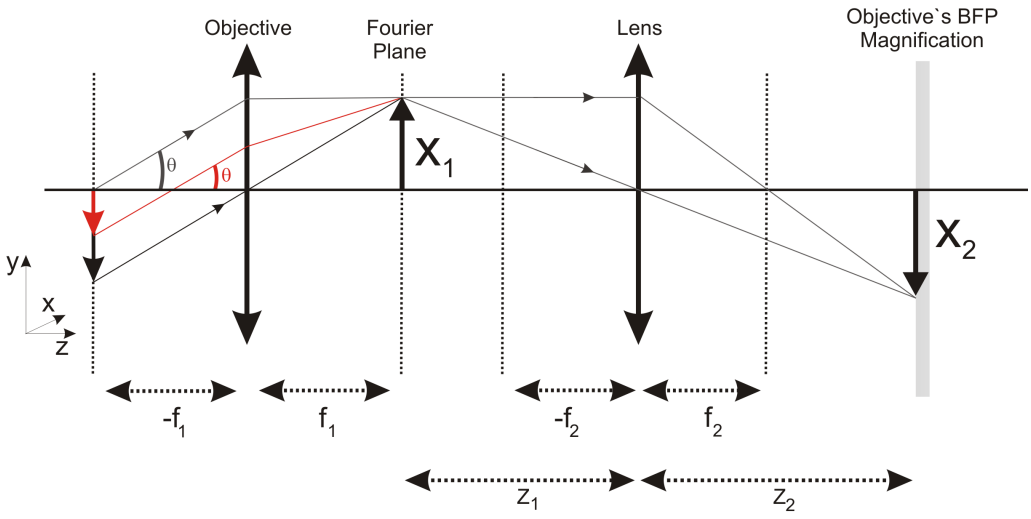


Figure 3.4: Fourier image plane magnification set-up for a plane situated at the focal plane of the objective. BFP image is magnified by the lens an the new image is formed at a distance $Z_1 + Z_2$ from the BFP.

Fig 3.4 shows a diagram of one possible set-up to obtain a magnified image of the BFP of an objective of focal distance f_1. Two objects with different sizes have been plotted and the ray tracing has been performed for those rays departing from both objects with the same angle. As previously explained, every wave with the same angle is focused by the objective in the same point of the BFP. An important point has to be stressed from the ray tracing shown in Fig. 3.4. That is, every light ray outgoing the focus plane with the same angle reach the same point at the BFP, no matter the position in the y axis. It is direct from the diagram that $X_1 = f_1 tan(\theta)$. This discussion can be extrapolated to a 2D case where every ray leaving the (x,y) focus plane with the same θ but also with equal precession angle Φ (angle formed respect to the y axis in the xy polane)) will be focused at the same point in BFP. In order to magnify the angular pattern (Fourier transform) in the BFP an extra lens of focal f_2 is placed at a given distance Z_1. It forms a new image at a position Z_2. By using the lens formula one can calculate that the magnification of the system: $M = X_2/X_1 = -Z_2/Z_1 = f/(f - Z_1)$ and therefore, the main equation decribing this set-up is:

$$X_2 = f_1 tan(\theta) M = \frac{f_1 f_2}{f_2 - Z_1} tan(\theta) \tag{3.1}$$

An isotropic point emitter placed at the focal plane of the objective is probably the simplest case but also a very intuitive one. If one consider the emission pattern of an isotropic punctual source at a given wavelength λ, it is straightforward that the spacial Fourier transform is a circular homogeneous pattern and then a homogenously illuminated circle will be collected at position Z_2 in Fig. 3.4. Experimental implementation of emission angular pattern measurements with this technique [122] consist on pumping the sample with a monochromatic source and collecting the outgoing emission pattern at the required frequency .

3.2.1 Reflection Fourier imaging

We have seen that the relation between an outgoing angular pattern and the image collected at the BFP is a straightforward procedure. However, we commented early in this chapter that reflectance measurements are a key technique in PC characterization. Unlike in most of the emission Fourier image experiments, reflectance angular pattern of a PC will be strongly dependent on the incident beam angular distribution. Therefore, it is important to show how we can use BFP imaging to collect a reflectance angular pattern.

In order to make a monochromatic collimated beam incident at a given angle over the focus plane one can place a beam splitter at some point between the BFP and the lens as shown in Fig. 3.5a.

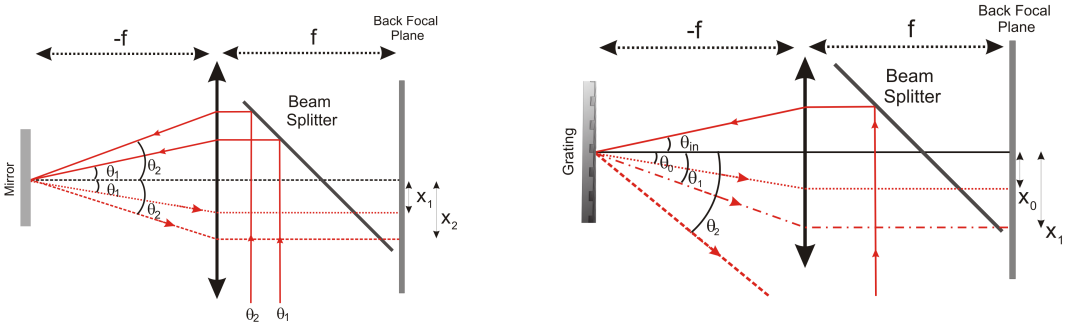


Figure 3.5: (a) Diagram of angular pattern for a mirror with two incident beams $\theta_{1,2}$ collected at BFP. $x_{1,2}(\theta_{1,2})$ are the corresponding position at the BFP. (b) Same example for a grating. θ_{in} is the incident angle and $\theta_{0,1,2}$ the diffracted orders for m=0,1,2 respectively.

As can be observed, the simplest case for reflection is a mirror. The incident beam at angles θ_1 and θ_2 are reflected with the same angle and collected at the corresponding distance from the optical axis (x_1 and x_2) in the BFP. Therefore, if one consider an objective with a given numerical aperture defined by the maximum angle collectable (θ_{NA}), a collimated beam will be impinging the mirror with all the angles $0 < \theta < \theta_{NA}$ at once. Then, the resultant Fourier image at BFP is an homogenous pattern.

Let‘s assume a more complicated case. Fig. 3.5b shows the same set-up used for the mirror but in this case the object is a grating. Without entering the details one can imagine

an incident beam with a given angle θ. The reflected zero order (θ_0) of the grating presents mirror behaviour. However, it is possible that some higher diffractive orders ($m = 1, 2, ..$) are being also excited. They will be reflected on non symmetric angles (θ_1,θ_2) and then collected at different distances (X_1) from the optical axis at BFP. This way, the far field diffractive pattern is obtained.

As can be observed in Fig. 3.5b for θ_2 an special feature take place. If $\theta_2 > \theta_{NA}$ that diffractive order (and the ones higher than that) is not collected and not shown as a spot in the BFP. Therefore, NA of the objective will determine the maximum angle which we can measure with this kind of set-up.

3.3 Set-up description

Our design is based on a modified commercial inverted microscope (Zeiss Axio-Observer). The microscope objective is a Zeiss EC Plan-Neofluar $40X/NA = 0.75$ which provides a maximum angular aperture of 48.5^{o} as calculated from $NA = n_s sin(\theta_{max})$ [2]. This objective is specially designed to obtain high quality images at visible frequencies which is our working spectral target. For the illumination, the only unmodified part was the transmission arm. Given that transmission spectra are, in most of the cases, not useful for the structures studied in this thesis, that part is not considered in the set-up description. A diagram of the reflectance set-up is shown on Fig. 3.6.As can be seen, an optical fiber-based collimated illumination system (lens L1) replaces the incandescent lamp originally attached to the microscope. The final collimated illumination beam has a diameter of 1 cm. This configuration allows a very simple way of changing the illumination spot size on the sample by just changing the fiber diameter.

The collimated beam is resized by the telescope formed by lens L2 and L3. The resultant beam is then focused on the sample by the HNA objective. This configuration is called "critical illumination" [123] and is probably the most widespread in optical microscopy. In our case the complete optical train has shown to have a conversion factor of 0.1. That is, when illuminating with a $200\mu m$ core diameter fiber we shine a circular $\sim 20\mu m$ diameter area of the sample. As mentioned before, by changing the fiber we can choose the total illuminated area over the sample. Given that critical illumination consists in forming the image of the illumination source over the sample, special care has to be taken on the shape of the outgoing beam from the collimation system.

Another advantage of this system is that L3 is placed at a distance f_3 from the BFP of the objective (where f_3 ifs the focal length of L3). This means that if L2 is removed , the collimated beam will be focused on the objective BFP and Köhler illumination will take place (both configurations are shown in Fig. 3.7). This kind of illumination can be useful in some cases, specially if we want to shine as much area as possible as for example in single molecule emission measurements. As this is not our case, we will keep L2 mounted in most cases. In terms of the angle resolved response it is important to note that both illuminations are opposite concepts. The beam coming out of the objective in the Kohler configuration is a collimated one, that is, incidence on the sample is always normal to its surface. In terms of of the optical response of the sample this means that only those states excitable at normal incidence will be probed. However, in critical illumination the incident beam is focused on the sample and then all those angles between $\theta_{min} = 0^{o}$ and $\theta_{max} = 48.5^{o}$ (determine by $NA = 0.75$) are being probed at once. This difference will

[2] n_s is the refractive index of the surrounding medium, in this case air. The optical resolution is calculated following the Rayleigh criterion and results in $r = 0.61\lambda/NA = 406$ nm for $\lambda = 500$ nm

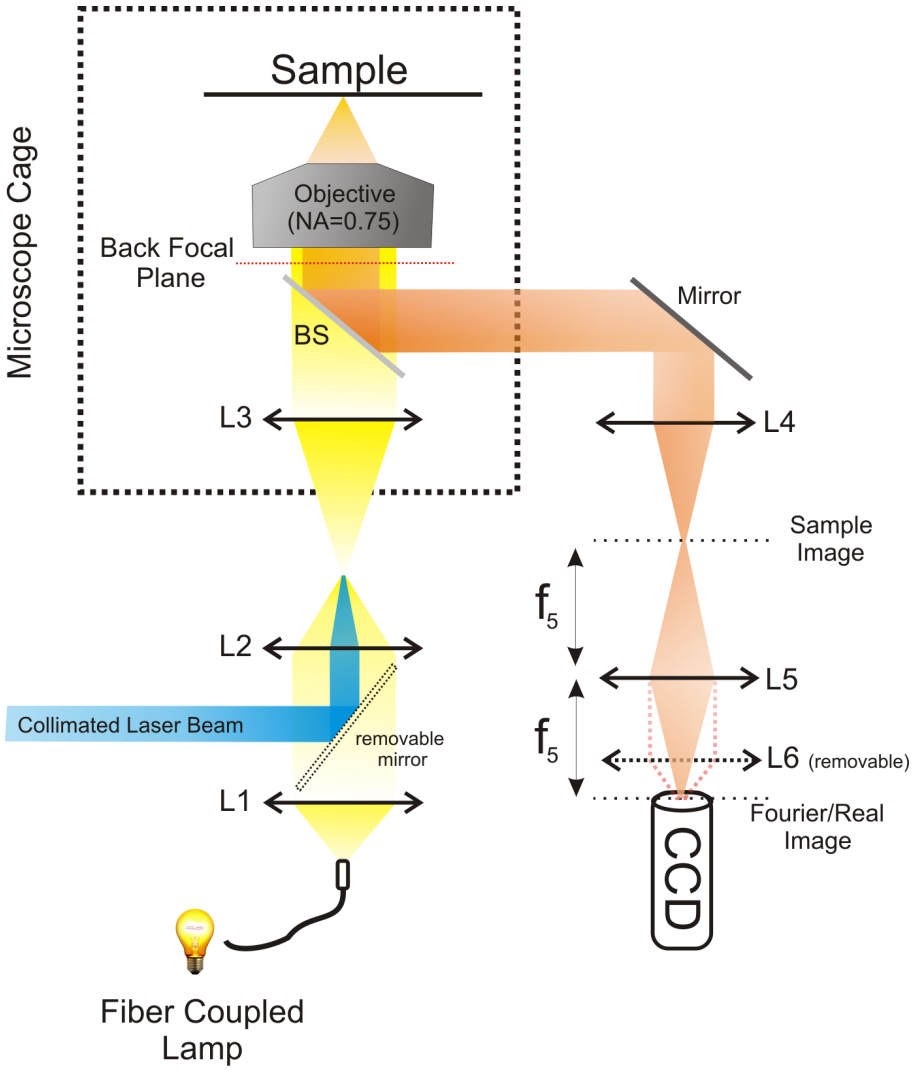


Figure 3.6: Diagram of the set-up for Fourier Image direct inspection. Both, white-light and laser illumination are considered. The chosen with or without L6 lens configuration determines if the Fourier or the real image respectively is collected at the CCD camera.

be shown as very important in the next chapters in order to understand the reflectance angular patterns of the samples under study.

As shown in figure 3.6 a mirror can be placed between L1 and L2 in order to introduce a complementary collimated beam that will be focused over the sample in the same way as that of the the fiber coupled lamp. In our case we have used a laser beam at $\lambda = 485nm$ usable either in continuous mode (CW) or pulsed with a pulse of 12 ps and repetition rate tunable from 32 kHz to 20 MHz. This allows us to optically pump samples with emission properties. The illuminated spot position on the sample can be controlled in the micrometer scale (spot size is $\sim 15\mu m$ in our case). Emission of samples containing a dye (as those shown in the previous chapter) have been measured in this way. It has to be stressed that the two illuminations (monochromatic and white light) can be interchanged without affecting the rest of the setup. As will be shown in the following sections this allows us to measure reflectance and emission being sure that both measurements are

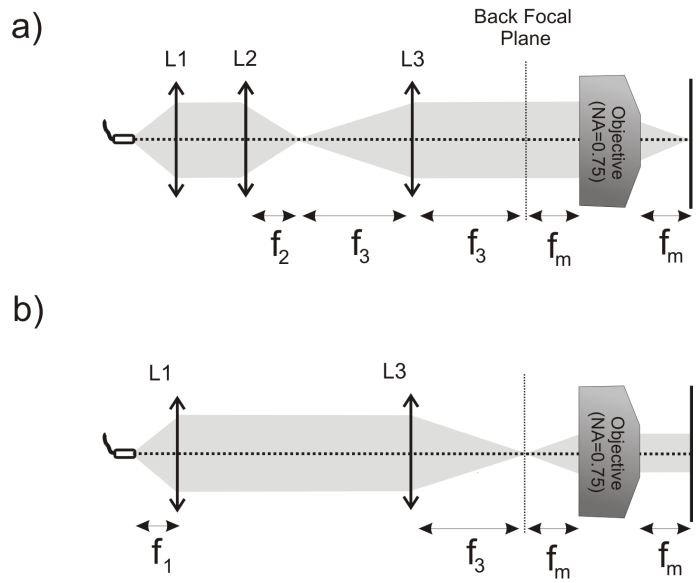


Figure 3.7: By removing the L2 lens the set-up changes from critical (a) to Köhler (b) illumination. The same configuration applies to the collimated laser beam.

performed exactly at the same point of the sample, and can therefore be compared.

3.3.1 Microscope output

In our set-up, regardless of the chosen illumination, the image collected by the objective is focused out of the microscope cage by lens L4. This forms a magnified image of the sample at the Sample Image plane as shown in Fig. 3.6. Next, lens L5 is placed at a distance f_5 from the Sample image plane in such a way that the Optical Fourier transform is obtained at BFP of L5. We have called it Fourier/Real Image in the diagram of the set-up. It has to be noticed that this configuration does not exactly match the diagram of Fig. 3.4 where OFT is formed at the BFP of the objective previously to its magnification with the lens. In the set-up of Fig. 3.6 the magnification is applied by L4 on the sample image previous to the Fourier transform of that plane by L5. This last configuration has shown to be more robust in terms of stability given that imaging the BFP of a 40X objective is a very critical situation due to the reduced size of the Fourier image formed in that plane.

Finally, an extra lens L6 can be added after L5 and at a distance f_6 from the Fourier/Real Image plane (f_6 being the focal distance of the lens). This lens is placed using a kinematic mount which allow us to remove it easily. When placed, a magnified image of the Sample Image plane is obtained at the Fourier/Real plane (dashed line shows ray tracing in that case). Therefore, both, OFT of the sample image and magnified "real images are available at the same plane by removing or not L6. We will focus in this chapter in the configuration for the Fourier transform imaging.

Therefore, from Fig. 3.3, the Sample Image plane presents a given pattern $f(x, y)$) while the Fourier Image plane after L5 presents an intensity distribution $I(k_x, k_y)$ which is proprtional to the Fourier transform of $f(x, y)$. As previously explained, each different point (x,y) at Fourier Plane collects all those waves leaving $f(x, y)$ with the same angle. This way, placing a CCD camera [3] at the Fourier plane, the angular response is obtained in one single image.

[3] In our case the camera is a Hamamatsu C8484-05G01 model

If a single working wavelength is considered, the image can be directly related to the angular response. However, if white light is being used (for example in reflectance measurements) the images can be misleading since the colection at the CCD will contain a superposition of the angular response for many different frequencies. To solve this problem a tunable filter (Semrock TBP01-700/13-25x36) was placed in front of the camera which allows us to collect the angular response at a given wavelength in a spectral range between 600-700 nm with a $\Delta\lambda = \pm 10nm$ spectral resolution.

Experimental limitations concerning the angular resolution were previously commented to arise in the first place from the NA of the objective used. The larger the NA the more angles can be introduced in the Fourier plane image. However, other important restriction is given by the pixel size of the CCD. As we increase the range of angles included in the Fourier plane, spatial separation between adjacent points decreases and pixel resolution might not be enough to resolve them. As the total size of the CCD is a constant, a compromise must be achieved between the largest NA and the CCD size. In our case the pixel is a square of lateral size $6.45\mu m$. The total size of the CCD chip is 1344x1023 pixels with a total cell of $8.67 \times 6.6mm^2$. The Fourier Image is expanded until it completely covered the CCD. As will be explained in the next section, this values allows an angular resolution of 0.5^o in the best of the situations.

3.4 Extracting data from the Fourier Image

Although qualitative information can be obtained from the Fourier image it is from quantitative measurements that we can accurately study the optical response of the sample. To obtain this kind of measurements we need to calibrate the system so that different points in the Fourier plane can be unambiguously associated with exit angles. In order to do so, an object whose Fourier image can be easily calculated is used and compared with the image obtained in the Fourier plane. In our case we consider a 1D grating in reflectance configuration whose Fourier transform is essentially a 1D collection of stripes. We detail below the calibration process which is, with some variations, the one described by Valentine *et al* [124].

As can be seen in Fig. 3.8, a given outgoing angle $\theta_{m=0}$ from the sample impinges in a point at the radial distance (x) respect to the optical axis in the Fourier plane. It is trivial that x is directly proportional to the sine of the scattering angle. However, due to image-deforming optical aberrations caused by the relay lens a nonlinear relation rules this relation in the experimental set-up. We measure this relationship making use of the diffration from a commercial metallic grating ($Thorlabs \quad GH25-24U$) with pitch $\Lambda = 417$ nm. The illumination correspond to the critical configuration.

Figure 3.8 shows a simplified case of the optical system under consideration to calibrate the set-up. A monochromatic focused beam impinges on the sample with an angle θ_{in} and the reflected beam produces an angular pattern at the CCD camera placed in the Fourier plane. Light is scattered by the grating according to Bragg condition:

$$\overrightarrow{\kappa}_{out||}(\lambda) = \overrightarrow{\kappa}_{in||}(\lambda) \pm m\overrightarrow{G} \tag{3.2}$$

where $k_{in||}$ and $k_{out||}$ are the components of the incident and scattered wave vectors parallel to the surface of the grating, i.e $k_{in||} = (\omega/c)sin(\theta_{in})$ and $k_{out||} = (\omega/c)sin(\theta_{out})$,$\theta_{in}$ and θ_{out} being the angles measured with respect to the surface normal, ω the angular frequency and c the speed of light in the dielectric medium on top of the grating. $\overrightarrow{G}$ is the reciprocal lattice vector of the grating that in this case $|\overrightarrow{G}| = G_x = 2\pi/\Lambda$ and which we

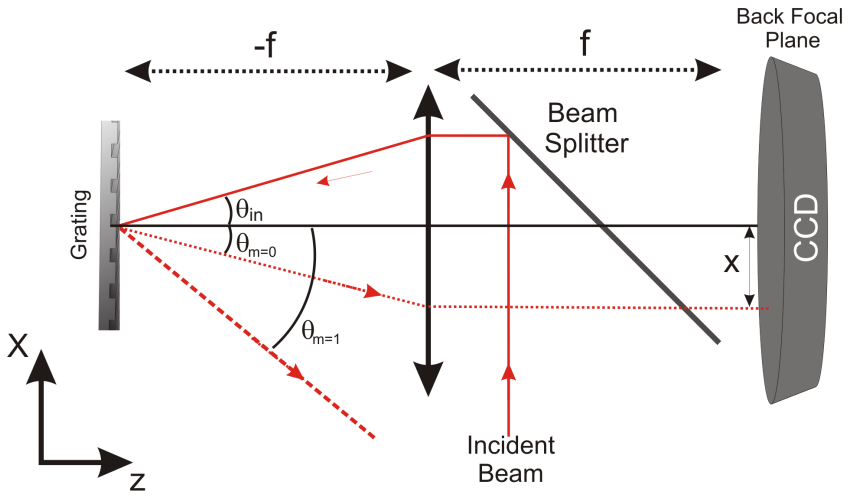


Figure 3.8: Simplified diagram for collection of the angular pattern of a grating at a CCD camera. θ_{in} is the incident angle while $\theta_{m=0}$ and $\theta_{m=1}$ are the zero and first diffracted order respectively.

consider along the x-direction, where Λ is the period of the grating and m is an integer. Then, we can obtain the diffraction condition for the first reflection diffraction order to take place. It will happen for that angle θ_{in} for which the order $m = 1$ is diffracted at grazing angle ($\theta_{m=1} = 90^0$). Therefore, for a given θ_{in}, the condition for the first diffraction order $m = 1$ occurs if:

$$\theta_{in} \geq asin(1 - m\frac{\lambda|\vec{G}|}{2\pi}) = asin(1 - \frac{\lambda}{\Lambda}) \tag{3.3}$$

In particular, we will call θ_{Bragg} the diffraction limit corresponding to $sin(\theta_{Bragg}) = 1-\lambda/\Lambda$. According to the discussion above, if we consider incidence with a fixed wavelength and a given angle in the set-up of Fig. 3.8 three different situations can take place:

1. If $\theta_{in} < \theta_{Bragg}$ diffraction condition is not satisfy for any incident so the grating behaves like a mirror and the whole intensity is reflected with $\theta_{m=0} = \theta_{in}$. As a result, a homogenous intensity distribution is expected at the CCD where the total incident intensity is reflected to the CCD.

2. $\theta_{in} \geq \theta_{Bragg}$ but $\theta_{m=1} > \theta_{NA}$. Diffraction takes place but the outgoing angle of the diffracted beam is larger than the maximum angle θ_{NA} collectable by the objective which produce that just the zero order impinges the Fourier plane and the CCD camera. Moreover, the total incident intensity is distributed between both orders of diffraction. As just zero order reach the CCD it suffers a reduction in the collected intensity respect to the $\theta_{in} < \theta_{Bragg}$ case.

3. Finally, $\theta_{in} \geq \theta_{Bragg}$ and $\theta_{m=1} < \theta_{NA}$. In this case the diffractive order is also collected and therefore shown in the image at the CCD camera.

Taking into account this conditions, we can adapt them to the specific set-up presented here. Consider critical illumination. In that case the whole set of incident angles are

inpinying the sample at the same time. That is, the collected signal at the Fourier plane is the integration of the angular response of the grating for all those diffractive angles within the limit $0 < \theta_{in} < \theta_{NA}$.

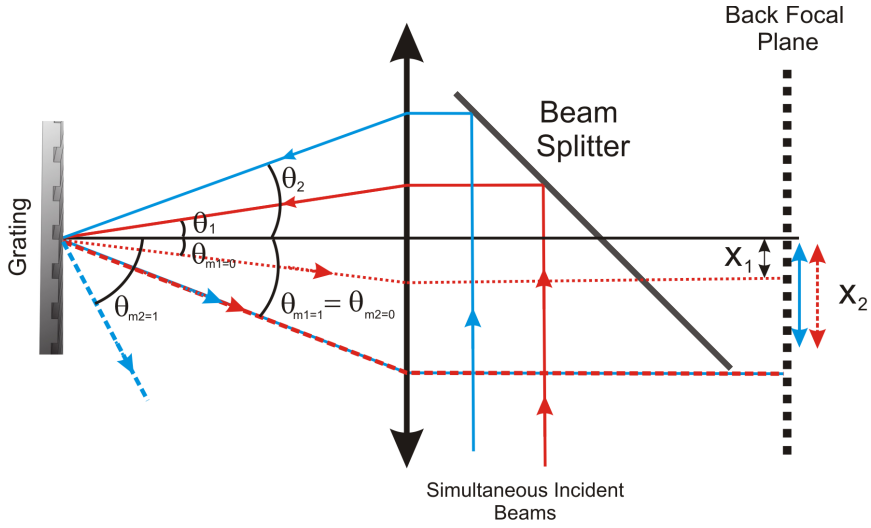


Figure 3.9: Diagram of the situation where first diffraction order (m=1) of an incident beam with θ_{in1} (red lines) matches the same point at Fourier plane that the zero diffraction order of a simultaneously incident beam with θ_{in2} (blue lines).

Fig. 3.9 shows a ray tracing for two incident beams with $\theta_1 < \theta_2$. While beam θ_1 presents the situation where the diffracted beam $m = 1$ reaches the Fourier plane, for θ_2 that condition is not satisfied. However, the zero order diffraction (m2=0) for θ_2 satisfy $\theta_{m2=0} = \theta_{m1=1}$ and therefore both of them are projected to the same point (x_2) in the Fourier plane. It means that the collected intensity at the CCD placed in the Fourier plane will show the adding of those two diffracted beams. One can extrapolate this to the case of the whole set of available angles to be excited at the same time. Taking into account the previous discussion, three situations in terms of total intensity reflected onto the CCD can be obtained according to the previously described: mirror behaviour (1), lack of reflectance due to non Fourier plane projected diffraction (2) and sum of different diffraction orders (3). Besides, regarding the Bragg conditions shown in equation 3.2 is is easy to obtain the condition for $m = 1$ being projected in the Fourier plane ($\theta_{out} < \theta_{NA}$).

$$\theta_{out} = asin(\frac{NA}{n_{work}} - \frac{\lambda|\vec{G}|}{2\pi}) \tag{3.4}$$

where $NA = 0.75$ stands for the numerical aperture of the microscope objective and n_{work} the refractive index of the dielectric between the sample and the objective. In this case this material is air ($n_{work} = 1$).

Let‘s apply this discussion to experimental data. Fig. 3.10 shows the images obtained at the CCD camera in set-up of Fig. 3.6 under critical illumination and different wavelengths for a metallic mirror (a) and the $\Lambda = 417nm$ grating ((b) and (c)).

X represent is the direction along which the grating presents its periodicity while y is the direction in which incident light can not be diffracted due to the lack of structuration (it will work as a mirror for any incident beam). We first consider the reflectance profiles along the x axis. As expected, the angular pattern for the reflectance of the mirror

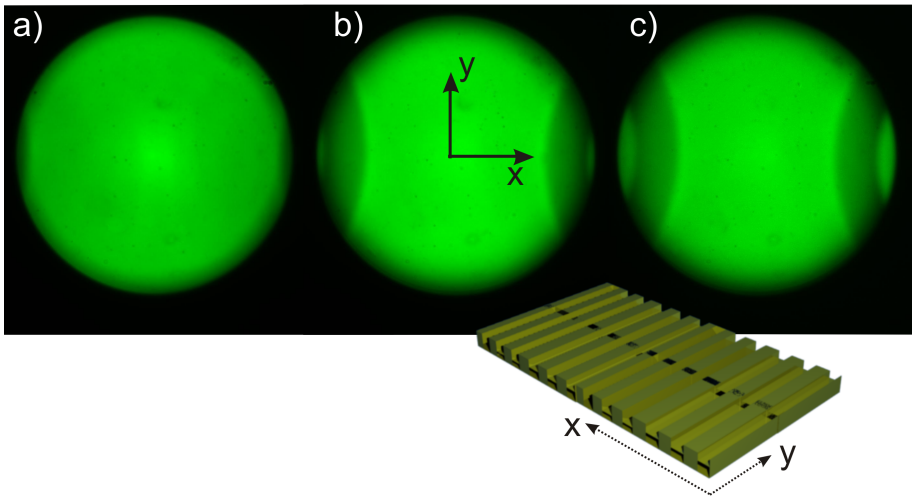


Figure 3.10: Fourier images in reflection for a mirror at $\lambda = 660$ nm (a) and a commercial metallic grating of pitch $\Lambda = 417nm$ at $\lambda = 620$ nm (b)and $\lambda = 590$ nm (c)

(case a) at the single wavelength considered ($\lambda = 660$ nm) presents homogenous intensity distribution. We focus now in the grating images b and c showing Fourier Images for reflectance collected in the CCD camera at $\lambda = 620$ nm and $\lambda = 590$ nm respectively. As can be seen, a dark ring appears at a given radial distance. The dark band of reduction in reflectance reflects the fact that the first order of diffraction limit is reached but not collected by the objective as shown for Fig. 3.8.

Once we have obtained a qualitative relation between the images and the grating response it is immediate to relate the first dark point (x_1 in Fig3.11) along x axis to the corresponding angle of incidence. From the conservation of $\kappa_{||}$ in equation 6.3 we find that if $\theta_{out} = 90^{o}$ then $\theta_{in}(x_1) = 24.5^{o}$ for incidence with $\lambda = 590nm$. Moreover, x_2 defines in the same image the point at which the first order of diffraction lies. That is, for $\theta_{in} = \theta_{NA}$ first diffractive order is diffracted with $\theta(x_2)$. Besides, the zero order for the simultaneously excited beam with $\theta_{in} = -\theta(x_2)$ impinges at the same point and therefore a higher reflectance is collected than for those angles corresponding to $x_1 < x < x_2$.

The above discussion has been made considering only the diffraction plane along the direction of periodicity but one can also consider light diffracted along other directions. The set-up here presented provides incidence with the whole set of angles θ but also for those angles φ (see Fig. 3.11) between the incidence plane and, in this case, the x axis. Therefore, the limit for diffraction in a more general expresion for a simple grating becomes:

$$\theta_{Bragg} \geq asin(1 - \frac{\lambda}{\Lambda cos(\varphi)}) \tag{3.5}$$

In that case one needs a larger incoming wave-vector to excite the diffraction order which, for a given wavelength, translates into a larger angle of incidence. This fact is

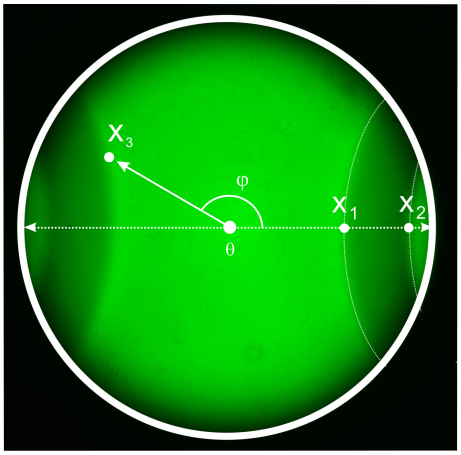


Figure 3.11: Fourier image in reflection for $\lambda = 590nm$ for a $\Lambda = 417nm$ grating. x_1 and x_2 show the angle matching the first diffractive order and re-entering of that order in the objective respectively. Calculations for the respective angles resulted in: $\theta(x_1) = 24.5^{o}$ and $\theta(x_2) = 42^{o}$

evident in the Fourier image of Fig. 3.10 and Fig3.11 where the dark band corresponding to the first diffraction order appears curved.

In order to fully calibrate the correspondence between angles of incidence and spatial positions on the Fourier image one needs to continuously change the incident wavelength and record the spatial positions of the onset of diffraction for the first diffraction edge. In doing so we first employed a broadband white light source which was spectrally filtered with a tunable dielectric filter before entering the CCD. This approach has the inconvenience of introducing a source of error in the calibration associated with the spectral width of the filter. In our case such width was 10 mm which translates into a variable error which for $\theta_{in} = 40^o$ becomes $\delta\theta = 3.6^o$. Another main source of lack of resolution in our set-up is related with the resolution of the CCD employed, as mentioned above.

Angular resolved spectroscopy

In order to obtain precise information and avoid the error sources intrinsic to the imaging set-up (mainly filter spectral width and CCD camera resolution) a new optical path was attached to the Fourier imaging system.

A magnified image of the Fourier plane was obtained on a complementary arm of the same output of the microscope (see Fig. 3.12). Both, imaging setup and the new path are interchangeable by means of a kinematic mounted mirror in order not to loose intensity in any branch. An optical fiber holder was mounted on a micrometer motorized (Thorlabs Z812) stage. The fiber attached had a core diameter of $\Phi = 100\mu m$. The output of the fiber was coupled to an Ocean $USB2000+$ spectrometer [4]. In this configuration and using white light illumination we obtained a spectral measurement of a small region in the Fourier plane image or, in other words, a spectral measurement at the angle corresponding to that point in the Fourier Image [5]. The optical fiber was mounted on a xy stage in order to make it easy to find the center of the image. An additional motorized stage was programmed and linked to the spectrometer driver in the computer. It allows us to scan

[4]The main characteristics are an spectral resolution of $\Delta\lambda \sim 1.5nm$ and an spectral range from 250 nm to 1100 nm with a collection efficiency at a given frequency dependent on the grating.

[5]This measurement is equivalent to that obtained in the case of the usual setup of Fig 3.6

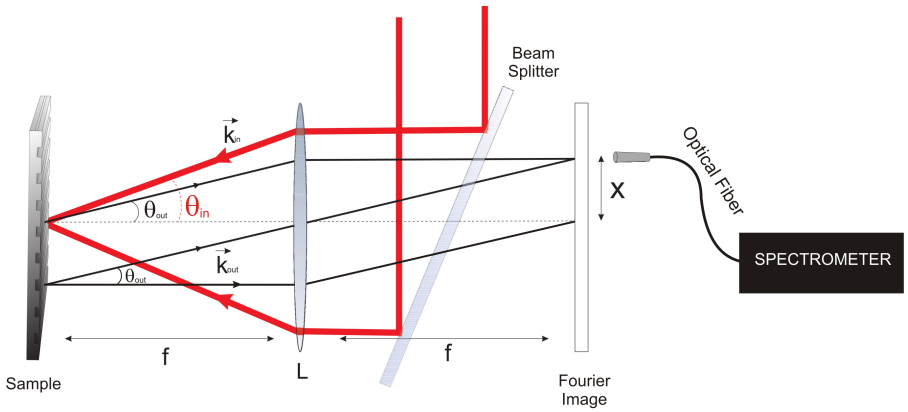


Figure 3.12: Simplified diagram of the set-up for angle resolved spectroscopy measurements. Optical fiber is moved with a computer controlled stepper motor.

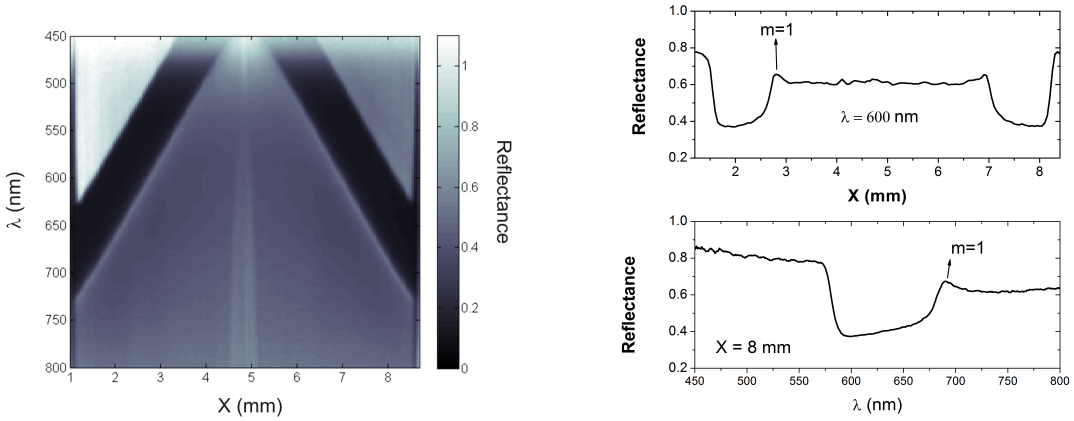
the image in one direction and collect a spectrum at each single step in an automatic process. The scanning is performed in lateral motion from one edge of the image to the other and always crossing the image center ($\theta = 0^0$).

The angular resolution is mainly limited by a compromise between the minimum space between two adjacent steps of the stepper motor and the diameter of the fiber. A fiber of 100 μm diameter was chosen to collect enough intensity with as short as possible integrating time at the spectrometer (30 ms for white light lamp was the commonly used value). Eventually a 50 μm core fiber was used for cases where large angular resolution was necessary although in this case noisier measurements were obtained. On the other hand, the shortest step provided by the microstage is $1\mu m$ [6] which is much shorter than the fober diameter making this parameter not necessary to be considered.

On the other hand, the collection fiber integrates the intensity of a given solid angle in each step of the motor stage. Therefore, that solid angle will be defined by the diameter of the fiber and thus, we can define the angular limitation as the minimum distance between two adjacent motor steps with an overlapping lower than half of the solid angle for each position. In our case, the optical fiber used in most of the measurements was a $100\mu m$ core diameter one. This sets the shorter distance between adjacent steps of the scanning motor to $50\mu m$ which is equivalent to $\Delta\theta = 0.5^o$. In general, the results presented in this thesis have been obtained using fiber diameters for collection between 200 and 50 μm for which a resolution better than 1^o was always obtained.

Fig. 3.13a shows reflectance collected by the optical fiber as a function of position along the scanning axis, presented as a contour plot. Two symmetric dark bands appear whose separation with respect to the center of the image increases with wavelength. According to the discussion for Fig. 3.11, these bands correspond to the excitation of the first diffraction order of the grating with the internal edge of each band associated with the onset of diffraction and the external on associated with the diffracted light re-entering the objective. Fig. 3.13b shows horizontal (up) and vertical (down) cross-sections of the contour plot showing how reflected intensity changes at a given wavelength and fiber position respectively. From the former graph, the point indicated as m=1 tells us the position in the scanning axis matching the angle at which the onset of diffraction takes

[6] Taking into account the magnification of the BFP performed in this system it is equivalent to $\Delta\theta = 0.05^o$



(a) (b)

Figure 3.13: a)Map of measured reflectance as a function of position along the stepper motor scanning axis. b) Reflectance profile along scanning distance for a single wavelength (top) and reflectance spectrum at a given position (bottom).

place. This point is equivalent to the one named as x_1 in Fig. 3.11. By taking a set of spectra for several points along the x axis in the Fourier Image one can extract from those points of the onset of diffraction the corresponding angle and then fit the resulting (X, θ) points to a third degree polynomial equation. This way, it is obtained a calibration for θ as a function of the absolute value X(mm). It has to be notice the non zero reflectance when the diffraction condition is satisfy. This is due to the efficiency of the grating in terms of diffracted intensity for a given order of diffraction.

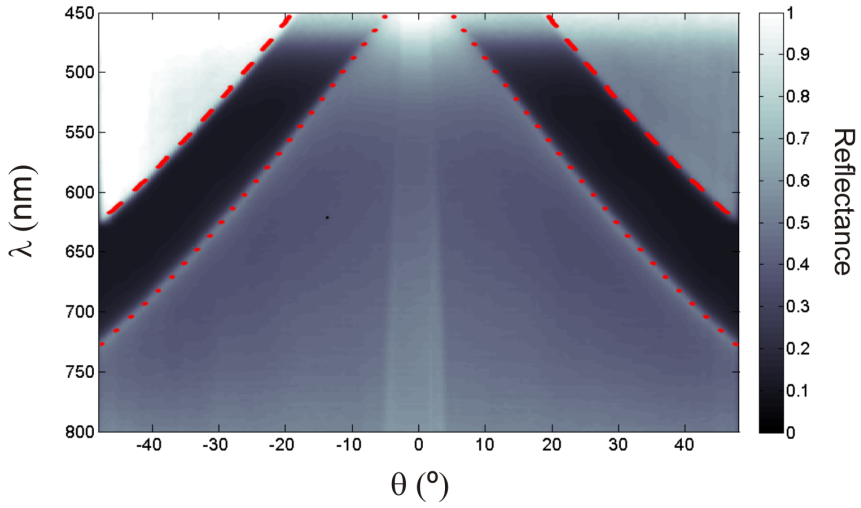


Figure 3.14: Contour-plot of reflectance as a function of angle for a $\Delta = 417$ nm period grating. Calculated values for first order diffraction (red dotted line) and the same order re-entering into the objective (red dashed line) are also shown.

Fig. 3.14 shows the total reflectance as a function of both wavelength and angle after the calibration $\theta(X)$ is applied to the results in Fig. 3.13a. A very good agreement is found

with the calculated angular dispersion for the first diffraction order (dotted red line). As a second check, the angle at which re-entering of that order into the angles captured by the objective happen was calculated [7]. It is shown as red dashed line and an excellent agrement is obtained.

3.5 Application to photonic crystals: spectroscopy of photonic modes

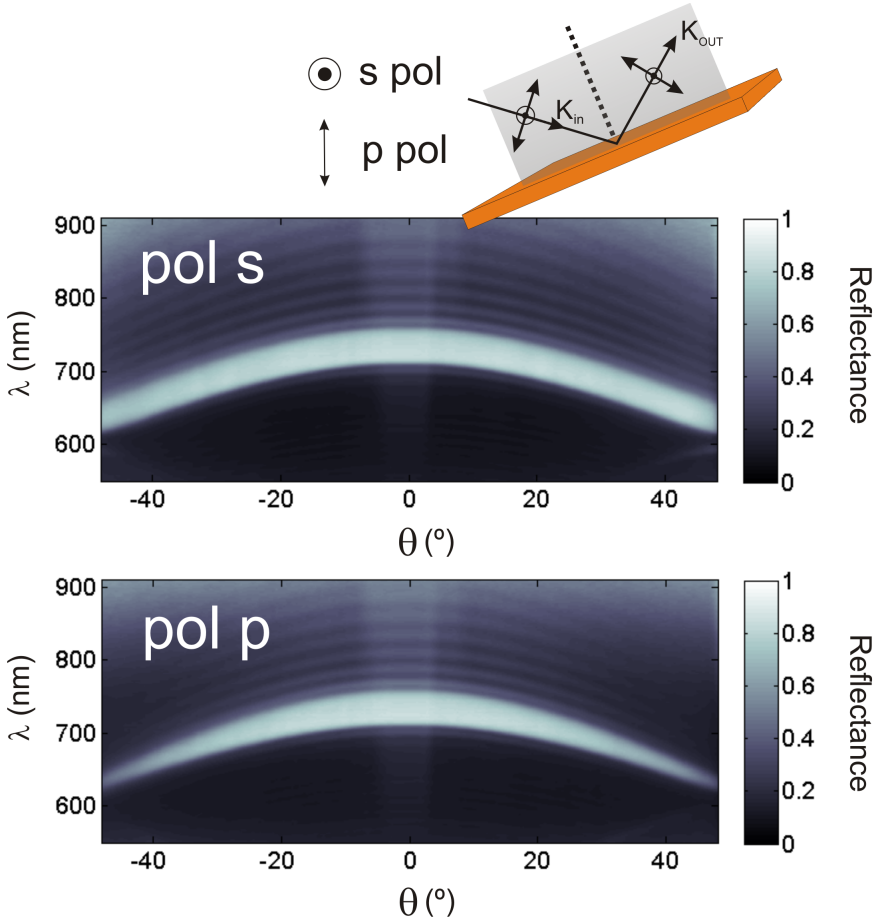


Figure 3.15: Angle resolved reflectivity for an opal made from Φ =320nm PS spheres both for s and p polarization.

So far we have shown that it is possible to perform angle resolved measurements with the described set-up with θ_{max} being determined by the NA of the objective. However,in order to fully characterize the dispersion relation of a photonic or plasmonic crystal it is necessary to be able to obtain polarization resolved measurements. To do this a linear polarizer was placed at the output of the microscope before the spectrometer. In the set-up shown in Fig. 3.6 every available photonic crystal mode is being excited at the same time. If just one polarization is observed at the Fourier plane it is possible to discriminate between s and p polarization where those letters stand for perpendicular and parallel

[7] $\sin(\theta_{out}) = \lambda/\Delta - sin(48^o))$

polarization with respect to the diffraction plane (see Fig 3.15 which is defined by the sample normal and the incident and reflected wave-vectors.

It is well known that artificial opals provide large normal incidence reflectance peaks at frequencies where Bragg diffraction by sphere planes paralel to the sample surface takes place [21]. It has also been studied by Galisteo *et al.* that bands away from the reciprocal lattice direction ΓL are not longer degenerate and therefore, the angular reflectance probed in that direction is strongly dependent on the polarization [125]. We have taken advantage of this properties to test the set-up in angle and polarization resolved measurements. We performed such measurements with s and p polarization for a $\Phi = 320nm$ polystyrene opal.

S and P positions were found on a first step by using a mirror as background and placing the fiber at a angle matching Brewster condition. After that the polarizer was rotated until a minimum in transmittance was found. Then we take a reflectance background for each polarization in order subtract the system response. Measurements for s and p polarization were performed on the above mentioned sample. From the results in Fig. 3.15 it is clear that large differences on the spectral shape of the reflectance are observed for large angles. While s-polarized reflectance peak width hardly changes with angle, for p-polarization, a pronounced narrowing of the Bragg peak takes place. These measurements agree with previous results found in the literature and provide a powerful test for our system.

As a final step, it is possible to apply the conservation of the parallel component of the wavevector to obtain $K_{||_{out}}$ at every pair (θ, ω). If mapped, a direct measurement of the dispersion relation is obtained. As an example, Fig 3.16 shows the dispersion relation for the low energy region of an opal made of polystyrene spheres with a diameter of 490 nm.

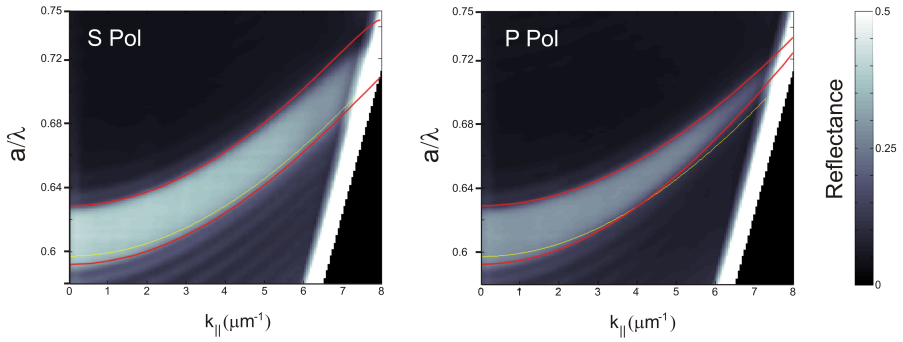


Figure 3.16: Experimental dispersion relation extracted from reflectance for a PS $\Phi = 320$ nm opal in both p and s polarization resolve measurement. Numerically calculated bands for a polystyrene opals are shown as red lines.

Here the relevance of imaging the Fourier plane before carrying out any spectral measurement should be pointed out for two reason. First is the fact that for 2D or 3D PCs, the large anisotropy induced by the periodicity introduces several high symmetry directions. The Fourier image can be used as a way to select the high symmetry direction along which one can scan the fiber and thus carry out the optical characterization. Finally, the Fourier image can provide us information regarding the presence os spurious effects such as dust on the optical path.

3.6 Conclusions

In this chapter we have presented a powerful experimental configuration for carrying out angle and polarization resolved measurements in a reflectance/emission configuration. At variance to usual angle resolved measurement set-ups it allows measurement on a reduced area of the sample with fixed dimensions. Given that no mechanic parts act over the sample or the illumination, very large angular and spectral resolution is achieved while the area under study is kept constant. Furthermore, white light or laser sources can be easily interchanged which is relevant in emission measurements where probing reflectance and emission at exactly the same point is essential as will be shown on Chapter 7 of this thesis. Also a set-up calibration procedure has been described. From these results, possible future improvements could be introduced. Using larger NA objectives will provide higher collecting angles, as well as higher spatial resolution. In that case, oil immersion objectives should be considered to study those systems that require from extremely large angles of collection. On the other hand, a more advanced improvement would consist on the use of a small micrometric aperture on the BFP of the objective in order to obtain illumination with a single angle.

Part II

Study of hybrid monolayers as photonic-plasmonic colloidal structures

Chapter 4

Optical properties of a monolayer of close-packed spheres

In this chapter we study from a numerical point of view the optical properties of a monolayer of organic spheres in a triangular lattice configuration when deposited on both dielectric and metallic substrates. It is shown that, by choosing the appropriate configuration large mode confinement as well as high field enhancements can be achieved with these kind of structures, specially for the metallic substrate case. Furthermore, it is demonstrated that surface plasmon resonances can be excited if the right sphere diameter/metallic material combination is chosen. Total field intensity profiles, spectral response and quality factors of the different modes are discussed.

4.1 Introduction

In chapter 1 the slab photonic crystal (PC) was introduced as one of the most efficient ways to confine light and modify its propagating properties [6]. In the search for a more low cost and straightforward technology, monolayers of polymeric spheres were presented in previous chapters as building blocks. Lattices of dielectric spheres were first proposed by Inoue *et al.* [1] as two dimensional (2D) photonic crystals. They also demonstrated that using dielctric spheres as building blocks introduces differences in light confinament compared with the slab PC case. However, despite the high mode confinement provided by these structures, it has been shown in several works [99] [126] that the use of a dielectric substrate under the spheres strongly reduces the potential for applications due to energy leakage towards the substrate.

Parallel to the study of 2D self-assembled PCs, colloidal lithography[1] has spread as a common technique to obtain control on surface plasmon resonance (SPR) propagation [127]. Recent work has pointed out that the structure formed by the monolayer of dielectric spheres and the metallic substrate may provide not just SPR propagation control [59] but modes supported by the monolayer itself [62] [128] [129]. In this Chapter, by means of finite difference time domain (FDTD) simulations, we present a theoretical study on how light couples and propagates in the combined structures monolayer-dielectric and monolayer-metal. We have paid special emphasis to the leaky modes and the differences in light confinement depending on whether they present either plasmonic or waveguided

[1] Where a monolayer of dielectric spheres is used as a periodic lithographic mask.

character. By comparison with the "ideal" case of a free-standing monolayer we have found that the metallic substrate structure provides many advantages.

The chapter is structured as follows. We first introduce the dielectric substrate monolayer of spheres and the main propagation channels available for light incident on such a system, with special interest on modes lying above the light line (leaky modes). Then total field intensity profiles are obtained too in order to check how electric field is distributed in the lattice for each resonance. Next, we report on the effect of a dielectric substrate on the losses of each type of mode. Then, we introduce the metal-dielectric system formed by a monolayer deposited over a gold thin film. Radiative and leaky modes are examined in the same way that we did for the dielectric substrate case. Main differences between the two structures are pointed out. As a final result, two different kinds of mode are defined and characterized depending on whether they confine most of the total field intensity in a small volume near the metal (SPP-like) or within the dielectric spheres (WG-like).

4.2 Monolayer on dielectric substrate

Let's consider one single layer of close-packed dielectric spheres of diameter ϕ and refractive index n_{sph} deposited on a substrate with n_s. As the diameter of the spheres is similar to the working wavelength, the scattering of one single sphere can be treated by mean of Mie scattering in the low Mie order. First Othaka [1] and next Miyazaky et al. [39] demonstrated that the optical response of a lattice of dielectric spheres can be calculated by coupling the scattering of the whole set of spheres. However, in order to present a simpler model accounting for the main properties of this system, the slab PC approximation can be an interesting approach. A close packed monolayer of spheres forms a hexagonal lattice with lattice parameter equal to the diameter of the spheres (ϕ). Therefore, the complete lattice can be defined by the two lattice vector $a_1 = \frac{\phi}{2}(\sqrt{3}, 1)$ and $a_2 = \frac{\phi}{2}(\sqrt{3}, -1)$ as shown in the diagram of Fig. 4.1. Those lattice vectors defined by vectors univocally define as $\mathbf{G}_1$ and $\mathbf{G}_2$ in reciprocal space shows two major symmetry directions: ΓM and ΓK. It is easily found that points $|\Gamma M| = \pi/\phi$ and $|\Gamma K| = 2\pi/(\sqrt{3}\phi)$. Hence, it is useful to define the reduced frequency $\omega = \sqrt{3}\phi/(2\lambda_0)$ that allow us to make all the results scalable with ϕ.

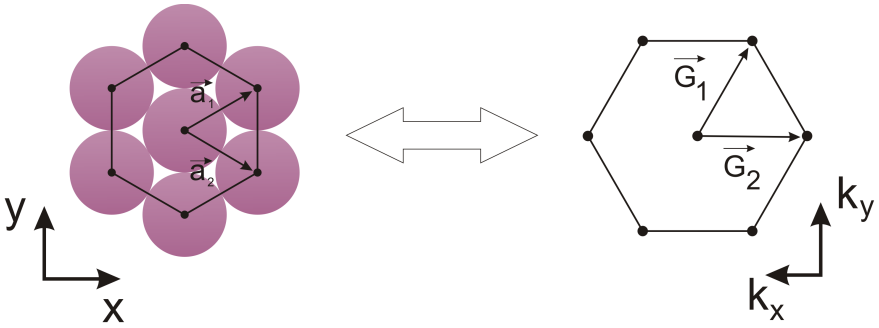


Figure 4.1: Diagram of the hexagonal lattice formed by close-packed spheres of diameter ϕ and defined by lattice vectors a_1 and a_2. G_1 and G_2 define the corresponding reciprocal lattice.

In the approximation of the monolayer as a PC slab we found that according to Fig. 4.1 the system may support light confinement as well as dispersion relation modification

for those modes propagating in the plane of the periodicity (x,y). Besides, confinement in the vertical (z) direction due TIR can also happen as described for a slab waveguided in the Introduction of this thesis.

Therefore, the modes can be radiative or leaky guided depending on the relation between the effective refractive index of the leaky mode and the substrate media (see Fig. 1.5 in chapter 1).

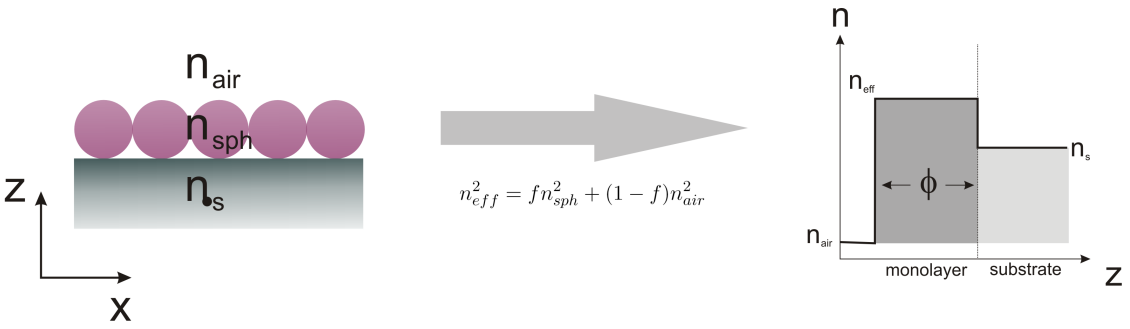


Figure 4.2: Monolayer of spheres on dielectric substrate approximated as a slab waveguide of effective refractive index n_{eff}.

In this case, the existence of a guided mode is determined by the refractive index of the spheres. Therefore, it is useful to approximate the monolayer as a slab waveguide with an effective refractive index extracted from the volume of the lattice occupied by the spheres, that is, the filling fraction of the dielectric material in the volume occupied by the monolayer. We can calculate n_{eff} using the well known approximation:

$$n_{eff}^2 = f n_{sph}^2 + (1-f) n_{air}^2 \tag{4.1}$$

with n_{sph} and n_{air} being the refractive index of the spheres and air respectively. f is the filling fraction of the lattice [2] which for a close packed monolayer results $f = \pi/3\sqrt{(3)} \sim 0.6$.

If then, one think the monolayer as a slab waveguide with core index n_{eff} and thickness equivalent to the diameter of the spheres, the final refractive index profile shows the form indicated in Fig. 4.2. Within this context, it is easily found that leaky modes presents a given effective refractive index N which correspond to an effective wavector β fullfilling the condition of $k_0 n_s < \beta < k_0 n_{eff}$. With $k_0 = 2\pi/\lambda_0$ and n_s being the substrate refractive index. It has to be noticed that under this approximation it may happen that although $n_{sph} > n_{sub}$, no leaky modes may propagate since it is the effective index which rules such a condition. Moreover, as n_{eff} increases does the field confinement as discussed for the case of a slab waveguide in the Introduction of this thesis.

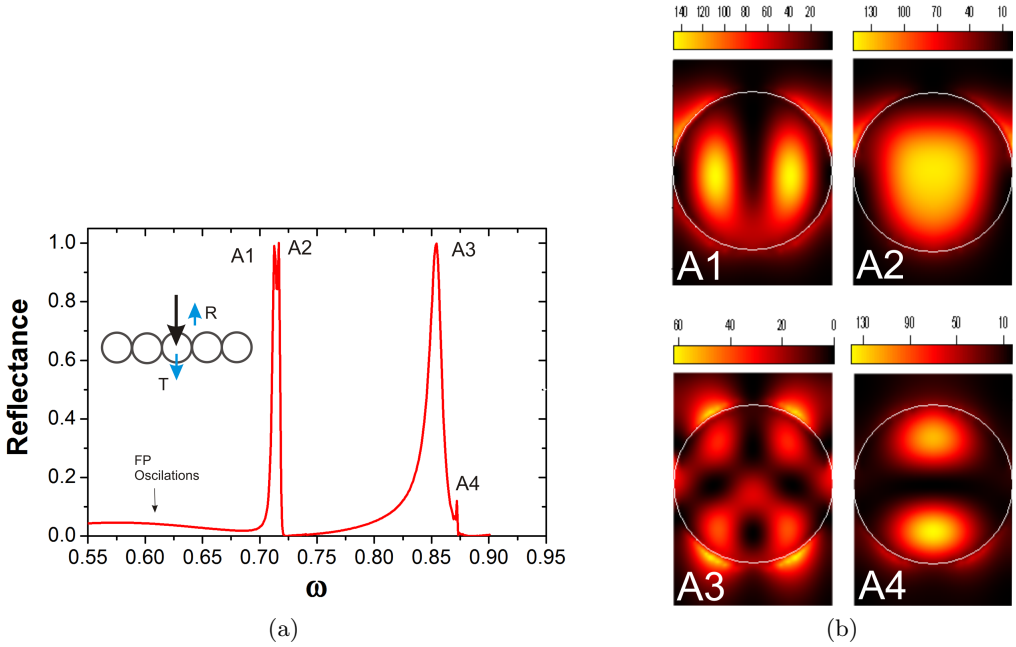
4.2.1 Simplest case: free standing monolayer

We define a free-standing monolayer as a hexagonal lattice of spheres surrounded by air with no substrate. Therefore, this case is very similar to the symmetric slab waveguide well described in chapter 1. First consideration is that due to the symmetry of the system, the field intensity profile inside the spheres for each mode must present mirror symmetry with the x-y plane at the center of the spheres. Other important point to be considered is

[2] Occupied volume for the spheres in each unit cell of the PC over cell's total volume

that due to its symmetric character, there is always at least one confined mode available for the structure regardless of the diameter of the spheres.

In order to test this we have considered a free standing monolayer of polystyrene spheres as this is the material to be used in the experiments along this thesis. In that case $n_{sph} = 1.58$ which implies $n_{eff} = 1.38$. Other parameters are $n_s = n_{air} = 1$ and $\Phi = 520nm$. Concerning modes calculation, in this thesis we have chosen not the exact calculations of the modes but the inspection of FDTD calculated reflectance/transmitance spectra where each leaky mode is shown as a resonance on the background due to non guided propagation [30]. The reason for this choice is mainly that it allows us a direct comparison with the experimental results presented in further chapters.



(a) (b)

Figure 4.3: a) Theoretical reflectance spectrum in normal incidence for PS spheres ($n_{sph} = 1.58$) in a close-packed monolayer lattice. b) Electric field intensity profile near the spheres at the two lower resonant frequencies and normal incidence.White lines delimit the spheres.

Therefore, let us consider a set o plane waves normally incident (Γ point in the reciprocal lattice) on the sample. Fig. 4.3a shows FDTD simulation[3] of reflectance spectrum for the hexagonal lattice configuration of PS spheres ($n_{ps} = 1.58$) [4]

Three kind of optical feature identified in this spectrum. On the one hand, a broad and low ondulation due to Fabry Perot interference is clearly seen. Secondly, out of plane diffraction due to the periodicity (reflection/transmission grating effect) of the structure happens for values $\omega \geq 1$ as extracted from the grating equation. That spectral region has not been considered along this discussion given that our interest is mainly focused on resonant states of the system. Finally, the sharp peaks (A1 to A4) correspond to those

[3]Check appendix A for in-depth explanation of how simulations were performed

[4]Reduced frequency has been chosen because by using it we take advantage of the scalability of these kind of PCs. The results that will be shown here can be scaled just by changing the sphere diameter (we consider the spectral dispersion for the polystyrene negligible in the vis-NIR range). From now on ω stands for frequency normalized to the parameter defined in the text.

confined modes with leaky character as they are folded back within the light cone by the periodicity of the system. Such kind of resonances are well known to be shown as peaks in reflectance or dips in transmission for confined modes of a slab PC [30]. It is worthy to comment that there are also a set of guided modes which fall out of the light cone and therefore not shown as reflectance peaks. Although not of much interest in this thesis, it is necessary to comment on the existence of this totally confined resonances given that they have been theoretically demonstrated to be present in this kind of structures [39].

In order to characterize the modes of the system we must look at the field intensity distribution within the PC. As they correspond to confined modes it is expected that large total field intensities in (or close to) the high refractive index part of the PC appears. FDTD calculation of the filed distribution at resonances A1 to A4 are shown in Fig. 4.3b. The shape of the field intensity profile depends on the order of the mode considered and is strongly related to Mie resonances of isolated spheres as well as the coupled array [39].

It can be noticed that the intensity profile is not symmetric with the center of the sphere. It has to do with the fact that we are not solving the modal profile but the direct optical response. As we are incident from upside it is expected for that profile not to be symmetric. This applies for all the intensity profiles simulations of optical coupling performed in this chapter.

4.2.2 Energy leakage with substrate refractive index

So far it has been shown that the free standing case of dielectric spheres presents a good optical response in terms of light confinement. However, when the structure is to be fabricated, 2D self-assembled free standing systems become very difficult to be implemented.

As a matter of fact, to the best of our knowledge, a large area free standing monolayer of microspheres operating at visible frequencies it has not being reported yet. Therefore, knowing how a dielectric substrate affects the optical properties of the system is essential.

During the Introduction of this thesis it was shown that the field confinement for the modes of an asymmetric slab waveguide presents a strong dependence on the refractive index of the substrate. In particular it is demonstrated that the lower the RI contrast between the core and the substrate the larger the leakage thorough the substrate and then the lower the field confinement (equation 1.14). Therefore, assuming the PC slab approximation for the monolayer it is expected that any dielectric substrate wit $n_s > 1$ will produce larger leakage of the modes compared to the free standing case. Several works have been publish about this issue specially by Miyazaky *et.al* [99] [126] .

Fig. 4.4 shows the calculation for normal incidence reflectance and its evolution from the free-standing scenario shown in Fig. 4.3 to the large refractive index ($n_{sub} = 3.5$) substrate case[5]. The spheres parameters are the same previously shown in the FS case.

As the refractive index of the substrate increases the reflectance peaks broaden and become less intense in agreement with the expected behavior from slab WG theory. Getting more into the detail, two different regimes are obtained with respect to the radiative losses introduced by the substrate. On the one hand, for $n_s < n_{eff}$, resonances are leaky but nevertheless affected by the presence of the substrate as can be seen in Fig. 4.5 which shows a zoom of Fig. 4.4 over the evolution of the resonant peaks as n_{sub} is increased.

As can be observed, as n_s increases, high energy modes are first to disappear from the reflectance spectrum (lack of guidance). The higher the order of one mode the higher

[5]It is important to notice here that due to the leaky character of each of these modes and to the fact that we are below the onset of of diffraction, reflectance and transmittance are complementary so, if transmission is calculated a dip in transmittance will be obtained if a peak in reflectance is observed.

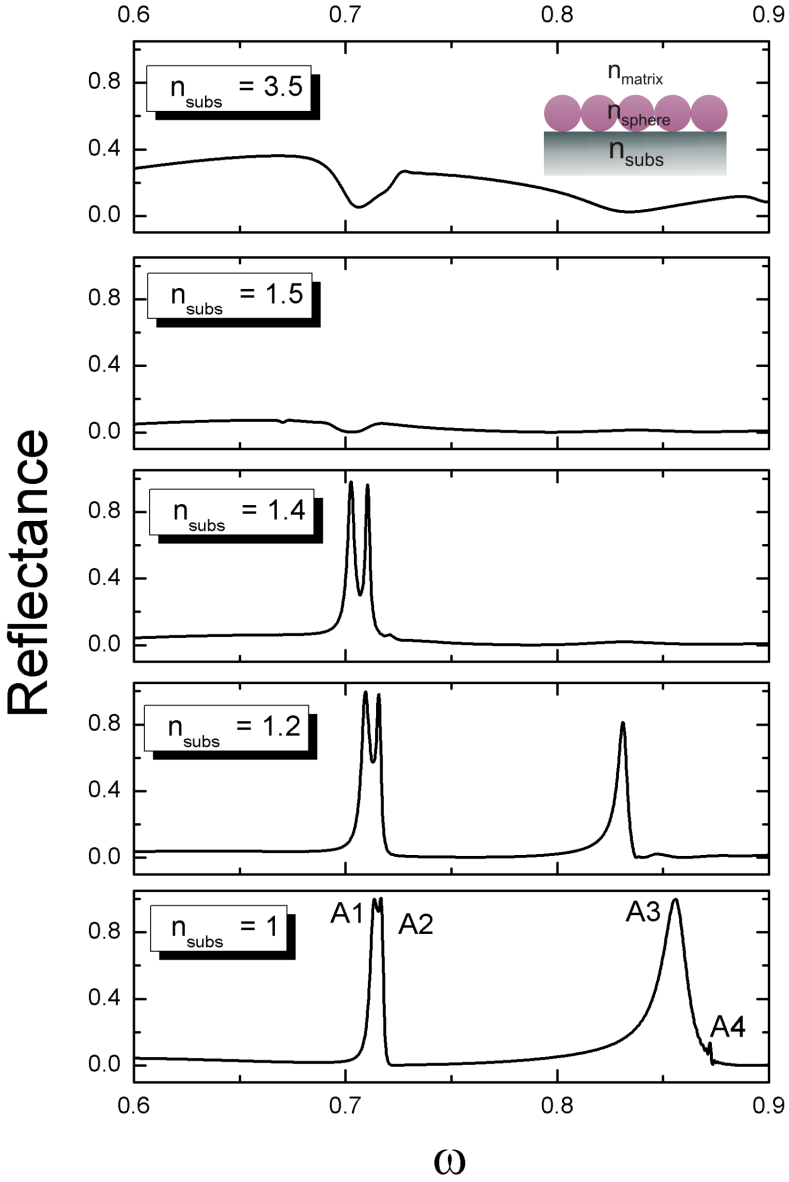
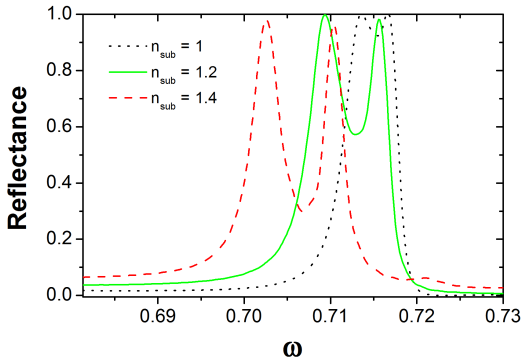
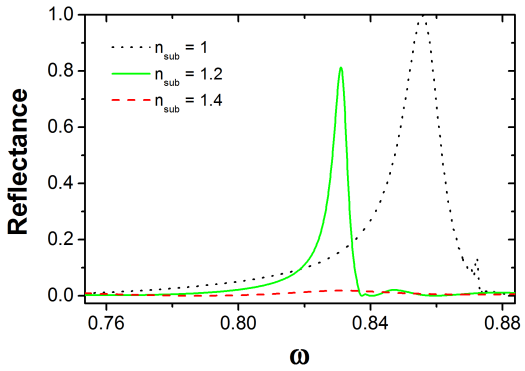


Figure 4.4: Calculated normal incidence reflectance spectra for a monolayer of polystyrene spheres on a dielectric substrate of increasing refractive index: from vacuum ($n_{sub} = 1$) to silicon ($n_{sub} = 3.5$).

its energetic position (see chapter 1) and the lower its modal effective refractive index (N) [29] . Therefore, the condition for waveguiding according to the slab approximation is $N > n_s$. Therefore, reflectance peaks disappear for $1.4 < n_s$ given that the original leaky modes become radative as the guiding condition is broken for $n_{eff} < n_s$. However, although totally removed as reflectance peaks, features related to resonances excitation in reflectance are still present in the spectrum as broad dips (energy flux taken out through the substrate). Several authors [130] [31] have reported that this approach is appropriate for PC slabs and we demonstrate here that for a monolayer of spheres the effect of increasing n_s can be qualitatively explained in this terms. It is worth to mention other effects as for example redshifting and separation in frequency as n_s is increased. This effects are known as the isolating oxide substrate effect in slab waveguide.



(a)



(b)

Figure 4.5: Calculation for the evolution of reflectance with refractive index of the substrate for A1 and A2 (a) and A3 and A4 (b) modes for a close packed lattice of polystyrene spheres.

The evolution of the radiative modes of the system has little interest. The increasing amplitude of the oscillating background in reflectance/transmisison has to do with the fact that, as n_s increases, reflectance coefficients at air-substrate interface increase making Fabry-Perot interference oscillations more visible. Another effect is the reduction (redshift) of the onset of out of plane diffraction by the 2D lattice as n_s is increased. Although not shown in the spectral range we are interested in, this is an already studied phenomena successfully explained for 3D self assembled photonic crystals [131] and for this specific system in Ref [99].

As a step forward, it is interesting to study the evolution of the total field intensity for the above discussed resonances. In particular, we are interested in those n_s values for which modes still remain as leaky states. That is, those satisfying $n_s \leq n_{eff}$ which in case of a monolayer of PS spheres would be $n_s \sim 1.4$ as shown in Fig. 4.6.

In Fig. 4.6 we show the evolution with increasing n_{sub} for field profiles at frequencies matching resonances A1, A2 and A3. A4 has not been plotted given that it almost vanishes for $n_{subs} = 1.2$. This means that n_{eff} for that resonance takes values similar to $n = 1.2$. Each mode field profile color scale has been normalized to the maximum field intensity which that mode presents in the whole set of n_{sub} calculated in order to stress the effect of the substrate. If A3 is considered it can be observed that for $n_{sub} = 1.4$ (c) there is almost no field confined in the PC structure. A1 and A2 still presents high field enhancement

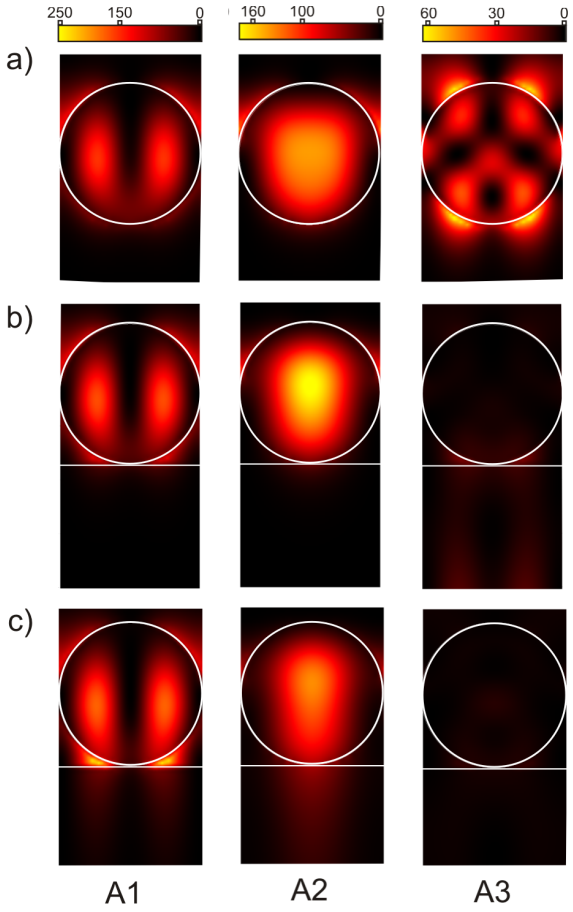


Figure 4.6: Calculation of the total field intensity at normal incidence when the substrate refractive index is changed from (a) to (c) corresponding to $n_{sub} = 1$, $n_{sub} = 1.2$ and $n_{sub} = 1.4$ respectively. Left to right correspond to A1, A2 and A3 modes as defined in 4.3

around the spheres as espected from the large peaks shown in Fig. 4.4 for that substrate refractive index values.

These simulations confirm the trend already observed from the spectra shown in Fig. 4.4. That is, as we increase substrate refractive index, leakage through the substrate becomes more relevant. For an asymmetric waveguide, refractive index contrast is lower in the substrate-monolayer region and then, fields tend to be concentrated closer to the low contrast region for every mode of the system [27]. Due to the spherical shape of the elements forming the slab, as field is concentrated at the bottom of the structure, changes in resonance shape yields a focusing towards the substrate. This effect can be observed specially for A1 and A3 although A2 present a slight variation in the field profile too [6].

Taking this into account it is worthy to take a look at the field intensity profiles evolution. It can be observed that maximum field confinement does not follow the same

[6]It is important to stress for further studies in this thesis that, while resonance A1 undergoes large profile changes, A2 maintains its shape. It presents just a little narrowing of the field profile distribution into the sphere. Furthermore, it has to be noticed that for $n_{sub} = 1.4$ field intensity decay into the substrate which is an expected effect from the loss of RI contrast between refractive index of the PC and the substrate. Actually, from the profiles shown in 4.6 this behavior is observed for any $n_{air}, n_{sub} > n_{eff}$

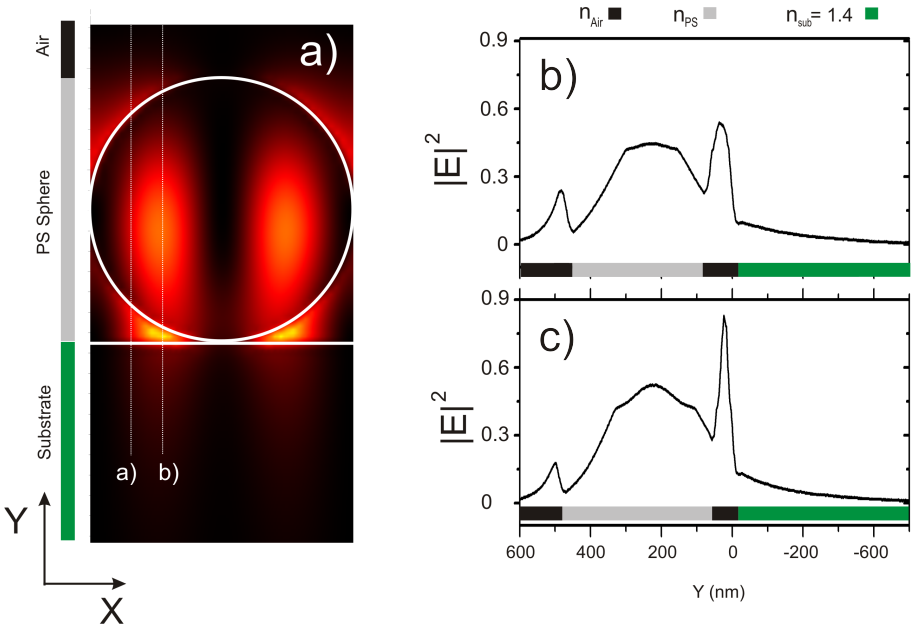


Figure 4.7: a) Total field intensity for A1 resonance of a monolayer made of PS spheres ($\Phi = 520nm$) on a dielectric substrate of $n_{sub} = 1.4$. b) and c) are field profiles in the Y direction at constant X corresponding to a characteristic distance sphere's surface-dielectric of $80nm$ and $50nm$ respectively.

evolution for all the modes (check scale bars). As confinement is closely related to the effective refractive index (N) for each mode it is expected that changes in n_s affects the total filed intensity. The maximum field intensity will be shown for the configuration in which n_{eff} acquires its largest value but always for $n_{eff} < n_{sub}$.

In order to study the field concentration under the spheres shown for A1 and A3 we have plotted in Fig. 4.7 field profiles along the y direction two different x positions. As can be observed, while the mode profile within the sphere is similar to that of the A1 mode in the free standing system, there is a large field enhancement at the space between the PS sphere and the dielectric substrate. Such an enhancement is well known in near field scattering of spherical nanostructures and has been widely used for applications as patterning by ablation with femtosecond laser pulses [132][133]. However, given that in this case we are dealing with propagating modes in the monolayer (instead of Mie scattering by a single sphere) effects derived from these leaky modes could lead to a behavior related to slot-waveguide effects [134] [135] . This possibility remains open for further studies.

4.3 Metallic substrate

So far we have studied the effect of a dielectric substrate on the optical response of a close-packed monolayer of dielectric spheres, specially for low n_{sph}/n_{sub} contrast. However, when a substrate with complex refractive index ($\overline{n} = n + \kappa i$) is introduced, absorbtion, high reflection and, eventually, SPR have to be taken into account.

Like in the case of finite dielectric substrate, the whole optical response can be understood as the sum of radiative and confined modes of the spheres monolayer plus those modes related to the metallic film. Fig. 4.8 shows a diagram of the type of structure we

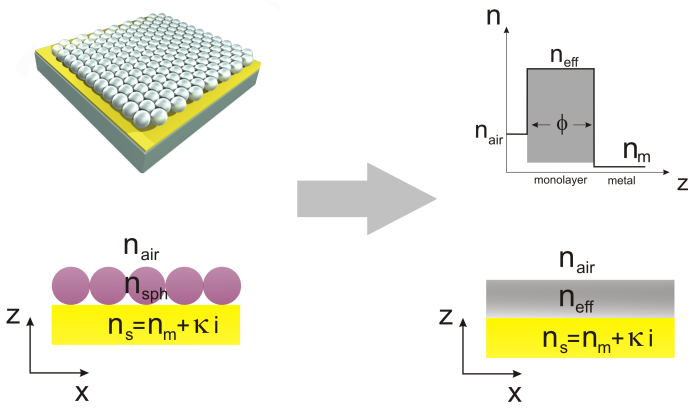


Figure 4.8: Diagram of the structure studied in this section (left) and effective refractive index slab approximation diagram.

will consider in this section. As it is obvious, the in-plane periodicity maintains the same shape than in the previous section so it is the confinement in the vertical direction that will be affected by the metallic substrate. Hence, we can apply the slab PC approximation in such a way that an index profile as the one shown in the figure can be consider to qualitatively understand the underlying physics. If one consider a metallic film under the monolayer, an coplex refractive index has to be considered for the substrate ($n_s = n_m + \kappa i$). In the refractive index profile of Fig. 4.8 only the real part has been plotted. For gold or silver, which are the metals we will be considering along this thesis, n_m presents values lower than 1 in the VIS-NIR spectral range [136]. Therefore, an increasing is expected in the field confinement for the modes of the system as it is known from general theory of metallic-dielectric waveguides [137]. However, metal absorbtion has also to be considered so reductions in the total confined field should affect the total field confinement of the system for those metals presenting non negligible values for κ.

Let's then perform the study of the optical response of this kind of systems by means of reflectance calculation. The system under consideration is formed by a close packed monolayer of $\Phi = 1\mu m$ polystyrene spheres ($n_{PS} = 1.58$) on a thin metallic film deposited over a seminfinite silicon substrate. The aim of using a silicon substrate under the gold film is to make the theoretical analysis as realistic as possible given that the fabricated samples present this configuration. We will consider a flat metallic film whose thickness is typically chosen to be between 50 and 80 nm. Depending on the material and the working wavelength such thickness can be large enough to allow an infinite thickness substrate approximation, so the silicon layer does not have to be taken into account. Then, on first approach, the optical response of the system can be thought as a monolayer over a semi-infinite gold substrate. As for the structure discussed on section 4.2.2, interaction between propagating channels of both systems (periodic array and metallic film) can lead to hybrid modes.

Fig. 4.9 shows FDTD calculations of the reflectance at normal incidence for $\Phi = 1\mu m$ PS spheres on a 55 nm thick gold film on the configuration of Fig. 4.8. In this case only reflectance has been plotted given that transmission is negligible in that spectral range for a gold substrate. As can be observed, the spectrum is formed by a flat reflectance background with dips at similar values as the resonances of the free standing monolayer (see Fig. 4.3a). We have named G1 to G5 those resonances.

The mirror-like flat background is similar to the calculated reflectance for a gold film

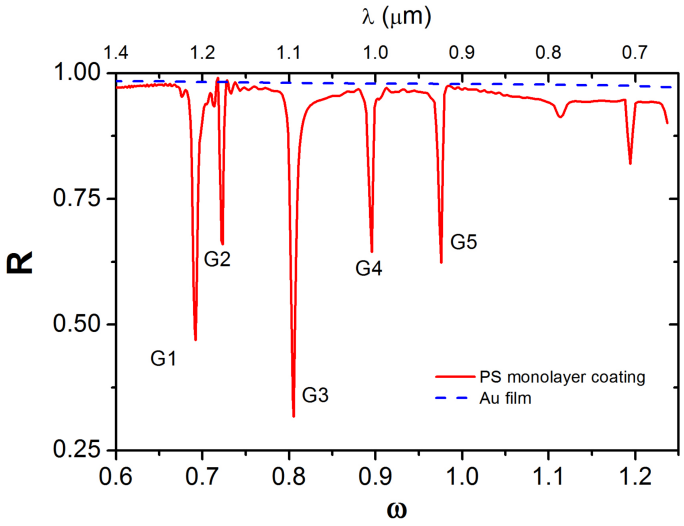


Figure 4.9: Simulation of reflectance spectrum at normal incidence of a monolayer of $\Phi = 1\mu m$ PS spheres over 60 nm gold (solid line). Blue dashed line shows reflectance for bare gold film.

without spheres (blue dashed line on Fig. 4.9) in this spectral range. However, the monolayer response presents optical features related either with radiative or resonant modes. The radiative modes available for this systems are the same ones as for the monolayer over the dielectric substrate. From those radiative contributions we obtain on the one hand weak Fabry-Perot oscillations, although not appreciable in the figure[7]. On the other hand, from our previous study of the free standing monolayer, a large drop in reflectance should take place for $\omega > 1$ at normal incidence due to the onset of out of plane diffraction. Such a drop is not present in the simulation due to the designed computational set-up (Check Appendix A).

Thin dips in reflectance spectrum are the signature of leaky modes of the system. In order to obtain a quantitative analysis of the light confinement properties of each mode a fitting for a Fano type resonance can be performed for each mode. Fano approximation to extract the properties of PC slab's modes have been successfully applied on reflectance spectra [30]. The model is appropriately defined in Appendix B of this thesis. The resulting fits are shown in Fig. 4.10.

According to this model, the optical response of the gold/monolayer system can be explained as the sum of the background plus the resonances of the system. When normal incidence is considered, it was demonstrated that the background provides a mirror-like behavior plus Fabry-Perot oscillations. Those features comprise the non-resonat features in the Fano resonances model. On the other hand, the resonant states (modes) of the system can be fitted by the equation B.1. Fig. 4.10 shows a very good agrement between the fitting and the spectra calculated by FDTD [8]. As a consequence, each dip in reflectance can be related to an in plane discrete state of the periodic structure corresponding to the leaky modes of the whole system. Three main parameters can be extracted from this model that can retrieve useful information: the central frequency of the resonance ω_0,

[7] They are spectrally broader than the represented spectral range. Their effect is not noticeable when a short ($\Delta\omega < 2$) spectral range is considered

[8] It has to be noticed that each peak was modeled on a separate fit due to the difficulties on implementing a fit curve with more than 20 fitting parameters (each resonance has 5 variables)

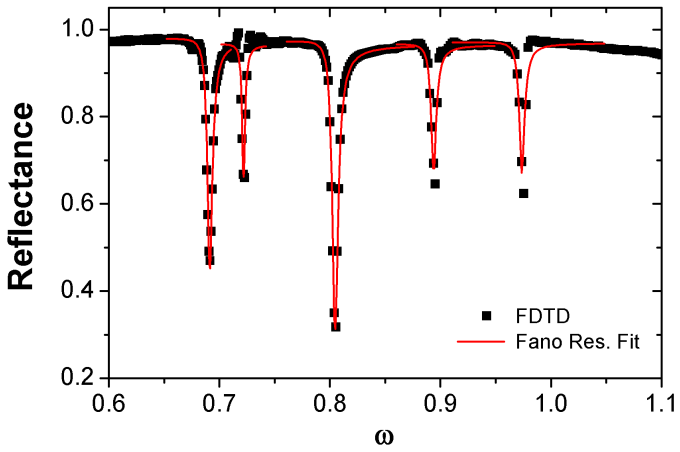


Figure 4.10: Calculated normal incidence reflectance for a monolayer of PS spheres over gold substrate (black dotted line). Gray line shows fits for Fano expression on B.1. Every peak was fit separably in order to obtain its main parameters.

paramtere q (accounting for the asymmetry of the resonance) and Γ accounting for the spectral width. Finally, quality factor ($Q = \omega_0/\Gamma$) can also be indirectly extracted from the fitting (see appendix B) which provides a quantitative value for the confinament of each mode of the system. Next table shows the values obtained for each mode in the fitting of fig. 4.10.

Mode	*G*1	*G*2	*G*3	*G*4	*G*5
ω_0	0.69	0.72	0.80	0.89	0.97
Γ	0.0028	0.00161	0.0031	0.0028	0.0028
q	13	22	11	16	17
Q	248	448	258	317	346

First thing to be noticed is that q is considerably larger than 1 for each of the peaks which stands for a strong resonance character. If one check at Q values in the table above, large values are obtained taking into account the low refractive index contrast of our structure ($\Delta n = 0.598$). Comparison with literature indicates the good performance of the hybrid monolayer as a light confining structure. Moreover, for the same fitting performed over the free-standing spectrum of Fig. 4.3a (not shown) the Q values are approximately twice lower than for the metallic substrate.

Therefore, the spectra for both free standing and metallic substrate case can be analyzed in the same terms of resonant and non-resonant states. However, in order to know if we are dealing with similar phenomena one should check the field distribution inside the structure at resonant frequencies. As in the last two sections, FDTD calculations were used to obtain total field intensity profiles after a given propagation time into the structure. Those simulations are shown in Fig. 4.11.

These profiles corroborate the conclusions from the fitting of Fig. 4.10. That is, each of the resonances correspond for leaky modes since all of them show very large intensity (for confined field) as large as $E/E_{incident} = 1300$. Furthermore, both parameters ($Q = \omega_0/\Gamma$ and field enhancement) show large values, well above those shown for the free standing case. This result shows that the the hybrid gold-PC structure performs even better than the "ideal" dielectric case in terms of light confinement. Similar results have been observed in the visible range using silver substrate by Shi et al. [62].

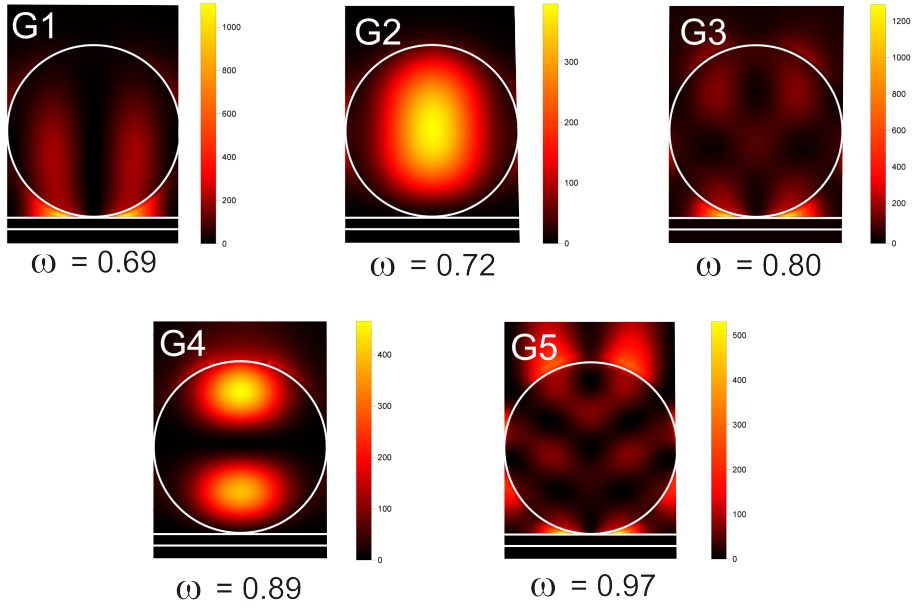


Figure 4.11: Field profiles after coupling at normal direction for the resonances shown on spectrum 4.9. Reduced frequency ω_1,ω_3 and ω_5 correspond to $\lambda = 1.25$, 1.1 and 0.94 μm respectively. White line delimits the different interfaces between materials (spheres and gold).

If the five resonances profiles are examined in detail it can be observed that two different kinds of field distribution are obtained as in the case of the dielectric substrate. On the one hand G2 and G4 resonances confine the field intensity mainly within the spheres with spatial profiles similar to those shown in Fig. 4.3b for the A2 and A4 modes. Taking into account this similarities we have named this kind of mode **WG-like**.

On the other hand, G1, G3 and G5 present most of the field distributed mainly below the sphere but with a small component within it. In the case of G1, its profile is very similar to the one obtained for the dielectric substrate (A1), specially for the case $n_{sub} = 1.4$ (Fig. 4.6c). G3 and G5 are not comparable to the dielectric substrate structure due to leakage towards the substrate. Because of this we have named these resonances as **SPP-like** due to their close confinement to the metallic layer and the large enhancements obtained.

4.3.1 SPP-like modes

From Fig. 4.11 one can see that the field profile for the SPP-like modes present a similar profile to the modes of the dielectric substrate case concentrating most of the field under the sphere (see Fig. 4.6). Therefore, we can trace the X profile at two different positions for G1 as shown in Fig. 4.12.

In this case, at maximum of field enhancement (a)) the difference between the under-sphere concentrated field and the rest of the intensity distributed into the sphere is very large if compared with the dielectric substrate case (check fig 4.7). This is expected since the refractive index contrast at metal-air surface is much larger that in the totally dielectric structure. From this large contrast, field discontinuity provides very large enhancements. It also has to be noticed that the intensity of the mode distributed into the sphere present a similar shape than for the dielectric substrate structure though with a higher total field intensity. In this respect, a more complex model in terms of slot waveguide approximation

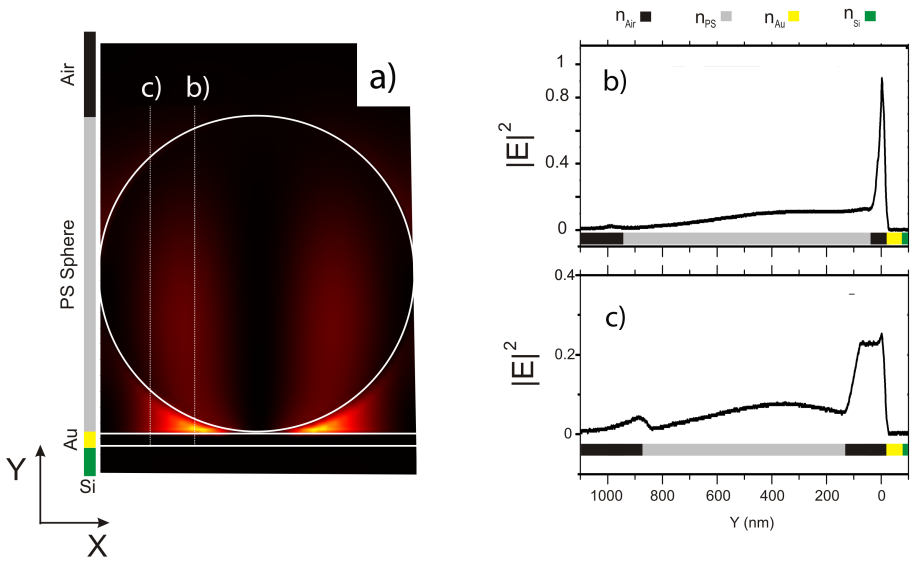


Figure 4.12: Total field intensity for the G1 mode of a $\Phi = 1\mu m$ PS sphere monolayer deposited on gold (a). Vertical sections along two different X positions are shown in (b) and (c).

could lead to accurate results. It has been applied in previous works for more simple but similar structures [138]. However, in this case, the spheres lattice plus the metallic susbtrate is much more complex system so it will not be studied here.

Despite the lack of a mode coupling model, one would expect that resonances of the PC whose field is mainly concentrated under the sphere, excites SPR of the metallic surface (gold in this case). In previous studies, Cole et al. [59] showed that SPR excitation is possible through coupling to leaky modes of different structures formed originally by dielectric microspheres.

In order to expand this study, the empty lattice approximation can be applied to the dispersion of the different kind of modes supported by the system. If a finite dielectric layer with a given thickness is considered on top of the metal, the field concentration on top of the metallic field is known to depart from the infinite dielectric case [58]. To take it into account we have calculated the dispersion of the SPR resonances for a monolayer of PS spheres with $\Phi = 520nm$ deposited on gold. However, in that calculation we have not considered the dielectric material refractive index to be the $n_{eff} = 1.38$ obtained from the filling fraction approximation of the monolayer. In order to find the n_{eff} that matches the effective refractive index of the hybrid SPP-like mode (N) several values for n_{eff} have been tested. The dispersion relation is calculated according to the equation for plasmonic modes (eq. 1.19) using gold dielectric constant at VIS range [136] and a trial n_{eff}. After that, the resulting dispersion relation have been folded back into the FBZ along the corresponding direction in the reciprocal space. Fig. 4.13 shows G1 and G3 dispersion relations for the most appropiate values of n_{eff}. The dispersion relation is compared in the same figure to reflectance at normal incidence for the corresponding monolayer. n_{eff} values have been chosen in order to match the spectral position of the dispersion relation at $k = 0\mu m^{-1}$ with the reflectance resonances accounting for the modes at normal incidence. As can be observed, the reflectance dips qualitatively agree with the position of the calculated SPR for G1 and G3 considering a dielectric with $n_{eff} = 1.44$ and $n_{eff} = 1.27$ respectively. ΓK folding has not been plotted as the spectral position of

the modes at $k = 0\mu m$ fall in the high energy region ($\omega > 1$).

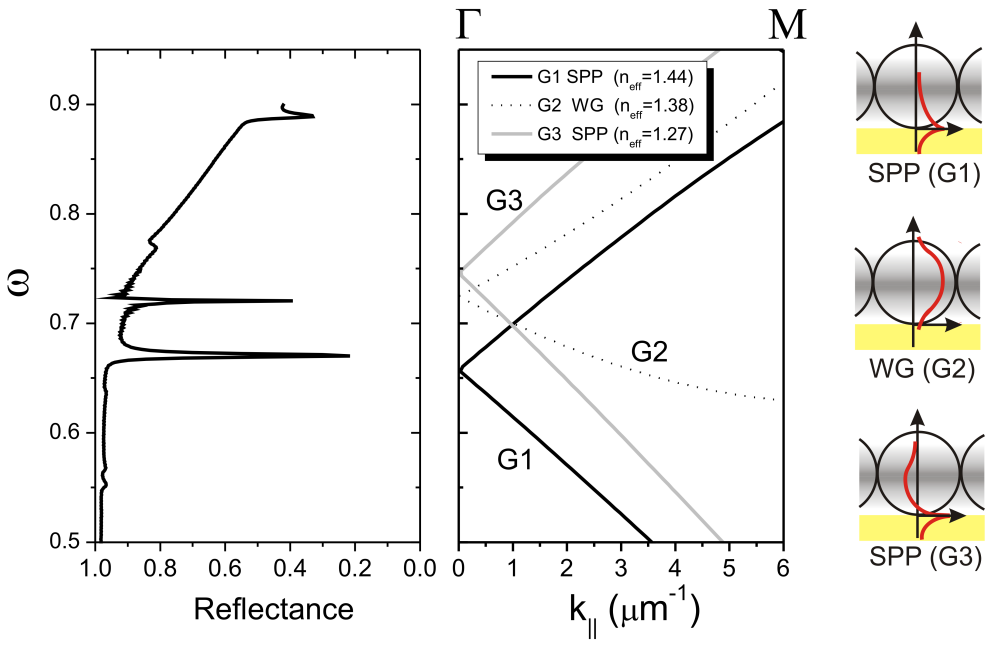


Figure 4.13: Calculated reflectance (left) of a PS monolayer of $\Phi = 520$nm on a 55 nm thick gold film. Right panel shows the empty lattice model for SPP-like modes (G1 and G3)and WG-like mode (G2) folded back to the FBZ along the ΓM direction.

As expected, none of the two SPP-like modes present larger values for the n_{eff} than that of the polystyrene spheres ($n_{ps} = 1.58$). The empty lattice model has also been plotted for the WG-like mode G2. It is important to noticed that, in this case, the n_{eff} to be considered for the empty lattice approximation is that of the monolayer previously calculated with the filling fraction aproximation as we are dealing now with photonic and not plasmonic resonances. A good agrement is also found with the calculated reflectance dips for G2.

It has to be notice that the normal incidence spectrum shown Fig. 4.13 corresponds to a monolayer of $\phi = 510nm$ which plots the resonances at VIS range while in the in the previous study of this section (see Fig. 4.9) larger spheres (IR range) have been considered. Several differences are found. As the optical absorbance in gold increases for wavelengths below 650 nm (that is $\omega > 0.7$ for $\Phi = 520nm$) a decay is observed on the reflectance of the whole system [9]. As this issue is studied in-depth in the next chapter we will not enter in detail here. However, in order to illustrate the effect of absorbance on the modes of the system, it is worth to compare the field intensity profiles in Fig. 4.14 with their counterpart for $\phi = 1 \quad \mu m$ shown in Fig. 4.11. The large reduction can be observed in the total field intensity concentrated below the sphere for G3 which is the one affected by the high absorbance of gold at $\lambda < 600nm$. This is an expected effect of the absortion since it mainly affect that filed concentrated closer to the metallic film.

Taking into account the large changes for both, spectral response and total field intensity profiles, we can see that the system is not fully scalable with the diameter of the

[9] We have performed these calculation and measurements with other metals like silver and similar results have been found depending on the absorbance band for each metal. Silver has shown the same results for VIS range than gold for IR spectrum as expectable from its SPR dispersion.

spheres. Therefore, once the spectral region of interest has been chosen, the other main parameter is the complex refractive index of the metal. As substrate absorbance is expected to strongly affect the optics of the whole system, the metal must work out of the its high absorption spectral region. Therefore, while gold works properly for IR range, the use of silver is more appropriate for the VIS spectrum given that the high absorbtion frequencies for bulk silver take place in the UV.

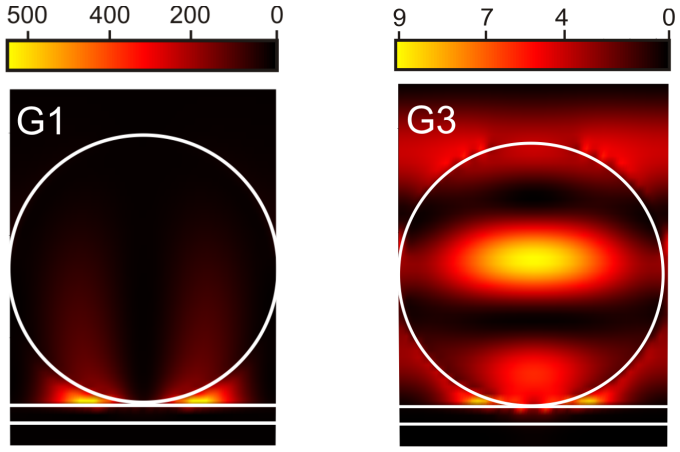


Figure 4.14: Total field intensity profiles for G1 and G3 resonances in a PS sphere monolayer over 55 nm thick gold substrate substrate for $\Phi = 520nm$.

4.3.2 WG-like modes

At variance with SPP-like, G2 and G4 resonances present in the profiles of Fig. 4.11 most of the field intensity distributed within the dielectric spheres. That provides this modes with a waveguided character where the metallic substrate plays the role of a metallic boundary in a slab waveguide. Using the empty lattice model considering the lab approximation with n_{eff} being that of the filling fraction approximation has shown to properly match the spectral position of the resonances as shown in Fig. 4.13. On the other hand, as mentioned in chapter 1, a metallic boundary in a slab waveguide reduces leakage of the modes through that part of the structure. In particular, if the case of a PC slab is considered, modes can just present leakage through the slab-air interface. Therefore, such a metallic substrate waveguide presents an increasing in the Q value for those modes of the structure when compared with the fully dielectric structure. In this case, a strong enhancement can be observed of the maximum total field intensity for WG-like modes of the structure when compared for those leaky modes of the fully dielectric monolayer.

A side effect of using a total reflector under the monolayer is the small blue shift of these resonances when compared to the free standing case. It has to be noticed that for the dielectric substrate increasing of n_s produces low energy shift for every mode. This is a clear evidence of the different nature of both kinds of mode. It is well known in slab PCs theory that as we increase the confinement into the structure a blueshift is produced in the resonances reflectance peaks [130]. Thats the case for G2 and G4 whose resonances in the spectrum moves to higher energies. It has been already commented that the SPP-like G1 and G3 shifts to lower energies (red-shift). This modes are also expected to be affected by spectral variations in the dielectric constant of the metallic film (mainly its absorbance) as previously shown for the SPP-like ones. However, as for WG-like modes most of the field intensity is distributed far from the metallic film the effect of absorbance would be

less intense than for the SPP-like resonances. This point will be studied in depth in the next chapter.

4.4 Conclusions

In this chapter, we have presented a theoretical study of the optical properties of a close-packed monolayer of dielectric spheres depending on the nature of the substrate that the structure is resting on. In particular, large attention has been paid to the metallic substrate case.

For the case of the dielectric substrate system, it was studied what kind of propagation channels are available on the PC structure. It was found that large field concentration can be obtained for leaky modes. The spectral working region was shown to be scalable with the diameter of the spheres. It was also shown that increasing the substrate‘s refractive index dramatically reduces field confinement.

As a main result, it was demonstrated that introducing a metallic substrate under the spheres allows the propagation of hybrid modes mixing SPRs and leaky PC resonances which take us to define two new kind of modes: SPP-like and WG-like. It has been shown that it is possible to efficiently couple to them on an normal incidence configuration. Both kind of modes present large field intensity values and therefor large Q are obtained for both types.

As future work, it would be very useful an improved model including expressions for the calculation of the wavectors of the hybrid modes as a relation between the eigenstates of the PC and those of the metallic film. An slot-waveguide approximation in case of SPP-like modes could be interesting too in order to obtain design parameter that could provide some control over the maximum field enhancement confined under the spheres.

Chapter 5

Intrinsic and extrinsic losses of self-assembled metal-dielectric systems

A study of the mechanisms reducing the light confinement efficiency for the modes of a monolayer of dielectric spheres on metallic substrate is presented in this chapter. These losses can be divided into two types: intrinsic (related with the optical properties of the materials forming the system) and extrinsic (accounting for unwanted defects in the fabricated samples). The former are numerically studied and the best conditions for increasing the confinement efficiency are identified. For the latter, the optical response of fabricated samples is compared with numerical simulations for perfectly ordered samples showing a reduction in the quality factor of the modes due to lattice defects.

5.1 Introduction

In previous chapters we showed that, as in a photonic crystal (PC) slab, monolayers of dielectric spheres support leaky modes [6] which can confine light. Therefore, identifying those mechanisms through which light confinement is reduced is key when devising possible applications for these systems. Although energy leakage is intrinsic to the modes supported by a PC slab [139], an appropriate engineering of the structures may lead to an efficient confinement represented by large quality factors (Q) [30] of the modes of the system. Structural disorder introduced during the fabrication process can reduce such confinement. This has been a largely studied issue in PC slabs in the past [33]. In this context, the main sources of losses are positional and size variations of the scattering units as well as surface roughness. For the particular case of 2D self-assembled systems, the main structural defects are polycrystallinity [93] and random vacancies in the lattice inherent to the fabrication process as studied in chapter 2 although positional and size disorder also play an important role.

In this thesis we are mainly interested in hybrid systems. Therefore, another source of losses must be taken into account which is that related to absorbtion by the metal substrate which is an important issue to be considered in any system supporting surface plasmon resonances (SPR) [60]. If a metal with low absorbtion at a given spectral range is placed under a photonic structure, we have seen in previous chapters that the Q factor can be increased thanks to a reduced leakage through the substrate [83]. However, for those metals with strong absorbance in the spectral region of the SPP-like modes (see chapter 4), one would expect enhanced losses due to absorbtion by the metal. Therefore, this kind

of losses can also be considered intrinsic to the system and dependent on the metal chosen as substrate. To illustrate this point, Fig. 5.1 shows a comparison between the complex refractive index of gold and silver showing that for wavelengths $\lambda < 650nm$ gold presents an anomalous dispersion region while silver works nearly as a lossless mirror. Therefore, placing gold or silver under a given photonic structure may lead to important differences as far as concerns absorbance losses.

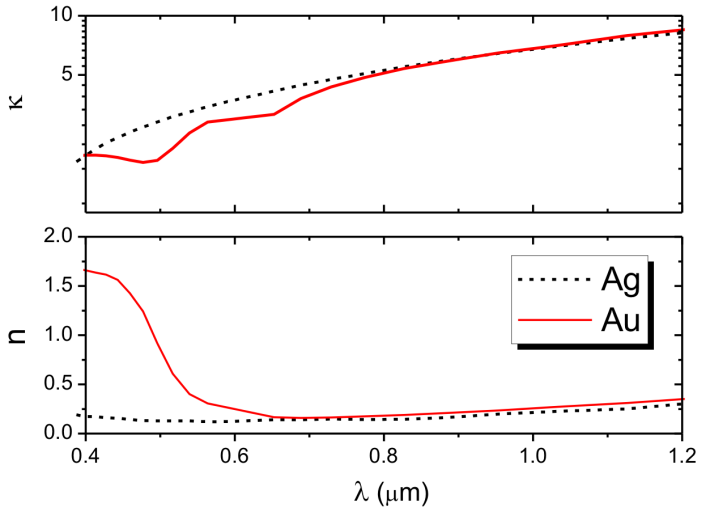


Figure 5.1: Complex refractive index for bulk gold and silver as extracted from reference [136].

The chapter is divided in two parts: In the first part, the effect of structural disorder on the experimental optical properties is identified by comparison with the calculated ideal case for each metal. Resonances corresponding to SPP-like and WG-like modes are analyzed obtaining lower confinement (measured as variations in their Q) for each mode with respect to the simulated ideal case.

In the second part of this chapter we study numerically how the gold optical constants affect the light confinement of each mode for a monolayer of polystyrene (PS) spheres deposited on this metal. This is done by tuning each mode of the system (by varying the sphere diameter) from the strong absorbance spectral region ($\lambda < 600$ nm) to the near infrared (NIR) where gold acts as an almost perfect mirror. Large changes in the spectral position of the modes as well as in their Q factors are obtained and correlated to the real and imaginary parts of substrate's refractive index (RI). Large differences are found on the dispersion of the modes depending on whether they present SPP-like or WG character. Finally, the Q factor for each mode is analyzed for every spectral position finding a strong dependence between the gold complex refractive index and the confinement factor of the modes.

5.2 Extrinsic losses: effect of lattice defects

In chapter 2 (section 2.2) it was shown that the main differences between hybrid monolayers fabricated by each of the described methods where related to polycrystallinity. While the vertical deposition method yields samples with randomly oriented domains, the wedge-shaped cell method is almost free from this problem. However, both of them produce

samples with randomly distributed vacancies, lattice dislocations and positional and size disorder (see Fig. 5.2). As all those defects are expected to introduce losses it is interesting to compare the experimental optical response with numerical simulations to evaluate the effect of structural disorder.

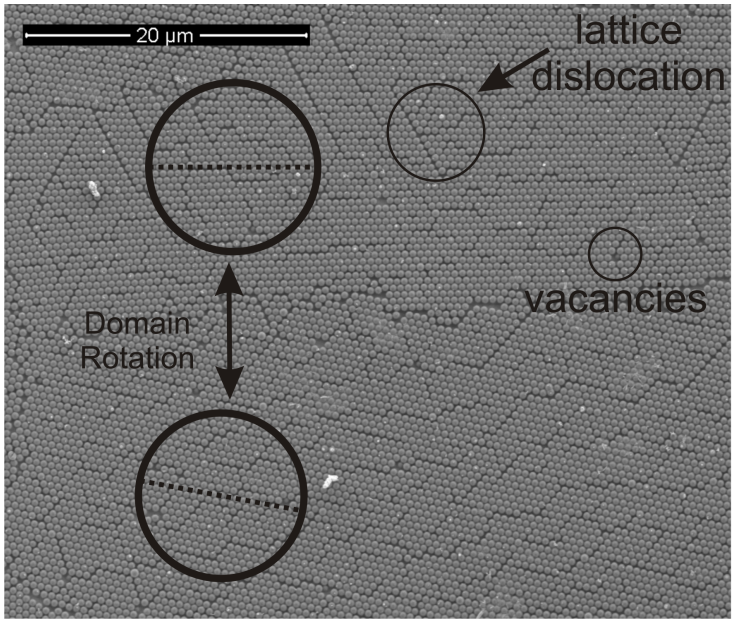


Figure 5.2: Three kinds of lattice imperfections are shown on a sample made of PS spheres with $\Phi = 520$ nm and grown on a silicon substrate by the vertical deposition method.

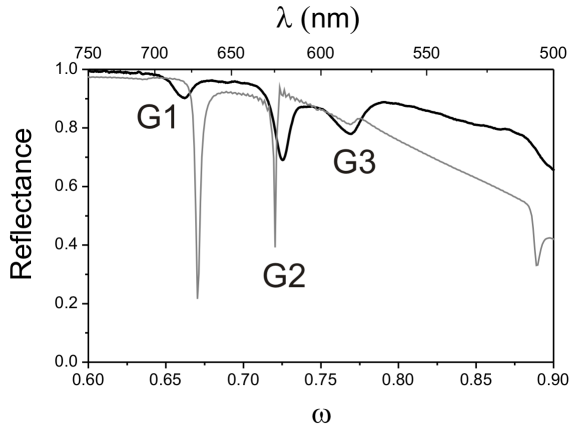
In this study we will only consider normal incidence reflectance measurements for monolayers of polystyrene spheres grown on silver and gold substrates. The effect of pollycristallinity is not expected to play an important role in the measured spectra. The reason for this is that, at normal incidence only those modes available at the Γ point of the reciprocal lattice are being excited. As seen in chapter 4 those resonances are independent of the orientation of the 2D lattice thus, although rotated among them, domain with good crystalline quality will show the same spectrum at normal incidence.

Other important point concerning the existence of rotated domains is what domain size is necessary to obtain a complete Bloch mode. In our case, uniform domains are usually formed by more than 100 spheres even in the vertical deposition case. It was demonstrated by Miyazaky et al. in [140] that for a monolayer formed by ~ 100 spheres, the Bloch modes for in-plane propagation are completely formed with no finite size effect in the optical response. Therefore we expect that the only effect of the existence of a polycristalline structure on the optical response will come from scattering by domain boundaries.

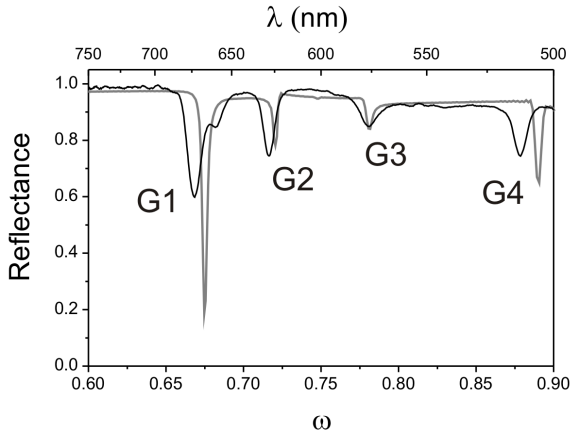
From the discussion above, we can conclude that the optical response at normal incidence for the samples presented in this thesis should not be strongly affected by domains rotations. However, this kind of lattice deffect can be important for the case of angle resolved measurements if large areas of the sample are probed. This point will be further considered in the next chapter.

Fig. 5.3 shows two examples of experimental normal incidence reflection spectra for $\phi =$ 520nm spheres monolayers on gold (a) and silver (b) together with numerical simulations. Results are shown in both , wavelength (λ) and normalized frequency $\omega = \sqrt{3}\phi/(2\lambda)$ where

ϕ is the diameter of the spheres and λ the wavelength for propagation in vacumm. In this case the gold substrate sample has been grown by the vertical deposition method while the silver one was fabricated by the wedge-shaped cell method. As can be observed, the former presents resonances superimposed on the absorbance profile described in the previous section. For the silver case resonances appear over a *ca.* 100% reflectance background as expected from the complex refractive indeces shown in Fig. 5.1.



(a)



(b)

Figure 5.3: Normal incidence reflectance measurements (black line) for ϕ = 520nm PS monolayer of spheres deposited on gold (a) and silver (b) together with numerical simulations (grey line).

Although the agreement between theory and experimental is quite good two main differences are found. The first one is that the spectral position of experimental and theoretical resonances do not perfectly match. In particular, experimental resonances appear red-shifted respect to the theoretical coounterpart. This could be related with a small lattice relaxation with respect to the close-packed lattice (simulations). Second, for both metals, experimental resonances are spectrally broader and present a smaller amplitude than the calculated perfect structure. Both these two effects are due to lattice imperfections described above.

Bloch modes are formed by coherent interference of the incident light by the periodic lattice and therefore any defect will introduce new states that translates into a broadening of the modes of the deffect-free structure. That is, defects causes leakage of energy from the modes of the perfect structure and therefore a reduction of its Q. This is evidenced by the changes in the measured spectra. As an example, Q values have been extracted for the G1 mode in both experimental and theoretical spectra for the silver substrate monolayer in Fig. 5.3b. While the theoretical case gives a value of $Q_{G1} = 136$, the experimental one is $Q = 60$. This twofold reduction in the Q value shows how disorder strongly reduces the confinement of the propagating field within the structure. Such effects are present almost for every mode in Fig. 5.3. In particular, the reflectance reduction is specially strong for G1 and G3 (which almost disappears in the silver case). These resonances present SPP-like character while G2 and G4 are WG-like. This behavior points to a different effect of structural disorder on modes having different nature, though further studies will be needed to clarify this point

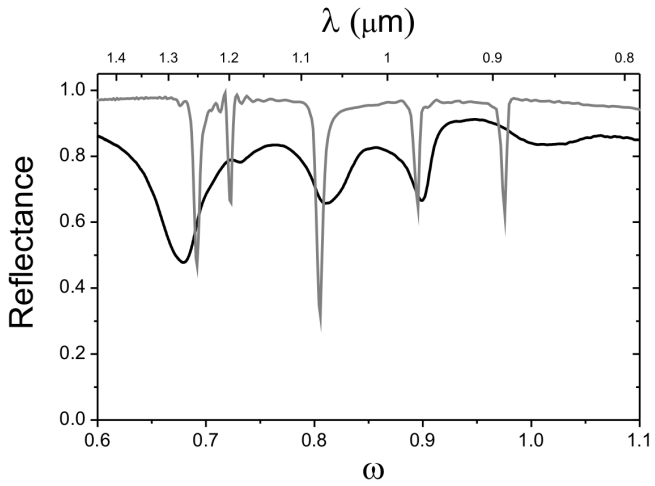


Figure 5.4: Normal incidence reflectance measurement (black line) for a monolayer of $\phi = 1\mu m$ PS spheres deposited on gold together with numerical simulation (grey line).

Finally, Fig. 5.4 presents a comparison between simulations and experiment for normal incidence reflectance of a PS monolayer of $\phi = 1\mu m$ deposited on gold. The spectral range for the resonances is in this case NIR and thus, the gold substrate acts as perfect reflector (see gold refractive index in Fig. 5.1) where absorbtion is negligible. This is the experimental implementation of the in-depth theoretically studied system in chapter 4.

As expected, the optical response departs from the theoretical one with the same features than for the visible case: spectral shift and and broadening of the resonances. The origin of the discrepancies is then the same already commented for the smaller spheres system. Other sources of spectral broadening in the experimental spectra can come from using large NA objectives [128]. This can introduce a further reduction in Q which could be mistaken as being related with disorder. As mentioned in chapter 3, for normal incidence measurements in the Fourier imaging set-up, we are collecting reflected beams with a resolution of less than 1^o and thus we expect no broadening effects. In case of Fig. 5.4 measurements have been performed in an FTIR spectrometer attached to 10X microscope where the signal is collected in a solid angle of $\sim 5^o$. Therefore, a contribution to the

broadening of the experimental spectrum could be also related with this fact.

5.3 Intrinsic Losses: effects of the optical constants of the metal substrate

Knowing the effect of the intrinsic losses on the light confinement properties of any PC is a fundamental issue since it tells us which is the best performance expected from a given structure. For the system formed by a dielectric substrate and a monolayer of organic spheres, intrinsic losses are due to the leaky character of the propagating modes as shown in previous chapters. The spectral position and energy leakage of the different modes is scalable with the diameter of the spheres if non dispersive materials are considered. However, if a metallic substrate is introduced under the monolayer absorbance appears, or, in other words, ohmic losses which are not scalable but fully dependent on the complex dielectric constant of the metal at each given frequency. Therefore, each metal will introduce losses at different frequencies. In that case, it is interesting to study what changes the confinement ability of a monolayer of polystyrene (PS) spheres on gold when the resonances of the system are placed at different frequencies undergoes.

Fig. 5.5 shows calculated reflection spectra at normal incidence for monolayers of PS spheres grown on a gold substrate with 450 and 750 nm diameter. The total field intensity associated with the three modes of the system is also shown for the sample with larger spheres and in the spectral range under consideration. For the case of the larger spheres, modes appear as dips over a nearly 100 % reflectance background coming from the gold substrate (red dashed line) as explained in chapter 4. For the case of the smaller spheres, a monotonic decrease in the background reflectance takes place for wavelengths below $\lambda \sim 650$ nm, due to the onset of absorption by the gold substrate, which hampers the observation of the modes of the system. In the intensity profiles of Fig. 5.5c, the two types of modes studied along this thesis can be identified: SPP-like (G1 and G3) and WG-like (G2).

As a next step we have calculated normal incidence reflectance spectra as we vary the sphere diameter in the range 450-1250 nm in steps of 100 nm. Fig. 5.6a shows the spectral position of G1, G2 and G3 in wavelength. Here we can see how the spectral evolution of each mode follows a linear trend. With the present diameter range the system modes can be shifted from $\lambda = 600$ nm up to 1500 nm. If the VIS range below 600 nm were preferred a substrate of a different nature, such as silver, would be more appropriate as absorption begins for smaller wavelengths.

Fig. 5.6b shows the same data in terms of reduced frequency ω. Here we can see how modes G1 and G3 are slightly dispersive while G2 hardly changes its spectral position with sphere size. The latter points to a scalability with the lattice parameter, characteristic of the dispersion relation of PC comprising non dispersive materials [5] and is a direct consequence of the scalability of Maxwell equations. This behavior can be explained by the total field intensity being strongly localized within the sphere size and hence not being able to sense the dispersive elements present in the structure, i.e. the metal substrate. On the other hand, modes G1 and G3 are strongly sensitive to the optical nature of the substrate as most of their field intensity is located in close vicinity to it. Therefore it is expected that their spectral position will be more dispersive than in G2 case.

In order to explore the losses of the different modes we have extracted the Q associated with each of them which gives us the efficiency with which they confine light. As shown in the previous chapter, the Q for each mode can be extracted from calculated reflectance

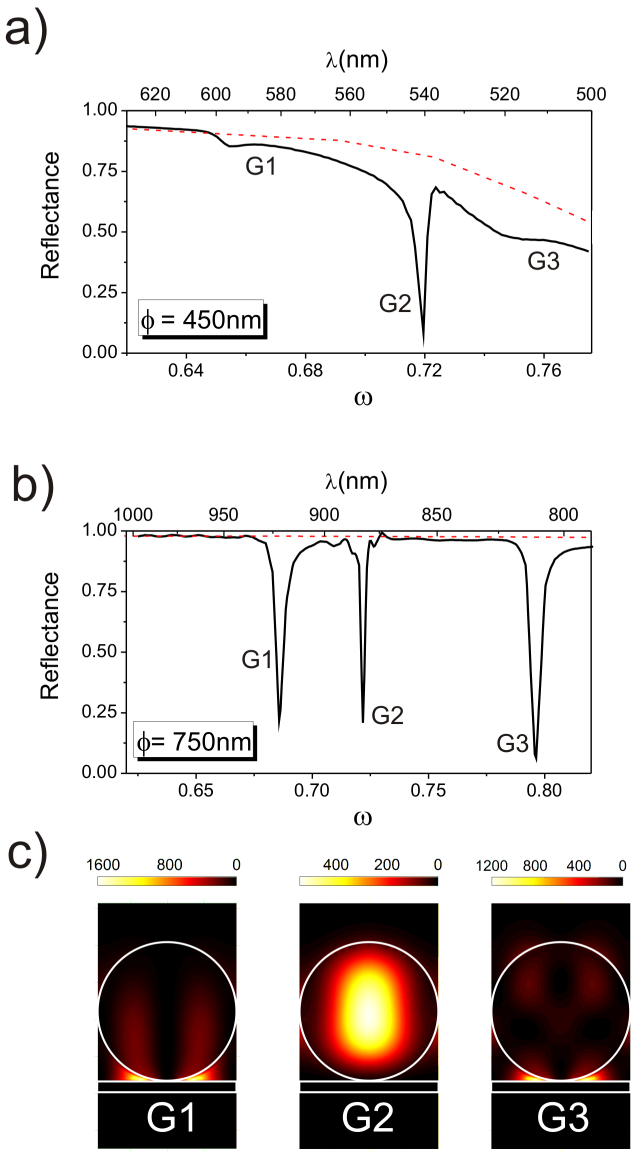


Figure 5.5: Numerical simulation of reflection spectra from monolayers of PS spheres deposited on a gold substrate having a 450 nm (a) and 750 nm (b) diameter. Red dashed line shows the calculated reflectance for a gold film. c) shows the total field intensity distribution for the three resonances shown in b).

spectra from $Q = \omega/\Delta\omega$ with $\Delta\omega$ being the full width at half maximum (FWHM) of each mode and ω its spectral position.

Fig. 5.7b shows the Q of each of the three modes considered as we increase the sphere diameter. Each point in the figure corresponds to a sphere diameter which for G2 covers the whole 450-1250 nm range while for G1 and G3 results could only be obtained for the 550-1250 nm and 650-1250 nm intervals respectively, as strong absorption by the gold substrate in the visible range hampers the observation of the modes when using smaller spheres. Here we can see how G2 undergoes a strong variation as its frequency is shifted, with a maximum close to 750nm, while G1 and G3 hardly change in the same spectral range. Regarding the absolute values of Q obtained we can see how in the case of G2 a Q

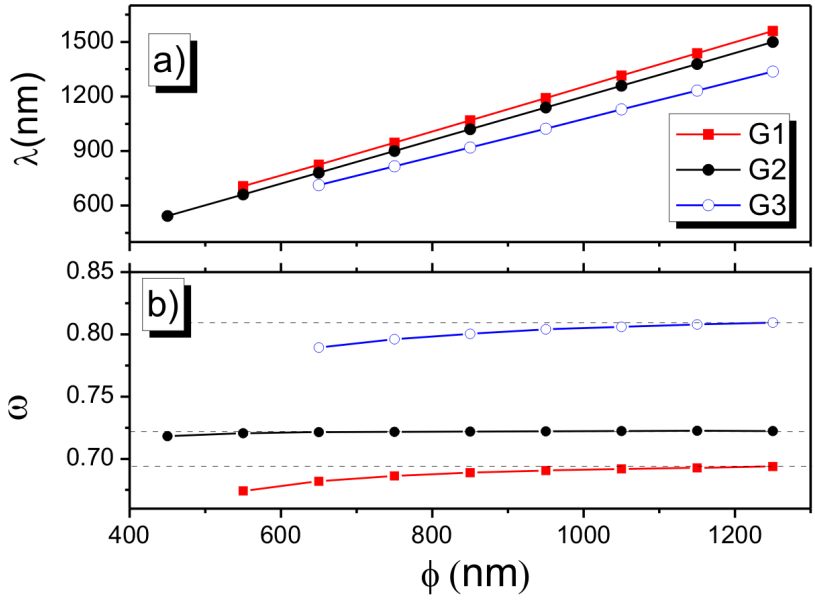


Figure 5.6: Spectral position of the G1, G2 and G3 modes for samples with increasing sphere diameter as a function of wavelength (a) and reduced frequency ω (b).

of up to 600 can be achieved for $\phi = 650$ nm spheres. These values, though not as large as those attainable in 2D PhC fabricated with other methods such as lithography from high refractive index semiconductors, are much larger than those which can be obtained in the ideal case of a free standing monolayer (*ca.* 100) as shown in chapter 4. For the case of G1 and G3 large values can be obtained up to 220, two-fold larger than those reported for similar systems [128].

To account for the results described above we have compared the evolution of the calculated Q with the optical constants of the gold substrate used in the calculations and which have been obtained from ellipsometry measurements on thin films deposited by sputtering (see Fig. 5.7a). For the case of G2, the evolution of Q is clearly correlated with the real part of the refractive index of gold (n). Due to the fact that the field intensity for this mode is concentrated within the dielectric spheres (see Fig. 5.5c) intrinsic losses will be mainly due to energy leakage to the environment with small contribution from absorption by the metal. Radiative losses are governed by the real component of the refractive index of the environment as light confinement is due to total reflection in the vertical direction and to Bragg diffraction in the plane of the periodicity. In order to improve the confinement within the monolayer one needs a refractive index below the effective index of the periodic dielectric array (which in our case is *ca.* 1.38). In the spectral range under consideration n of gold is always below 1 and hence the confinement obtained is superior to the case of the free-standing monolayer (surrounded by vacuum) with a maximum near $\lambda = 750$ nm where n=0.1.

Finally we consider the confinement for G1 and G3, where part of the total field intensity is located close to the metal surface. In this case both Q have similar values which oscillate between 220 and 130 depending of the dielectric sphere diameter considered. In principle for these modes losses are due to both out-of-plane radiative losses and absorption, where the contributions of one or the other will be dependent on the way the field intensity is distributed. But the fact that the obtained values are much lower than those

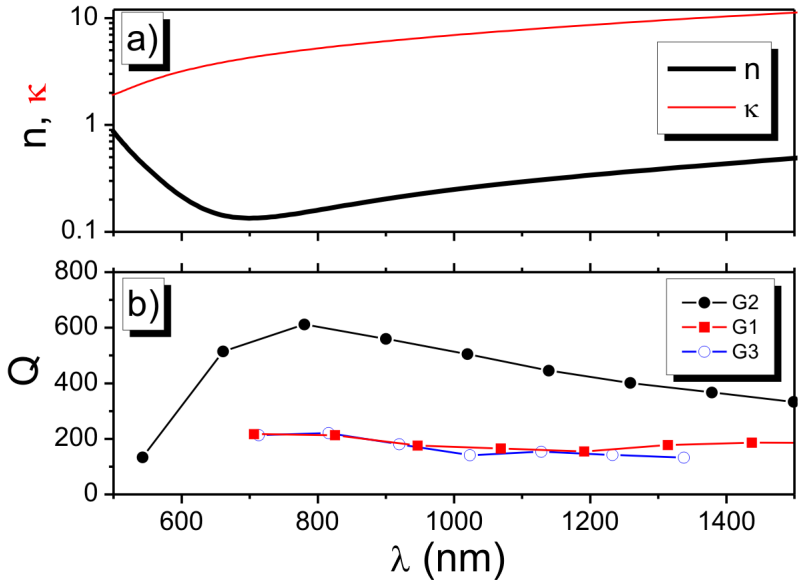


Figure 5.7: a) Optical constants of the gold substrate measured by ellypsometry. b) Quality factors (Q) of the different modes of the system for the same structure with different sphere diameter.

obtained for G2 indicates that absorption is likely the dominant source of losses. Returning to the dispersion in the spectral position of the modes presented in Fig. 5.6 and comparing it with the optical constants of the gold substrate we can see how the spectral evolution of the G1 and G3 modes follow a trend similar to k. As mentioned above, these modes should be more sensitive to the dispersion of the gold substrate as a significant part of their field intensity is located in close vicinity to the metal interface.

5.4 Conclusions

We have studied the effects on the optical response of the two kind of losses affecting the field confinement in a monolayer of spheres deposited on a metallic substrate. For extrinsic losses, we have seen that a little amount of disorder strongly reduced the Q factors to half those of the perfect lattice. Hence, minimizing the defects is critical in obtaining a high performance for each mode. The different effect of extrinsic disorder on each kind of mode remains an open question and could be investigated in further work introducing a controlled amount of disorder in the samples as has already been done for other self-assembled photonic structures, such as artificial opals [141].

Concerning intrinsic losses it has been shown that they affect differently the two kinds of mode of the system depending on whether they are SPP-like or WG-like. The former seem to suffer from some reduction in their Q values due to ohmic losses. They also shown a lack of scalability in the spectral position when high absorbance regions of the metal's dispersion relation are considered. For the WG-like modes the spectral position is fully scalable with the diameter of spheres. However, the effect of chosen diameter strongly affects the Q value depending on the metal's real part of the refractive index for a given frequency. In conclusion, it has been shown that Q can be strongly increased if the appropriate metal and spectral region is considered.

Chapter 6

Angle and polarization resolved spectroscopy of monolayers of organic spheres

In this chapter an in-depth study of the angular response of monolayers of organic spheres is presented. By using the angle-resolved spectroscopy technique described in previous chapters we have obtained the dispersion relation of monolayers deposited over dielectric and metallic substrates. A comparison between the optical properties of each case as well as a study of the dispersion relation regarding the character of each mode (SPP-like or WG-like) with an empty lattice approximation is also presented. Finally, experimentally obtained equifrequency surfaces in reflectance are analyzed.

6.1 Introduction

We have shown in chapters 4 and 5 of this thesis that the best performance as photonic crystal (PC) of a monolayer of organic spheres is obtained when a metallic substrate is used in such a way that energy leakage of the confined modes is minimized. However, we have characterized the system only for normal incidence where symmetry and propagation directions are not being taken into account. In order to fully chracterize the optical properties of the structure the angular dependance of its optical response has to be studied. Given that incident and outgoing angles can be easily related to wavectors with a component contained in the plane of periodicity, angle resolved spectroscopy has shown to provide valuable information about the optical properties of two (2D) [111] and three dimensional (3D)[142] PCs as we pointed out in the introduction of this thesis. If 2D PCs are considered each angle of incidence can be associated with an in-plane propagating wavector. Hence angle-resolved spectroscopy can be used to retrieve the angular dispersion of photonic modes and the presence of forbidden frequency gaps. Furthermore, one can easily retrieve valuable information such as the spectral position of photonic gaps or the spectral regions where slow light effects are expected [143]. Moreover, if measurements are polarization resolved, the symmetry of each mode can also be obtained [6]. This kind of measurement has been applied to monolayers of dielectric spheres in the past mostly with dielectric substrates [93] [99] or freestanding (FS) [140] [144] configurations. In those works authors characterized by means of angle resolved reflectance/trasmittance

the dispersion relation of the modes available for those systems although their experimental study suffered from the lack of confinement for that kind of structures as shown in previous chapters which resulted in poorly resolved dispersion relations. Other sphere lattices different from the hexagonal close-packed (HCP) [95] [145] as well as monolayers over active dielectric substrates [146] have also been characterized but always finding poorly resolved modes evidencing weak confinement of light.

From the surface plasmon resonance (SPR) point of view, angle-resolved spectroscopy is a common technique to obtain information about (SPR) propagation on a metallic surface [41]. If a periodically corrugated surface is considered, a well defined dispersion relation can be obtained from the dips observed in reflectance spectra [50]. For the case of self-assembled hybrid structures, as the one under study here, several works have mapped SPR by means of angle-resolved spectroscopy. Cole et al. [59] used angle-resolved measurements to demonstrate the evolution from propagating plasmonic modes to localized ones in gold nanovoids formed originally by self-assembled organic monolayers. In this chapter we show that in our hybrid system photonic bands can be obtained by this method which completes the study of chapters 4 and 5 on how light propagates in this kind of structures.

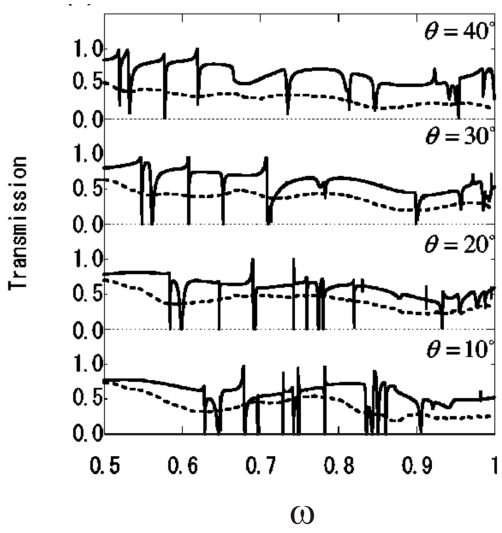
We have used the experimental methods described in chapter 3 to obtain equifrequency surfaces (EFSs) of light propagating in the plane of periodicity. That is the reciprocal space direct image inspection. This study was performed for the metallic substrate as the dielectric substrate samples presents a not well resolved reflectance pattern.

This chapter is structured as follows: First we introduce the dielectric substrate case and show results for monolayers of polystyrene (PS) spheres deposited on silicon and glass in the visible (VIS) spectral range. Next, metallic substrate structures are measured in the same way and complex dispersion relations are obtained by spectrally scanning high symmetry reciprocal lattice directions. We identify each relevant optical feature and relate it with the normal incidence study presented on chapters 4 and 5. The physical origin of the modes is further retrieved from a comparison with an empty lattice approximation. After that, experimental EFSs are collected and interpreted taking into account the previously measured dispersion relations. Finally, we present preliminary measurements of the dispersion relation in the high energy spectral range of this system.

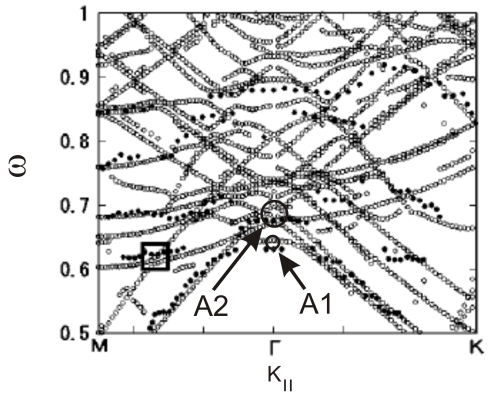
6.2 Dielectric substrate

As we have already shown in previous chapters monolayers of organic spheres can be considered as 2D PCs slab when grown on metal substrates or in a free-standing configuration and present complex dispersion relations. However, when dielectric substrates are considered angle resolved spectroscopy has not shown, to the best of our knowledge, well defined resonances [95] due to the already explained energy leakage through the substrate. Nevertheless, monolayers grown on dielectric substrates have been optically characterized and their dispersion relations retrieved [99] [140]. To obtain these results, transmission spectra [1] are measured at different incidence angles and for different polarizations. After that, the spectral position of each resonance can be plotted as a function of the angle of incidence (θ) to form the dispersion relation as the example taken from [99] and shown in figure 6.1.

[1] Usually, dispersion relation measurements shown in the literature are extracted from transmission measurements for the monolayer over a dielectric substrate. We have performed reflectance measurements given that our set-up is optimized for the metallic substrate case.



(a)



(b)

Figure 6.1: a) Calculated (solid) and experimental (dashed) transmission spectra for a monolayer of PS spheres deposited on a glass substrate. Spectra are taken for P polarization and measured along the ΓK direction. b) Band structure for P polarization. Solid circles correspond to the spectral position of the resonances shown in (a) for different angles of incidence. Open circles show calculated modes. In both cases data have been taken from reference [99]

As can be observed in Fig. 6.1a while theoretical results show sharp resonances, experiments do not show well defined dips. This effect is a result of both, leakage through the substrate [2] and extrinsic disorder in the fabricated sample in the form of structural defects. As a result, the comparison in Fig. 6.1b of measured and calculated angle resolved spectra do not show a good agrement apart from the lower energy spectral range where the dispersion relation presents a simpler behavior.

In order to probe the dispersion relation of the monolayers deposited on dielectric substrates we have performed angle resolved reflectance measurements with the method described in chapter 3 and the results are shown in Fig. 6.2. We present below the case

[2]Simulations of Fig. 6.1 are performed for an optically thin substrate which allow resonances to be well defined as opposed to the case shown in chapter 4 for the semi-infinite silicon substrate.

of monolayers grown on silicon substrates although glass substrates were also used with only small differences as previously mentioned in chapter 4.

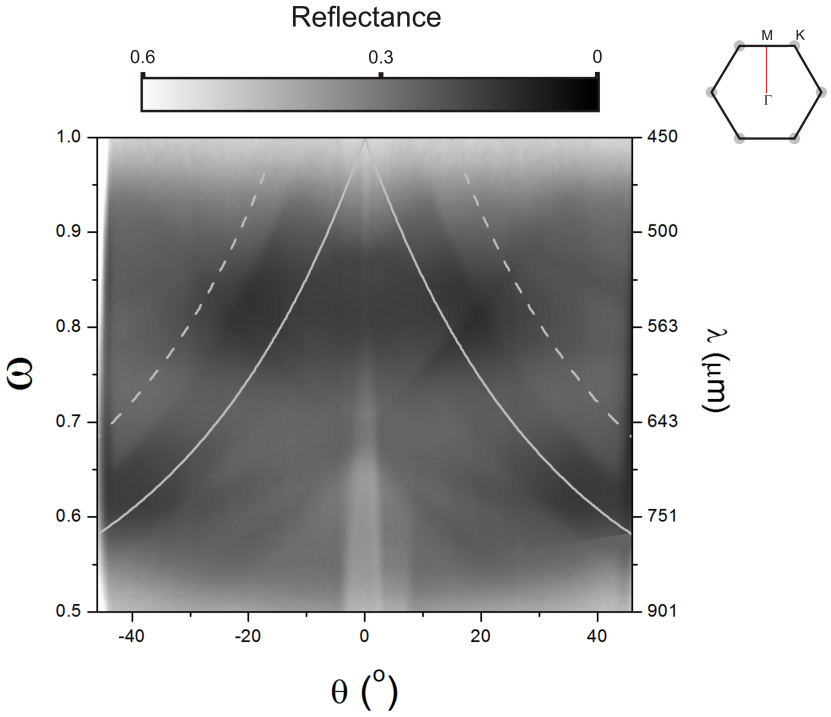


Figure 6.2: Angle resolved spectra response for a monolayer of PS spheres with diameter $\Phi = 520nm$ deposited on a silicon substrate measured along the ΓM direction using unpolarized light. Full and dashed line shows calculation for Bragg diffraction limit (full line) and diffracted orders reentering the objective (dashed line) in the ΓM direction.

In figure 6.2 we show a contour plot of experimental reflectance for a monolayer of PS spheres with $\Phi = 520nm$ deposited on a silicon substrate and measured at angles θ between 0 and 48^0 degrees (notice that unpolarized light is used). By inspection of the Fourier image in the CCD camera we choose the ΓM direction in reciprocal space as an example (although ΓK was also inspected).

The effect of out-of-plane Bragg diffraction is now also evident as an abrupt decrease in reflectance similar to that shown in figure 3.14 of chapter 3. It appears as two dark bands in the contour plot. A simple calculation of the diffraction limit taking into account the scanning direction (ΓM) is also shown as two sets of grey line delimiting those bands. The full line corresponds to the onset of diffraction of the specular beam extracted from the diffraction condition as explained for the grating case in chapter 3. Above a certain collection angle, light diffracted at smaller angles re-enters the fiber and the collected intensity rises again. This limit is shown as dashed lines. It can be observed that the calculated limits do not agree completely probably due to deviations from the close-packed lattice in the form of small lattice relaxations.

Regarding the optical resonances of this system shown in previous chapters for normal incidence, we can see that their angular evolution present a nearly linear trend. As expected from the normal incidence study, just the resonance appearing at reduced frequency $\omega = \sqrt{(3)}\Phi/2\lambda = 0.71$ (A2 in chapter 4) for $\theta = 0^o$ presents a clear splitting into three different modes. This lack of resonances in the optical response of the system is again related to losses due to leakage through the substrate ($n_{sub} > n_{eff}$) as well as structural

disorder. This effect increases for oblique incidence for the silicon substrate as compared to the glass one as a result of a larger substrate refractive index.

While photonic bands can be qualitatively described with a hexagonal PC slab approximation [147], a more refined theory is needed if one wants to evaluate the coupling efficiency for a given frequency for any available mode of the structure [3] . Such a quantitative study would require Mie resonance theory in our case in order to obtain the optical response due to the spherical shape of each building block of the periodic lattice. This study has already been reported in several works by Miyazaky et al [39] [140].

6.3 Metallic substrate

In previous chapters we saw that if a metallic substrate is considered, the modes of the system appear in a reflectance measurement as spectrally narrow dips over a mirror-like background evidencing a more efficient confinement of electromagnetic radiation in this kind of system. Then, for any angle of incidence, the modes available to be excited are expected to appear also as narrow dips at the appropriate frequency according to the dispersion relation of the crystal.

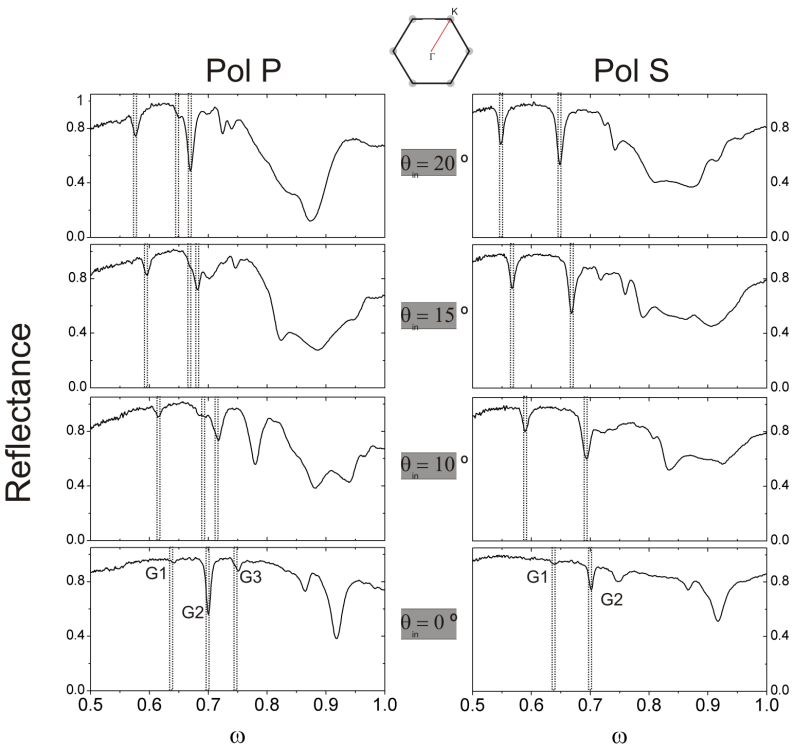


Figure 6.3: Reflectance spectra for different angles of incidence and both polarizations for a monolayer of PS spheres ($\Phi = 520nm$) deposited on silver. Measurements where performed along the ΓK direction in reciprocal space. Inset shows the Brillouin zone of the sample.

Figure 6.3 shows several examples of reflectance versus reduced frequency measured for four different angles of incidence on a monolayer of $\Phi = 520nm$ PS spheres deposited

[3] In PCs slab, specially for air-bridged ones, the scattering process is more simple but still exact numerical calculations are necessary if a complete description of the resonances is needed [31]

on a silver substrate. The spectral range under study is the VIS ($400 < \lambda < 900$). The spectra were measured along the ΓK direction in reciprocal space for both S and P polarizations. As can be observed the evolution of lower order modes (G1, G2 and G3) can be followed as θ increases while higher order ones are hidden in the low reflectance background associated with radiative losses due to out of plane diffraction. From all the radiative channels commented in previous chapters, out of plane Bragg diffraction is the most important for what concerns Q reduction for each resonance. This fact combined with the complex dispersion for each resonance can make following its evolution a non trivial task. It can be observed that, for example, for $\theta = 20^o$ out of plane diffraction takes place for frequencies as low as $\omega \sim 0.8$ for both polarizations which hides the response of higher order modes. Besides, as shown in chapter 5, losses increase for higher frequencies and hence decreases the coupling efficiency which reduces the visibility of the resonances in the spectra. Strong differences are also evident when both polarizations are compared.

As a step further we have performed measurements with high angular resolution which appear as contour plots in figures 6.4a and 6.4b. Such plots show reflectance for the same sample shown in figure 6.3. In this case reflectance for the two main high symmetry directions in reciprocal space (ΓK and ΓM) and both polarizations are shown. The angular resolution is $\Delta\theta = 0.2^o$. As can be observed, at variance with the single spectra of Fig. 6.3, this kind of plots allow us to follow the mode dispersion even when we enter the diffraction limit. This effect is shown as a dark broad vertical band as explained in chapter 3. Therefore, it would not appear in a calculated photonic band diagram (where just propagating in the plane of periodicity is considered). As for any periodic 2D or 3D lattice, the scanned direction determines the diffraction limit shown by the black solid line in Fig. 6.4a. In this case such differences can be observed in figure 6.4 for the two high symmetry directions. ΓK requires larger angles of incidence than ΓM to fulfill the Bragg diffraction condition. Since the latter corresponds to the shorter boundary of the First Brillouin Zone (FBZ), a shorter $K_{||}$ has to be added to the incoming wave to reach the diffraction limit [4]. For the G1 to G3 resonances (see chapter 4) at normal incidence no difference is found with polarization as for this particular symmetry both are equivalent (this can also be observed in Fig. 6.3) .

Several anticrossings appear for modes propagating along both directions and polarizations (for example for $\theta = 18^o$ and $\omega = 0.78$ in ΓK and P polarization). An anticrossing between two modes happens when they have identical symmetry and their dispersion relation crosses at some point in the (k, ω) plot so they present the same energy and wavevector. The importance of anticrossings is stressed by two facts: photonic gaps (if present) may take place in such spectral regions. Also slow light due to almost flat dispersion of the photonic bands at that points can also take place. Moreover, they are very sensitive to variations in the angle of incidence and the scanning direction. If one looks at the plots obtained in Fig. 6.4 anticrossings are well defined in the measurements which is a proof of the high crystalline quality of our structure given that for disordered samples, several lattice directions are integrated in the same measurements.

The evolution of each mode is qualitatively similar to the numerical simulations performed for similar systems by P.V. Braun and co-workers in [128]. They employed the Korringa-Kohn-Rostoker (KKR) method which has proved to describe well the optical properties of PCs of different dimensionality fabricated by self-assembly methods [148] .

We next compare these contour maps with the one shown for the same sphere size but grown on silicon in Fig. 6.2 (note that no polarization was taken into account in

[4] $|k_{out}| = k_0 sin(\theta)$

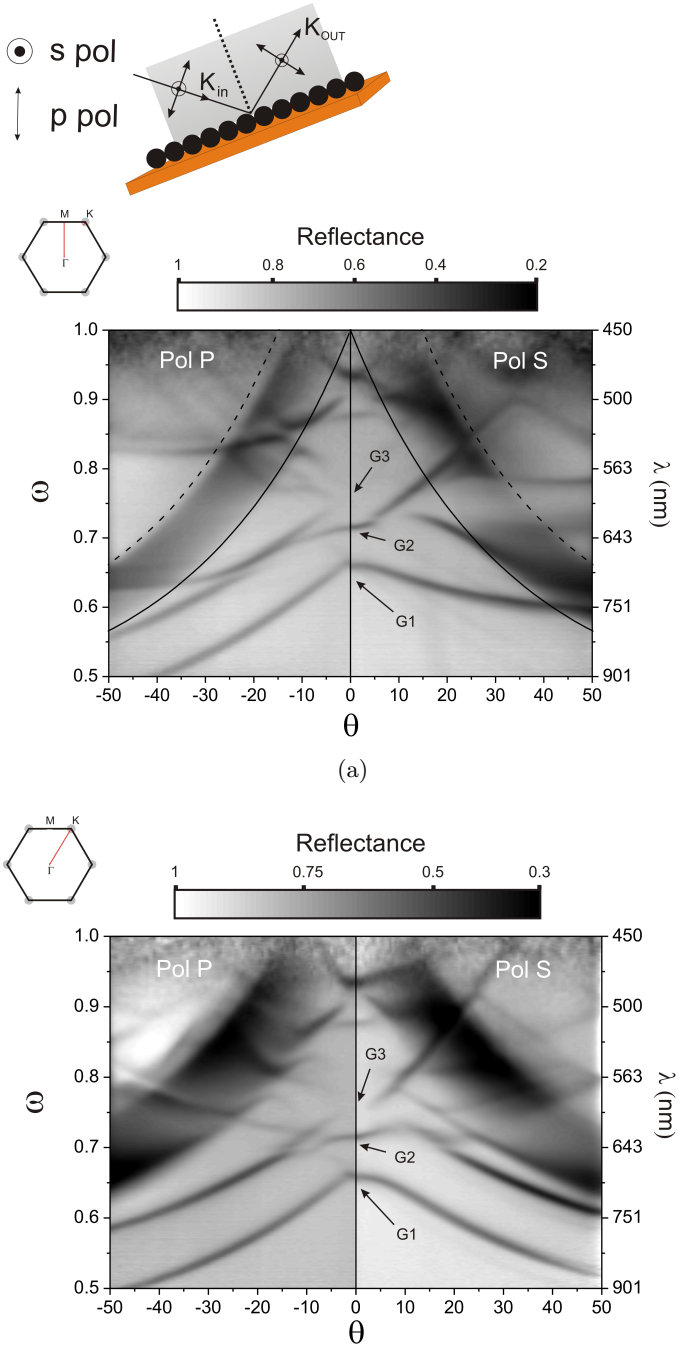


Figure 6.4: Reflectance spectra as a function of angle and reduced frequency for a monolayer of PS spheres with $\Phi = 520nm$ deposited on a silver substrate measured along the ΓM (a) and ΓK (b) directions for both polarizations. Solid and dashed line in a) shows Bragg diffraction and first order diffraction order objective collection respectively.

that case). As shown in chapter 4 by analysis of the field intensity spatial profiles A1 and A2 modes in the dielectric substrate can be considered analogous to G1 and G2 for the metallic substrate case. We found for silicon that A1 and A2 present a splitting as

we move away from normal incidence.The same behavior is found for G1 and G2 in Fig. 6.4. The main difference between dielectric and metallic substrate cases has to do with the complexity of the dispersion relation. While for the former case the modes present a nearly linear dispersion, for the latter a more complex behaviour is found evidencing stronger interaction between the different modes as a consequence of stronger light-mater interaction.

6.3.1 Experimental dispersion relation

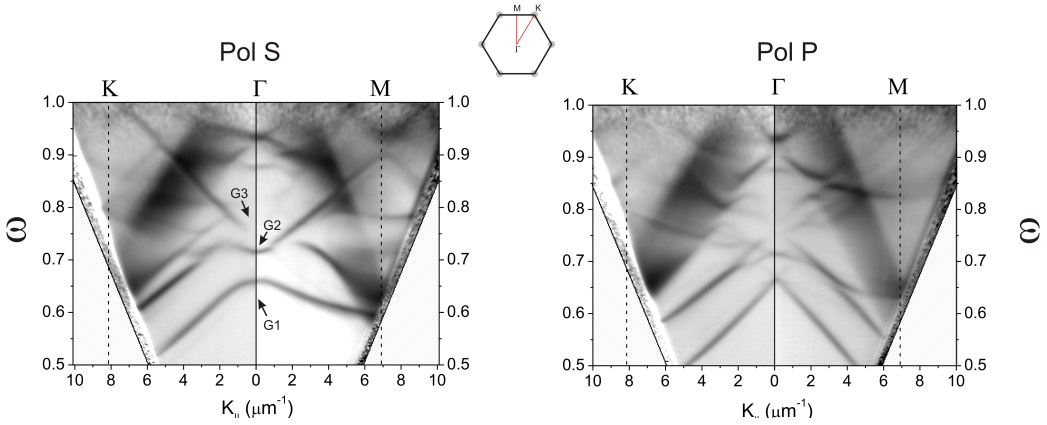


Figure 6.5: Dispersion relation extracted from angle resolved measurements for a monolayer of $\Phi = 520nm$ PS spheres deposited on silver.

In order to study the above reflectance measurements from a dispersion relation point of view, it is worth to plot them as a function of the component of the incident wave-vector parallel to the plane of periodicity $(k_{||}, \omega)$. As shown in chapter 3 we can obtain $k_{||}$ from the measured angle given that $k_{||} = k_0 sin(\theta)$ where k_0 is the wavevector of light in vacuum for the frequency considered in each case. This leads to figure 6.5 where the same data shown in fig. 6.4b and 6.4a are plotted as a photonic band diagram. In this case ΓK and ΓM directions are shown together for each polarization.

When the dispersion relations shown in Fig. 6.5 are compared with those reported in literature and previously plotted in Fig. 6.1b we find an overall qualitative agreement with some differences, as already discusses for the normal incidence case. These differences are spectral shifts (specially for the SPP-like modes), as well as mode splitting from A1 and A2 to G1 and G2. The origin of this is again related to the different nature of the substrate as in detailed studied in chapter 4.

In the introduction of this thesis it was shown that an empty lattice model has been demonstrated to properly describe the physical origin of the bands in the dispersion relation of a PC slab [31]. Therefore, it is worth to compare the experimental dispersion relation shown in Fig. 6.5 with the calculated photonic bands using empty lattice approximation, taking into account the two different types of mode available for the monolayer on metal.

Therefore, the dispersion relations that are folded back into the FBZ of the reciprocal lattice of the monolayer are, on the one hand a wave propagating on an homogeneous medium of effective index n_{eff} (WG-like mode) and on the other hand a SPR (SPP-like).

For those modes propagating in an homogenous medium the dispersion relation can be expressed in terms of reduced frequency ($\omega = \frac{\sqrt{3}\Phi}{2\lambda_0}$). Where λ_0 is the wavelength

propagation in vacuum. Therefore, in an homogenous medium of refractive index n the propagating is $k = nk_0 = n\frac{2\pi}{\lambda_0}$and the dispersion relation (k, ω) is found to be:

$$\omega = \frac{\sqrt{(3)}\phi}{4n}k \tag{6.1}$$

For a monolayer of PS spheres we consider that $n = n_{eff} = 1.38$. Regarding the SPR, we can write the dispersion relation as a function of the reduced frequency ω resulting in:

$$\omega = \frac{\sqrt{3}\phi}{4\pi}\sqrt{\frac{\epsilon_m + n_d^2}{\epsilon_m n_d^2}} \tag{6.2}$$

where ϵ_m is the real part of the complex dielectric constant of the metal and n_d is the refractive index of the dielectric material on top of the metal. In this case that material is not a homogeneous slab but a monolayer of spheres so it is again necessary to consider an effective refractive index. However, as the SPR modes have most of their total field intensity confined close to the metal surface, the calculated n_{eff} of the monolayer may not be valid.

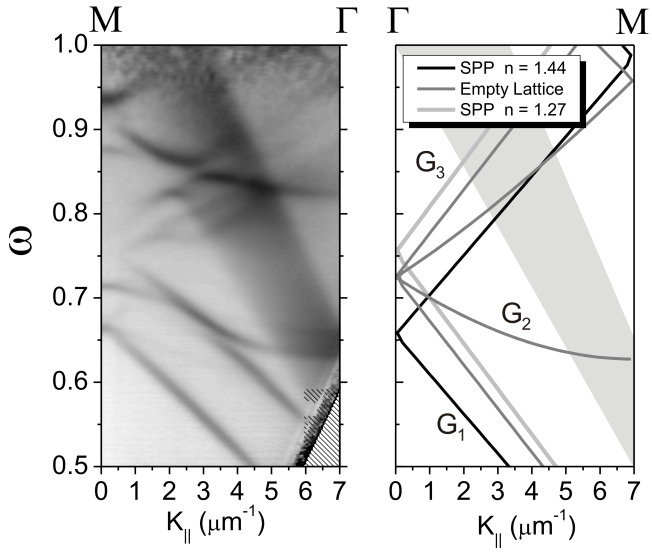


Figure 6.6: Left: Experimental dispersion relation for a monolayer of $\Phi = 520$ nm PS spheres on silver measured along ΓM direction and P polarization. Right: Empty lattice model for G1,G2 and G3 modes. Grey band shows the calculated onset of diffraction limited by the NA of the objective.

The left panel in Fig. 6.6 shows the experimental dispersion relation for a monolayer of $\Phi = 520$ nm PS spheres deposited on silver along the ΓM direction in the reciprocal space. The right panel shows the results of applying the empty lattice approximation to the two type of modes. We find that the main features in the spectral region we are considering are reproduced by this simple model. This further confirms the waveguided and SPR origin of the modes we already observed from the numerical calculations for normal incidence in chapter 4.

In particular, for the SPP-like modes G1 ($\omega = 0.65$) and G3 ($\omega = 0.75$) it is necessary to assume a value of $n_d = 1.44$ and $n_d = 1.27$ respectively in order fo those resonances to take place at the experimental spectral positions. This values reflect the fact that G1 is more confined into the dielectric region than the G3 as was demonstrated with the field

profile simulations in chapter 3. Concerning the G2 dispersion relation, it perfectly agrees with the dispersion relation of the homogeneous medium n_{eff} diffracted by the lattice vectors.

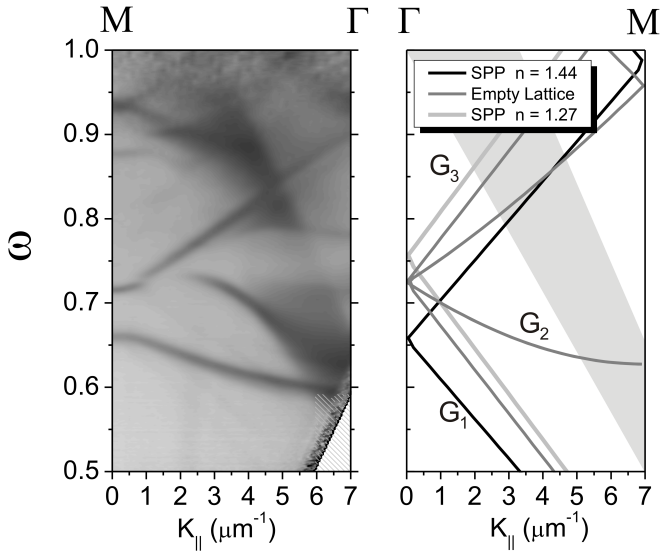
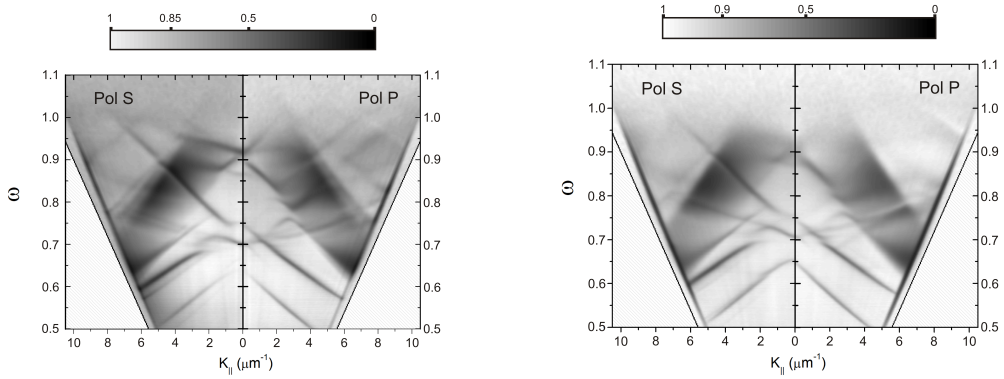


Figure 6.7: Left: Experimental dispersion relation for a monolayer of $\Phi = 520$ nm PS spheres on silver measured along the ΓM direction and S polarization. Right: Empty lattice model for G1,G2 and G3 modes. Grey band shows the calculated onset of diffraction limited by the NA of the objective.

Although the same behaviour is found for the ΓK direction, the agreement worsens when S-polarization is considered (see Fig. 6.7). In fact, G1 and G3 modes are also observed in S-polarization which is not possible for pure SPRs. This disagreement is probably due to hybrid character of both types of modes in the monolayer. However, although very simple, this model provides a physical insight into the character of the several modes of the system. Obviously, if an accurate dispersion relation were required, the use of other numerical approaches as KKR would be mandatory.

So far we have inspected the case of the silver substrate, but it is interesting to compare how does the dispersion relation change when other metallic substrates are considered. In Fig. 6.8 we show angle-resolved spectra along the ΓK direction for both polarizations in the case of gold and silver substrates and PS spheres of $\Phi = 520nm$. As expected from the conclusions of chapter 4 only small differences such as the previously explained spectral shift of the SPP-like modes (G1 and G3) are found for $\omega < 0.9$ ($\lambda > 500nm$). This similarities were also found when the empty lattice model was applied to the monolayer on gold. This was expected since the dispersion relation in the spectral range $0.5 < \lambda < 1.12 \quad \mu m$ ($0.4 < \omega < 0.9$) for the SPR resonances of gold and silver are very similar. For $\omega > 0.9$ ($\lambda < 500$nm) strong variations in the dispersion relation with respect to the silver case are expected for G1 and G3 given that for those frequencies $\epsilon_{Au} > 0 > \epsilon_{Ag}$ (see $\epsilon_{silver}(\omega)$ and $\epsilon_{gold}(\omega)$ plots in chapter 5). However, in Fig. 6.8 it is observed that the resonances completely disappear for the case of gold in that range. As in case of normal incidence, this effect is due to absorbtion by gold in this spectral range and affects the measurements independently of the angle of incidence.



(a) (b)

Figure 6.8: Experimental dispersion relations extracted from angle resolved reflectance along the ΓK direction for a monolayer of $\Phi = 520nm$ PS spheres deposited on silver (a) and Gold (b).

6.3.2 Equifrequency surfaces

So far we have extracted most of the information regarding the optical response of our system from the measured photonic bands. However, the inspection of the EFS has demonstrated to be a very powerful tool to understand light propagating in plasmonic systems [149] [150] but also on dielectric [151] and hybrid [59] [152] 2D PCs. In the next discussion we will explain how to relate the EFSs and the photonic bands with the far field patterns obtained by imaging the back focal plane of the objective as explained in chapter 3 and the useful information that can be retrieved from these measurements.

EFS are sections of the dispersion relation at a fixed frequency and therefore represent the set of allowed wavectors that can propagate in the sample for that frequency. In the case of 2D PCs, EFSs are 2D surfaces which represent those wavectors that can propagate in the plane of periodicity. Therefore, for a homogenous medium, EFSs are circumferences due to the isotropic dispersion relation while for PC EFSs can present complex shapes evidencing a strongly anisotropic energy band [151].

Fig. 6.9a shows the simplest situation in an EFS representation in reciprocal space. That is, transmission from one dielectric medium with refractive index n_1 into another with larger refractive index n_2. Each wavector (k_1) available in the first medium for a given frequency (not scaled) $\omega = |k_0|c = |k_1|c/n_1$ is represented as a circle of radius $|k_1|$. If we consider an incident angle θ_1 with respect to the interface normal, the angle θ_2 of propagation in the second medium will be determined by the conservation of $k_{||}$ considering the EFS in the second medium as another circle of radius $|k_2|$. This simple case describes Snell's law in a graphical manner in reciprocal space. For the case of Fig. 6.9a we have plotted the situation where light impinges from air [5] to a medium with $n_{eff} = 1.38$.

If instead of a homogeneous medium, we consider the second medium a periodic system, as for example a grating, this representation becomes more useful. Fig. 6.9b shows the case where a wavector k_0 is incident on a diffraction grating of period d. Due to the Bloch theorem [4] the allowed wavectors are now the set of circles having identical radius —k— centered at the reciprocal lattice points and separated a distance $|\overrightarrow{G}| = 2\pi/d$. Again, taking into account $k_{||}$ conservation it can be observed that more than one nonidentical beams can be excited. Two examples of excited waves are shown in this case.

[5] Note that as $n_1 = n_{air} = 1$ then $|k_1| = k_0 n_1 = k_0$

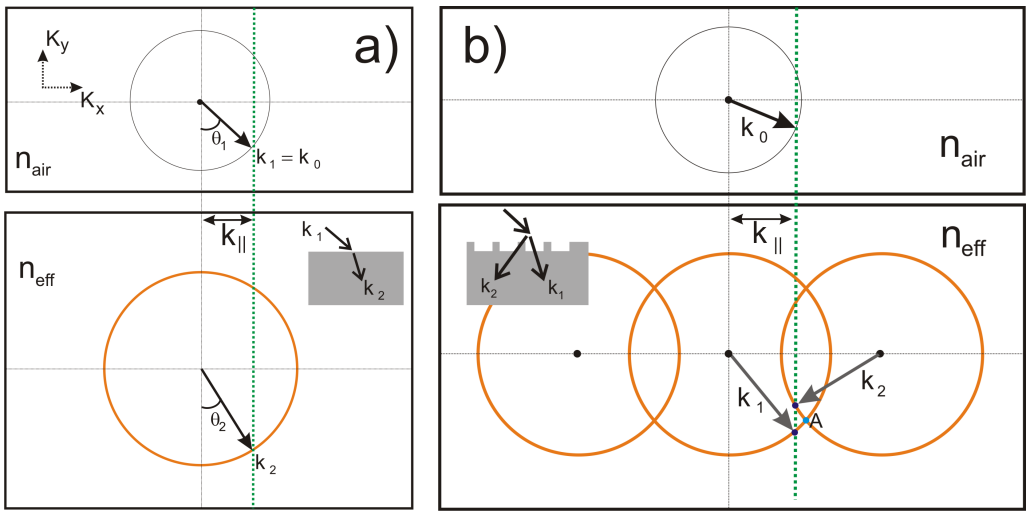


Figure 6.9: (a) EFS plot for light incident from air on a dielectric of refractive index $n_{eff} = 1.38$ (b) Example of two transmission diffractive orders through the same material for a grating with period d and vanishing refractive index contrast.

k_1 corresponds to the transmitted wave or, in other words, the zero order diffracted beam. On the other hand, k_2 represents a diffraction order. Then, what we obtain is a graphical representation of the formula for a diffraction grating [6]in transmission although the same procedure could be applied to the reflection diffraction orders with similar results. It can be seen that at the point marked as A (not excitable by the wavector considered in this case) in Fig. 6.9b the two circles intersect. This is physically meaningless since, if any refractive index contrast is considered, no intersection can happen between equifrequency lines [153]. Although in this case this position of the reciprocal space is not relevant we will see later in this section that it is the origin of several important optical features of PCs. It has also to be commented that the onset of diffraction at a given frequency is shown in this representation as a set of circles that touch but do not cross. That is the case for $k_1 = |\mathbf{G}|/2$ according to the notation in 6.9b.

Let us now consider a beam propagating on air and incident on a 2D periodic system instead of a 1D one. We have plotted in Fig. 6.10 an example of the EFS for a vanishingly small refractive index modulation and hexagonal lattice. The corresponding FBZ is also plotted. As can be observed, we obtain basically the same features already commented for the 1D grating case. However, due to the six-fold symmetry of the periodicity, the EFS become more complex as expected from the reflected/transmitted diffraction patterns for this system. It has been demonstrated by Notomi [151] that the anomalous beam propagation for a low refractive index contrast 2D PC as the one considered here can be explained by the same mechanism already shown for the 1D grating empty lattice. However, if the refractive index contrast is increased, the empty lattice approximation is not valid any more and the EFS undergoes strong changes loosing its circular shape. This means that the energy velocity, whose direction is normal to the EFS, is not paralell to the wave vector anymore, as in the case of the circular EFS [153]. This can lead to interesting phenomena such as the superprism effect or even negative refraction, which cannot be

[6]

$$\vec{k}_{out||}(\omega) = \vec{k}_{in||}(w) \pm m\vec{G} \tag{6.3}$$

where $k_{in} = k_0 sin(\theta_{in})$ and $k_{out} = k_0 sin(\theta_{out})$. Being θ_{in} and θ_{out} the incident and diffraction angle respectively.

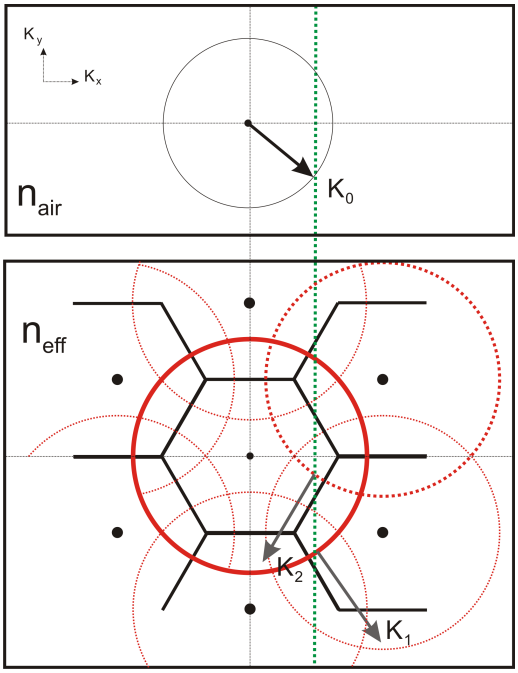


Figure 6.10: Example of a EFS plot for light incident from air to a 2D hexagonal photonic crystal with $n_eff = 1.38$ and a vanishingly small refractive index contrast. Dark hexagonal lines define the FBZ of the lattice.

observed in isotropic media [33]. Such anomalous refraction takes place at points in the EFS where strong changes of curvature take place and the behavior departs strongly from the circular shape.

Earlier in this chapter we showed how scanning the Fourier plane of the microscope objective we were able to collect the dispersion relation in a given direction in the reciprocal space. Analogously, collecting an image of the whole Fourier plane at a single frequency give us a direct measurement of the dispersion relation in every direction, that is, an EFS at that given frequency.

Fig. 6.11a shows the dispersion relation along the ΓM direction in reciprocal space for a monolayer of $\Phi = 520nm$ PS spheres deposited on a silver substrate. In this case, polarization was not considered in order to obtain every available mode in the system. The three red dashed lines mark the frequencies at which the EFSs shown in 6.11b, c and d were taken. The three of them show far field reflectance patterns for the same sample. We have chosen the EFSs for $\omega = 0.65$, $\omega = 0.71$ and $\omega = 0.74$ by using a tunable filter in front of the CCD camera (see chapter 3 for the details). To obtain the final EFS in reciprocal space ($k_{||}$ space) it is necessary first to obtain the angles corresponding to each point of the image. This was done by means of the calibration procedure explained in chapter 3. Finally each angle can be associated with a $k_{||}$ value in the same way it was done in previous sections to obtain the dispersion relation of the system under study. It should be noticed that, while changing the working frequency, the maximum angle collected (the edge of the image) by the objective does not change. Therefore, in our setup the maximum $k_{||}$ available for each ω will change as:

$$|\overrightarrow{k}_{||}|_{max}(\omega) = |k_o|sin(\theta_{max}) = \frac{4\pi}{\sqrt{(3)}\Phi}\omega sin(\theta_{max}) = 10.4\omega \qquad [\mu m^{-1}] \qquad (6.4)$$

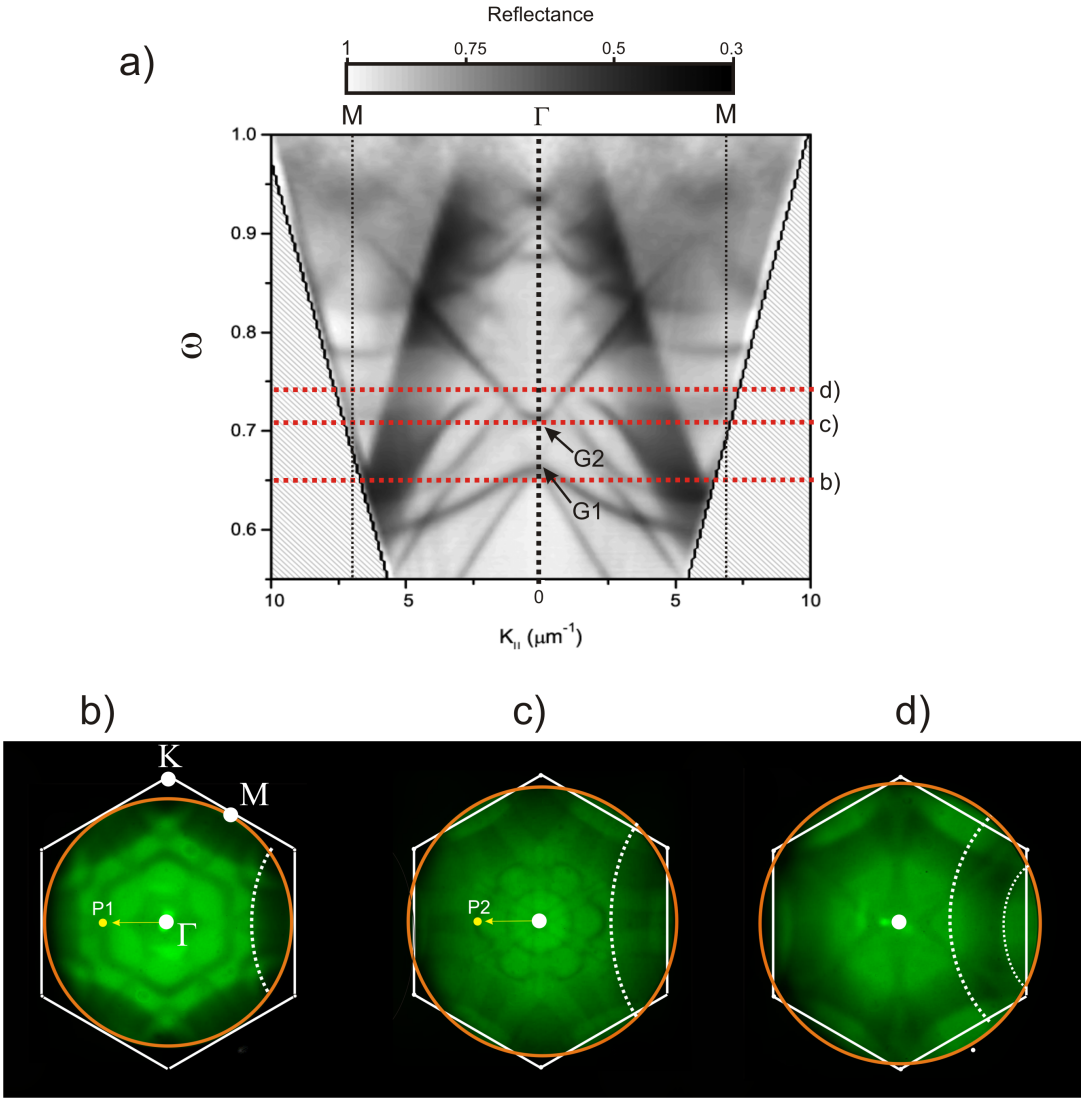


Figure 6.11: a) Experimental dispersion relation along the ΓM direction in reciprocal space for a monolayer of $\Phi = 520nm$ PS spheres deposited on silver. b), c) and d) shows three measured EFSs at frequencies $\omega = 0.65$, 0.71 and 0.74 respectively. White hexagon limits FBZ. Maximum $k_{||}$ measurable with our set-up is shown as an orange circle.

The final value in equation 6.4 is calculated taking into account that $\Phi = 0.520\mu m$ for the samples under study and $\theta_{max} = 48^o$ for our experimental set-up. Therefore, the $k_{||}|_{max}$ available in the images of Fig. 6.11 for $\omega = 0.65$, $\omega = 0.71$ and $\omega = 0.75$ are $k_{||}|_{max} = 6.8$, 7.4 and 7.7 μm^{-1} respectively. Those values correspond to the radius of the colored circles for each EFS. The FBZ of the lattice is shown as a white hexagon over each of the measured EFS so it is evident that for the largest ω we are exploring part of the second Brillouin zone. As can be observed, the area of the reciprocal space covered in each image almost matches the whole FBZ. If we examine each EFS we can clearly see two main features. First, a bright hexagonal pattern defined by circular broad dark band and whose area decreases with frequency. The second feature to be noticed is the set of thin dark bands again with hexagonal symmetry but distributed either within the bright hexagon shape or in the broad dark bands. This distribution strongly varies with

frequency.

According to the study shown in chapter 3 the six broad dark bands correspond to the limit of out of plane diffraction appearing as two broad dark bands in the experimental dispersion relation. The white dotted lines show the diffraction limit along one reciprocal space direction. As expected, the limit aproaches the center (normal incidence) as we increase the working frequency as it happens in the dispersion relation of 6.11a. The effect of the diffraction orders reentering the objective NA is also visible in the case of 6.11d. That limit has been again marked with a second dotted white line.

The thin dark lines correspond to the excitation of leaky modes of the system which can be easily related to the corresponding frequency in the dispersion relation and the appropriate direction. We have marked two points P_1 and P_2 as an example. Each of those points lie in the ΓM direction so they can be related with the corresponding point (k, ω) in the dispersion relation of Fig. 6.11a. Finally, notice that, in spite of the low refractive index contrast of the monolayer, the non-circular shape of the EFS for most of the leaky modes denotes a departure of their propagation direction from that of the homogenous medium behavior so that they could show anomalous refraction for some frequency and angle of incidence.

To illustrate this point we have plotted in Fig. 6.12 the EFS for the same sample in Fig. 6.11 measured at $\omega \sim 0.71$ and plotted together with two wavectors $k_{1,2}$ incident from air. As can be observed, for the k_2 case, the EFS shows a circular shape and then the propagation direction (red arrow) is parallel to k_2. Therefore, the propagation of that mode can be defined by means of a given effective refractive index in an homogenous medium. However, for k_1 the EFS in the PC to which we can couple is highly anisotropic and the propagating wavector inside the crystal for this particular angle differs from the propagation of the energy velocity [7].

6.3.3 High energy bands

So far we have presented an in depth study of the low-energy spectral region. Such range corresponds to frequencies where out of plane diffraction does not take place at normal incidence [8] which was shown to happen for $\omega < 1$ in a simple grating. Given that our set-up allows us to measure in the UV-VIS range we can use spheres having larger diameters to explore reduced frequencies in the high energy range.

Taking into account previous discussions, we obtain that for the experimental spectral range available (300-900 nm) spheres larger than $\phi = 750nm$ present their optical response in the high energy region. As it is well known from 3D PCs, for the high energy region the dispersion relation becomes more complicated due to the excitation of several Bragg diffraction orders together with the leaky modes of the system at those frequencies. An example of this complexity is shown in Fig. 6.13 where we have plotted the experimental dispersion relation for $\Phi = 1\mu m$ spheres deposited over a gold substrate and measured along the ΓK direction for the UV-VIS spectral range.

At variance to the well defined modes shown in Fig. 6.8 for the low energy region of the same system, the photonic bands presented in Fig. 6.13 show a very complex structure for both polarizations. The resonances are spectrally broader than in the low

[7] The energy velocity propagation (red allow) has been plotted outgoing as an example. The exact determination of the sense of that arrow would make it necessary an study on how the EFS evolve with frequency [153].

[8] This definition is taken from opal based PCs where the in-plane diffraction limit determines whether the system operates as a 1D PC or a real 3D periodic structure [154]

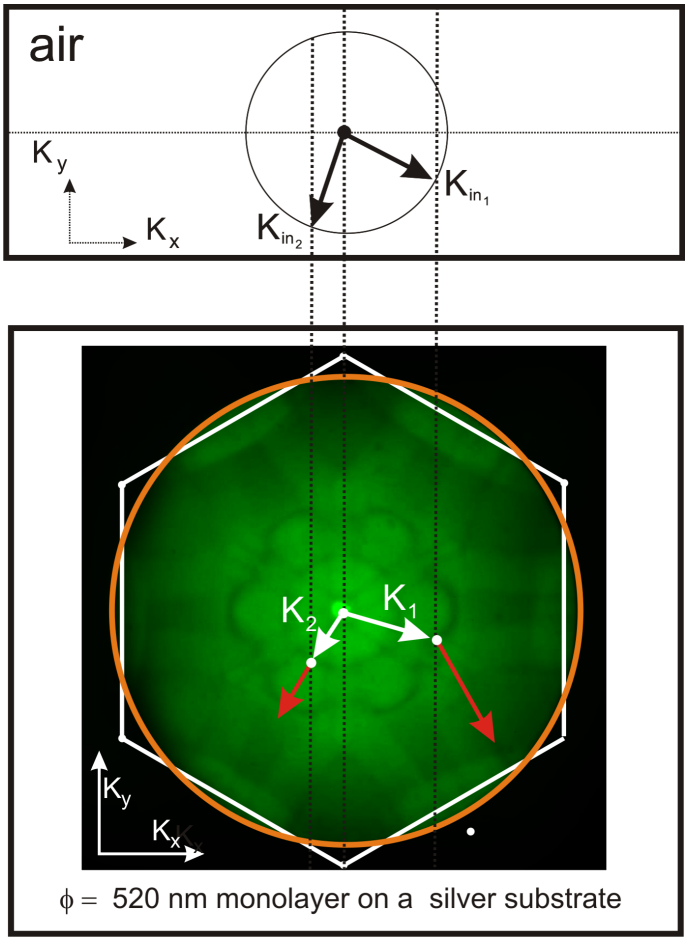


Figure 6.12: Experimental EFSs for in plane propagation after excitation of two different (k_1 and k_2) modes of a PS $\Phi = 520$ monolayer at $\omega = 0.71$. The hexagon shows the FBZ for this lattice while the orange circle shows the k_{max} measurable in our set-up at that frequency. Red lines indicates energy propagation direction at the corresponding points in the EFS.

energy region. This is probably a consequence of the fact that we are above the out-of plane diffraction limit which enhance losses (reduction of Q). Another probably reason is the tighter packing of bands in the high energy reason for any kind of PC. It produces too close bands to be measured as one broader resonance. Also the effects of disorder are expected to be larger as the probe wavelenght is smaller than the lattice parameter which increases the measurement sensitivity to structural imperfections.

If both polarizations are compared it is observed that the dispersion of the modes is quite different in both cases. For P polarization the interaction between modes at anti-crossings is barely noticeable showing the grid-like pattern characteristic of an almost vanishing refractive index contrast structure. For S polarization however a strong interaction is observed, specially at the frequency range between $\omega = 1.22$ and $\omega = 1.28$ and $k_{||} = 6.2$. In this case that region can be considered of low dispersion and then, low group velocities are expected.

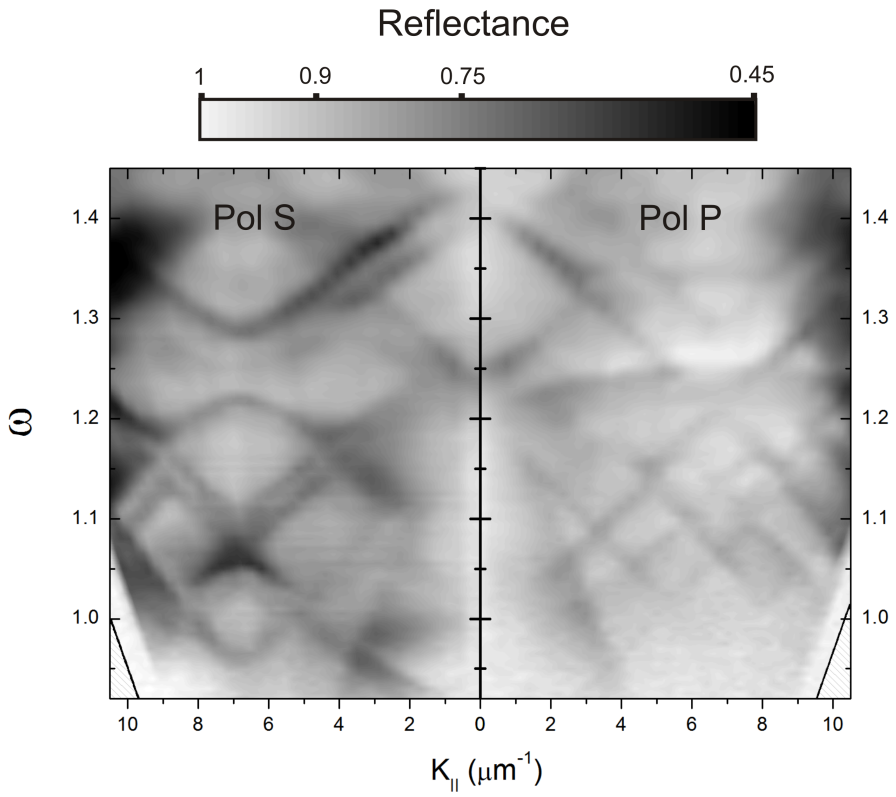


Figure 6.13: Dispersion relation for $\Phi = 1\mu m$ PS spheres deposited on gold substrate along the ΓK direction.

6.4 Conclusions

In this chapter we have presented angle and polarization resolved reflectivity measurements for close packed monolayers of spheres on both dielectric and metallic substrates. We have paid special attention to the metallic case and shown the large dependence of the excitation energy with the angle of incidence. It has also been shown too that different modes can be chosen varying the polarization for the same energy. Potential applications could be those were coupling to the structure needs to be engineered as a function of the angle as for example organic emitting devices (OLED) technology.

We have also compared the experimental dispersion relation with an empty lattice model in which we have taken into account modes propagating in an effective homogeneous dielectric material and also SPR modes. The good agreement has allowed us to relate them with the physical origin of the different modes of the system. It has been also demonstrated the feasibility of retrieving EFS in reflection configuration, which provides valuable information about light propagation within the sample. Finally we have obtained dispersion relations in the high energy range.

Part III

Emission and tuning of the optical properties: adding functionality to hybrid monolayers

Chapter 7

Strongly modified spontaneous emission in hybrid self-assembled photonic-plasmonic structures

In this chapter we present an in depth study of the emission properties of hybrid photonic-plasmonic systems consisting of monolayers of organic spheres deposited on substrates of different nature. By placing an organic molecule within the spheres we show experimental results on the enhancement of the emission as well as the angular and polarization distribution due to the local density of states (LDOS) modification introduced by the periodic structure. Several dielectric and metallic substrates are tested and their performance is studied taking into account the properties of the passive system studied in previous chapters.

7.1 Introduction

In the Introduction of this thesis we discussed how 3D and specially 2D photonic crystals (PC) could be key components in many types of light emitting devices since they allow both, enhancement of light-matter interaction [68] as well as extremely efficient light extraction [71]. We have also shown how the combination between plasmonic and photonic modes has recently provided an efficient way of enhancing and controlling light emission [57]. In particular, self-assembly based structures have been extensively used in the last decade to fabricate 2D hybrid metallo-dielectric structures suitable for emission control [82]. However, in most cases, the original bare structure of close-packed spheres is removed as it serves mainly as a mask for further processing [155]. On the contrary to these systems, some approaches have been proposed as structures that do not need further processing after the sphere monolayer is deposited [146]. These structures maintain the fabrication advantages explained in chapter 2 and allow the use of organic materials which have shown to work as appropriate emissive devices by means of structuration [156]. However, in the self-assembled bare resulting structures the low refractive index contrast represents an important handicap in emission control through local density of states (LDOS) modification [157]. In this chapter we have employed the hybrid monolayer previously studied to strongly modify the spontaneous emission from the as-grown structure employing dye doped spheres. The system consists of a distribution of organic molecules homogenously

distributed into the spheres. Therefore, we have obtained an strong modification of the spontaneous emission for those frequencies where the position of the molecules matches the a high LDOS modification due to a mode of the monolayer. An in-depth study of the emission properties of the 2D hybrid self-assembled PC is presented. It is shown that by controlling the LDOS we can effectively control the emission of the active medium placed inside the sample, specially concerning the angular and polarization characteristics. This way we have used the resonances of the metal-dielectric structure to modify the emission of an organic dye homogenously distributed within the spheres.

The chapter is structured as follows. First, the emission properties of the monolayer deposited on a dielectric substrate is experimentally studied for the case of glass and silicon substrates by using dye doped spheres as building blocks of the lattice. Next, we study the gold substrate structure for those frequencies where a resonance of the system is available. After that, we present the angle and polarization resolved emission spectra along the two highest symmetry directions. A comparison with the previously measured dispersion relation is presented and emission enhancement is found to take place for some of the modes available in the structure. Next, we have compared emission from samples fabricates with the two metallic substrates considered in this thesis: gold and silver. Finally, emission iso-frequency surfaces (IFS) are compared with their reflectance counterpart and the evolution with wavelength is discussed.

7.2 Dielectric substrate

In chapter 4 we demonstrated how for a monolayer of dielectric spheres no truly leaky modes are confined in the plane of periodicity if $n_{eff} < n_{sub}$ with n_{eff} and n_{sub} being the effective refractive index of the monolayer and the dielectric substrate, respectively. However, a little field enhancement was shown for the resonances of the system. As n_{sub} is increased the total intensity confined under the spheres grows because of the slot effect between sphere and substrate. We found the most representative case to be that of the silicon substrate ($n_s = 3.5$) as shown in the total field intensity profiles on chapter 4.

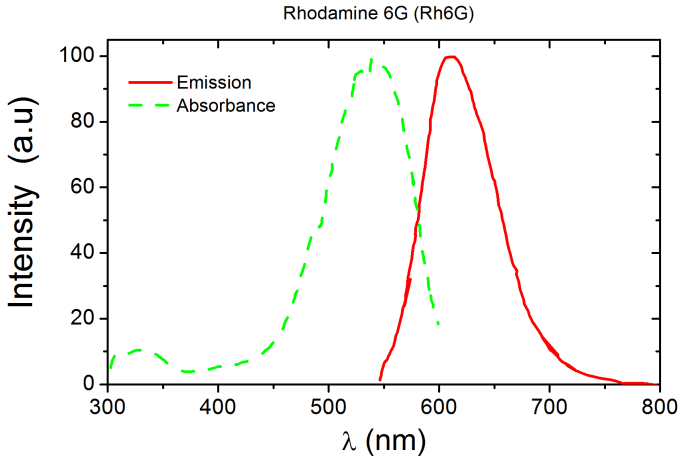


Figure 7.1: Normalized absorbance and emission spectra for Rodhamine 6G distributed within the polystyrene spheres used for the experiments.

Therefore, previous to study the metallic substrate case it is worth to briefly study emission by monolayers made from dye doped polystyrene (PS) spheres with a given

diameter (Φ) and deposited on glass and silicon substrates. The fabrication method was vertical deposition for silicon substrate while the wedge cell method (see chapter 2) was applied to obtain monolayers on glass. In the results presented below we have used $\Phi = 520nm$ spheres homogenously doped with Rodhamine 6g (Rh6G) whose tabulated absortion/emission spectra can be seen in Fig.7.1. It presents a broad emission with its maximum at $\lambda = 612nm$. We have chosen this molecule due to the compromise between the spectral stokes shift (difference between emission and absorbtion maxima) and emission efficiency which is known to be close to one [158].

High quality samples were obtained and reflection and emission measurements were carried out by means of the set-up described in chapter 3. As it was previously explained, the source used for optical pumping is a pulsed diode laser working at $\lambda = 485nm$ with a variable repetition rate although in this case we have used the continuous wave (CW) configuration. As can be observed when compared with Fig. 7.1, the pump wavelength does not match the maximum of absorbtion ($\lambda = 542nm$) for the Rh6G. The reason to use that wavelength is avoiding gold absorbance at $\lambda = 532nm$ as will be evident in the next sections of this chapter.

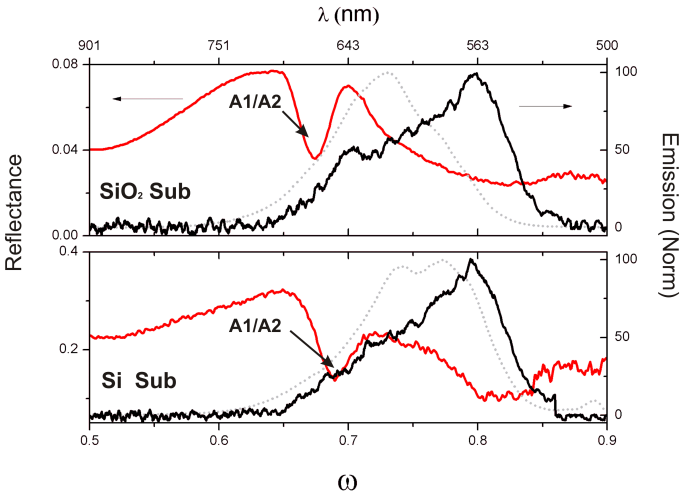


Figure 7.2: Reflectance (red line) and emission (black solid line) spectra for a close-packed monolayer of Rh6G doped PS spheres of $\Phi = 520nm$ deposited on glass and silicon. Grey dashed line shows emission of a disordered monolayer of Rh6G doped $\Phi = 160nm$ PS spheres deposited on each substrate in a disordered way.

We have first studied the effect of a structured environment on this emitter. Fig. 7.2 shows reflectance and emission collected for some of the samples described above. In this case we present measurements for a monolayer of Rh6G doped PS spheres of $\Phi = 520nm$ deposited on glass (top) and silicon (bottom) with $n_{sub} \sim 1.45$ and $n_{sub} \sim 3.5$ respectively. Reflectance spectra were collected the same way as those shown in previous chapters (see chapter 5). As a reference for emission in this case we have used dye doped spheres with a much smaller diameter ($\Phi = 160nm$) droped on each substrate. Therefore, no effects due to the periodicity are expected. Besides, given that $\lambda_{emiss} >> \Phi$, no Mie resonances due to the spherical shapes are expected to play an important role. The differences in the emission spectra for silicon and glass substrate are probably due to the modifications on the DOS for an emitter close to an interface as shown in this thesis introduction [73]. The grey dotted lines of Fig. 7.2 shown that, when compared with the commercial data shown in Fig. 7.1, the larger change on the shape of the emission spectrum is obtained

for silicon as it presents a much larger refractive index contrast with the environment of the dye molecules (PS) than the glass substrate.

If one takes a look at the emission of the monolayer of spheres with $\Phi = 520nm$ deposited on both substrates, the spectral shape differences shown for the reference vanish and both black lines in Fig. 7.2 show an almost identical shape. It is interesting to compare the emission spectra with the reflectance measured at the same point of the sample. As it can be observed, the reflectance spectra do not show any resonance beside the dip corresponding to unconfined resonances (A1 and A2) due to the substrate ($n_{sub} > n_{eff}$) as already explained in chapter 4 (see Fig. 4.4). Because of substrate leakage no emission enhancement is found at that point as expected from the total field intensity distributions for that modes (see chapter 4).

Regardless of enhancement at those frequencies of the resonances, the emission shown in Fig. 7.2 present the Rh6G spectrum modulated according with the optical response of the monolayers as can be depicted from comparison with the reflectance spectrums in the same figure. It has to be mentioned that the total intensity for the same pumping conditions was shown to be larger in case of silicon substrate, as expected from the larger refractive index of this material compared to glass.

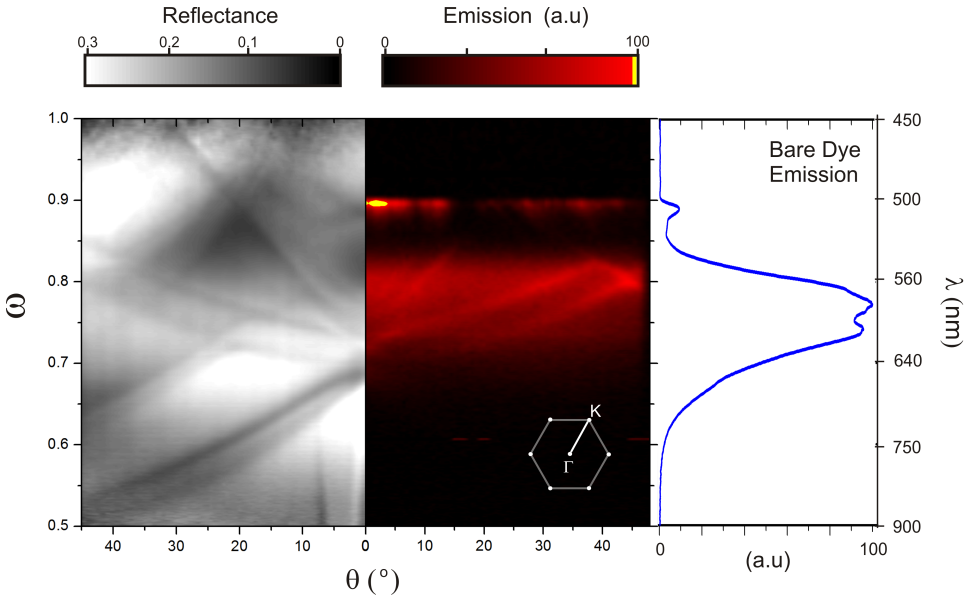


Figure 7.3: Angle resolved reflection (left) and emission (middle panel) measurements for a close-packed monolayer of Rh6G doped PS spheres of $\Phi = 520nm$ deposited on silicon and measured in the ΓK direction. The plot at the right shows normal incidence emission for Rh6G doped $\Phi = 160nm$ PS spheres deposited on silicon and in a disordered structure.

Let's consider next the angular emission for the monolayer of spheres here presented. As explained in the introduction of this thesis, emission generated within a waveguiding can be either be emitted directly to the outside medium or propagated as a guided mode. By using an appropriate lattice it is possible to obtain coupling between radiative and leaky modes so the total intensity emitted by the structure can be largely enhanced. It has effects in the total intensity outside the structure but also in the emission angular pattern. The experimental measurements in Fig 7.3 show the angular reflectance map for $\Phi = 520nm$ PS-Rh6G spheres over silicon substrate and the angular evolution of its emission. It is known from previous chapters that the two main features measurable in

this structure by reflectance are the onset of diffraction depending on the periodicity of the scanning direction (which is shown as a dark broad band in reflectance map of 7.3) and the semiradiative modes which are the result of system resonances (A1 and A2) shown as weak dips in reflectance/transmitance.

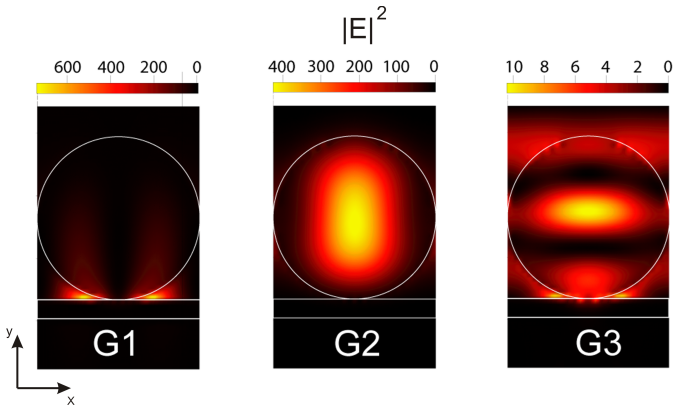
As we showed before for normal incidence (Fig. 7.2), the angle resolved emission measurements in Fig 7.3 show a small enhancement for the spectral positions of A1 and A2 at their dispersion relation positions. Although the enhancement is very weak, it can still be observed that the maximums of emission are channeled by the dispersion of the resonances shown as reflectance dips for A1 and A2. As was explained for normal direction emission, the enhancement at specicfic frequencies is due to the small but still present field confinement due to the slot-waveguide effect under the spheres that was shown to take place for a monolayer on a dielectric substrate in chapter 4. However, the angular pattern is determined by the dispersion relation of each mode which brought above the cone of light by the lattice periodicity as demonstrated in chapter 6.

Finally, from the study of chapter 4 it is known that for A1 and A2 most of the field is concentrated below and not within the PS spheres. It is translated onto the emission properties as a very low enhancement at the PC resonances of the monolayer. Other approaches as for example placing the emitter on top of the substrate, just under the spheres [146] have been tested but the emission enhancements obtained are not larger than the ones shown here for the emitter-inside the spheres system.

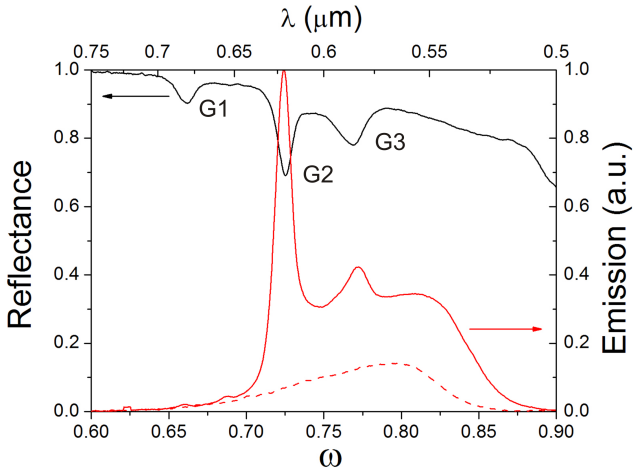
7.3 Metallic substrate

In the previous section it has been shown that an emitter placed within organic spheres forming a monolayer over a dielectric substrate does not experience a noticeable change in its spontaneous emission. However, we have already seen both theoretically and experimentally in previous chapters that the introduction of a metallic film under the spheres strongly modifies the optical response of the system, specially concerning its ability to confine light. To study the effect of a metallic substrate on the spontaneous emission of internal sources, the Rh6G doped PS spheres of $\Phi = 520nm$ were deposited over a 60 nm thick gold film. The structure is the same one already studied in previous chapters although in this case, absorbance of the dye molecule has to be taken into account when considering the optical response of the sample. Fig. 7.4a shows the calculated field intensity profiles for this system. Fig. 7.4b shows the unpolarized emission spectra at normal incidence for a sample grown on a gold substrate and on a silicon substrate, together with a reflectance spectrum for the gold substrate sample.

At variance with the dielectric substrate case, for the sample grown on the gold substrate, a large enhancement of the emission takes place for the mode located at $\omega = 0.72$. It can be observed that the spectral position matches that of the dips in reflectance which was termed G2 in the study of chapter 4. As G2 is a WG-like resonance the electric field is mainly confined within the spheres, where the emitter is homogeneously distributed. A factor 20 enhancement in emission is observed for this mode when compared with that of the reference sample grown on silicon. This agrees with the large enhancement in the total field intensity within the spheres for the gold case when compared to the silicon substrate structure. Emission is also enhanced over the background for the mode at $\omega = 0.77$, though much less than for the G2 case. This is in agreement with the fact that this resonance corresponds to the SPP-like mode that we named G3 in previous chapters. In general G3 presents most of the field intensity distributed below the spheres (Fig. 4.11).



(a)



(b)

Figure 7.4: (a) Total field intensity profiles for G1 to G3 resonances for $\Phi = 520nm$ PS spheres deposited on a 55 nm thick gold film (b)Reflectance and emission spectra for $\Phi = 520nm$ dye doped spheres deposited on a 60 nm thick gold substrate. Dotted line shows emission for the same structure on silicon.

However, if the spectral position of G3 is close to the gold absorbance [1] the field intensity profile dramatically change showing most of the field intensity within the spheres [2] (see Fig. 4.14 in chapter 4).

Although one would expect a larger enhancement associated with the G2 mode (notice in Fig. 7.4a that the total electric field at the sphere center is 40 times that of G3), it should be noted that the WG-like mode lies at the emission tail while the hybrid one lies at its spectral maximum. Of course, extrinsic and intrinsic losses (see chapter 5) will influence the performance of each mode.

A barely noticeable enhancement in emission is observed for those frequencies corresponding to the G1 SPP-like mode. The reason for this is twofold: on the one hand, the spatial overlap between the electric field and the dye molecules is at a minimum and, on

[1] Which is just the spectral region we have tuned the optical response of the monolayer to by choosing spheres with $\Phi = 520nm$.

[2] Although total field intensity is lower in this spectral range for gold due to ohmic losses through absorbtion

the other hand, frequencies corresponding to this mode lie far into the low-energy tail of the dye's emission. In fact, if emitters were distributed near the gold film, a stronger enhancement would be expected for the SPP-like modes. Finally it has to be noticed that, regardless of the mode resonances, the emission of the monolayer grown on the metal presents an overall enhancement when compared with the silicon one. This is due to two factors. On the one hand, placing a reflector under an emitter in a matrix reduces losses at every frequency given that no radiation can be emitted in that direction. On the other hand, the extraction of radiation can be strongly enhanced for an emitter placed at the appropriate distance from a metallic surface [159]. The combination of these two factors may provide that total enhancement as well as the slight spectral shift of the emission of the gold substrate structure when compared to the silicon one.

Once we have confirmed the emission enhancement associated with the confined modes of the structure we perform an angular characterization of the emission. In chapter 6 we obtained the dispersion relation for the two polarizations (s and p) along the highest symmetry directions in the reciprocal space: ΓK and ΓM. Such modes appeared as dips in reflectance. Now, we have performed photoluminiscence measurements with the set-up in the same configuration for the four possible combinations of polarization direction but pumping the sample continuously with a diode laser in critical illumination. The experimental conditions are the same as for the normal incidence case shown in the previous section. As the dye withing the spheres provides a broad band emission of $\Delta\lambda \sim 150nm$ these measurements will map the corresponding photonic bands for that spectral range, with an efficiency given by the spatial overlap between emitter and total field intensity.

Fig. 7.5 shows the dispersion relation for the same sample grown on gold for which normal incidence measurements were previously presented. Results along the ΓK direction in reciprocal space are presented, although similar results were also obtained along the ΓM direction. It can be observed how emission is channeled only by certain modes, as happened for normal incidence. This fact provides both directionality and polarization selectivity of the dye's emission. For p-polarized light, one can observe how most of the dye's emission couples to two modes originating from the WG-like mode G2 in normal incidence. For s-polarized light, emission couples mainly to two modes originating from the G2 and G3 modes, respectively, although with different efficiency. As we mentioned above, these two modes have WG-like (G2) and hybrid (G3) nature. No emission couples to the plasmon-like modes observed at normal incidence since, as we increase the angle, the energy of these modes decreases (see Fig. 7.5) and hence we move away from the dye's emission spectral range. As for normal incidence, for each pair (κ, ω) where a mode of the system is available a large enhancement of the emission takes place when compared with the non confined resonances of the silicon substrate case (see Fig. 7.3)

However, the combination of a monolayer of spheres and a metallic substrate is not only advantageous from the point of view of enhanced spontaneous emission or polarization selectivity, as we have just seen. Directionality is also a consequence of the channeling of emission through the modes of the sample. This becomes more evident if one plots emission in polar coordinates for a given frequency, as shown in Fig. 7.6. For the case of the reference sample grown on a silicon wafer (grey line), we observe a constant angular profile with hardly any noticeable peaks related to the low enhancement we explained above (section 7.2). Introducing the gold substrate produces the previously shown enhanced emission background for those frequencies where no modes are available and a directional enhancement where emission may couple to a mode. For the chosen reciprocal space direction (ΓM) and reduced frequency ($\omega = 0.8$), emission takes place in a reduced angular

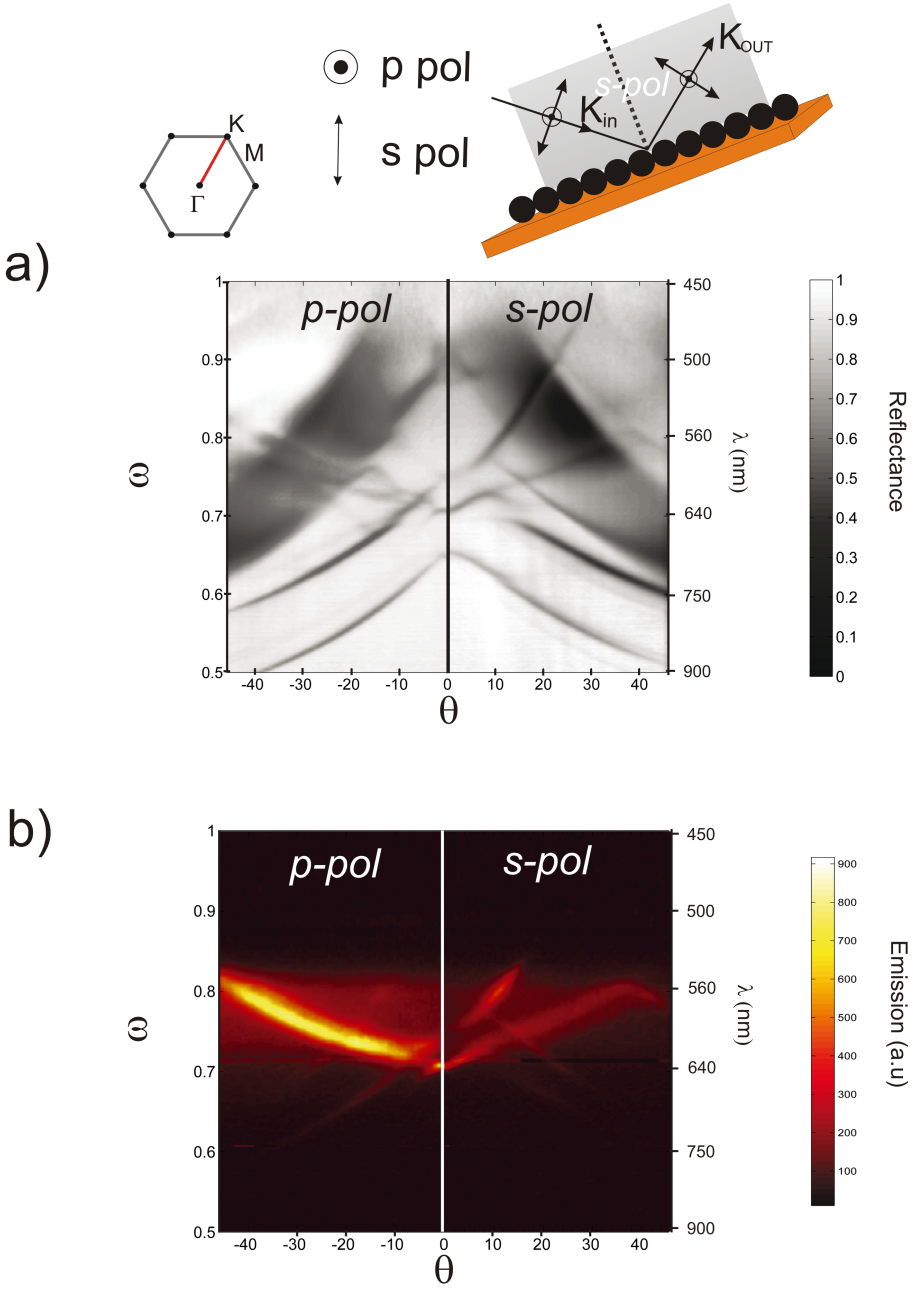


Figure 7.5: (a) Angle-resolved reflectance measurements for a PS spheres monolayer with $\Phi = 520nm$ measured along the ΓK direction for both p (left) and s polarization (right panel). b) Angle resolved emission under identical conditions as the reflectance ones.

range close to the sample normal but, since a wide range of tunability is possible through the periodicity of the dielectric lattice, directionality can be tailored for a given frequency by adjusting the sphere diameter relative to the emission wavelength.

7.4 Comparison beteween silver and gold substrates

In previous chapters we shown both experimentally and theoretically that the optical properties of the metallic substrate may heavily influence the performance of the system. In

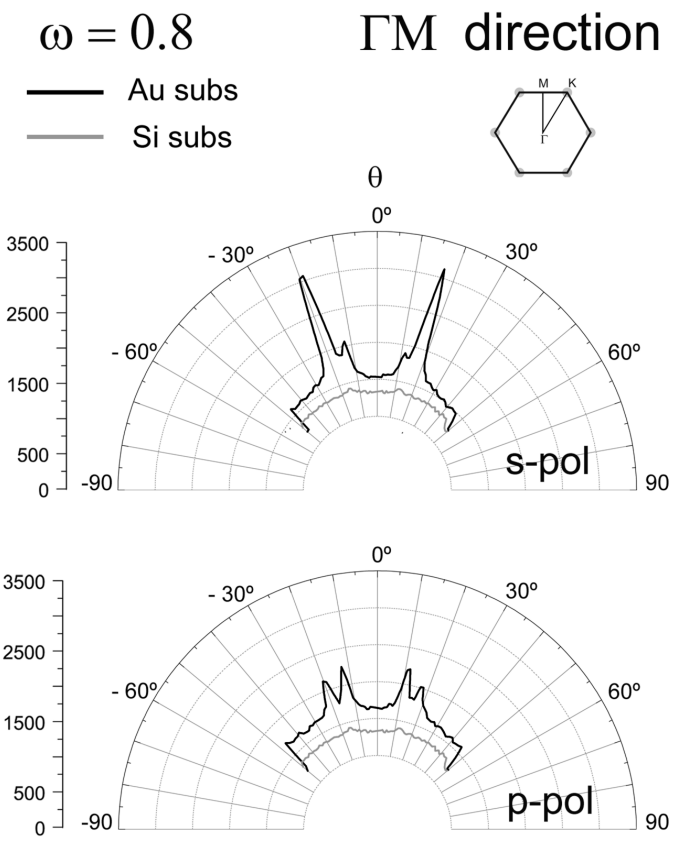


Figure 7.6: Emission plotted in polar coordinates for a monolayer of PS $\Phi = 520nm$ spheres deposited on silicon (grey line) and gold (black line) for a reduced frequency $\omega = 0.8$.

chapter 5 it was determined that when the working frequency is close to the strong absorbtion spectral range of the metal, confinement can be strongly reduced due to absorbtion during mode propagation.Then, it is worth studying how such effects on the resonances affect the emission enhancement in this kind of structures.

So far we have studied emission in samples deposited on gold substrates, although, we have shown along this thesis that silver can perform even better at visible (VIS) wavelengths due to the spectral position of its absorbtion band ($\sim 420nm$) compared to that of gold ($\sim 550nm$)[136]. In Fig. 6.8 of chapter 6 we saw how the dispersion relation for both systems were basically the same if the optical response was tuned to the VIS region by choosing $\Phi = 520nm$ PS spheres. However, the total field intensity was shown to decrease for G3 and higher energy modes due to the absorbtion of gold.

These differences are shown in Fig. 7.7 where angle and polarization resolved emission measurements are shown for samples made of $\Phi = 520nm$ dye doped PS spheres and grown on silver and gold substrates. The pump conditions are the same in both cases (CW diode laser at $\lambda = 485nm$) as well as the probed reciprocal space direction ($\Gamma KFlarger$). As can be observed, the two figures present the same emission pattern as expected from the dispersion relation shown in Fig. 6.8 of chapter 6 for both materials. However, the silver case presents a more intense emission which results in a more defined pattern for all frequencies. This is in agrement with the absortion effects mentioned above which

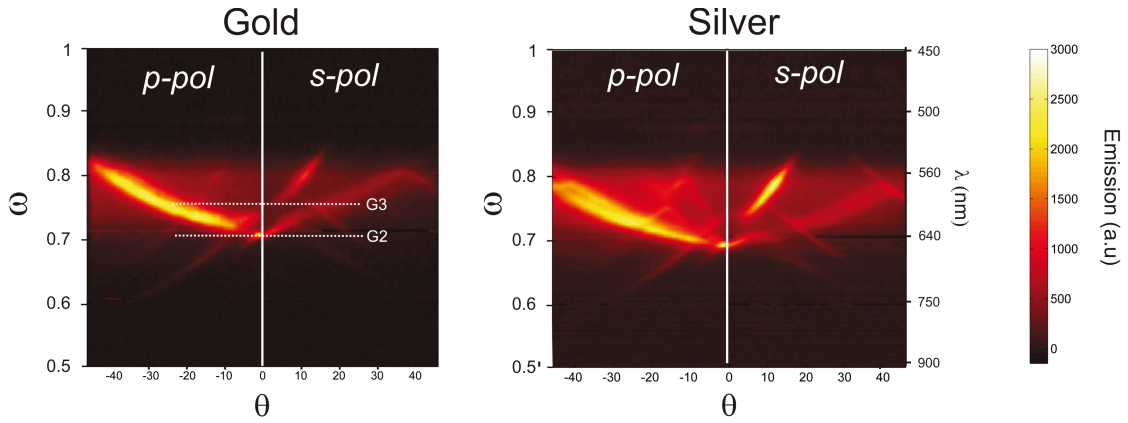


Figure 7.7: Angle resolved emission plots scanned along ΓK direction of a monolayer of dye doped $\Phi = 520nm$ PS spheres deposited over gold (left) and silver (right).

are negligible for the case of silver allowing a more efficient emission. In fact, this effect is specially evident for the evolution of the G3 mode. As its dispersion relation moves into the higher energy region of the emission spectrum it is more affected by the gold absorbtion that increases at higher energies.

7.5 Study of equifrequency surfaces in emission

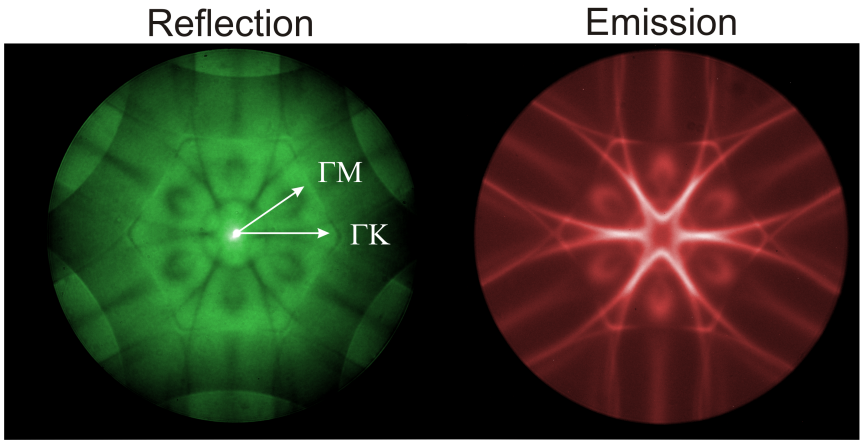


Figure 7.8: Equifrequency surfaces measured in reflection (left) and emission (right) configuration at $\omega \sim 0.73$ ($\lambda = 633nm$) for a monolayer of dye dopped $\Phi = 520nm$ PS spheres on a silver film.

As we did for the reflectance measurements in chapter 6, we can use the same set-up described in chapter 3 to collect equifrequency surfaces (EFS) at single wavelengths within the cone defined by the numerical aperture (NA) of the microscope objective. We already showed in previous chapters how dark bands in the far field reflectance from a monolayer can be associated with either out of plane diffraction or the excitation of leaky modes of the structure which can be retrieved from experimental photonic bands (see Fig.6.11). Hence one can compare reflectance and emission EFSs collected at the same sample region in order to evaluate which are the "active" modes concerning emission.

As can be observed in Fig. 7.8 maximum of emission takes place at those points

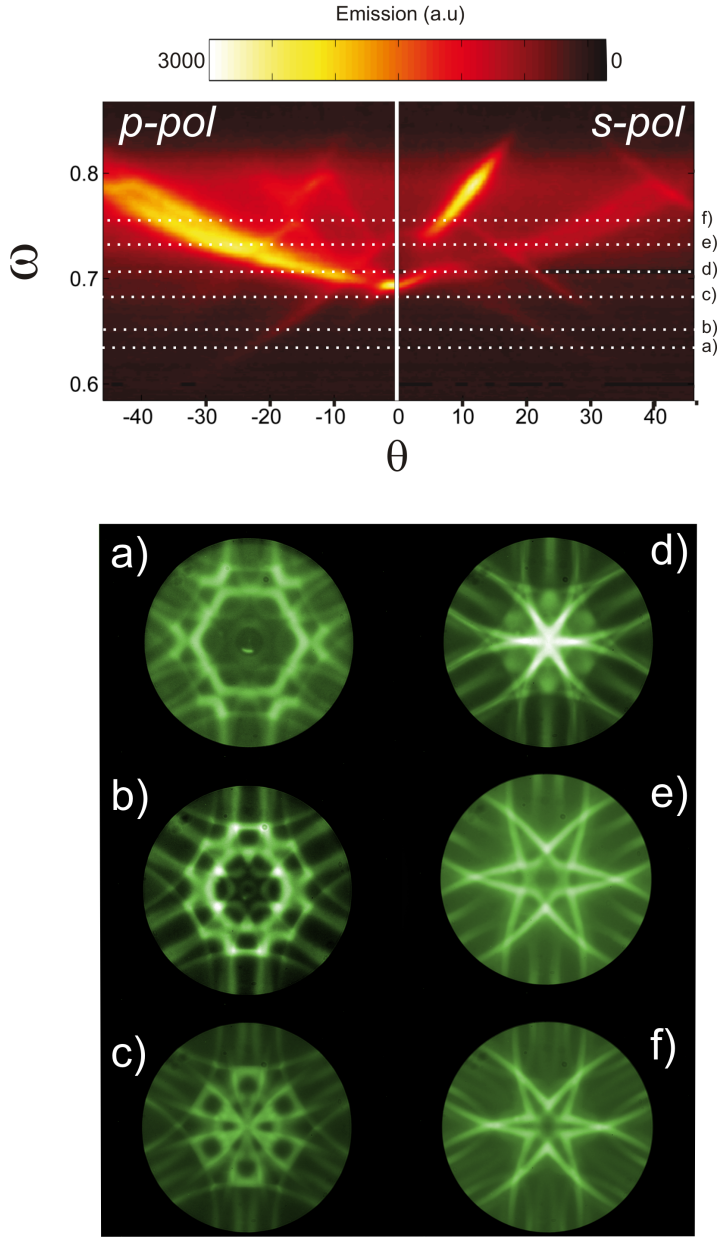


Figure 7.9: a) to f): EFSs in emission for a monolayer of dye doped $\Phi = 520n$ PS spheres grown on a silver substrate for $\omega = 0.64$, $\omega = 0.66$, $\omega = 0.69$, $\omega = 0.71$, $\omega = 0.73$ and $\omega = 0.75$. These energies are shown as dotted lines in the contour plot of emission for the ΓK direction at both polarizations. EFS images are not polarization discriminated.

where a resonance of the system (dips in reflectance) is available in agreement with the previous study in Fig 7.7 for the silver substrate and the ΓK direction. It has to be noticed that the maximum of emission for the chosen frequency takes place at $\sim 10^o$ for the ΓK direction while for ΓM the maximum of emission takes place at $\sim 5^o$ and always showing the six-fold symmetry of the lattice. From the study of the angular response in chapter 6 we can associate the given angle and reciprocal space direction with the WG-like mode G2 which is in agreement with the position of the emitter within the spheres and the regions of the sample where the field enhancement is taking place. For what

concerns the effect of out-of-plane diffraction on the emission measurements we confirm in Fig 7.9 that it is not noticeable for the modes of the system. This agrees with the angle resolved measurements of Fig. 7.5 where reflectance shows the onset of diffraction (dark broad band) while emission is unperturbed by this effect. This is due to the fact that the emission enhancement will be dependent on the Q factor of each mode as previously demonstrated and this emission will be channeled away from the sample mainly through the angular distribution of each mode.

If one performs the same measurement at different frequencies it is obtained a set of EFSs that map the emission of the sample in every direction an polarization for the whole dispersion relation of the PC [3]. Fig. 7.9 shows a set of images for frequencies $\omega = 0.64$, $\omega = 0.66$, $\omega = 0.69$, $\omega = 0.71$, $\omega = 0.73$ and $\omega = 0.75$ taken for the same sample of Fig. 7.8. The evolution of the emission pattern due to light confinement is obtained [4].

As in the reflectance case, it has to be mentioned that due to the low refractive index contrast no discontinuities are observed in the EFSs for any frequency [151] as it would happen in case of an structure showing a photonic gap (large refractive index contrast). This result agrees with the absence of gaps in the photonic bands measured in chapter 6 for this structure. Nevertheless, the refractive index contrast in the samples is high enough to obtain EFSs which depart from the circular shape for those modes in the vanishingly small refractive index contrast approximation studied in section 6.3.2 of chapter 6. This evidences (as we demonstrated for reflectance in chapter 6) that emission will experience anomalous refraction for some propagation directions contained in the plane of periodicity.

7.6 Conclusions

We have shown that monolayers of dielectric spheres deposited on metallic substrates can strongly modify the emission of organic dyes contained within the spheres through coupling to the hybrid modes of the structure. Emission enhancement due to strong field confinement inside the spheres has been demonstrated together with its polarization dependence. We have also shown through field intensity profiles calculations that the modes providing larger emission enhancements are those presenting a stronger field confinement at the position of the emitters in the structure. Evidence for the directionality of the emission has been also presented. Finally, the study of the iso-frequency surfaces in emission has provided us with a full characterization on the angular pattern of emission. Therefore, the here studied properties are suitable for those applications where control over emission needs to be achieved using organic materials as, for instance, organic light emission devices (OLED) technology.

As future work, other emitter positions could be explored for the same structures in order to use other modes of the system. In particular it could be interesting to place a single emitter in a very controlled position within or at the bottom of the spheres in order to obtain a quantitative measurement of the effect of the LDOS on the emission of the light sources.

[3] It is the same association between photonic bands and different EFSs that was shown for reflectance in Fig. 6.11

[4] The broad emission lines are due to the use of a spectrally wider filter in front of the CCD. In this case we have used the tunable $\Delta\lambda = 20nm$ filter while the one used for the images in Fig. 7.8 is a notch filter with a bandwidth below 5 nm

Chapter 8

Tuning the optical properties of a monolayer of spheres

We present here an in-depth study on the tuning of the optical response of monolayers of dielectric spheres deposited over metallic substrates when their filling fraction is accurately modify. This is achieved by plasma etching to reduce the diameter of organic spheres while the lattice parameter is maintained. We show in this chapter that it is possible to change the spectral position of the optical resonances for this structure as well as their light confinement properties. Finally, by using dye doped spheres, we experimentally demonstrate that changes in the filling fraction can also provide us with an efficient method to control the emission properties of this kind of structures.

8.1 Introduction

So far we have demonstrated in this thesis that self-assembled two dimensional (2D) photonic crystals (PCs) deposited over metallic films can provide a good optical performance in terms of its ability for light confinement. However, the functionality of these systems can certainly be enhanced if one can change their the optical response under an external stimulus, turning them into tunable devices. Tuning of the optical properties is a challenging task in both PCs and plasmonics systems. For the latter some possible strategies are optical [160], electrical [161], magnetic [162][163] or acoustic [164] modifications of the plasmonic modes. Alternatively, for the case of PCs one can modify the refractive index or lattice constant of (in our case) the periodic organic lattice to tailor the photonic dispersion and hence the optical response of the system [21] [157]. Certain stimuli could even be employed to simultaneously tune both types of modes and the hybrid modes arising from them.

In this chapter we present an in-depth study of the changes in the optical response of self-assembled monolayers of polymeric spheres deposited on metallic films introduced by tuning the filling fraction (*ff*) following the process previously described in section 2.3 of chapter 2. As already described in that section, the tuning of their optical response is achieved by homogeneously reducing each sphere while keeping the lattice parameter constant, i.e. by changing the filling fraction of the hexagonal lattice as studied previously for similar systems on dielectric substrates [165]. This technique has been used by several authors in the past for example to improve the coupling in 3D opal-based PCs to slow modes [166] or to introduce planar defects in such systems [167].

In our study, we use polystyrene (PS) spheres of two different diameters ($\Phi = 0.52$ and $\Phi = 1\mu m$) forming a close-packed monolayer over a gold substrate for which the two kinds of modes investigated in previous chapters, that is, waveguide-like (WG-like) and plasmon-like (SPP-like), fall in the visible-near infrared (VIS-NIR) spectral region. We demonstrate for both cases that the two kind of modes can be spectrally shifted by reducing the spheres in a controlled manner. A theoretical study of their field intensity profiles is also provided. We show that not just the spectral position of the modes but the emission enhancement associated with the system modes and discussed in chapter 7 can be efficiently tuned by this method.

The chapter is structured as follows: first we present the evolution of the experimental and theoretical reflectance spectra for PS monolayers with $\Phi = 1\mu m$ spheres as their *ff* is reduced up to 30 %. Next, the total field intensity is calculated for each resonance at every reduction step and the changes in the nature of each mode is discussed. After that, we characterize the changes introduced by the tuning process in the optical properties of dye doped PS spheres with $\Phi = 0.52 \quad \mu m$ on gold substrates for the VIS range. Finally, measurements of the emission of these samples at each etching step are presented showing an enhancement at the modes spectral position for each reduction step as we previously demonstrated for the close-packed structure in previous chapters (see chapter 7).

8.2 Effect of filling fraction modification in the optical response of a monolayer of spheres on a metal substrate

Recalling the study we performed in chapter 2 about the homogeneous diameter reduction of PS spheres in a close-packed lattice on gold we can now focus on the changes of the optical response for those systems during the tuning process. In order to track the evolution of the optical response, normal incidence reflectance spectra were collected for a monolayer of $\Phi = 1\mu m$ spheres from the close-packed lattice scenario until a 100 nm diameter reduction ($\gamma = 0.9$)[1].

Figure 8.1 shows both experimental [2] and simulated normal incidence reflectance for three different sphere diameters. As explained before, this kind of system supports hybrid modes which can be divided in SPP-like and WG-like depending on whether the total field intensity is distributed mainly below the spheres (SPP-like) or within them (WG-like). The five dips shown in the reflectance spectra correspond to the modes of the sample. The coupling efficiency as well as the field spatial profile are dependent on the nature of each mode. For this study we will consider the first three modes (G1 to G3), representative of the two types of modes sustained by these systems, although the same behavior is obtained for the other two modes available (G4 and G5). A good agreement between simulations and experimental data is found. However, some differences in spectral width and peak position are observed, most likely due to residual disorder introduced during the growth process. Polydispersity of the spheres can also be a source of disorder, though in our case its effect should not be significant due to the low values for the spheres used (less than 3 % according to the manufacturer)

[1] In chapter 2 we defined $\gamma = \Phi/\Phi_o$ where Φ_o is the original sphere's diameter and Φ the one at the end of the reduction process. Then, the filling fraction is related with this parameter through $ff = \gamma^3 \frac{\pi}{3\sqrt{3}}$

[2] For close-packed $\Phi = 1\mu m$ spheres the optical range of interest falls in the near infrared region (NIR). For such range the microscope set-up shown in chapter 3 does not work properly and other techniques must be used. In this case measurements were performed with a microscope coupled to a Bruker FTIR in normal incidence and a maximum angular aperture of $\sim 5^0$

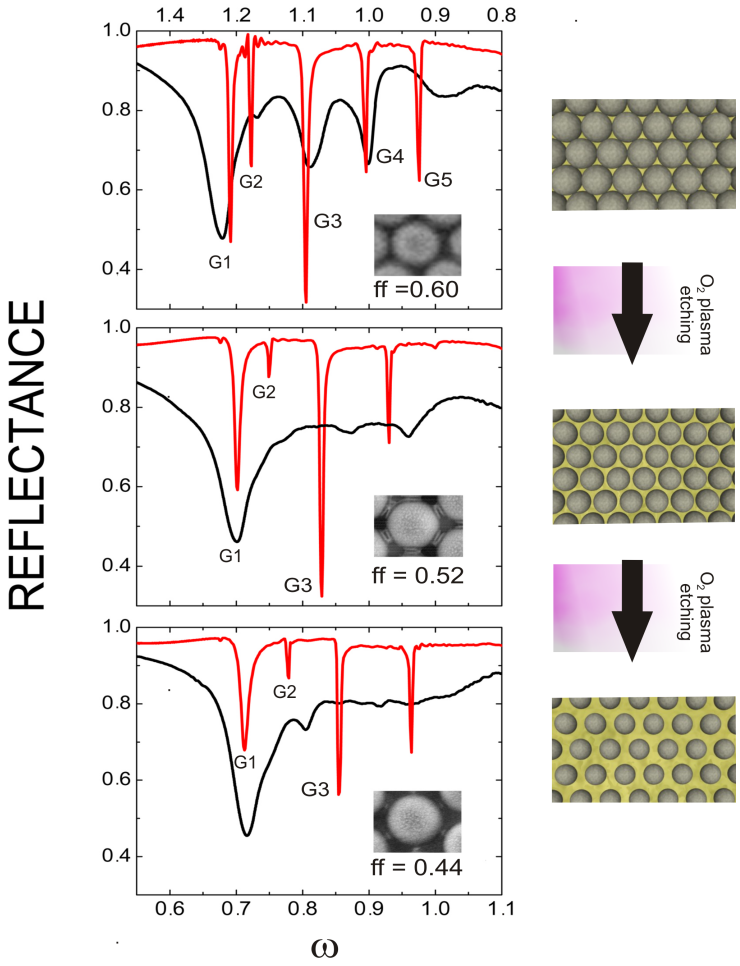


Figure 8.1: Normal incidence reflectance spectra for three different *ff*s. Top to bottom: $ff = 0.6$, $ff = 0.52$, and $ff = 0.44$, corresponding to $\gamma = 1.0$, $\gamma = 0.95$ and $\gamma = 0.9$ respectively. Experimental (black) and theoretical spectra (red) are presented.

In chapter 4 we investigated the nature of each mode by means of finite difference time domain (FDTD) calculations of the total field intensity profile for each of the resonances of the system. Therefore, in this case we can perform the same study in order to observe how the light confinement changes as the filling fraction of the lattice is reduced. Fig. 8.2 shows the intensity profiles corresponding to modes G1, G2 and G3 (each column shows the same mode) for $\Phi = 1\mu m$ PS spheres deposited over gold film. The plotted filling fractions are ff=0.6 [3] (upper row), ff=0.52 (middle) and ff=0.44 (bottom). These values correspond to the spectra shown in Fig. 8.1. As explained before the structure is illuminated at normal incidence at those frequencies matching the G1, G2 and G3 modes. For the maximum filling fraction ($\gamma = 1$ or $ff = 0.6$), G1 and G3 present the already studied SPP-like character while G2 shows WG-like nature. If we examine the total field

[3]The first case corresponds to the close-packed spheres lattice and hence matches the profiles shown in Fig. 4.11 of chapter 4

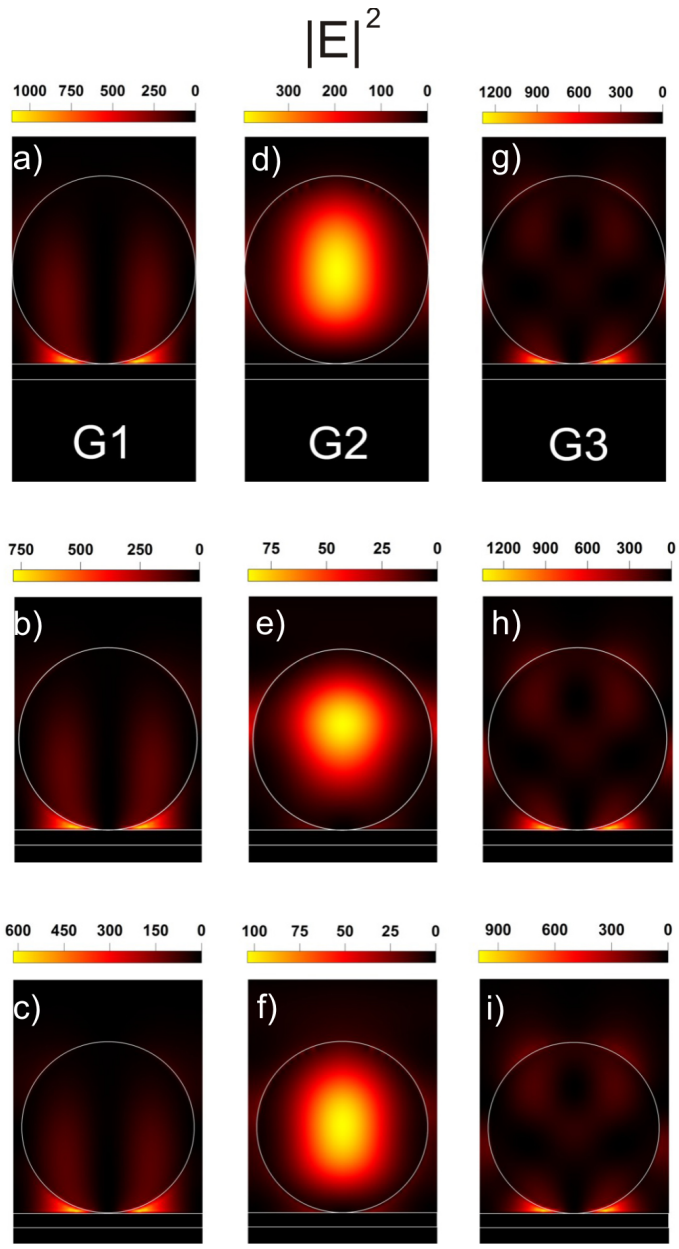


Figure 8.2: Total field intensity distribution and its evolution with sphere resizing for the first three modes of the spectra shown in Fig. 8.1: G1 (left column), G2 (middle column) and G3 (right column). Corresponding filling fractions are $ff = 0.6$ (upper row), $ff = 0.52$ (middle) and $ff = 0.44$ (bottom).

intensity distribution of the different modes as the filling fraction is reduced we can see that the WG and SP characters of the modes remain unchanged and only a slight decrease in the total field intensity is observed.

So far we have considered just three single sphere diameters. However, the tuning procedure can be carried out in a quasi continuous manner allowing a fine degree of control of the sample topology and hence of its optical response. To show this, reflectance

spectra were recorded after each 30 seconds etching step over a 12.5 minute period [4]. As a result, $\Phi = 1\mu m$ spheres were reduced by as much as 100 nm in diameter ($0.44 < ff < 0.60$). Theoretical spectra like those in Fig. 8.1 were calculated for each diameter. For the experimental case, an initial diameter of $\Phi = 1020nm$ was required in order to match the theoretical spectra, probably a consequence of the 3 % polydispersity of the spheres. Nevertheless, the filling fraction reduction was comparable in both cases. The two reflectance maps obtained for simulations and experiments are plotted in Fig. 8.3 .

Fig. 8.3a shows how as the filling fraction of the sample is reduced, the optical response undergoes two major changes. There is an overall blue-shift of the modes attributed, as already discussed, to a decrease in the effective refractive index of the dielectric part of the system. Also there is a change in the intensity of the dips in the reflectance spectra. While those modes that have a marked SPP-like character (G1, G3) hardly change, those with a WG-like character (G2, G4) present strong variations in intensity. This indicates that for the latter, as we reduce the sphere diameter, the spatial distribution of the field undergoes strong changes in the mode profiles of Fig. 8.2. A clear example is the case of G2, where for $\gamma = 0.94$ the associated dip all but vanishes and then recovers upon further reduction. Accompanying this result is the increase of *ca.* an order of magnitude in the field intensity inside the spheres (see Fig. 8.2). Special attention has to be paid to the G5 resonance. In Fig. 4.11 of chapter 4 we demonstrated, by inspecting total field intensity profile of this resonance, that it presents a SPP-like character. However, in Fig. 8.3a it can be observed that it is the only one which completely vanishes for $ff < 0.55$. This behavior is probably related with two phenomena. On the one hand its high energy spectral position which makes it more sensitive to radiative losses. On the other hand, in spite of the SPP-like character, some field intensity remains distributed within the spheres. Hence it is expected that this mode will be heavily affected by the spheres reduction.

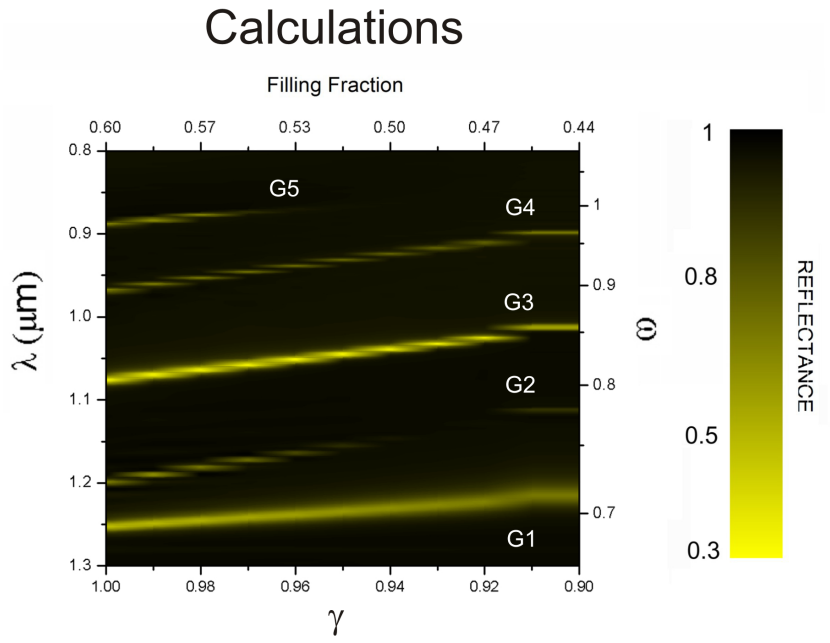
When measurements are compared with calculations a good agreement is found. Modes G1, G3 and G4 present an identical linear blue-shift with *ff* reduction in both cases. Some differences are observed regarding the mode spectral positions for *ff* below 0.5. This is due to the fact that the plasma reduction rate becomes slightly higher as the spheres diameter is reduced as we demonstrated in the calibration for the spheres reduction process shown in chapter 2. For the close-packed structure, G2 can not be appreciated due to the proximity of G1 which presents a spectrally broad and intense dip, hiding the real value for reflectance at $\gamma = 0.71$. However, after reduction G1 and G2 become spectrally separated allowing G2 to be clearly visible. This effect can be seen, for instance, in Fig. 8.3b for $ff = 0.47$ ($\gamma = 0.92$).

As a final comment on mode evolution, it has to be stressed that the linear blue-shit (see Fig. 8.3a) of the modes with reduction can be useful from the point of view of tuning different systems fabricated from the same initial spheres. Once the ratio has been estimated for one sample we can use optical characterization as a means to control the sphere diameter of the rest without employing SEM inspection [108], thereby making the process of tuning the optical features faster. Furthermore, the etching rates obtained could be slowed down or sped up depending on the conditions of the plasma process.

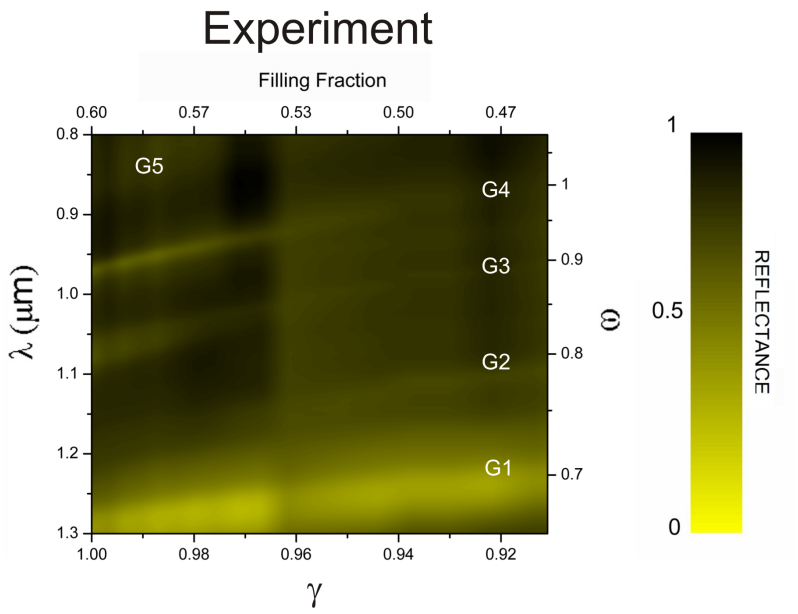
8.3 Tuning the spontaneous emission of dye dopped spheres

So far we have considered the tunability of the optical response of optically passive samples as we vary the diameter of the spheres. The same tuning strategy can be adopted to modify

[4] Check Fig. 2.7 in chapter 2 for the calibration on the diameter reduction-time ratio.



(a)



(b)

Figure 8.3: Calculated (a) and experimental (b) reflectance spectra represented as a contour plot for a monolayer of $\Phi = 1\mu m$ spheres as the filling fraction is varied from the close-packed lattice ($ff = 0.6$) to one with a 100 nm reduction in diameter ($ff = 0.44$).

the emission properties of similar samples with luminescent properties (an optically active sample). In this case we have used the same kind of samples used in the emission study of chapter 7: Rhodamine 6G doped spheres with $\Phi = 520nm$ deposited over a gold substrate.

As shown in chapter 7 this diameter allows us to overlap the dye emission with the main modes we are interested in (G1,G2 and G3 in this case).

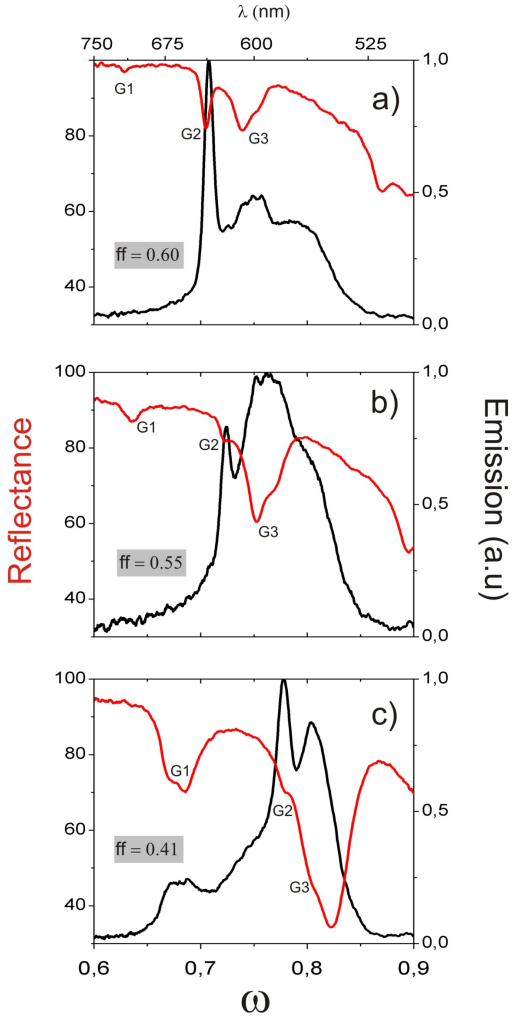
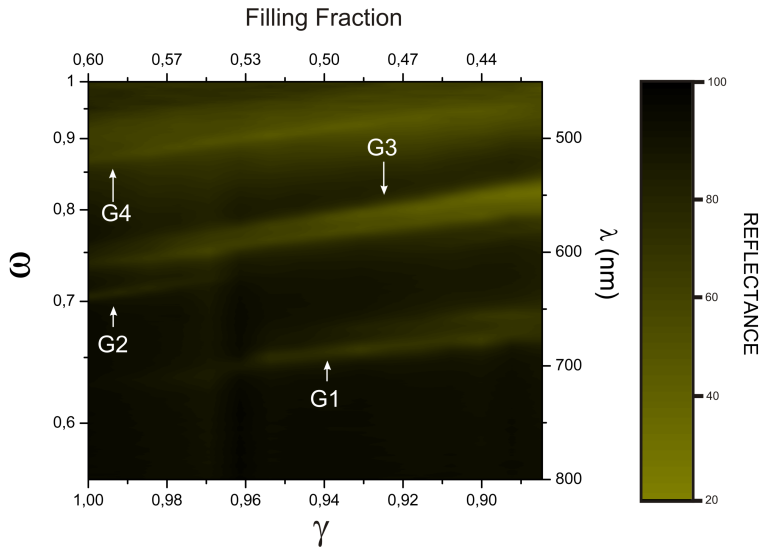


Figure 8.4: Normal incidence reflectance (red) and emission (black) spectra for $\Phi = 520nm$ dye-doped spheres at three different filling fractions corresponding to $\gamma = 1$ (a), $\gamma = 0.97$ (b), and $\gamma = 0.88$ (c).

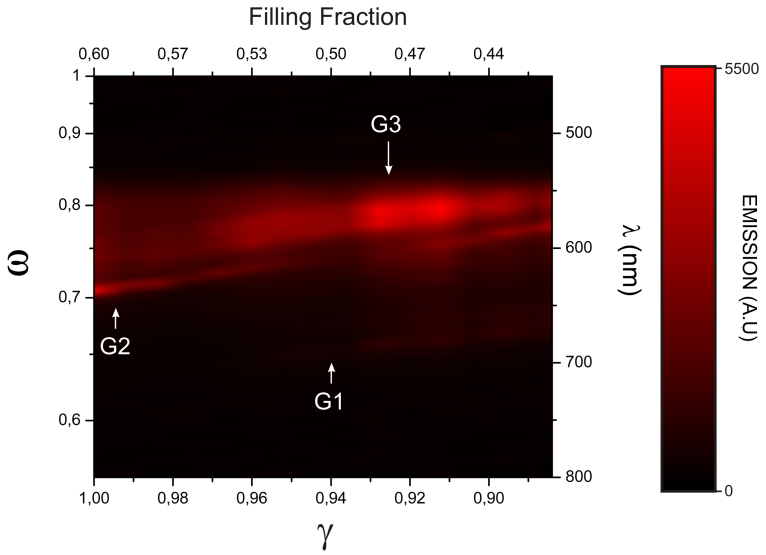
Close-packed samples were subjected to an etching process for up to 7.5 min (corresponding to $\gamma = 0.88$ or a final $ff = 0.41$). Etching times were chosen in order to restrict the process to the linear reduction-rate regime (see Fig. 2.7) as in the $\Phi = 1\mu m$ case. Fig. 8.4 shows normal incidence reflectance and emission spectra for three different steps of the etching process. The reflectance obtained for the close-packed case is the same as the one shown in previous chapters for this diameter. When the diameter of the spheres is reduced under plasma etching the blue-shift of the modes, already studied for the $\Phi = 1\mu m$ case, now takes place in the visible spectral range. However, it has to be mentioned that in this case the absorbtion of gold plays a more relevant role since the blueshift produced by the tuning process will shift each mode towards the spectral region of gold strong absorbance. Unlike the case of the $\Phi = 1\mu m$ spheres (where the field enhancement for the SPP-like modes is barely affected by the tuning) in this case such modes (G1 and G3) will suffer a strong reduction in the total field intensity as we approach the strong absorbance region. This is specially evident for G3. Despite this fact, numerical simulations

have demonstrated that the conclusions about the linear blueshift evolution for the larger sphere samples are still valid in this case.

If we now consider the emission of the monolayer, the peaks of enhanced spontaneous emission follow the trend of dips in reflectance, corresponding to the modes of the structure. From those results it is also expected that in Fig. 8.4a (close-packed sample, $ff = 0.6$) the stronger emission enhancement takes place for $\omega = 0.71$, corresponding to the G2 mode but with a smaller enhancement taking place for G3. In this way one can effectively tune the sample's emission by controlling the plasma process.



(a)



(b)

Figure 8.5: Reflectance (a) and emission (b) as a contour plot for a monolayer of $\Phi = 520nm$ dye-doped PS spheres in a continuous filling fraction reduction process. Oxygen-plasma etching was carried out from the closepacked scenario ($ff = 0.60$) to a final filling fraction of $ff = 0.41$.

Beside the spectral shift, changes in the magnitude of emission enhancement taking

place as the etching process advances are a combination of two factors. The first can be associated with the variations in the field confinement (see Fig. 8.2) and the second to the fact that the modes of the system are swiped across the dye's broad emission so that enhanced emission should be more noticeable the closer a mode is to the dye's emission maximum. A clear example of the above is that of mode G1, of SPP-like character. While for $ff = 0.6$ (Fig. 8.4a) no enhanced emission takes place at the spectral position of this mode ($\omega = 0.62$) owing to the fact that it is far from the dye's emission, as we decrease the sphere diameter we shift its spectral position until for $\gamma = 0.95$ it eventually overlaps the dye's emission ($ff = 0.51$). At that point, emission enhancement is already visible; moreover it is clear that as *ff* reduces and the mode blue-shifts, the emission increases what can be seen for $ff = 0.41$ and $\omega = 0.68$ in Fig. 8.4c. The fact that such enhancement is not as large as for the other modes is due to the small spatial overlap between the dye and the field intensity, mainly concentrated near the gold surface. Finally it must be noted that as the etching process takes place the effects of disorder, broadening the peaks in reflectance, become more evident. This is probably to be responsible for the discrepancy between reflectance and emission of the G3 peak in the case of the smallest filling fraction (Figure 4c). Here the reflectance peak broadens considerably, causing a part of the peak to fall in the high energy tail of the emission (where it is less efficient) and hence causing an asymmetry of the emission peak. A possible reason for this broadening could be a spatially inhomogenious etching of the spheres, which would add up to the intrinsic polydispersity of the spheres.

The same way that was done for the $\Phi = 1\mu m$ spheres with reflectance measurements (see Fig. 8.3), as the sphere size is reduced in small steps we have plotted a map of the reflectance and emission with the measured spectra at normal incidence for the $\Phi = 520nm$ spheres (Fig. 8.5). Here, several facts are worth mentioning. Firstly, it is observed in the reflectance measurements map (Fig. 8.5a) that modes G2,G3 and G4 are better defined during the spheres reduction than in the experimental map for larger spheres (Fig. 8.3b). This effect is probably due to the experimental set-up. As already mentioned, for monolayers with $\Phi = 1\mu m$ spheres the optical response falls in the NIR spectral region. Hence, we performed the measurements with an FTIR spectrometer coupled to a microscope objective with smaller angular resolution than the Fourier imaging set-up described in chapter 3. As commented in chapter 5 the former collects light from a range of *ca.* 10^o full angle while for the latter this range can be reduced to values lower than 1^o, allowing better resolved spectra.

Other possible effect is that the larger the spheres, the longer the plasma etching time needed to reduce to the same value the filling fraction of the lattice. As explained in chapter 2 longer plasma time can affect the spheres in several ways (for example increasing their porosity) which can introduce differences between these two processes. Nevertheless, the behavior observed in reflectance for the $\Phi = 520nm$ qualitatively matches that of $\Phi = 1\mu m$ one, indicating that although we are considering different spectral regions, where the dielectric constant of gold changes, the system still presents acceptable scalability.

Let us analyze now the evolution of the emission (Fig. 8.5b) which can be observed to follow the reflectance variations for every point in the contour map. In particular we can trace the evolution of mode G2 and see that as we reduce the sphere diameter we can not only continuously shift its spectral position but also modulate its intensity, taking it to a minimum for $\omega = 0.94$ ($ff = 0.49$). For even larger reductions we see how emission intensity recovers. The SPP-like G1 mode now appears as an enhancement in emission for $\omega = 0.95$, as we shift it towards the dye's emission. Finally mode G3 is also seen

to blue-shift and reach a maximum as it overlaps the highest value of the dye's emission for $ff = 0.47$. This clearly shows how the etching process allows us to precisely control the emission of our samples within the limits imposed by the emission properties of the internal sources.

8.4 Conclusions

We have shown a straightforward method to fine-tune the plasmonic-photonic hybrid modes of monolayers of PS spheres deposited on a gold substrate. It has been demonstrated that a small reduction of filling fraction of the dielectric lattice produces large spectral blue-shifts as well as variations on the spatial distribution of the total field intensity depending on the character (SPP-like or WG-like) of the mode studied. These changes are accompanied by a strong modification of the sample's optical response both in reflectance and emission when optically active spheres are used. Experimental results have been numerically modeled and a good agreement has been found. This is remarkable since the spatial distribution of the field intensity has been found to be very sensitive to small changes in the structure's morphology. The straightforward and cost-effective method to fine tune the optical properties of the samples could find application in some active research fields such as organic emitting devices. Further, since the magnitude of the structural changes we have imposed on our samples are similar to those achievable with tunable polymeric spheres made from hydrogels, these results could be applied for future sensing devices where tunability is achieved by means of external stimuli. As future work, the combination of spheres with different etching ratios as for example PS and polymetilmetacrylate (PMMA) in the same lattice could lead to structures where it would be possible to obtain random distribution of nanocavities within the lattice. These nanocavities could be tuned by changing again the surrounding lattice filling fraction.

General Conclusions

In this thesis, we have fabricated and optically characterized monolayers of spheres deposited on both dielectric and metallic substrates. We have also performed numerical simulations showing with agreement with the experimental results. In case of the metalo-dielectric structures, hybrid photonic-plasmonic modes has been reported and in depth studied obtaining two well different types depending on the field distribution they present within the structure. We have measured the angular response (therefore the dispersion relation) and equifrequency surfaces for these modes and a qualitative good agreenemtn has been found with some of the models available to define the optical performance of the structure. Finally we demonstrated the applicability of the efficient light confinement of this structure with two different applications. On the one hand it has been demonstrated that the emission by of dye-doped spheres can be conveniently channeled and enhance by the modes of the system. On the other hand, a simple method for tailoring the optical properties of hybrid monolayers has been reported.

The main conclusions presented in this thesis are :

- Monolayers of polystyrene spheres with diameters of the order of the visible-near infrared wavelength were fabricated on metallic substrates obtaining the same crystalline quality that for those dielectric substrates reported in literature. Vertical deposition has shown to be the most polyvalent method although at cost of a high polycrystallinity. Wedge-shaped cell method, however, allow fabrication of large area samples (which can reach centimeter size) with an almost lack of polycrystallinity. The inclusion of dye-doped organic spheres do not modify this behavior. Other kind of defects like punctual vacancies of spheres are present for monolayers grown with both methods. Oxygen plasma etching has also been shown to efficiently modify the filling fraction of the lattice while the sample's quality is maintained.

- It has been demonstrated that angular resolved spectroscopy can be accurately performed scanning the back focal plane of a lens with the sample under study placed at its focusing plane. For high numerical aperture microscope objectives this technique as been shown to provide measurements of angular and polarization resolved spectrums on an small area of the sample without mechanically moving neither the sample nor the illumination path. It has also been extracted an equifrequency pattern from the Fourier imaging.

- We have shown that monolayers of organic spheres deposited on metallic substrate can support two type of modes: SPP-like (plasmonics -like) and WG-like (photonic-like). Although related (in their field distribution) with those modes of the fully

dielectric structure, they present strongly increased field confinements respect to the latest and despite of the low refractive index contrast ($\Delta = 0.58$ in the studied case). Also the different nature of the two types of modes studied has shown to provide this system with a large functionality depending on the required field distribution for each application: closely concentrated to the metallic surface or mainly distributed within the dielectric material.

- The main effect of different types of losses for the modes have been studied. The extrinsic losses (induced by lattice defects) has shown as main effect the resonance‘s Q value reduction. Intrinsic losses due to metallic substrate absorbtion have been demonstrated to affect differently SPP-like or WG-like modes. While the latest presents quasi-full scalability with sphere diameter, the former shows spectral dispersion as the region of strong absorbtion of the metal is reached. For that part of the spectrum, Q values of the SPP-like modes are strongly reduced while the WG-like ones presents its best performance in term of light confinement.

- Experimental dispersion relation for polystyrene monolayers at gold and silver have been measured presenting a complex band structure dependent on both, in-plane chosen direction and polarization. Empty lattice and plasmon resonances dispersions have qualitatively agreed with the measured photonic bands. On the other hand, experimental eigenfrequency surfaces extracted from reflectance Fourier images present anomalous dispersion for light propagating in the plane of the periodicity which agree with the expected behaviour of a slab-like photonic crystal.

- It has been shown that a strong enhancement of the emission rate can be obtained for dye doped monolayers on gold and silver substrates contrary to the same structure on dielectric substrates. The spectral position of the maximum enhancement is obtained for the modes of the system and, in particular, for the WG-like as expected from field profile and emitters distribution within the structure. Besides, the emission is effectively channeled by the polarized angular response of the system. Fourier image of the emission patterns also show a good agreement with the equifrequency surfaces obtained in reflectance configuration.

- As final remark, it has been obtained that the reduction of the filling fraction of the spheres lattice strongly affects the spectral position of the structure‘s modes. A controlled blueshift can be obtained which was corroborated by a good agrement of this tailoring of resonance‘s position with simulated ideal structures. It has been shown that this process can be successfully applied to spectrally tailor the spontaneous emission peaks for a dye doped monolayer of spheres deposited on gold.

Part IV

Appendixes

Appendix A

Finite difference time domain simulation

The calculation of photonic band structures and, in general, the optical response of photonic crystals has been accomplish with several methods [168] during the last two decades. Mainly three methods are the most widespread : Plane wave method (PWM)CITA, Korringa-Koh-Rostoker method (KKR)CITA and finally the Finite difference methods.

Among the three methods, the two first ones are limited to periodic structures (PWM) or scatterers with almost spherical shapes (KKR). However, finite difference methods are based on the discrimination of system under study which make them appropriate to solve any kind of structure. The optical properties of the structure are independently defined at any point of the gridding which allow a very accurate sample definition. Maxwell equation can then be solved as an eigenvalue problem according to the discretization. Among its several advantages, it permits calculation of reflection and transmittance of any system. For that reason FDTD has become main tool to simulate E and H field propagation in photonic structures.

Finite difference methods are divided mainly in two types : finite difference frequency domain (FDFD) and finite difference time domain (FDTD). Both of them consist on the discretization of Maxwell equation in the respective domain. Although the spatial discretization is similar in both cases [7] , FDFD presents problems when solving non-linear or gain media due to frequency conservation issues [6]. Besides, and probably the most important advantage, is that FDTD can compute the response of a linear system at many frequencies with one single computation. It make use of the Fourier transform of a single short pulse propagation into the system and retrieve the resulting $\mathbf{E}(t)$ and $\mathbf{H}(t)$ at any position of the grid. By Fourier transform the fields one obtain $\mathbf{E}(\omega)$ and $\mathbf{H}(\omega)$. Of course, FDFD still present some advantages in specific problems as when steady states at a give frequency are to be studied or when very sharp spectral features have to be solved. In that cases, the pulse is reaquirerd to propagate until transient effects pass. It can lead the FDTD simulation not affordable in time if high resolutions are required. F Other important advantage of the FDTD method is the relatively simple implementation of systems with imaginary or non-linear refractive indexes. That is the reason for this method to be one of the most widespread in plasmonic system‘s optical response calculation [169].

FDTD was first pointed out by Yee [170] but it was Taflove that fully described the method [171]. FDTD is a direct solution for Maxwell‘s time dependent equations. It is based on a volumetric sampling (grid) of the system under study. This way, unknown near-field distribution of $\mathbf{E}$ and $\mathbf{H}$ in the region of interest and along a discredited period

of time. Obviously, the sample in space has to be defined at subwavelenght resolution if the near field is to be resolved. The sampling for the time variable depends on the stability required for the calculation.

From Maxwell equations it is obtained that :

$$\frac{\partial \mathbf{H}}{\partial t} = -\frac{1}{\mu}\nabla \times \mathbf{E} - \frac{\rho}{\mu}\mathbf{H} \tag{A.1}$$

$$\frac{\partial \mathbf{E}}{\partial t} = -\frac{1}{\epsilon}\nabla \times \mathbf{H} - \frac{\sigma}{\epsilon}\mathbf{E} \tag{A.2}$$

then, the vector components of the curl operator can be written in a separate manner yielding a system of six coupled equations:

$$\begin{aligned} \frac{\partial H_i}{\partial t} &= -\delta_{ijk}\frac{1}{\mu}\left(\frac{\partial E_j}{\partial k} - \frac{\partial E_k}{\partial j} - \rho H_i\right) \\ \frac{\partial E_i}{\partial t} &= \delta_{ijk}\frac{1}{\epsilon}\left(\frac{\partial H_k}{\partial j} - \frac{\partial H_j}{\partial k} - \sigma E_i\right) \end{aligned} \tag{A.3}$$

with $x, y, z = i, j, k$. As both time and space have been discretized with steps ($\Delta_{i,j,k}$) one can define any space point to be calculated as part of a three dimensional grid defined by $(i, j, k) = (i\Delta x, j\Delta y, k\Delta z)$ (see diagram of Fig. **??**). Any value for time propagation is also discretized to be $t = n\Delta t$ with N being an integer. Therefore, centered finite differences (central-diifference) expressions can be used for space and time derivatives. The kind of grid and discrete derivative approximation chosen strongly affect the final performance of the simulation in both, accurately and time consuming [172]. In Yee's notation, the first time partial derivative of a given function u, evaluated at the space point (i,j,k) can be written as:

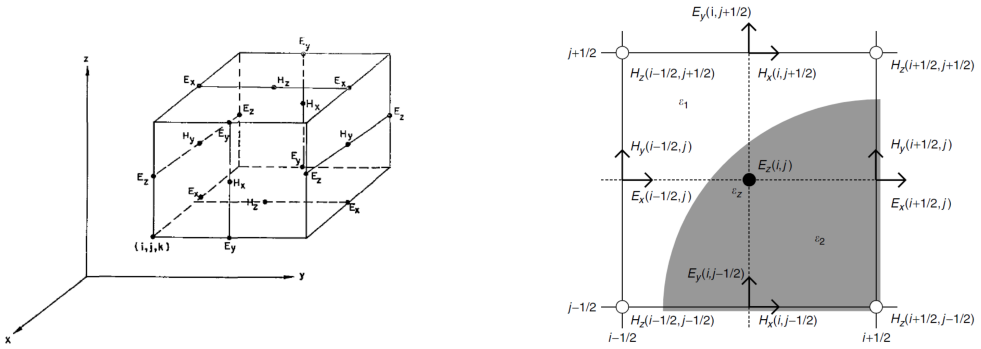
$$\frac{\partial u}{\partial t}(i\Delta x, j\Delta y, k\Delta z, n\Delta t) \sim \frac{u_{i,j,k}^{n+1/2} - u_{i,j,k}^{n-1/2}}{\Delta t} \tag{A.4}$$

This approximation of the discrete derivative is one of the simplest but still can be applied to the six equation system shown in A.1 A.2, such a way that a system of six discretized equations is obtained. In this case, each of that equations shown that each $H_{i,j,k}$ or $E_{i,j,k}$ at a time step n is assume to be simply the arythmetic average of the stored value of $H_{i,j,k}^{n-1/2}$ (or E) at a time $n-1/2$ and the yet to be computed new value of $H_{i,j,k}^{n+1/2}$.

Without entering too much detail, and as a result of the previous spatial and temporal discretization, when both fields are known on a single surface ($E(x, y, z_0)$ and $H(x, y, z_0)$), the far field can be calculated from the discrete time derivative equations shown before at any discrete position in z ($E(x, y, z)$ and $H(x, y, z)$). In order to solve that, it has to be notice that the functions for both field have to be known at the initial position.

As follows from the previous discussion, the gridding is a fundamental parameter in the resolution which we solve the fields propagation. However, as the considered value must be finite, the boundary conditions at the edge of the grid can introduce significant artifacts. Among the several methods developed to make this boundaries to perform as infinite mediums most known are the absorbing boundary condition (ABC) and the perfectly matched layer (PML). PML has been demonstrated to show the best results [1]. First

[1] http://math.mit.edu/ stevenj/18.369/pml.pdf



(a) (b)

Figure A.1: (a) Positions of various field components in the spatial grid taken from reference [170]. The E components are in the middle of the edges and the H components are in the center of the faces. (b) Two dimensional grid representation valid. Shadow area represent different a different material. Figure extracted from reference [173].

defined by Berenger [174], its main difference with total absorbance boundaries is that such waves incident from anon-PML medium are not reflected back into the calculation grid in the analytical case. However, if discretization is being used, as in this case, little reflectance artifacts can be generated although not as lrge as in the ABC case.

FDTD method allow for many approximations taking into account the systems to be solved. Due to the large amount of applications in photonics that needs from FDTD simulations, several computational tools have been implemented such a way that just the geometry and optical properties of the structure must be defined before simulation. Some of the most widespread are Meep [26] (free) or Rsoft (commercial). For our simulations we have used the software *FDTD solutions* provided by Lumerical company [175].

A.1 Geometry and material properties definition

Lumerical FDT solutions allows us to define any structure by means of a CAD tool where each component of the structure can be accurately described in both, structure and optical properties. In the case of a monolayer on a given substrate, we first define a single sphere on the required substrate. It has to be notice that, as for any FDTD simulation, the time step is dependent on the size of the smallest finite difference cell in the grid for stability. The grid is defined to be a 3D cube with $3\Phi/2$ total dimension in the (x,y) plane while the z direction is chosen appropriately depending on the simulation parameters as will be explained below. The dielectric constants of sphere and substrate are set to values obtained either from literature tables (polystyrene) or from ellipsometry measurements (gold, silver and silicon). Surrounding media is always considered to be vacuum in this case.

As previously commented, the resolution chosen for the grid is a crucial parameter, specially when working with non rectangular structure. If the grid resolution is not high enough, the shape is not accurately described. Therefore, the chosen gridding strongly affects the final accuracy of the calculated field distribution.

Moreover, the grid truncation which define the total volume may introduce artifacts. In this case, we choose the walls in the vertical direction (z) to be PML layers in order

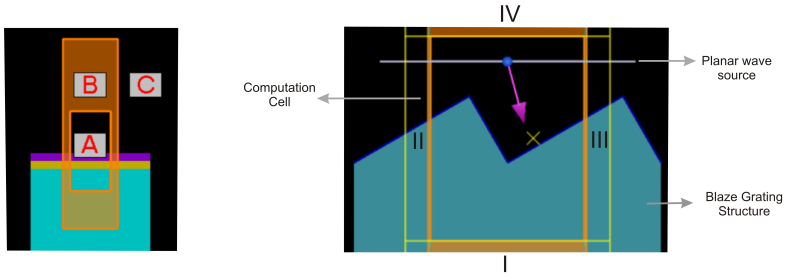


Figure A.2: Positions of various field components in the spatial grid taken from reference [170]. The E components are in the middle of the edges and the H components are in the center of the faces.

to avoid reflectance in that direction. Concerning the in-plane direction (x,y) there are two possible approaches. The most usual in non-periodic or complex structures is the definition of a total volume including the whole system. In this case, as we want to obtain the effect of an infinite 2D photonic crystal a cell as large as, at least, 100 spheres would be necessary to reproduce the effect of a infinitely large monolayer [140]. However, this approach means solving the field propagation at any point of the grid in a very large volume which is not affordable in terms of computational resources in most of the cases [2]. Moreover, effects of finiteness of the lattice may introduce artifacts even if PML layers are used.

The other approach, which is the one chosen for the simulations shown in this thesis, take advantage of the in-plane symmetry for 2D PCs and, in particular in the monolayer of spheres. A total volume for simulation of just one cell of the lattice is included in the simulation but the boundary conditions at the periodicity plane are set to reproduce the equivalent condition within the calculate volume. As a result, just one cell volume (approximately) must be calculated in each case. This approach strongly reduces the resources needed in each simulation as well as it increase the accuracy of the results. Fig. **??** shows an example of the main regions involved on the simulation and also an specific set-up for a blaze grating. Although represented in 2D it corresponds to a 3D calculation

The general picture (left) define the main regions in the simulation volume. In that figure one find a region A which define the simulation volume of interest. B zone, defined by the yellow area accounting for the boundary condition area. C area is totally ignored. An blaze grating is defined in the right picture. Again, the total volume to be calculated is marked by the yellow box which length in the longitudinal direction match a period of the grating. Four regions are defined as I-IV. For I and IV regions the boundary of the simulation cell is set as PML. It avoids any beam reaching that boundaries to be reflected which ideally would be equivalent to an infinite volume in that directions. Concerning regions II and III, that boundaries are set to be periodic with the period of the grating. The white line correspond to the planar wave source covering the same surface than the grating in the periodicity plane. The arrow shows the angular incidence for the planar waves emitted by the source.

[2]Remember that, as $\lambda = \lambda_0/n$ for light propagating in an homogenious media with refractive index n, the higher the refractive index the higher the resolution to be used.

A.2 Sources definition

As we have shown, FDTD is a time domain method. Therefore, the electromagnetic fields are calculated as a function of time. As a consequence, the system being simulated can be excited by different type of sources (dipole, beam, modes, etc) depending on the problem to be solved. In our case, we are mainly interested on the optical response (in particular reflectance) of the monolayer when light is incident on the sample in normal incident way. As result, the most suitable source for our porpoise is a broadband continuous wave. However, most of the sources used in FDTD are pulsed in their temporal part. In the case of the the software considered here that pulse present a temporal shape given by :

$$s(t) = sin(\omega_0(t - t_0)e^{-\frac{(t-t_0)^2}{2\Delta^2}} \tag{A.5}$$

where ω_0 is the central frequency, t_0 the pulse initio and Δt the pulse width. This way, a beam injected into free space at a a position z_0 is described by $E(x, y, z_0, x, t) = E(x, y, z_0, x)s(t)$ at a given time t during the simulation. Taking into account the Fourier transform of eq. A.5[3], the optical response at any single frequency could be obtained with one single simulation if s(t) is a dirac delta. However, when discretization is considered, that limit can not be achieved and a broad pulse has to be used by simulation stability reasons. Therefore, the width of the pulse determines the frequency range to be calculated while it is the total number of samples (N) that the pulse is divided in that will determine the resolution of the final spectrum obtained from simulation.

After the temporal component of the source has been set, it is propagated along the grid which make it necessary to spatially define the source. Fig. **??** shows the spatial configuration chosen for the simulation of this thesis. In that case, the source present a planar shape parallel to the grating surface. The source fulfills is placed at a given distance from the top of the grating. Using an infinite source matches the experimental set-up where a plane wave impinges the sample in its whole structure area at the same time. Moreover, using finite sources can introduce artifacts as diffraction at the source boundaries.

The other kind of source very common in FDTD simulations is a punctual source describes as a dipole oscillating at a given frequency. This kind of sources are very useful when a polarized source is required or if the source has to be placed within the structure. This is the most common technique on simulating emissive devices as for example PC cavities with an inside emitter. It is also de usual approach to obtain the dispersion relation of PC slabs photonic crystals CITA.

A.3 Retrieving information from simulations

Once the source has been set, next step is defining the points of the grid where one is interested on collecting the field profile. This points we call monitors and can be defined as a point but also as a surface or a volume. As we know the vectorial field at each given point, the power at each monitor defined is calculated as the integration of the Pointing vector. Both reflectance and transmittance at a given point are calculated as the power collected at that point divided by the total power injected by the source.

As we have performed normal incidence reflectance calculations, we have place monitors above and behind the monolayer of spheres. The chosen size for the monitors in our case

[3] $s(\omega) = \int exp(i\omega t)s(t)dt$

fulfilling the whole periodicity plane at a given distance from the monolayer in order to match the size of the source an make the reflectance calculation meaningful.

Therefore, the pulse is injected at a given position, propagated for time long enough to collect its response in the monitors and plotted as the ratio between the injected and the power collected at the given monitor (see Fig. **??**).

Finally, one can also define a monitor to collect the value of each filed component at a given point. If storaged, it is easily obtained a map of the field distribution at final step of the simulation. In fact, if field is collected for each temporal step, it is obtained the total evolution of the field while propagating into the system. This kind of analysis has been performed during this thesis for those frequencies matching resonances of the monolayer of spheres obtaining the field distribution after normal incidence in several cases.

Appendix B

Fano line-shape: extracting Q factor of them modes from reflectance spectra

If information about the physical properties of the modes of a slab PC are required (as for example confinement factors or Q-factors) FDTD calculations are routinely employed.An approach is to study the temporal decay of a dipole oscillating at the frequency of the mode at the spatial position where the mode is confined. Alternatively, one can extract the main characteristics of leaky modes directly from the reflectance/transmittance spctrum of the system. This approach is based on the Fano resonances largely studied in solid state and atomic physics [176]. This effect take place whenever a scattering process from any input state can take two different pathways, either directly to a continuum of extended states or resonantly through a discrete energy level. The interference between the two configurations gives rise to an asymmetric scattering lineshape. If light scattered by a periodic system is considered, the continuum of states available are all the radiative modes we can couple to. On the other hand, discrete states are those modes of the system defined as resonances itself (for example a leaky mode in a slab PC). As pointed out by Fan *et.al*, the optical response of high RI contrast slab PCs [30] account for this kind of resonance.

On that study it was shown that the transmisison/reflection of a 2D PC slab can is formed by the sum of a set of sharp resonant features superimposed upon a smoothly varying background. The shape and intensity of those resonances accurately fit the behavior previously reported for Fano resonances which typically present a Lorentzian shape. If one consider a hybrid monolayer of dielectric spheres, the same model can be applied for the reflectance peaks (dips in transmission) shown in Fig. 4.3a. Radiative modes contributing to the mirror-like background can be associated to the Fabry-Perot oscillations described in chapter 4. On the other hand, if the leaky modes of the system are considered, we can fit any dip of a leaky mode to a Fano shape. The Fano resonance can be expressed as :

$$R(\omega) = A_0 + F_0 \frac{[q + 2(\omega - \omega_0)/\Gamma]^2}{1 + [2(\omega - \omega_0)/\Gamma]^2} \tag{B.1}$$

where ω_0 is the central frequency of the resonance, Γ is the resonance linewidth, A_0 correspond to the amplitude of the non-resonant pathways and F_0 is a constant factor. The dimensionless parameter q is the ratio between resonant and the background amplitudes in the scattering process. This parameter accounts for the asymmetry of the resonance and can take positive or negative values.There are three different regimes.

First, for large q, resonant scattering dominates direct scattering pathways and the

lineshape tend to a symmetric Lorentzian. Second, for small q, radiative scattering dominates and an inverse Lorentzian is obtained. Finally, when $q \sim 1$, the radiative scattering presents a similar amplitude than the guided ones and a strong asymmetric resonance is observed.

Probably the most important value available from fitting the reflectance spectrum to a Fano shape is the Q factor of the resonance as shown in literature [177]. As already explained, the Q of leaky modes of a slab PC is related to the lifetime of those modes before they are re-scattered out of the structure. It is defined as :

$$Q = 2\pi \frac{E_{total}}{E_{disipated}} = \frac{\omega_0}{\Gamma} \tag{B.2}$$

Although Q can be also calculated directly from spectrums as $Q = \omega_0 / FWHM$ (as shown in chapter **??**) where FWHM is the full width half maximum, Fano's approximation provides valuable extra information. In particular, q parameter allows an study on the asymmetry of the resonances [178] which provides a measurement of the resonant effect respect to the radiative modes of the system.

Bibliography

[1] M. Inoue, K. Ohtaka, and S. Yanagawa, "Light scattering from macroscopic spherical bodies. ii. reflectivity of light and electromagnetic localized state in a periodic monolayer of dielectric spheres," *Physical Review B*, vol. 25, p. 689, 1982.

[2] E. Yablonovitch, "Inhibited spontaneous emission in solid-state physics and electronics," *Physical Review Letters*, vol. 58, p. 2059, 1987.

[3] S. John, "Strong localization of photons in certain disordered dielectric superlattices," *Physical Physics Letters*, vol. 58, 1987.

[4] C. Kittel, *Introduction to Solid State Physics*. John Wiley and Sons,Inc, 1971.

[5] K. Sakoda, *Optical Properties of Photonic Crystals*. Springer, 2001.

[6] J. D. Joannopoulos, S. Johnson, J. Wing, and R. Meade, *Photonic Crystals: Molding the Flow of Light*. Princeton University Press, 2008.

[7] B. Thompson, *Electromagnetic Theory and Applications for Photonic Crystals*. Taylor and Francis Group, 2006.

[8] E. Yablonovitch, T. J. Gmitter, and K. M. Leung, "Photonic band structure: The face-centered-cubic case employing nonspherical atoms," *Physical Review Letters*, vol. 67, no. 17, p. 2295, 1991.

[9] A. Blanco, E. Chomski, S. Grabtchak, M. Ibisate, S. John, S. W. Leonard, C. Lopez, F. Meseguer, H. Miguez, J. P. Mondia, G. A. Ozin, O. Toader, and H. M. van Driel, "Large-scale synthesis of a silicon photonic crystal with a complete three-dimensional bandgap near 1.5 micrometres," *Nature*, vol. 405, p. 437, 2000.

[10] C. Mazzoleni and L. Pavesi, "Application to optical components of dielectric porous silicon multilayers," *Applied Physics Letters*, vol. 67, p. 2983, 1995.

[11] J. B. Pendry, "Symemtry and transport of waves in one-dimensional disrdered systems," *Advances in Physics*, vol. 43, p. 461, 1994.

[12] B. Temelkuran, S. D. Hart, G. Benoit, J. D. Joannopoulos, and Y. Fink, "Wavelength-scalable hollow optical fibres with large photonic bandgaps for co2 laser transmission," *Nature*, vol. 420, p. 650, 2002.

[13] M. C. Fuertes, F. J. Lopez-Alcaraz, M. C. Marchi, H. E. Troiani, V. Luca, H. Miguez, and G. Soler-Illia, "Photonic crystals from ordered mesoporous thin-film functional building blocks," *Advanced Functional Materials*, vol. 17, p. 1247, 2007.

[14] S. Colodrero, A. Mihi, L. Häggman, M. Ocaña, G. Boschloo, A. Hagfeldt, and H. Míguez, "Porous one-dimensional photonic crystals improve the power-conversion efficiency of dye-sensitized solar cells," *Advanced Materials*, vol. 21, p. 764, 2009.

[15] H. Kosaka, T. Kawashima, A. Tomita, M. Notomi, T. Tamamura, T. Sato, and S. Kawakami, "Photonic crystals for micro lightwave circuits using wavelength-dependent angular beam steering," *Applied Physics Letters*, vol. 74, p. 1370, 1999.

[16] S. Y. Lin, J. G. Fleming, D. L. Hetherington, B. K. Smith, R. Biswas, K. M. Ho, M. M. Sigalas, W. Zubrzycki, S. R. Kurtz, and J. Bur, "A three-dimensional photonic crystal operating at infrared wavelengths," *Nature*, vol. 394, no. 6690, p. 251, 1998.

[17] A. Chelnokov, K. Wang, S. Rowson, P. Garoche, and J. M. Lourtioz, "Near-infrared yablonovite-like photonic crystals by focused-ion-beam etching of macroporous silicon," *Applied Physics Letters*, vol. 77, no. 19, p. 2943, 2000.

[18] M. Campbell, D. N. Sharp, M. T. Harrison, R. G. Denning, and A. J. Turberfield, "Fabrication of photonic crystals for the visible spectrum by holographic lithography," *Nature*, vol. 404, p. 53, 2000.

[19] M. Deubel, G. Von Freymann, M. Wegener, S. Pereira, K. Busch, and C. M. Soukoulis, "Direct laser writing of three-dimensional photonic-crystal templates for telecommunications," *Nature Materials*, vol. 3, p. 444, 2004.

[20] J. Park, J. Moon, H. Shin, D. Wang, and M. Park, "Direct-write fabrication of colloidal photonic crystal microarrays by ink-jet printing," *Journal of Colloid and Interface Science*, vol. 298, p. 713, 2006.

[21] J. F. Galisteo-Lopez, M. Ibisate, R. Sapienza, L. S. Froufe-Perez, A. Blanco, and C. Lopez, "Self-assembled photonic structures," *Advanced Materials*, vol. 23, p. 30, 2011.

[22] V. Astratov, V. Bogomolov, A. Kaplyanskii, A. Prokofiev, L. Samoilovich, S. Samoilovich, and Y. Vlasov, "Optical spectroscopy of opal matrices with cds embedded in its pores: Quantum confinement and photonic band gap effects," *Il Nuovo Cimento D*, vol. 17, p. 1349, 1995.

[23] V. L. Alexeev, S. Das, D. N. Finegold, and S. A. Asher, "Photonic crystal glucose-sensing material for noninvasive monitoring of glucose in tear fluid," *Clinical Chemestry*, vol. 50, p. 2353, 2004.

[24] S. Guldin, S. HuÌttner, M. Kolle, M. Welland, P. MuÌller-Buschbaum, R. Friend, U. Steiner, and N. TeÌtreault, "Dye-sensitized solar cell based on a three-dimensional photonic crystal," *Nano Letters*, vol. 10, p. 2303, 2010.

[25] A. Arsenault, D. Puzzo, I. Manners, and G. Ozin, "Photonic-crystal full-colour displays," *Nature Photonics*, vol. 1, p. 468, 2007.

[26] D. S. G. Jhonson, "http://ab-initio.mit.edu/photons/tutorial/."

[27] C. Pollok, *Fundamentals of Optoelectronics*. Tom Casson, 1995.

[28] D. M. Hammer, "http://wwwhome.math.utwente.nl/ hammer/index.html."

[29] D. L. Lee, *Electromagnetic principles of integrated optics*. Wiley, 1986.

[30] S. Fan and J. D. Joannopoulos, "Analysis of guided resonances in photonic crystal slabs," *Physical Review B*, vol. 65, p. 235112, 2002.

[31] K. B. Crozier, V. Lousse, O. Kilic, S. Kim, S. Fan, and O. Solgaard, "Air-bridged photonic crystal slabs at visible and near-infrared wavelengths," *Physical Review B*, vol. 73, p. 115126, 2006.

[32] L. C. Andreani and D. Gerace, "Photonic-crystal slabs with a triangular lattice of triangular holes investigated using a guided-mode expansion method," *Physical Rreview B*, vol. 73, p. 235114, 2006.

[33] M. Notomi, "Manipulating light with strongly modulated photonic crystals," *Reports on Progress in Physics*, vol. 73, p. 096501, 2010.

[34] M. Notomi, K. Yamada, A. Shinya, J. Takahashi, C. Takahashi, and I. Yokohama, "Extremely large group-velocity dispersion of line-defect waveguides in photonic crystal slabs," *Physical Review Letters*, vol. 87, p. 253902, 2001.

[35] M. Eichenfield, J. Chan, R. M. Camacho, K. J. Vahala, and O. Painter, "Optomechanical crystals," *Nature*, vol. 462, p. 78, 2009.

[36] S. Zanotto, M. Liscidini, and L. C. Andreani, "Light trapping regimes in thin-film silicon solar cells with a photonic pattern," *Optics Express*, vol. 18, p. 4260, 2010.

[37] Y. Akahane, T. Asano, B.-S. Song, and S. Noda, "High-q photonic nanocavity in a two-dimensional photonic crystal," *Nature*, vol. 425, p. 944, 2003.

[38] Q. Xu, V. R. Almeida, R. R. Panepucci, and M. Lipson, "Experimental demonstration of guiding and confining light in nanometer-sizelow-refractive-index material," *Optics Letters*, vol. 29, p. 1626, 2004.

[39] H. Miyazaki and K. Ohtaka, "Near-field images of a monolayer of periodically arrayed dielectric spheres," *Physical Review B*, vol. 58, p. 6920, 1998.

[40] L. A. Dorado, R. A. Depine, G. Lozano, and H. Míguez, "Physical origin of the high energy optical response of three dimensional photonic crystals," *Optics Express*, vol. 15, p. 17754, 2007.

[41] H. Raether, *Surface plasmons on smooth and rough surfaces and on gratings*. Springer-Verlag, 1988.

[42] W. L. Barnes, A. Dereux, and T. W. Ebbesen, "Surface plasmon subwavelength optics," *Nature*, vol. 424, p. 824, 2003.

[43] J. N. Anker, W. P. Hall, O. Lyandres, N. C. Shah, J. Zhao, and R. P. Van Duyne, "Biosensing with plasmonic nanosensors," *Nature Materials*, vol. 7, p. 442, 2008.

[44] L. Kennedy, L. Bickford, N. Lewinski, A. Coughlin, Y. Hu, E. Day, J. West, and R. Drezek, "A new era for cancer treatment: gold-nanoparticle-mediated thermal therapies," *Small*, vol. 7, p. 169, 2011.

[45] D. K. Gramotnev and S. I. Bozhevolnyi, "Plasmonics beyond the diffraction limit," *Nature Photonics*, vol. 4, p. 83, 2010.

[46] T. W. Ebbesen, H. J. Lezec, H. F. Ghaemi, T. Thio, and P. A. Wolff, "Extraordinary optical transmission through sub-wavelength hole arrays," *Nature*, vol. 391, p. 667, 1998.

[47] K. F. MacDonald and N. I. Zheludev, "Active plasmonics: current status," *Laser and Photonics Reviews*, vol. 4, p. 562, 2010.

[48] M. C. Gather, K. Meerholz, N. Danz, and K. Leosson, "Net optical gain in a plasmonic waveguide embedded in a fluorescent polymer," *Nature Photonics*, vol. 4, p. 457, 2010.

[49] R. H. Ritchie, E. T. Arakawa, J. J. Cowan, and R. N. Hamm, "Surface-plasmon resonance effect in grating diffraction," *Physical Review Letters*, vol. 21, p. 1530, 1968.

[50] H. Gao, W. Zhou, and T. W. Odom, "Plasmonic crystals: A platform to catalog resonances from ultraviolet to near-infrared wavelengths in a plasmonic library," *Advanced Functional Materials*, vol. 20, p. 529, 2009.

[51] S. C. Kitson, W. L. Barnes, and J. R. Sambles, "Full photonic band gap for surface modes in the visible," *Physical Review Letters*, vol. 77, p. 2670, 1996.

[52] S. Bozhevolnyi, J. Erland, K. Leosson, P. Skovgaard, and J. Hvam, "Waveguiding in surface plasmon polariton band gap structures," *Physical Review Letters*, vol. 86, no. 14, p. 3008, —2001—. Copyright (C) 2011 The American Physical Society Please report any problems to prola@aps.org PRL.

[53] V. Shalaev, "Optical negative-index metamaterials," *Nature Photonics*, vol. 1, p. 41, 2007.

[54] R. M. Cole, J. J. Baumberg, F. J. Garcia de Abajo, S. Mahajan, M. Abdelsalam, and P. N. Bartlett, "Understanding plasmons in nanoscale voids," *Nano Letters*, vol. 7, p. 2094, 2007.

[55] C. Ma, Q. Zhang, and E. Van Keuren, "Analysis of symmetric and asymmetric nanoscale slab slot waveguides," *Optics Communications*, vol. 282, p. 324, 2009.

[56] R. F. Oulton, V. J. Sorger, D. A. Genov, D. F. P. Pile, and X. Zhang, "A hybrid plasmonic waveguide for subwavelength confinement and long-range propagation," *Nature Photonics*, vol. 2, p. 496, 2008.

[57] R. Oulton, V. Sorger, T. Zentgraf, R. Ma, C. Gladden, L. Dai, G. Bartal, and X. Zhang, "Plasmon lasers at deep subwavelength scale," *Nature*, vol. 461, p. 629, 2009.

[58] S. Randhawa, M. U. González, J. Renger, S. Enoch, and R. Quidant, "Design and properties of dielectric surface plasmon bragg mirrors," *Opt. Express*, vol. 18, p. 14496, 2010.

[59] R. M. Cole, Y. Sugawara, J. J. Baumberg, S. Mahajan, M. Abdelsalam, and P. N. Bartlett, "Easily coupled whispering gallery plasmons in dielectric nanospheres embedded in gold films," *Physical Review Letters*, vol. 97, p. 137401, 2006.

[60] J. Grandidier, S. Massenot, G. C. des Francs, A. Bouhelier, J. C. Weeber, L. Markey, A. Dereux, J. Renger, M. U. González, and R. Quidant, "Dielectric-loaded surface plasmon polariton waveguides: Figures of merit and mode characterization by image and fourier plane leakage microscopy," *Physical Review B*, vol. 78, p. 245419, 2008.

[61] A. Christ, S. G. Tikhodeev, N. A. Gippius, J. Kuhl, and H. Giessen, "Waveguide-plasmon polaritons: Strong coupling of photonic and electronic resonances in a metallic photonic crystal slab," *Physical Review Letters*, vol. 91, p. 183901, 2003.

[62] L. Shi, X. Liu, H. Yin, and J. Zi, "Optical response of a flat metallic surface coated with a monolayer array of latex spheres," *Physics Letters A*, vol. 374, p. 1059, 2010.

[63] E. Fermi, "Quantum theory of radiation," *Reviews of Modern Physics*, vol. 4, p. 0087, 1932.

[64] E. M. Purcell, "Spntaneous emission probablities at radio frequencies," *Physical Review*, vol. 69, pp. 681–681, 1946.

[65] R. Sprik, B. A. VanTiggelen, and A. Lagendijk, "Optical emission in periodic dielectrics," *Europhysics Letters*, vol. 35, p. 265, 1996.

[66] R. G. Hulet, E. S. Hilfer, and D. Kleppner, "Inhibited spontaneous emission by a rydberg atom," *Physical Review Letters*, vol. 55, p. 2137, 1985.

[67] P. Lodahl, A. Floris van Driel, I. S. Nikolaev, A. Irman, K. Overgaag, D. Vanmaekelbergh, and W. L. Vos, "Controlling the dynamics of spontaneous emission from quantum dots by photonic crystals," *Nature*, vol. 430, p. 654, 2004.

[68] M. Fujita, S. Takahashi, Y. Tanaka, T. Asano, and S. Noda, "Simultaneous inhibition and redistribution of spontaneous light emission in photonic crystals," *Science*, vol. 308, p. 1296, 2005.

[69] K. Hennessy, A. Badolato, M. Winger, D. Gerace, M. Atature, S. Gulde, S. Falt, E. L. Hu, and A. Imamoglu, "Quantum nature of a strongly coupled single quantum dot-cavity system," *Nature*, vol. 445, p. 896, 2007.

[70] J. J. Wierer, A. David, and M. M. Megens, "Iii-nitride photonic-crystal light-emitting diodes with high extraction efficiency," *Nature Photonics*, vol. 3, p. 163, 2009.

[71] C. Wiesmann, K. Bergenek, N. Linder, and U. Schwarz, "Photonic crystal leds - designing light extraction," *Laser and Photonics Review*, vol. 3, p. 262, 2009.

[72] S. Fan, P. R. Villeneuve, J. D. Joannopoulos, and E. F. Schubert, "High extraction efficiency of spontaneous emission from slabs of photonic crystals," *Physical Review Letters*, vol. 78, p. 3294, 1997.

[73] W. L. Barnes, "Fluorescence near interfaces: The role of photonic mode density," *Journal of Modern Optics*, vol. 45, p. 661, 1998.

[74] K. H. Drexhage, "Influence of a dielectric interface on fluorescence decay time," *Journal of Luminescence*, vol. 1, p. 693, 1970.

[75] J. G. Rivas, G. Vecchi, and V. Giannini, "Surface plasmon polariton-mediated enhancement of the emission of dye molecules on metallic gratings," *New Journal of Physics*, p. 105007, 2008.

[76] E. Hwang, I. I. Smolyaninov, and C. C. Davis, "Surface plasmon polariton enhanced fluorescence from quantum dots on nanostructured metal surfaces," *Nano Letters*, vol. 10, pp. 813–820, 2010.

[77] X. Q. Cui, K. Tawa, K. Kintaka, and J. Nishii, "Enhanced fluorescence microscopic imaging by plasmonic nanostructures: From a 1d grating to a 2d nanohole array," *Advanced Functional Materials*, vol. 20, p. 945.

[78] D. Nau, Sch, ouml, A. nhardt, C. Bauer, A. Christ, T. Zentgraf, J. Kuhl, M. W. Klein, and H. Giessen, "Correlation effects in disordered metallic photonic crystal slabs," *Physical Review Letters*, vol. 98, p. 133902, 2007.

[79] M. A. Noginov, G. Zhu, A. M. Belgrave, R. Bakker, V. M. Shalaev, E. E. Narimanov, S. Stout, E. Herz, T. Suteewong, and U. Wiesner, "Demonstration of a spaser-based nanolaser," *Nature*, vol. 460, p. 1110, 2009.

[80] L. Novotny and B. Hecht, *Principles of Nano-Optics*. Cambridge University Press, 2006.

[81] T. H. Taminiau, F. D. Stefani, F. B. Segerink, and N. F. van Hulst, "Optical antennas direct single-molecule emission," *Nature Photonins*, vol. 2, pp. 234–237, 2008.

[82] Y. Sugawara, T. A. Kelf, J. J. Baumberg, M. E. Abdelsalam, and P. N. Bartlett, "Strong coupling between localized plasmons and organic excitons in metal nanovoids," *Physical Review Letters*, vol. 97, p. 266808, 2006.

[83] P. Viktorovitch, B. Ben Bakir, S. Boutami, J. L. Leclercq, X. Letartre, P. Rojo-Romeo, C. Seassal, M. Zussy, L. Di Cioccio, and J. M. Fedeli, "3d harnessing of light with 2.5d photonic crystals," *Laser and Photonics Reviews*, vol. 4, p. 401, 2009.

[84] S. Noda, A. Chutinan, and M. Imada, "Trapping and emission of photons by a single defect in a photonic bandgap structure," *Nature*, vol. 407, p. 608, 2000.

[85] W. Stöber, A. Fink, and E. Bohn, "Controlled growth of monodisperse silica spheres in the micron size range," *Journal of Colloid and Interface Science*, vol. 26, p. 62, 1968.

[86] A. Philipse, "Solid opaline packings of colloidal silica spheres," *Journal of Materials Science Letters*, vol. 8, p. 1371, 1989.

[87] P. Jiang, J. F. Bertone, K. S. Hwang, and V. L. Colvin, "Single-crystal colloidal multilayers of controlled thickness," *Chemistry of Materials*, vol. 11, p. 2132, 1999.

[88] M. Holgado, F. Garcia-Santamaria, A. Blanco, M. Ibisate, A. Cintas, H. Miguez, C. J. Serna, C. Molpeceres, J. Requena, A. Mifsud, F. Meseguer, and C. Lopez, "Electrophoretic deposition to control artificial opal growth," *Langmuir*, vol. 15, p. 4701, 1999.

[89] F. García-Santamaría, H. T. Miyazaki, A. Urquía, M. Ibisate, M. Belmonte, N. Shinya, F. Meseguer, and C. López, "Nanorobotic manipulation of microspheres for on-chip diamond architectures," *Advanced Materials*, vol. 14, p. 1144, 2002.

[90] S. Reculusa and S. Ravaine, "Synthesis of colloidal crystals of controllable thickness through the langmuir-blodgett technique," *Chemistry of Materials*, vol. 15, p. 598, 2003.

[91] A. Mihi, M. Ocaña, and H. Míguez, "Oriented colloidal-crystal thin films by spin-coating microspheres dispersed in volatile media," *Advanced Materials*, vol. 18, p. 2244, 2006.

[92] P. Jiang, T. Prasad, M. J. McFarland, and V. L. Colvin, "Two-dimensional nonclose-packed colloidal crystals formed by spincoating," *Applied Physics Letters*, vol. 89, p. 011908.

[93] J. Sun, C.-j. Tang, P. Zhan, Z.-l. Han, Z.-S. Cao, and Z.-L. Wang, "Fabrication of centimeter-sized single-domain two-dimensional colloidal crystals in a wedge-shaped cell under capillary forces," *Langmuir*, vol. 26, p. 7859, 2010.

[94] A. Van Blaaderen, R. Ruel, and P. Wiltzius, "Template-directed colloidal crystallization," *Nature*, vol. 385, p. 321, 1997.

[95] J. Sun, Y. Li, H. Dong, P. Zhan, C. Tang, M. Zhu, and Z. Wang, "Fabrication and light-transmission properties of monolayer square symmetric colloidal crystals via controlled convective self-assembly on 1d grooves," *Advanced Materials*, vol. 20, p. 123, 2008.

[96] N. N. Khanh and K. B. Yoon, "Facile organization of colloidal particles into large, perfect one- and two-dimensional arrays by dry manual assembly on patterned substrates," *Journal of the American Chemical Society*, vol. 131, p. 14228, 2009.

[97] N. Denkov, O. Velev, P. Kralchevski, I. Ivanov, H. Yoshimura, and K. Nagayama, "Mechanism of formation of two-dimensional crystals from latex particles on substrates," *Langmuir*, vol. 8, p. 3183, 1992.

[98] D. Norris, E. Arlinghaus, L. Meng, R. Heiny, and L. Scriven, "Opaline photonic crystals: How does self-assembly work?," *Advanced Materials*, vol. 16, p. 1393, 2004.

[99] Y. Kurokawa, H. Miyazaki, and Y. Jimba, "Optical band structure and near-field intensity of a periodically arrayed monolayer of dielectric spheres on dielectric substrate of finite thickness," *Physical Review B*, vol. 69, p. 155117, 2004.

[100] H.-G. Boyen, G. Kastle, F. Weigl, B. Koslowski, C. Dietrich, P. Ziemann, J. P. Spatz, S. Riethmuller, C. Hartmann, M. Moller, G. Schmid, M. G. Garnier, and P. Oelhafen, "Oxidation-resistant gold-55 clusters," *Science*, vol. 297, p. 1533, 2002.

[101] www.thermofisher.com.

[102] www.microparticles.de.

[103] E. Palacios-Lidon, B. H. Juarez, E. Castillo-Martinez, and C. Lopez, "Optical and morphological study of disorder in opals," *Journal of Applied Physics*, vol. 97, p. 063502, 2005.

[104] S. Im, M. H. Kim, and O. Park, "Thickness control of colloidal crystals with a substrate dipped at a tilted angle into a colloidal suspension," *Chemistry of Materials*, vol. 15, p. 1797, 2003.

[105] S. Yang, S. Jang, D. Choi, S. Kim, and H. Yu, "Nanomachining by colloidal lithography," *Small*, vol. 2, p. 458, 2006.

[106] G. N. Taylor and T. M. Wolf, "Oxygen plasma removal of thin polymer films," *Polymer Engineering and Science*, vol. 20, p. 1087, 1980.

[107] T. Ding, K. Song, K. Clays, and C.-H. Tung, "Bottom-up photonic crystal approach with top-down defect and heterostructure fine-tuning," *Langmuir*, vol. 26, p. 4535, 2009.

[108] A. Plettl, F. Enderle, M. Saitner, A. Manzke, C. Pfahler, S. Wiedemann, and P. Ziemann, "Polystyrene arrays: Non-close-packed crystals from self-assembled polystyrene spheres by isotropic plasma etching: Adding flexibility to colloid lithography," *Advanced Functional Materials*, vol. 19, p. 3279, 2009.

[109] C. Haginoya, M. Ishibashi, and K. Koike, "Nanostructure array fabrication with a size-controllable natural lithography," *Applied Physics Letters*, vol. 71, p. 2934, 1997.

[110] L. Yan, K. Wang, J. Wu, and L. Ye, "Hydrophobicity of model surfaces with loosely packed polystyrene spheres after plasma etching," *The Journal of Physical Chemistry B*, vol. 110, p. 11241, 2006.

[111] V. N. Astratov, D. M. Whittaker, I. S. Culshaw, R. M. Stevenson, M. S. Skolnick, T. F. Krauss, and R. M. De La Rue, "Photonic band-structure effects in the reflectivity of periodically patterned waveguides," *Physical Review B*, vol. 60, p. R16255, 1999.

[112] V. Astratov, V. Bogomolov, A. Kaplyanskii, A. Prokofiev, L. Samoilovich, S. Samoilovich, and Y. Vlasov, "Optical spectroscopy of opal matrices with cds embedded in its pores: Quantum confinement and photonic band gap effects," *Il Nuovo Cimento D*, vol. 17, p. 1349, 1995.

[113] K. Wostyn, Y. Zhao, G. de Schaetzen, L. Hellemans, N. Matsuda, K. Clays, and A. Persoons, "Insertion of a two-dimensional cavity into a self-assembled colloidal crystal," *Langmuir*, vol. 19, p. 4465, 2003.

[114] L. C. Andreani, A. Balestreri, L. Galisteo, oacute, J. F. pez, M. Galli, M. Patrini, E. Descrovi, A. Chiodoni, F. Giorgis, L. Pallavidino, and F. Geobaldo, "Optical response with threefold symmetry axis on oriented microdomains of opal photonic crystals," *Physical Review B*, vol. 78, p. 205304, 2008.

[115] D. Bajoni, D. Gerace, M. Galli, J. Bloch, R. Braive, I. Sagnes, A. Miard, Lema, icirc, A. tre, M. Patrini, and L. C. Andreani, "Exciton polaritons in two-dimensional photonic crystals," *Physical Review B*, vol. 80, p. 201308, 2009.

[116] P. García, A. Blanco, A. Shavel, N. Gaponik, A. Eychmüller, B. Rodríguez-González, L. M. Liz-Marzán, and C. López, "Quantum dot thin layers templated on zno inverse opals," *Advanced Materials*, vol. 18, p. 2768, 2006.

[117] C. Billaudeau, S. Collin, C. Sauvan, N. Bardou, F. Pardo, and J. Pelouard, "Angle-resolved transmission measurements through anisotropic two-dimensional plasmonic crystals," *Opt. Lett.*, vol. 33, p. 165, 2008.

[118] E. A. Saleh, *Fundamentals of Photonics*. Wiley Interscience, 1991.

[119] M. Richard, J. Kasprzak, R. Romestain, Andr, eacute, R., gis, and L. S. Dang, "Spontaneous coherent phase transition of polaritons in cdte microcavities," *Physical Review Letters*, vol. 94, p. 187401, 2005.

[120] W. J. Cottrell, J. D. Wilson, and T. H. Foster, "Microscope enabling multimodality imaging, angle-resolved scattering, and scattering spectroscopy," *Optics Letters*, vol. 32, p. 2348, 2007.

[121] J. Goodman, *Introduction to Fourier Optics*. Roberts and Company Publishers, 1968.

[122] M. Richard, J. Kasprzak, R. Romestain, R. André, and L. S. Dang, "Spontaneous coherent phase transition of polaritons in cdte microcavities," *Physical Review Letters*, vol. 94, p. 187401, 2005.

[123] "http://www.olympusmicro.com/primer/anatomy/kohler.html."

[124] M. T. Valentine, A. K. Popp, D. A. Weitz, and P. D. Kaplan, "Microscope based static light scattering instrument," *Optics Letters*, vol. 26, p. 890, 2001.

[125] J. Galisteo-López, F. López-Tejeira, S. Rubio, C. Lopez, and J. Sánchez-Dehesa, "Experimental evidence of polarization dependence in the optical response of opal-based photonic crystals," *Applied Physics Letters*, vol. 82, p. 4068, 2003.

[126] Y. Kurokawa, H. Miyazaki, and Y. Jimba, "Light scattering from a monolayer of periodically arrayed dielectric spheres on dielectric substrates," *Physical Review B*, vol. 65, p. 201102, 2002.

[127] R. M. Cole, J. J. Baumberg, F. J. Garcia de Abajo, S. Mahajan, M. Abdelsalam, and P. N. Bartlett, "Understanding plasmons in nanoscale voids," *Nano Letters*, vol. 7, p. 2094, 2007.

[128] X. Yu, L. Shi, D. Han, J. Zi, and P. V. Braun, "High quality factor metallodielectric hybrid plasmonicphotonic crystals," *Advanced Functional Materials*, vol. 20, p. 1910, 2010.

[129] S. G. Romanov, A. Korovin, A. Regensburger, and U. Peschel, "Hybrid colloidal plasmonic-photonic crystals," *Advanced Materials*, vol. 23, p. 2515, 2011.

[130] D. Gerace and L. C. Andreani, "Gap maps and intrinsic diffraction losses in one-dimensional photonic crystal slabs," *Physical Review E*, vol. 69, p. 056603, 2004.

[131] F. Garcia-Santamaria, J. F. Galisteo-Lopez, P. V. Braun, and C. Lopez, "Optical diffraction and high-energy features in three-dimensional photonic crystals," *Physical Review B (Condensed Matter and Materials Physics)*, vol. 71, p. 195112, 2005.

[132] P. Leiderer, C. Bartels, J. Konig-Birk, M. Mosbacher, and J. Boneberg, "Imaging optical near-fields of nanostructures," *Applied Physics Letters*, vol. 85, p. 5370, 2004.

[133] Y. Tanaka, G. Obara, A. Zenidaka, N. N. Nedyalkov, M. Terakawa, and M. Obara, "Near-field interaction of two-dimensional high-permittivity spherical particle arrays on substrate in the mie resonance scattering domain," *Optics Express*, vol. 18, p. 27226, 2010.

[134] V. R. Almeida, Q. Xu, C. A. Barrios, and M. Lipson, "Guiding and confining light in void nanostructure," *Optics Letters*, vol. 29, p. 1209, 2004.

[135] T. Baehr-Jones, M. Hochberg, C. Walker, and A. Scherer, "High-q optical resonators in silicon-on-insulator-based slot waveguides," *Applied Physics Letters*, vol. 86, p. 081101, 2005.

[136] E. D. Palik, *Handbook of Optical Constants of Solids*. Elsevier, 1998.

[137] S. X. She, "Metal-clad multilayer dielectric waveguide: accurate perturbation analysis," *J. Opt. Soc. Am. A*, vol. 7, p. 1582, 1990.

[138] Y. Bian, Z. Zheng, Y. Liu, J. Zhu, and T. Zhou, "Dielectric-loaded surface plasmon polariton waveguide with a holey ridge for propagation-loss reduction and subwavelength mode confinement," *Optics Express*, vol. 18, p. 23756, 2010.

[139] S. G. Johnson, S. Fan, P. R. Villeneuve, J. D. Joannopoulos, and L. A. Kolodziejski, "Guided modes in photonic crystal slabs," *Physical Review B*, vol. 60, p. 5751, 1999.

[140] T. H. Miyazaki, H. Miyazaki, K. Ohtaka, and T. Sato, "Photonic band in two-dimensional lattices of micrometer-sized spheres mechanically arranged under a scanning electron microscope," *Journal of Applied Physics*, vol. 87, p. 7152, 2000.

[141] P. D. García, R. Sapienza, L. Froufe, and C. López, "Strong dispersive effects in the light-scattering mean free path in photonic gaps," *Physical Review B*, vol. 79, p. 241109, 2009.

[142] J. F. Galisteo-López, E. Palacios-Lidón, E. Castillo-Martínez, and C. López, "Optical study of the pseudogap in thickness and orientation controlled artificial opals," *Physical Review B*, vol. 68, p. 115109, 2003.

[143] T. Baba, "Slow light in photonic crystals," *Nature Photonics*, vol. 2, p. 465, 2008.

[144] A. Andueza, R. Echeverria, and J. Sevilla, "Evolution of the electromagnetic modes of a single layer of dielectric spheres with compactness," *Journal of Applied Physics*, vol. 104, p. 043103, 2008.

[145] T. Fujimura, T. Tamura, T. Itoh, C. Haginoya, Y. Komori, and T. Koda, "Morphology and photonic band structure modification of polystyrene particle layers by reactive ion etching," *Applied Physics Letters*, vol. 78, p. 1478, 2001.

[146] S. G. Romanov, M. Bardosova, I. M. Povey, C. M. S. Torres, M. E. Pemble, N. Gaponik, and A. Eychmuller, "Modification of emission of cdte nanocrystals by the local field of langmuir–blodgett colloidal photonic crystals," *Journal of Applied Physics*, vol. 104, p. 103118, 2008.

[147] K. Ohtaka, J.-i. Inoue, and S. Yamaguti, "Derivation of the density of states of leaky photonic bands," *Physical Review B*, vol. 70, p. 035109, 2004.

[148] L. A. Dorado, R. A. Depine, D. Schinca, G. Lozano, and H. Miguez, "Experimental and theoretical analysis of the intensity of beams diffracted by three-dimensional photonic crystals," *Physical Review B*, vol. 78, p. 5, 2008.

[149] B. Stein, J. Y. Laluet, E. Devaux, C. Genet, and T. W. Ebbesen, "Surface plasmon mode steering and negative refraction," *Physical Review Letters*, vol. 105, p. 4, 2010.

[150] M. U. González, A. L. Stepanov, J. Weeber, A. Hohenau, A. Dereux, R. Quidant, and J. Krenn, "Analysis of the angular acceptance of surface plasmon bragg mirrors," *Optics Letters*, vol. 32, p. 2704, 2007.

[151] M. Notomi, "Theory of light propagation in strongly modulated photonic crystals: Refractionlike behavior in the vicinity of the photonic band gap," *Physical Review B*, vol. 62, p. 10696, 2000.

[152] L. Shi, H. Yin, X. Zhu, X. Liu, and J. Zi, "Direct observation of iso-frequency contour of surface modes in defective photonic crystals in real space," *Applied Physics Letters*, vol. 97, no. 25, p. 251111, 2011.

[153] C. López, "Materials aspects of photonic crystals," *Advanced Materials*, vol. 15, no. 20, p. 1679, 2003.

[154] J. Galisteo-López and C. Lopez, "High-energy optical response of artificial opals," *Physical Review B*, vol. 70, p. 035108, 2004.

[155] S.-M. Yang, S. G. Jang, D.-G. Choi, S. Kim, and H. K. Yu, "Nanomachining by colloidal lithography," *Small*, vol. 2, p. 458, 2006.

[156] M. Notomi, H. Suzuki, and T. Tamamura, "Directional lasing oscillation of two-dimensional organic photonic crystal lasers at several photonic band gaps," *Applied Physics Letters*, vol. 78, p. 1325, 2001.

[157] S. Furumi, H. Fudouzi, and T. Sawada, "Self-organized colloidal crystals for photonics and laser applications," *Laser and Photonics Reviews*, vol. 4, p. 205, 2009.

[158] R. F. Kubin and A. N. Fletcher, "Fluorescence quantum yields of some rhodamine dyes," *Journal of Luminescence*, vol. 27, p. 455, 1982.

[159] H. Benisty, H. De Neve, and C. Weisbuch, "Impact of planar microcavity effects on light extraction-part i: basic concepts and analytical trends," *Quantum Electronics, IEEE Journal of*, vol. 34, p. 1612, 1998.

[160] D. Pacifici, H. J. Lezec, and H. A. Atwater, "All-optical modulation by plasmonic excitation of cdse quantum dots," *Nature Photonics*, vol. 1, p. 402, 2007.

[161] P. R. Evans, G. A. Wurtz, W. R. Hendren, R. Atkinson, W. Dickson, A. V. Zayats, and R. J. Pollard, "Electrically switchable nonreciprocal transmission of plasmonic nanorods with liquid crystal," *Applied Physics Letters*, vol. 91, p. 043101, 2007.

[162] J. B. González-Díaz, A. García-Martín, G. Armelles, J. M. García-Martín, C. Clavero, A. Cebollada, R. A. Lukaszew, J. R. Skuza, D. P. Kumah, and R. Clarke, "Surface-magnetoplasmon nonreciprocity effects in noble-metal/ferromagnetic heterostructures," *Physical Review B*, vol. 76, p. 153402, 2007.

[163] V. V. Temnov, G. Armelles, U. Woggon, D. Guzatov, A. Cebollada, A. Garcia-Martin, J. Garcia-Martin, T. Thomay, A. Leitenstorfer, and R. Bratschitsch, "Active magneto-plasmonics in hybrid metal-ferromagnet structures," *Nature Photonics*, vol. 4, p. 107, 2010.

[164] D. Gèrard, V. Laude, B. Sadani, A. Khelif, D. Van Labeke, and B. Guizal, "Modulation of the extraordinary optical transmission by surface acoustic waves," *Physical Review B*, vol. 76, p. 235427, 2007.

[165] T. Fujimura, T. Tamura, T. Itoh, C. Haginoya, Y. Komori, and T. Koda, "Morphology and photonic band structure modification of polystyrene particle layers by reactive ion etching," *Applied Physics Letters*, vol. 78, p. 1478, 2001.

[166] G. V. Freymann, S. John, V. Kitaev, and G. Ozin, "Enhanced coupling to slow photon modes in three-dimensional graded colloidal photonic crystals," *Advanced Materials*, vol. 17, p. 1273, 2005.

[167] T. Ding, K. Song, K. Clays, and C. Tung, "Bottom-up photonic crystal approach with top-down defect and heterostructure fine-tuning," *Langmuir*, vol. 26, p. 4535, 2009.

[168] K. Busch, "Photonic band structure theory: assessment and perspectives," *Comptes Rendus Physique*, vol. 3, p. 53, 2002.

[169] W. L. Barnes, "Comparing experiment and theory in plasmonics," *Journal of Optics A: Pure and Applied Optics*, vol. 11, 2009.

[170] K. Yee, "Numerical solution of initial boundary value problems involving maxwell's equations in isotropic media," *Antennas and Propagation, IEEE Transactions on*, vol. 14, pp. 302–307, 1966.

[171] A. Taflove, "Application of the finite-difference time-domain method to sinusoidal steady-state electromagnetic-penetration problems," *IEEE Transactions on Electromagnetic Compatibility*, vol. 22, p. 191, 1980.

[172] A. Taflove, *Computational Electromagnetics: The Finite-Difference Time-Domain Method*. Artech House, 2005.

[173] C. Yu and H. Chang, "Yee-mesh-based finite difference eigenmode solver with pml absorbing boundary conditions for optical waveguides and photonic crystal fibers," *Optics Express*, vol. 12, p. 6165, 2004.

[174] J. Berenger, "A perfectly matched layer for the absorption of electromagnetic waves," *Journal of Computational Physics*, vol. 114, pp. 185–200, 1994.

[175] L. Solutions, "http://www.lumerical.com/fdtd.php."

[176] U. Fano, "Effects of configuration interaction on intensities and phase shifts," *Physical Review*, vol. 124, p. 1866, 1961.

[177] P. Viktorovitch, B. Ben Bakir, S. Boutami, J. L. Leclercq, X. Letartre, P. Rojo-Romeo, C. Seassal, M. Zussy, L. Di Cioccio, and J. Fedeli, "3d harnessing of light with 2.5d photonic crystals," *Laser and Photonics Reviews*, vol. 4, p. 401, 2009.

[178] M. Galli, S. L. Portalupi, M. Belotti, L. C. Andreani, L. O'Faolain, and T. F. Krauss, "Light scattering and fano resonances in high-q photonic crystal nanocavities," *Applied Physics Letters*, vol. 94, p. 071101, 2009.

Agradecementos

Durante estes anos foron moitas as persoas e intitucions que participaron neste traballo e as que quero expresa a miña gratitude polo apoio e a confianza prestada. Un sincero agradecimiento a mis Directores, Cefe y Juan, por todo el tiempo que me han dado, por sus sugerencias e ideas de las que tanto provecho he sacado, por el respaldo y la amistad. Debo un especial reconocimiento a la Minsiterio de Ciencia e Innovacion por la confianza que mostraron en mí al concederme una beca FPI. Tambien me complace agradecer la acogida, el apoyo y los medios recibidos en el Insitituto de Ciencia de MAteriales. Non podo olvidarme de agradecer tame a USC e especialmente a Vicente por todo-los bos ratos e o seu apoio constante durante estes anos.

Tampouco podo olvidarme de todo-los meus amigos de MAdrid dentro e fora do ICMM, o grupo "galego",a todo-los amigos de Bueu e Santiago, a xente do IO e a todo-los compañeiros cos que compartín despacho todos estes anos. Finalmente todo esto nunca tivera sido posible sen o apoio incondicional da miña familia,os eus pais e amiña irma.

Finalmente todo este traballo no e mais que unha parte moi pequena dos ultimos 5 anos da miña vida. O resto dese tempo está cheo das cousas verdaderiamente importantes na meirande parte gracias a Sara e a ela é a quen vai adicado todo este libro... e moitas mais cousas.

Martin 22 de Xuño de 2011